High Pressure Study of High-Temperature Superconductors

Von der Fakultät Mathematik und Physik der Universität Stuttgart
zur Erlangung der Würde eines Doktors der Naturwissenschaften
(Dr. rer. nat.) genehmigte Abhandlung

Vorgelegt von

Sofia-Michaela Souliou

aus Thessaloniki (Griechenland)

Hauptberichter:	Prof. Dr. Bernhard Keimer
Mitberichter:	Prof. Dr. Martin Dressel
Tag der mündlichen Prüfung:	29 September 2014

Max-Planck-Institut für Festkörperforschung
Stuttgart 2014

Contents

Zusammenfassung in deutscher Sprache

Die vorliegende Arbeit beschäftigt sich experimentell mit dem Einfluss von hohem, externen Druck auf Hochtemperatursupraleiter. Die Dynamik von Struktur- und Gitterparametern verschiedener Vertreter der cuprat- und eisenbasierten Supraleitern wurde unter präzise kontrolliertem, hohem hydrostatischen Druck und tiefen Temperaturen mittels Ramanspektroskopie und Röntgendiffraktion untersucht.

In den komplexen Phasendiagrammen dieser Systeme beeinflussen externe Parameter, wie z.B. chemische Dotierung und hohe Drücke, das Wechselspiel zwischen den unterschiedlichen, konkurrierenden Grundzuständen empfindlich. Hoher hydrostatischer Druck ist ein idealer, "sauberer" Parameter, da die Komplexität, die durch chemische Substitution oft eingebracht wird, vermieden wird und parallel dazu Messungen an chemisch dotierten Proben einen direkten Vergleich der beiden Parameter - Druck und Dotierung - auf die Phasenübergänge in diesen Systemen ermöglichen.

Die Gitter-Schwingungen des Hochtemperatur-Supraleiters $YBa_2Cu_3O_{6+x}$ wurden systematisch mittels Raman-Spektroskopie als Funktion von Dotierung (x = 0.95, 0.75, 0.60, 0.55, und 0.45) und externem Druck untersucht. Bei Normaldruck und tiefen Temperaturen, jedoch noch deutlich oberhalb des Übergangs zum supraleitenden Zustand, beobachten wir für unterdotierte Proben neue Raman-aktive Phononen zusätzlich zu den gemäß der Gruppen-Theorie erwarteten Raman-Moden. In den Raman-Spektren von optimal dotierten Proben wurden keine entsprechenden neuen Phononen beobachtet. Die neuen Phononen sind in Resonanz mit dem eingestrahlten roten Laserlicht (1.96 eV) und besitzen gemäß den Raman-Auswahlregeln A_g-Symmetrie. Das Einsetzen der neuen Raman-Moden unterhalb bestimmter Temperaturen und ihre Dotierungsabhängigkeit legen einen Zusammenhang mit der inkommensurablen Ladungsdichtewelle (CDW) nahe, die kürzlich durch Methoden der Synchrotron- Röntgenstreuung in unterdotierten Cupraten entdeckt wurde [1, 2]. Im CDW-Zustand würde die Rückfaltung der ursprünglichen $YBa_2Cu_3O_{6+x}$ Phononen-Dispersion in die neue Brillouin-Zone zu neuen optische Moden am Γ-Punkt führen und ihre Beobachtung in den Raman-Spektren ermöglichen.

Unter hohem Druck und innerhalb des von uns untersuchten Bereichs (von 2 bis 12 GPa) zeigen unsere Raman-Messungen an hochgeordnetem, unterdotiertem $YBa_2Cu_3O_{6.55}$ keine der neuen Raman-Phononen, die bei Normaldruck beobachtet wurden. Hierfür gibt

es zwei mögliche Ursachen. Erstens könnte dies, im Rahmenkonzept der CDW, mit einer druckinduzierten Unterdrückung der Ladungsordnung zusammenhängen. Dies wird in einem Szenario mit konkurrierenden Phasen erwartet und ist in Übereinstimmung mit früheren Beobachtungen in $La_{1.875}Ba_{0.125}CuO_4$ mit Streifenordnung [3, 4]. Andererseits könnte unsere Beobachtung auf druckinduziertes Relaxationsverhalten der Sauerstoffatome innerhalb der sauerstoffdefizitären Cu-O-Ketten zurückzuführen sein, worauf auch ältere Magnetisierungsmessungen bei hohen Drücken hinweisen [5]. Ferner beobachten wir in unseren Hochdruck-Daten eine ausgeprägte, druckinduzierte Rotverschiebung der Resonanzbedingungen für Raman-Moden, die auf Defekte in den Ketten zurückgehen. Eine analoge druckinduzierte Verschiebung der Resonanzbedingungen für die neuen Moden würde auch ihr Ausbleiben bei hohen Drücken erklären.

Ramanmessungen unter hohem Druck und tiefen Temperaturen wurden an dem unterdotierten Supraleiter $YBa_2Cu_4O_8$ durchgeführt, der, aufgrund der stöchiometrischen Zusammensetzung, nicht durch das komplexe Zusammenspiel von Sauerstofffehlstellen und druckinduziertem Relaxationsverhalten beeinflusst wird. Dabei wird unterhalb der kritischen Temperatur eine deutliche Renormalisierung einiger Ramanmoden beobachtet, die eine Folge von Veränderungen in der Phononeigenenergie durch die Öffnung der supraleitenden Bandlücke ist. Die markanteste hiervon ist die B_{1g}-ähnliche Buckling-Mode. Das Ausmaß dieser Renormalisierung nimmt mit dem Druck stark zu, ähnlich dem Einfluss von Lochdotierung in $YBa_2Cu_3O_{6+x}$. In $YBa_2Cu_3O_{6+x}$ ist die Phononrenormalisierung im unterdotierten Bereich schwach und steigt in Richtung optimaler Dotierung an, wo sie vergleichbar ist mit der Renormalisierung in $YBa_2Cu_4O_8$ bei 10 GPa. Bei einem Druck von etwa 10 GPa geht das System durch einen reversiblen, druckinduzierten, strukturellen Phasenübergang zu einer nicht-punktsymmetrischen Struktur über, in der die CuO_2-Ebenen fast unbeeinflusst bleiben, während die doppelten Cu-O-Ketten kollabieren (Raumgruppe *Imm*2) [6]. Der Strukturübergang spiegelt sich durch das Auftreten neuer Moden eindeutig in den Ramandaten wider. Dadurch ist es uns möglich das (P,T)-Phasendiagramm im Detail abzubilden und die Grenze zwischen den beiden Phasen zu bestimmen. In der neuen Phase wird die Renormalisierung der Buckling-Mode vollständig unterdrückt. Zugleich werden in keinem anderen Raman-aktivem Phonon Anomalien beobachtet. Ab-initio-Berechnungen, die sehr genau die neue Struktur und die zugehörigen, experimentell bestimmten Phononfrequenzen reproduzieren, zeigen, dass die Kopplung zwischen der Buckling-Mode und dem elektronischen System nicht signifikant durch den Phasenübergang beeinflusst wird. Die Abwesenheit von Phononrenormalisierungen bei gleichzeitiger Anwesenheit beträchtlicher Elektronen-Phononen-Kopplung weist darauf hin, dass, im Gegensatz zu älteren Transportmessungen [7], $YBa_2Cu_4O_8$ unter einem hydrostatischen Druck von über 10 GPa nicht mehr supraleitend ist.

Abschließend untersuchten wir die strukturellen Eigenschaften und Gitterschwingungen von SmFeAsO unter hohem Druck. Dieses ist ein Vertreter der "1111"-Familie (Raumgruppe *P*4/*nmm*) der eisen-basierten Supraleiter, in der die Supraleitung für gewöhnlich entweder durch die Substitution von O durch F/H oder durch den Einsatz hoher Drücke

im undotierten Material hervorgerufen wird, dessen magnetischer Übergang durch eine Änderung der Struktur von tetragonal zu orthorhombisch begleitet wird. Beides wird normalerweise durch das Auftreten der Supraleitung unterdrückt. Während der magnetische Übergang in dem System von $SmFeAsO_xF_{1-x}$ bereits bei niedriger Dotierung komplett unterdrückt wird, zeigten strukturelle Untersuchungen entweder die allmähliche Verdrängung der orthorhombischen Verzerrung [8] oder ihre Beibehaltung über einen weiten Bereich der supraleitenden Phase [9]. Diese Kontroverse brachte uns dazu, hohe Drücke als weiteren, fein justierbaren Parameter anzuwenden, um den magneto-strukturellen Übergang zu unterdrücken und im undotierten Material Supraleitung hervorzurufen. Unsere Röntgenbeugungsmessungen unter hohem Druck und bei niedrigen Temperaturen an SmFeAsO-Einkristallen zeigten, dass der strukturelle Übergang bei Drücken bis zu 85 kbar fortbesteht. Bei höheren Drücken wird hingegen die Temperatur des strukturellen Phasenübergangs zu niedrigeren Werten gedrängt und der Grad der orthorombischen Verzerrung sinkt. Der strukturelle Übergang spiegelt sich auch in unseren Niedertemperatur-Ramanspektren von SmFeAsO durch die Aufspaltung der doppelt-entarteten Phononmoden mit E_g-Symmetrie wider. Außerdem zeigten unsere Ramandaten eine Renormalisierung der Linienbreite der in Richtung der c-Achse polarisierten A_{1g}- und B_{1g}-Raman-Phononen beim Durchschreiten des magnetischen Übergangs. Ähnliches wurde zuvor im "122"-System beobachtet und der Öffnung einer Bandlücke durch das Auftreten einer Spindichtewelle zugesprochenen [10]. Die Renormalisierung wird durch hohe Drücke graduell unterdrückt. Dies ist in Übereinstimmung mit früheren Magnetisierungsmessungen, die gezeigt hatten, dass die magnetische Übergangstemperatur bei höheren Drücken sinkt [11]. Die Anomalie in der Linienbreite verschwindet bei 8 GPa, was die vollständige Unterdrückung des magnetischen Übergangs bei diesem Druck andeutet.

Schließlich befasst sich ein zusammenfassender Kommentar mit der Bedeutung der Untersuchung von Hochtemperatur-Supraleitern unter hohen Drücken. Solche Messungen leisten vielfältige Beiträge zur Studie des Phänomens, wie beispielsweise durch die Entwicklung neuer Supraleiter, das Erreichen von Rekordwerten für T_c, neue experimentelle Erkenntnisse, die für ein besseres Verständnis der verantwortlichen Mechanismen zuständig sind, sowie das Überprüfen bestehender Theoriemodelle. Wie in dieser Arbeit an verschiedenen Punkten ausdrücklich betont wurde, ist eine präzise Kontrolle des angelegten Drucks von ausschlaggebender Bedeutung, um ein detailliertes und quantitatives Verständnis zu erlangen. Um dies zu erreichen, wurden alle Hochdruckmessungen unter genauester Kontrolle der hydrostatischen Bedingungen und mit hochentwickeltem, experimentellem Equipment durchgeführt, was eine hohe Qualität der Daten gewährleistete. Der Vergleich oder das Zusammenführen von Hochdruckdaten, insbesondere von anisotropen und stark korrelierten Elektronensystemen mit fein justierbaren, miteinander konkurrierenden Wechselwirkungen, ist nur dann zu rechtfertigen, wenn diese Daten unter vergleichbaren hydrostatischen oder uniaxialen Bedingungen entstanden sind.

Introduction

Almost one hundred years after its first discovery, superconductivity remains a fascinating field of active research and scientific excitement. The driving force behind this ongoing interest is not only achieving a deep understanding and control of the underlying mechanism but also the huge potential for technological and commercial applications. To this purpose and up to date, there is a continuous effort to find new materials exhibiting higher T_c values, with the ultimate objective of realizing room temperature superconductivity.

The phenomenon of superconductivity was first observed by H. Kammerlingh Onnes in 1911 in metallic mercury [12]. During the following years superconductivity was found in a number of metallic elements, such as Pb and Nb, as is shown in the timeline of Fig. 0.1. An important discovery came in 1933, with the observation of the diamagnetic behavior of superconductors by W. Meissner and R. Ochsenfeld (Meissner effect), establishing the superconducting state as a thermodynamic phase and offering new input for the theoretical understanding of the phenomenon [13]. Important theoretical contributions came from the London theory in 1935 [14] and from the macroscopic Ginzburg-Landau theory in 1950 [15], but the fundamental breakthrough took place in 1957 with the development of the microscopic BCS theory by J. Bardeen, L. N. Cooper, and J. R. Schrieffer [16]. According to the BCS theory the superconducting state is realized when the conduction electrons pair up under an attractive interaction to form Cooper pairs, condensing coherently in a macroscopic wavefunction. In conventional metallic superconductors the attractive interaction is mediated by phonons (electron-phonon interaction), as was nicely experimentally demonstrated by the isotope effect [17, 18]. The huge success of the BCS theory was followed by a scientific effort to raise the observed T_c through the synthesis of materials with high density of states and electron-phonon coupling constants (A-15 type compounds, e.g. Nb_3Ge). Later on, the observation of superconductivity in heavy fermion systems [19] brought new insights on the interplay between magnetism and superconductivity and on non-phonon-mediated superconductivity.

A true revolution in the field came in 1986 when K. Müller and J. Bednorz discovered superconductivity in copper-oxide based compounds (cuprates) [20] and inaugurated the era of high temperature superconductivity. The T_c values of the cuprates range between 35 K and 160 K (under pressure) and therefore exceed the boiling point of liquid nitrogen.

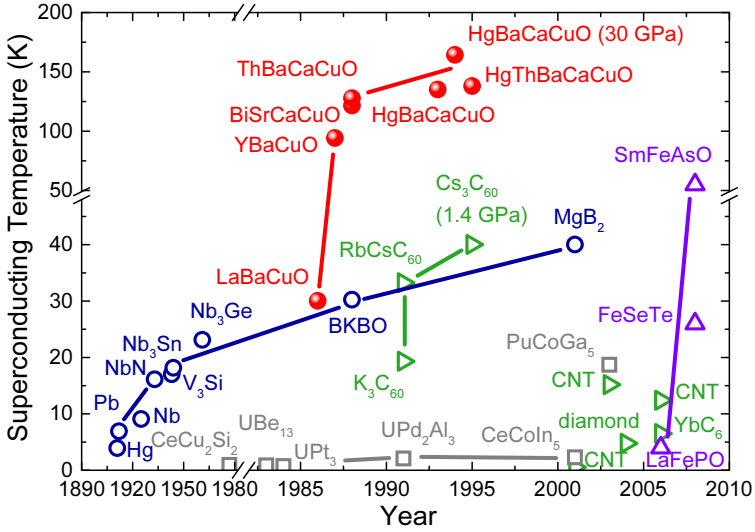

Figure 0.1: Timeline of the superconducting transition temperature of a number of selected compounds belonging in different superconductor families: the blue circles correspond to conventional superconductors, the green triangles to the carbon-based materials, the red spheres to the cuprates family, the grey squares to the heavy-fermion compounds, and the purple triangles to the iron-based superconductors. The solid lines are guide to the eye. The figure is adapted from Wikipedia (History of superconductivity).

Soon it became clear that the cuprates bear significant differences to the conventional superconductors and that most importantly a phonon-mediated BCS picture is insufficient to describe their physics and to account for their high T_c values. The differences start already in the normal state of these systems, in which they exhibit a clear deviation from the Fermi liquid theory. A key element in the physics of high-T_c cuprates (following also the discovery of heavy-fermion superconductivity) was proven to be their close proximity to a magnetic phase, which in combination with numerous experimental and theoretical studies have suggested spin-fluctuations as the most plausible origin of the superconducting pairing. Detailed experimental work has revealed a complex phase diagram consisting of various phases (competing or not with superconductivity) commonly tuned by controlling the charge carrier concentration (doping).

A new surprise in the field came in 2006 with the discovery of superconductivity in an Fe-based compound in the group of H. Hosono [21]. Very fast a whole new family of superconductors was generated, exhibiting a maximum T_c of ~55 K and leading to a boost of experimental and theoretical activity. Fe-based superconductors have opened

new perspectives in addressing the problem of high-T_c superconductivity and testing existing theories. The rich experience accumulated during the detailed investigation of high-T_c cuprates was successfully exploited in the study of Fe-based superconductors. It soon became clear that the two families have many similarities, such as the layered crystal structure and the close vicinity to static magnetism, displaying moreover very similar phase diagrams. In addition, early calculations have indicated that also in the iron-based superconductors, a solely phonon-mediated pairing mechanism is not adequate for their description.

In the current experimental thesis, several members of the cuprate and Fe-based high-T_c superconductor families are studied experimentally using Raman scattering and x-ray diffraction under high pressure conditions. Pressure constitutes a powerful external variable, capable of tuning the ground state of a system without modifying its chemical composition. This is particularly useful in the case of cuprates and Fe-based multinary superconductors, in which superconductivity is delicately controlled through chemical doping. High pressure application offers an alternative "clean" route to induce and optimize superconductivity in these systems, while keeping the lowest possible physical and chemical complexity. Hydrostatic pressure studies of oxide superconductors have shed light on the interplay of the various competing ground states of their phase diagrams and contributed to a better understanding of the mechanism of superconductivity [22].

The thesis is organized as follows: after this general introduction, chapter 1 presents a small overview of the cuprate and Fe-based high-T_c superconductors with special emphasis on the information relevant to the results of this work, and more specifically on the studied systems and on previous high pressure studies. A brief theoretical introduction to Raman scattering, focused mostly on phononic Raman scattering and on Raman scattering under high pressure conditions is given in chapter 2. The same chapter includes a detailed description of the Raman active phonon modes of the studied systems based on group theory considerations, as well as details of the data analysis. Chapter 3 introduces the main experimental equipment used for the application of the high pressure and low temperature conditions of our experiments as well as the Raman and x-ray diffraction setups used to acquire high quality experimental data. Chapters 4, 5 and 6 are dedicated to the presentation of the experimental results on the $YBa_2Cu_3O_{6+x}$, $YBa_2Cu_4O_8$ and SmFeAsO systems respectively. Finally, a brief summary is included, giving the main experimental observations and conclusions for the different compounds studied in this thesis, together with some general remarks.

Chapter 1

High-Temperature Superconductors

1.1 Cuprate superconductors

1.1.1 Crystal Structure and Carrier Doping

Since the discovery of the first high-temperature (high-T_c) cuprate superconductor, a quite large number of structures belonging to the cuprate family has emerged. The main motivation behind this growth has been the search for compounds with modified structures exhibiting higher superconducting transition temperatures. The same interest in maximizing the T_c has led to the implementation of high pressure techniques in the study of the cuprates. The outcome of this effort is the current record of T_c=134 K at ambient pressure and T_c=164 K under a pressure of ~30 GPa in $HgBa_2Ca_2Cu_3O_{8+x}$ [23, 24, 25].

The cuprate superconductors are divided into structural subgroups. The most widely studied structural systems are the $YBa_2Cu_3O_{6+x}$ family ("123"), the Bi-, Tl- and Hg-type families described by the generic formula $A_mM_2Ca_{n-1}Cu_nO_x$, where A = Bi, Tl, Hg and M = Ba, Sr, and the $La_{2-x}Sr_xCuO_{4+\delta}$ family ("214"). The crystal structures of four members of these families are plotted in Fig. 1.1 [26].

All the different high-T_c cuprates display a layered structure with a stacking sequence along the c-axis composed of two main building blocks: the CuO_2 planes and the charge-reservoirs blocks. The one key structural element that all cuprate superconductors have in common are the CuO_2 planes, highlighted in the low part of Fig. 1.1, whereas their structural diversity lies in the nature of the charge reservoir.

It is in the CuO_2 planes where superconductivity occurs as the charge carrier concentration is varied [23, 27, 28, 29]. The number n of CuO_2 planes per unit cell is not fixed and it is generally observed that T_c increases with increasing n (the maximum T_c is observed for n=3 [30]). In single-layered compounds, each plane copper ion is surrounded by five oxygen ions, four of which are located in the CuO_2 plane and one of them in the

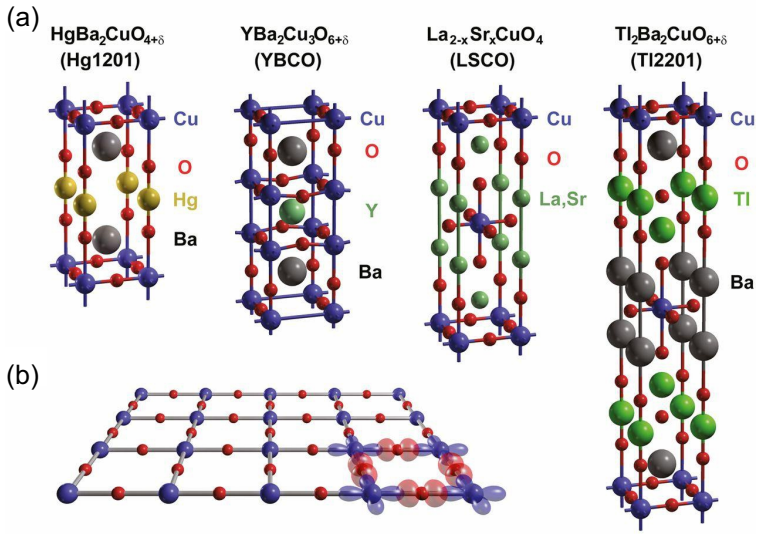

Figure 1.1: (a) Crystal structures of four cuprates: $HgBa_2CuO_{4+\delta}$ (Hg1201), $YBa_2Cu_3O_{6+\delta}$ (YBCO), $La_{2-x}Sr_xCuO_4$ (LSCO) and $Th_2Ba_2CuO_{6+\delta}$ (Tl2201). For Hg1201, YBCO, and Tl2201, the hole concentration in the CuO_2 planes is altered by varying the oxygen content, whereas in LSCO holes are introduced by replacing La^{3+} with Sr^{2+}. (b) The universal building block of the high-T_c cuprates is the CuO_2 plane. In the figure are shown the Cu $d_{x^2-y^2}$ and O p_σ electronic orbitals. The figure is taken from reference [26].

out-of-plane c-axis direction (the so-called apical oxygen). The resulting structure is a variation of the perovskite structure with corner-sharing CuO_6 octahedra. The anisotropy between the directions parallel and perpendicular to the CuO_2 layers highlights the two-dimensional character of the cuprate superconductors and is clearly reflected in many of their properties, e.g. in their transport properties (a recent review is given in [31]).

While the key-role in the emergence of superconductivity is played by the CuO_2 planes, the contribution of the charge-reservoir blocks is nevertheless critical. The physical properties and the superconducting T_c of cuprates are strongly influenced by the concentration of charge carriers (holes) on the CuO_2 planes[i]. The charge carriers are promoted from the charge reservoir block to the CuO_2 planes, and their concentration is regulated through the variation of the charge reservoir block composition, a procedure commonly referred

[i]For the sake of accuracy it should be mentioned that superconductivity can also be induced through electron doping within a narrow doping range. Electron-doped cuprates exhibit superconducting transition temperatures smaller compared to hole-doped ones and present significant differences in their electronic and magnetic properties, as well as in their phase diagram, as is summarized in the review of reference [32]. For the current thesis, only hole-doped cuprates will be examined and therefore there will be no further remarks on the electron-doped case.

as "chemical doping", or through the application of external pressure. The hole doping level p is defined as the number of holes per planar copper atom and is the most important parameter in determining the properties of high-T_c cuprates. There are two main ways to chemically hole-dope the cuprates: either by substituting the metallic atoms with higher valence atoms, as is typically performed in the case of the 214 family, or by changing the oxygen content, as is typically performed in the case of the 123 family.

The superconducting transition temperature T_c has a parabolic dependence on the hole doping level p which is approximately described for a large number of cuprates by the universal formula [33, 34]:

$$T_c = T_c^{max}[1 - 82.6(p - p_{opt})^2] \tag{1.1}$$

The resulting dome-like shape of the doping dependence of T_c is plotted in Fig. 1.2 with the red dotted line, together with experimental data for $YBa_2Cu_3O_{6+x}$ from reference [34]. In the same figure, the different regions of the phase diagram are marked: superconductivity appears as charge is transferred from the charge reservoir blocks to the CuO_2 planes above a critical doping level $p \gtrsim p_c$. The maximum value of T_c is observed for the *optimal doping* level, which for a large number of compounds has the value $p_{opt} \sim 0.16$. In the *underdoped regime* of the phase diagram T_c increases with doping, whereas in the *overdoped regime* T_c decreases upon doping increase. For higher doping levels superconductivity disappears and a metallic region appears in the phase diagram ($p \geq 0.27$, not shown in Fig. 1.2). The generally good agreement of the expression given in Eq. 1.1 deviates significantly from the experimental values of T_c for $p \sim 0.12$, where T_c is suppressed and a plateau is formed in the p dependence. The origin of this plateau will be discussed in the section 1.1.3 where the different phases of the cuprate phase diagram will be analyzed.

Upon increasing the charge carrier concentration not only the values of T_c but also

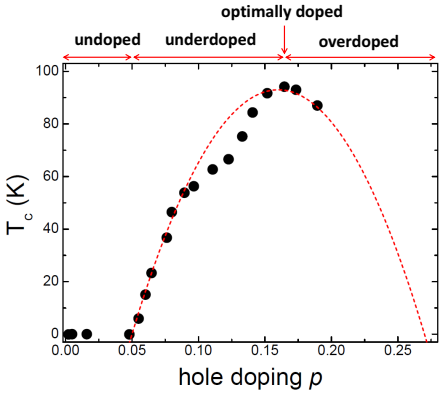

Figure 1.2: Doping dependence of T_c. The different doping regions of the phase diagram are marked on top. The red curve corresponds to the universal expression of Eq. 1.1 for T_c^{max}=93K and p_{opt}=0.16, whereas the experimental data points correspond to the $YBa_2Cu_3O_{6+x}$ system and are taken from reference [34].

the normal state behavior changes drastically from insulating in the undoped cuprates to metallic in the overdoped cuprates. What is crucial to emphasize in anticipation of the electronic properties that will be discussed next, is that the parent compounds of the copper-oxide superconductors are at low temperatures antiferromagnetic Mott insulators. This is in contrast to the predictions of DFT band structure calculations according to which the undoped compounds should be metallic. The reason behind this failure of band theory lies in the existence of strong electronic correlations due to the strong Coulomb repulsion between two copper d-electrons, as will be analyzed in the next section.

1.1.2 Electronic Structure

The crucial role of the CuO_2 planes is highlighted not only by the structural description, but even better by the description of the electronic structure. The Cu-O bands are the lowest-energy occupied electronic states and therefore directly determine the macroscopic electronic properties. The current short summary of the electronic properties of high-T_c cuprates will be based on references [23, 35, 36] where a more detailed description can be found.

In the undoped parent compounds, like the $YBa_2Cu_3O_6$ compound of the 123 family, the plane copper is in a $3d^9$ electronic configuration. In the octahedral environment of the surrounding oxygens the fivefold degeneracy of the d orbitals is lifted by the crystal field. In a crystal field of cubic symmetry O_h (like the one of a proper octahedron CuO_6), the $e_g = \{d_{z^2}, d_{x^2-y^2}\}$ orbitals which point directly towards the p orbitals of the surrounding oxygens experience a higher overlap and have a higher electrostatic energy compared to the $t_{2g} = \{d_{xy}, d_{xz}, d_{yz}\}$ orbitals which point in the direction between the oxygens. The partial occupancy of the e_g orbitals leads to a degeneracy of the ground state which induces a Jahn-Teller distortion of the octahedron and a reduction of symmetry from the cubic O_h to the tetragonal D_{4h}. As a result, the e_g levels split further into the non-degenerate $d_{3z^2-r^2}$ and $d_{x^2-y^2}$ levels, with the latter lying higher and being the copper state with the highest energy. The degenerate atomic $2p$ oxygen levels p_x, p_y, p_z split in the crystal field of D_{2h} site symmetry into three levels $\pi_\perp$, $\pi_\parallel$ and σ. The π-type states correspond to the p orbitals which are directed perpendicular to the Cu-O bonds, whereas the σ-type states to the ones which are directed along the Cu-O bonds.

The large overlap of the copper $3d$ orbitals with the $2p$ orbitals of the ligand oxygens causes a strong hybridization between them. The hybridization of the π-type states with the copper orbitals is weak and leads to narrow π bands. The t_{2g} states are not influenced by the σ-type states, whereas the e_g levels combine with the σ-states. More specifically, the combination of the four oxygen σ-type orbitals with a $d_{x^2-y^2}$ copper orbital produces a broad bonding σ and anti-bonding σ^* state, whereas they do not couple with the $d_{3z^2-r^2}$ orbital and result in a narrow non-bonding oxygen band which is positioned between the bonding σ and anti-bonding σ^* states. A schematic illustration of the formation of hybridized Cu-O bands is given in Fig. 1.3.

From the picture of the electronic structure depicted in Fig. 1.3 and from band structure

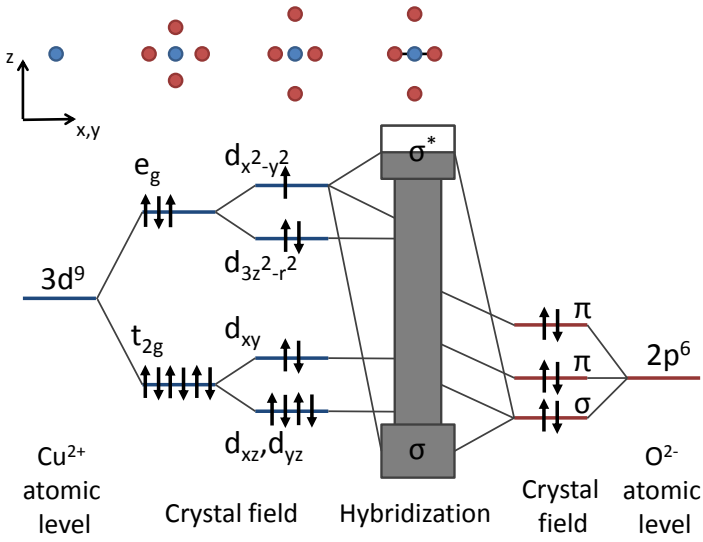

Figure 1.3: The electronic structure in the Cu-O planes of the cuprates. The atomic positions and atomic levels of copper are shown with blue, whereas the ones of oxygen are shown with red. The atomic levels of Cu^{2+} and O^{2-} split under the influence of the cubic crystal field of the CuO_6 octahedra. The Jahn-Teller distortion decreases the symmetry from cubic to tetragonal and further splits the the e_g and t_{2g} levels. The hybridization of the copper and oxygen states leads to the formation of well separated bonding and antibonding bands with the latter one being half filled. The figure is adapted from [36]

calculations using the local density approximation (LDA) it follows that the undoped parent cuprates are non-magnetic metals with a half filled conduction band (the anti-bonding σ^* band). As already mentioned, this is in clear disagreement with the observed insulating antiferromagnetic behavior of the parent compounds, manifesting the importance of the electron-electron correlations in the physics of high-T_c cuprates. On one hand, electrons have a certain probability to hop to their next neighbor copper site and lower the energy of the system and on the other hand there is a strong Coulomb repulsion between two electrons on the same copper site.

The most well-known theoretical model capable of describing these correlation effects is the *Hubbard model* [37]. The Hamiltonian of the one-band Hubbard model is a sum of two terms:

$$H = -t \sum_{\langle i,j\rangle,\sigma} c^{\dagger}_{i,\sigma} c_{j,\sigma} + U \sum_{i,\sigma} n_{i\uparrow} n_{i\downarrow} \tag{1.2}$$

The first term is the kinetic term of the electron hopping in a conduction band of width W,

where t is the hopping amplitude (W=2zt, where z is the number of nearest neighbors), $\langle ij \rangle$ identifies the nearest-neighbor pairs over which the summation is performed and $c^{\dagger}_{i,\sigma}$ and $c_{j,\sigma}$ are creation and annihilation operators for an electron on site i with spin σ= ($\uparrow$,$\downarrow$). The minus sign in front of the kinetic term indicates the energy gain of the system via hopping. The hopping amplitude depends on the orbital overlap and offers a measure of the bandwidth W.

The second term is the potential term expressing the local Coulomb interaction, which acts in favor of the electron localization. U is energy cost of double occupancy on a single copper site (the so called "Hubbard-U") and $n_{i,\sigma}$ is the electron occupation number.

The relative magnitude of U and t (or of U and W) determines which of the two terms prevails. For $U \ll t$ the hoping term dominates and the Hamiltonian describes a metallic state, whereas in the case of $U \gg t$ the Coulomb repulsion governs the Hubbard model. For a very large Coulomb repulsion U, the Hubbard Hamiltonian simplifies into the t-J Hamiltonian, which is commonly used for the study of the low-energy excitations of the cuprates:

$$H = -t \sum_{\langle i,j \rangle,\sigma} (\tilde{c}^{\dagger}_{i,\sigma} \tilde{c}_{j,\sigma} + c_{i,\sigma} c^{\dagger}_{j,\sigma}) + J \sum_{i,\sigma} (\mathbf{S}_i \cdot \mathbf{S}_j - \frac{1}{4} n_i n_j) \tag{1.3}$$

where the operator $\tilde{c}^{\dagger}_{i,\sigma}$= $c_{i,\sigma}$(1-$n_{i,-\sigma}$) excludes double occupancy, J=$\frac{4t^2}{U}$ is the antiferromagnetic exchange coupling constant, and $\mathbf{S}_i$ is the spin operator. At half filling at low energies the charge excitations are gapped and the remaining spin excitations are according to Eq. 1.3 described by the antiferromagnetic Heisenberg Hamiltonian H_j=$J\sum_{i,\sigma}\mathbf{S}_i \cdot \mathbf{S}_j$.

In the case of the parent compounds of high-T_c cuprates the Coulomb energy is $U \simeq$8-10 eV, which is much larger than the typical width of the antibonding band $W \simeq$3 eV (strong correlation limit). This leads to the splitting of the antibonding band in two subbands, the lower Hubbard band (LHB) and the upper Hubbard band (UHB), with the UHB being empty, as shown in Fig. 1.4. The system therefore becomes an insulator. The antiferromagnetic state derives then from the fact that the electrons gain kinetic energy by undergoing virtual hopping to neighboring sites, which can be realized only when nearest-neighbor spins are antiparallel to each other due to the Pauli principle.

Different types of electronic structure are realized depending on the values of the Coulomb repulsion U and the charge-transfer excitation energy Δ_{pd}. Δ_{pd} is the energy required to move a charge from an oxygen site to a copper site, which in our case corresponds to the energy difference between the non-bonding oxygen band and the UHB. The different cases are illustrated in Fig. 1.4:

1. In the extreme case of U=0 (non-interacting system) the system is metallic with a half filled antibonding band as shown in the first panel of Fig. 1.4.

2. In the case that $\Delta_{pd} > U > 0$ then the band gap is determined by U and the system is a *Mott-Hubbard insulator*. The gap U is separating the two Hubbard bands and corresponds to the charge transfer between two d^n_i copper ions of charges n at lattice sites i, j: $d^n_i + d^n_j \rightarrow d^{n-1}_i + d^{n+1}_j$.

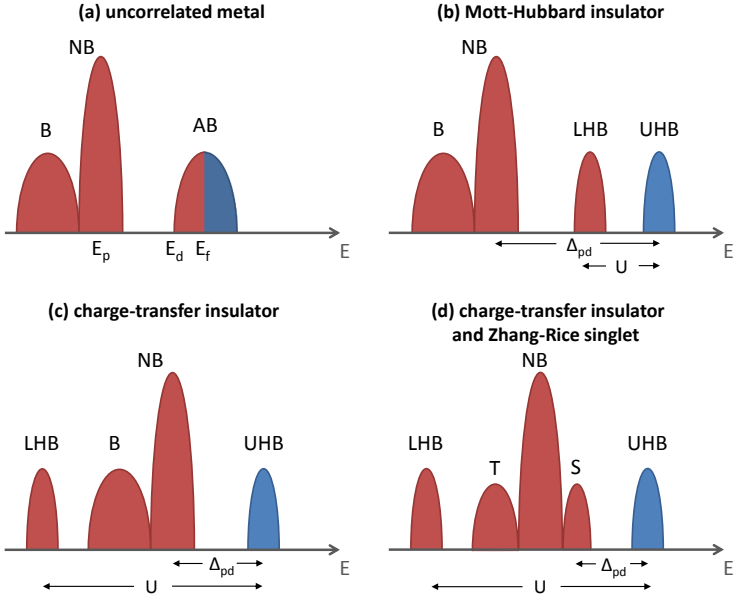

Figure 1.4: Schematic illustration of the density of states of the cuprates in the case of (a) a metallic state at half-filling of the antibonding band with U=0, (b) a Mott-Hubbard insulator when $\Delta_{pd} \gg U$, (c) a charge-transfer insulator when $\Delta_{pd} \ll U$ and (d) a charge-transfer insulator with the bonding band splitting into triplet and Zhang-Rice singlet states upon doping. The red color corresponds to filled and the blue to empty states. The figure is adapted from [35]

3. In the case that $U > \Delta_{pd} > 0$ then the insulator correlation gap is determined by Δ_{pd} and the system is a *charge-transfer insulator*. The gap Δ_{pd} is separating the UHB and the non-bonding oxygen band and corresponds to a charge transfer from an oxygen p level to a d level of an adjacent copper: $d_i^n \rightarrow d_i^{n+1} + L$, where with L denotes a hole in the oxygen level. It is just this situation of a *charge-transfer insulator* that is realized in undoped cuprates, for which the hole transfer energy from Cu^{2+} to Cu^{3+} $\Delta_{pd} \simeq$3-4 eV is smaller than the correlation energy of two holes $U \simeq$8-10 eV. Taking into account the charge-transfer character of the insulating state and considering explicitly both the Cu $3d_{x^2-y^2}$ and the O 2_{px} and 2_{py} orbitals, brings us to the *three-band Hubbard model* as described in reference [38].

While for the undoped case an electronic structure similar to that shown in the third panel of Fig. 1.4 is realized, upon hole doping the parent compounds a relatively diverse picture arises: due to the strong hybridization between the copper and the oxygen orbitals there exists a strong exchange interaction between the spin of a doped hole on a square of

oxygens and the hole spin of the central copper. As a result the *p-d* band splits into a triplet (S=1) and a singlet (S=0) band and the so-called *Zhang-Rice singlet* is formed [39]. The first electron removal states corresponds to the Zhang-Rice singlet and the system can be described by an effective single-band Hubbard model with the Zhang-Rice singlet band playing the role of the lower Hubbard band.

The insulating undoped and metallic overdoped cuprates fit reasonably well in the framework of the electronic structure described here. The major challenge is the understanding of the underdoped part of the phase diagram and especially the evolution of the electronic structure as holes are introduced in the parent insulating compounds. In order to better elucidate the issue the doping evolution of the physical properties of high-T_c cuprates will be described next.

1.1.3 Phase diagram

The strongly correlated electronic nature of high-T_c cuprates leads to the emergence of various competing phases as a function of hole doping. The generic doping-temperature phase diagram of hole-doped high-T_c cuprates is presented in Fig. 1.5.

With increasing the hole doping p, the system evolves from an antiferromagnetic insulating phase at zero/low doping to a metallic phase, successfully described by Fermi liquid theory, at high doping [40]. At intermediate doping levels between the insulating

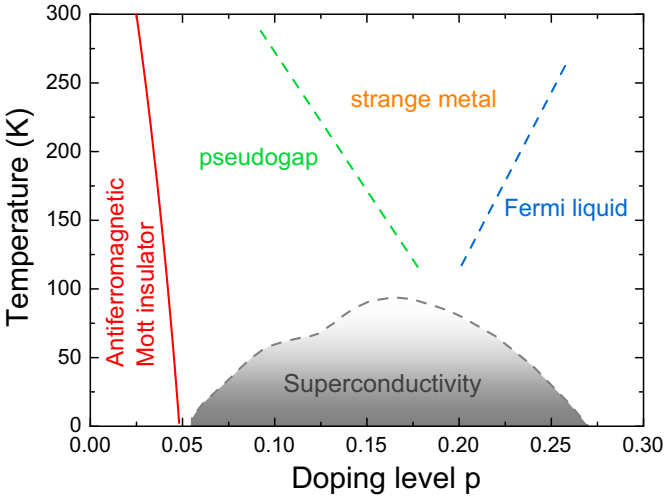

Figure 1.5: Generic phase diagram of the hole-doped high-T_c cuprates as a function of temperature and hole doping p. The different phases are discussed in the text.

and the metallic phase, superconductivity appears. Above the superconducting transition temperature, in the underdoped regime the so-called pseudogap regime appears, whereas in the region of optimal doping a strange metallic regime appears. The different phases of the generic phase diagram are shortly described in the followings.

The Antiferromagnetic Phase

The high-T_c cuprates are characterized by strong antiferromagnetic (AF) spin correlations between the copper spins of the CuO_2 planes. In the undoped parent compounds, the planar copper ions are in a $3d^9$ configuration (S=1/2 spin). A strong superexchange interaction through the oxygen ions gives rise to a three-dimensional AF order with high Neel temperatures (T_N=300-500 K) [41].

The magnetic structure in the AF state and the dynamical spin correlations have been extensively studied by means of neutron scattering (a recent review is given in reference [42]. Since large samples are required for neutron studies, most of the results have been obtained on the La_2CuO_4 and $YBa_2Cu_3O_{6+x}$ systems for which relatively larger single crystals were available. Focusing on the $YBa_2Cu_3O_{6+x}$ family studied in the current thesis, in the parent compound the planar copper spins lie on the CuO_2 planes pointing towards the Cu-O bonds direction. The in-plane antiferromagnetic wavevector characterizing the magnetic ordering is $\mathbf{Q}_{AFM}$=(1/2,1/2). A schematic illustration of the AF structure of $YBa_2Cu_3O_6$ is plotted on the left panel of Fig. 1.6 [43]. The in-plane antiferromagnetic order is induced by a strong superexchange coupling $J_{\parallel}$ between the plane copper spins of the same plane through the oxygen atoms. In the out-of-plane direction antiferromagnetic order is also established via two exchange mechanisms: the two neighboring CuO_2 planes of a bilayer are coupled antiferromagnetically through direct exchange interaction $J1$, whereas two next-nearest-neighbor CuO_2 planes separated by the charge reservoir block are antiferromagnetically coupled through a higher order superexchange process $J2$. The magnetic interaction exchange parameters and their anisotropy have been determined by inelastic neutron scattering results in combination with spin wave theory [44].

In $YBa_2Cu_3O_6$ the magnetic moment m connected with the antiferromagnetic order has been found to be $\sim 0.5\mu_B$ using neutron diffraction [45, 46]. The observed value of the magnetic moment is much lower than the mean field prediction of $g\mu_B S \approx 1\mu_B$ with g=2 and S=1/2, a fact that has been attributed to quantum spin fluctuations and to hybridization effects [42]. The doping and temperature dependence of the magnetic Bragg peak intensity ($\propto m^2$) in $YBa_2Cu_3O_{6+x}$ is plotted on the right panel of Fig. 1.6 [43]. In the undoped compound, upon temperature increase the magnetic moment continuously decreases and disappears completely for $T_N \simeq 410$ K. Concerning the doping dependence, for oxygen content $x \lesssim 0.2$ the value of the magnetic moment and its temperature dependence do not change significantly with doping, due to the relatively small number of transferred holes. For higher oxygen content $x \gtrsim 0.2$ the effect of doping in the magnetic moment is more drastic: while the main features of the magnetic order are preserved, including the magnetic ordering wavevector $\mathbf{Q}_{AFM}$, the magnetic moment and the Neel temperature are

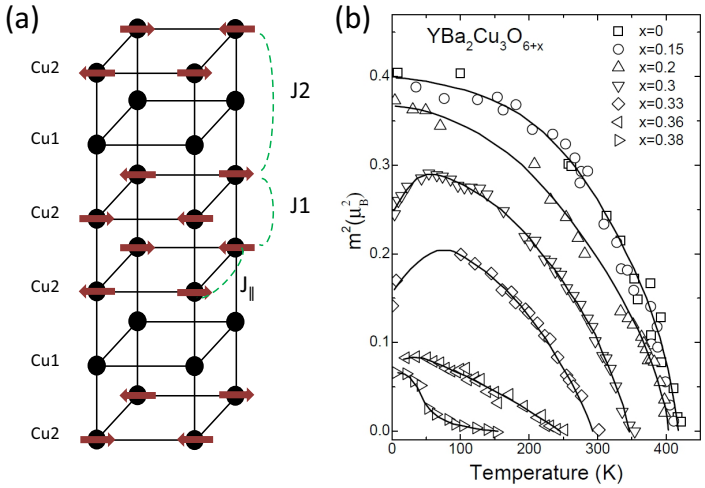

Figure 1.6: (a) The antiferromagnetic structure of $YBa_2Cu_3O_6$. The in-plane, $J_\parallel$, and out-of-plane, *J1* and *J2*, exchange interactions are indicated. Cu2 are the planar copper ions and Cu1 are the copper ions of the charge reservoir layers. (b) Temperature dependence of the antiferromagnetic Bragg peak intensity for various doping levels between x=0.1 and x=0.38. The figure is based on the data of [43].

both reduced upon doping increase. Antiferromagnetic long range order vanishes completely at $p \simeq 0.05$ and almost immediately superconductivity sets in at low temperatures. In some cuprates families, including the $YBa_2Cu_3O_{6+x}$ family studied here, for low doping levels superconductivity coexists with a short range incommensurate uniaxial static magnetic order [47, 48].

The Superconducting Phase

Upon cooling below T_c a superconducting state appears exhibiting zero resistance with a Meissner effect (the superconducting state in the cuprates is reviewed in references [23, 49, 50, 51]).

High-T_c cuprates have large magnetic penetration depths λ and small coherence lengths ξ compared to the respective values of conventional superconductors. The penetration depth has typical values for $YBa_2Cu_3O_{6+x}$ $\lambda_a \simeq 1600$ Å, $\lambda_b \simeq 1000$ Å and $\lambda_c \simeq 6000$ Å, while the coherence lengths are of the order of 20 Å in the CuO_2 planes and 2 Å in the direction perpendicular to the planes, both reflecting the anisotropy of the electronic structure [29, 52]. In view of such small coherence lengths along the c-axis compared to the interlayer distance, the cuprates are essentially composed of Josephson coupled planes.

Moreover, the resulting very large value of λ/ξ renders the superconducting cuprates *type-II* superconductors.

The formation of Cooper pairs in the superconducting state has been verified very early, through a plethora of observations including the observation of the magnetic flux quantization with a flux quantum value of $h/2e$ [54]. Several different experiments, including angle resolved photoemission spectroscopy (ARPES), infrared spectroscopy, tunneling experiments, Raman spectroscopy etc. have indicated the presence of an energy gap in the electronic excitation spectrum below the superconducting transition temperature.

The Ginzburg-Landau order parameter $\Psi(r)$ identifies with the pair wave function of the microscopic theory and is proportional to the energy gap $\Delta(r)$, $\Psi(k) \propto \Delta(k)$. The order parameter represents the extent of macroscopic phase coherence of the superfluid condensate and is characterized by a phase $\phi(r)$ and a modulus $|\Psi(r)|$, with the quantity $|\Psi(r)|^2$ constituting a measure of the local superfluid density $n_s(r)$ [53]. Useful insights into the nature of the pair condensate state can be gained based on symmetry considerations. Results of Josephson tunneling experiments have shown that the paired electrons in the cuprates are in a spin singlet state, $S=0$. The spin singlet pair state corresponds to an orbital pair wave function with even parity $\Psi(k)=\Psi(-k)$, and so $\Delta(k)=\Delta(-k)$. Superconductivity in cuprates basically originates from the CuO_2 layers and therefore the pairing symmetry should reflect the symmetry of the underlying CuO_2 square lattice. A schematic k-space presentation of the candidate even parity pair wave functions for the point-group symmetry of the CuO_2 square lattice (C_{4v}) is shown in Fig. 1.7, where black and white represent opposite signs of the order parameter.

For conventional superconductors, the pairing state is s-wave and thus the value of the superconducting gap is independent of the wavevector $\mathbf{k}$ of the electron. In the cuprates

Group-theoretic notation	A_{1g}	A_{2g}	B_{1g}	B_{2g}
Order parameter basis function	constant	$xy(x^2-y^2)$	x^2-y^2	xy
Wave function name	s-wave	g	$d_{x^2-y^2}$	d_{xy}
Schematic representation of $\Delta(k)$ in B.Z.	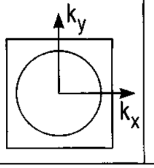		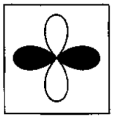	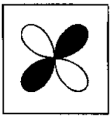

Figure 1.7: k-space representation of the allowed even-parity orbital pair wave functions for the C_{4v} symmetry of the CuO_2 planes in the high-T_c superconductors. The figure is taken from [53].

experimental observations from phase-sensitive techniques along with evidence from a number of non-phase-sensitive techniques, provide evidence in favor of a predominantly *d*-wave pairing symmetry. Wollman *et al.* [55] did the first phase-sensitive test of pairing symmetry, based on Josephson tunneling measurements in the so-called corner-SQUID geometry. Their result suggested an order parameter of the form $\Delta(k)=\Delta(0)(\cos(k_x)-\cos(k_y))$, characteristic of a $d_{x^2-y^2}$ symmetry. For this symmetry the gap changes sign and has four nodes on the 2D Fermi surface where the lines (0,0) and (0,±π), (±π,0) cross the Fermi surface [23].

ARPES spectroscopy has on one hand the advantage of directly investigating the momentum dependence of the gap and on the other hand the limiting disadvantage of being extremely sensitive to the surface conditions of the studied sample, requiring thus sample cleavage prior to the measurement. Unfortunately the $YBa_2Cu_3O_{6+x}$ crystals tend to cleave between the chain layer and the Ba-O layer, leading to a polar surface unfavorable for ARPES measurements. The superior surface cleavage for $Bi_2Sr_2CaCu_2O_{8+x}$ crystals has allowed for high quality ARPES measurements which suggest that the superconducting gap is anisotropic and in particular it is largest along the Γ-M directions (parallel to *a*- or *b*- axis) and smallest along Γ-Y (the diagonal line between *a*- and *b*- axis, i.e. the nodal direction), consistent with a $d_{x^2-y^2}$ symmetry [35, 53]. In Fig. 1.8 is plotted the amplitude of the energy gap inferred from ARPES data as a function of angle on the Fermi surface (solid circles), together with the prediction of a simple *d*-wave model (solid line) [56]. The data indeed indicate the disappearance of the gap in the nodes and the maximum value of the gap amplitude in the antinodes, while the agreement with the d-wave fit is remarkable. While the predominantly $d_{x^2-y^2}$ symmetry of the superconducting

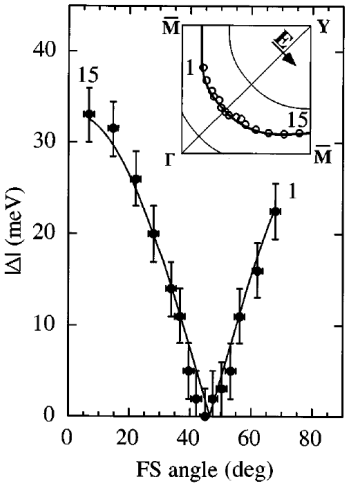

Figure 1.8: ARPES measurement of the superconducting gap amplitude measured at 13 K on $Bi_2Sr_2CaCu_2O_{8+x}$ (T_c=87 K) as a function of the angle along the normal-state Fermi surface (see sketch of the Brillouin zone in in the inset), together with a *d*-wave fit (solid line). The figure is taken from [56].

gap in the cuprates is well established, it is worth mentioning that theoretical predictions and experimental observations suggest that for the case of orthorhombic cuprates, like $YBa_2Cu_3O_{6+x}$, there is a subdominant *s*-wave admixture, leading to a modification of the pure *d*-wave pairing symmetry to an admixed $d_{x^2-y^2}+s$ pair state [57].

The vicinity of the superconducting and the antiferromagnetic state in the phase diagram together with the experimental determination of the unconventional $d_{x^2-y^2}$ symmetry of the Cooper-pair wavefunction has positioned spin fluctuations as the most plausible candidate for mediating Cooper pairing in the high-T_c cuprates, in analogy to the phonon-mediated pairing mechanism in conventional superconductors [58, 59]. The connection between spin dynamics and the *d*-wave superconducting state in the cuprates is further manifested through the observation of the magnetic resonance mode, extensively studied by neutron scattering measurements [42]. Moreover, evidence has been reported that the coupling between spin fluctuations and fermionic quasiparticles is strong enough to mediate high temperature superconductivity [60]. Experimental results from inelastic neutron scattering for the underdoped regime and more recently from resonant inelastic x-rays scattering for the entire doping range, have provided evidence for the existence of damped, dispersive magnetic excitations, which have significant spectral weight in an appropriate spectral range to produce pairing [61].

The Strange Metal Regime

The "normal state" properties above the superconducting dome in the optimally doped regime deviate significantly from what is predicted by Fermi liquid theory. The most

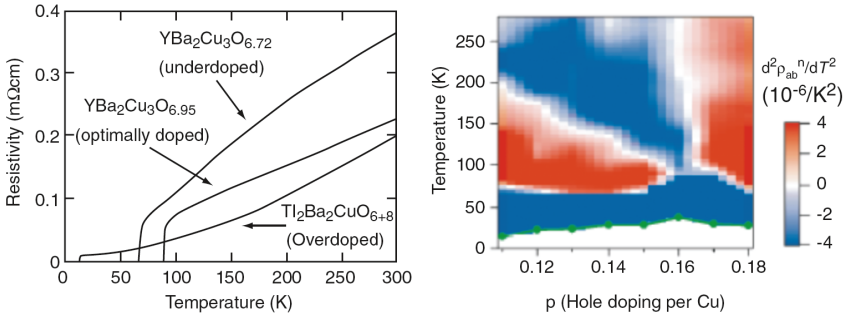

Figure 1.9: (a) Temperature dependence of the in-plane resistivity for underdoped, optimally doped and overdoped cuprates. While for the optimally doped case a linear dependence is observed, in the overdoped case the quadratic dependence expected from Fermi liquid theory is recovered. (b) Color map of $d\rho_{ab}^2/dT^2$ for $Bi_2Sr_{2-x}La_xCuO_{6+\delta}$. The solid green circles show T_c for the measured compositions. The almost vertical white line around x~0.16 highlights the linear temperature dependence of the resistivity at optimal doping. The plots are taken from [62, 63].

prominent example is the temperature dependence of the resistivity which presents a linear behavior over a wide temperature range, as shown in Fig. 1.9 [62, 63]. This is a universal feature observed for many different cuprate families at optimal doping, confirming that it is intrinsic to the CuO_2 planes [31]. The persistence of the linear dependence of the resistivity, or equivalently of the scattering rate τ^{-1} of the electronic quasiparticles, is considered to be evidence for an anomalous metallic state, incompatible with the expectations from the Fermi liquid model where a T^2 dependence of τ^{-1} is expected. This behavior has been considered more suggestive of electron correlation effects rather than strong phonon interactions and has been regarded as a signature of quantum criticality [64]. Adding up to this, as highlighted in [65], the linewidths in photoemission spectra have been shown to grow linearly with both temperature and binding energy [66]. Both observations are classic signatures of "quantum critical" scaling, as will be discussed next in the framework of the observed pseudogap phase.

The Fermi Liquid Regime

In contrast to the rest of the phase diagram, this regime is successfully described by conventional Fermi liquid theory [40]. Most of the work in the Fermi liquid part of the phase diagram has been performed on the $Tl_2Ba_2CuO_{6+\delta}$ family for which, unlike the $YBa_2Cu_3O_{6+x}$ family, the overdoped regime is accessible within the tunable doping range. Signatures of Fermi liquid behavior include ARPES and quantum oscillations results which have revealed a large hole-like Fermi surface with a volume containing $1+p$ holes per Cu atom, which appears to be consistent with conventional band theory as described earlier in the electronic properties section. Heat and charge conduction in the normal state obey the Wiedemann-Franz law and beyond the superconducting phase the electrical resistivity exhibits a standard quadratic T^2 temperature dependence (Fig. 1.9), both of them constituting hallmarks of Fermi-liquid theory [62, 67, 68].

The Pseudogap Regime

The pseudogap regime appears above the superconducting phase in the underdoped part of the phase diagram and is described as a depletion of the density of states below a characteristic temperature T^*. Although it was first observed only 3 years after the discovery of high-T_c cuprates and has been widely investigated both experimentally and theoretically, it still remains enigmatic. Up to date, the nature of pseudogap is not firmly established, and in particular it is not clear whether it is a real thermodynamic phase or not.

The temperature T^* below which the pseudogap is formed is doping dependent and significantly higher than the superconducting transition temperature T_c [29, 65, 69]. Contrary to the behavior of T_c, T^* decreases upon increasing doping towards the optimal conditions. There exists however a clear discrepancy in the literature concerning the value of T^* inferred from different experimental techniques, potentially because of the variety

of criteria used to identify this phenomenon in the various probes. Nevertheless, all the available experimental results agree that T^* is considerably higher than T_c [29].

The pseudogap was first observed in nuclear magnetic resonance (NMR) measurements by Warren *et al.* as a reduction in the imaginary part of the low frequency dynamic spin susceptibility for temperatures below T^* [71]. The opening of the pseudogap was reflected both in NMR Knight shift measurements and in ^{63}Cu spin relaxation measurements, as is shown in Fig. 1.10 where the NMR relaxation rate is plotted for various samples of $Bi_2Sr_2CaCu_3O_{8+\delta}$ [70, 71, 72].

Following the initial NMR indications numerous different experimental probes have been employed to elucidate the pseudogap effect. Some of them will be presented in the current description but for a detailed overview one can refer to the reviews of references [65, 69, 73]. DC resistivity measurements reveal a deviation from the normal state linear temperature dependence upon entering the pseudogap regime. A decrease in the planar resistivity is observed for temperatures below T^* which is found close to the temperature where the spin gap opens in the NMR results, as shown e.g. for the case of underdoped $YBa_2Cu_4O_8$ in the data of Bucher *et al.* [74]. The formation of the pseudogap is also reflected in infrared spectroscopy measurements (for a review see [75]). The pseudogap produces a strong gap-like suppression in the *c*-axis conductivity, shown in the right panel of Fig. 1.10 for the case of $YBa_2Cu_3O_{6.7}$, while the frequency at which the suppression sets in is temperature independent.

ARPES measurements have clearly identified the opening of an energy gap below T^* [35]. Similar to the superconducting gap, the pseudogap was proven to be highly

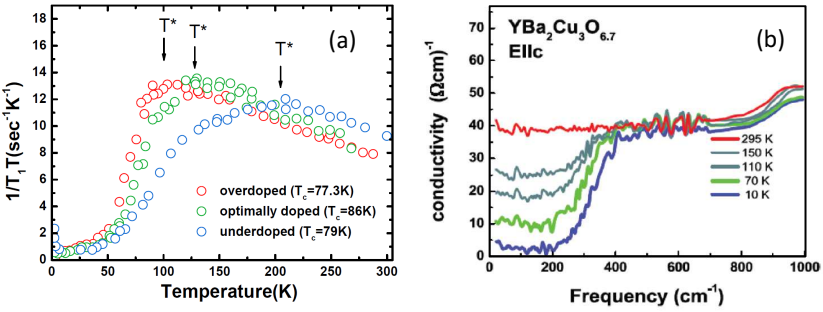

Figure 1.10: Experimental evidence for a pseudogap. a) NMR relaxation rates for underdoped, optimally doped and overdoped $Bi_2Sr_2CaCu_3O_{8+\delta}$. A suppression of $1/T_1T$ associated with the pseudogap formation sets in at a temperature T^* well above T_c. The data are taken from [70]. (b) *c*-axis conductivity experimental data (phonons subtracted) for underdoped $YBa_2Cu_3O_{6.7}$. A suppression of the conductivity takes place at low frequencies when the pseudogap sets in. The figure is taken from [65].

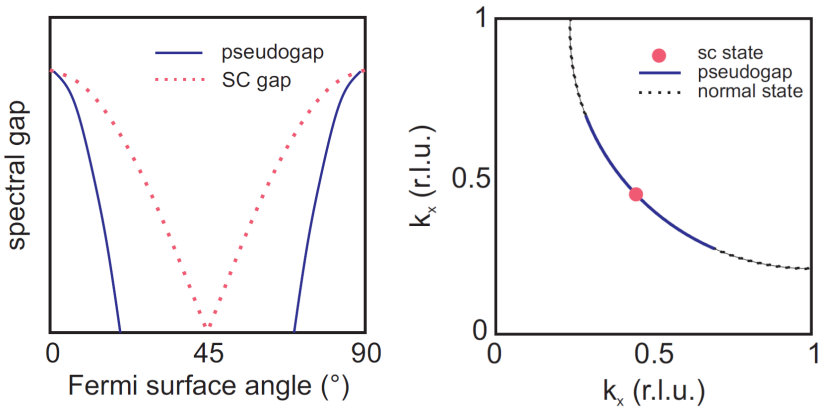

Figure 1.11: Momentum anisotropy of the superconducting gap and the pseudogap. The spectral gap around the Fermi surface is plotted on the left panel. The d-wave node of the superconducting state evolving into the gapless Fermi arc of the pseudogap phase and the full Fermi surface of the normal state is plotted on the right panel. The figure is prepared based on [49].

anisotropic around the Fermi surface and to exhibit a momentum dependence reminiscent of the $d_{x^2-y^2}$ symmetry of the superconducting gap. More specifically the pseudogap is largest at Fermi momenta close to the antinodal region in the Brillouin zone, i.e. at the same regions of the Fermi surface where the superconducting gap is largest, and vanishes along the nodal direction. Unlike the superconducting gap though, instead of vanishing at isolated points on the Fermi surface (nodes) the pseudogap vanishes along segments of the Fermi surface centered at these nodes, known as Fermi arcs [76]. A schematic representation of the angular anisotropy of the pseudogap is plotted in Fig. 1.11.

As already mentioned, a unique representation for the pseudogap line T^*, as the one illustrated in the generic phase diagram of Fig. 1.5, does not exist up to now [77]. Two different phase diagrams are usually considered with respect to the pseudogap line, schematically illustrated in Fig. 1.12. In the two phase diagrams the T^* line either coincides with T_c on the overdoped side as in the first case, or cuts through the T_c dome and vanishes inside the dome at a T=0 in a quantum critical point as in the second case. These two different cases come together with different approaches on the physical origin of the pseudogap. In the first case, it has been proposed that the pseudogap is a precursor to the superconducting state, signaling the formation of Cooper pairs without long range phase coherence [78]. This idea was first formed by P. W. Anderson in his resonating valence bond (RVB) model [79]. According to this suggestion Cooper pairs are formed at temperatures T^* much higher than T_c but obtain long range phase coherence only when entering the superconducting dome. This implies the existence of two crossover lines,

one being T^* where Cooper pairs are formed, and the other being T_{coh} where the pairs become phase coherent, and only below both crossover lines is superconductivity possible. In the case of the second phase diagram, T^* marks the onset of an ordered phase. In this framework, the pseudogap and the superconducting phases arise from different, even competing, underlying mechanisms. In other words, a different state of matter, a so-called *"hidden-order"*, competes with superconductivity for the same Fermi surface, and as one of them prevails the other is suppressed. Regarding the possible nature of the competing phase, suggested examples include competing phases of commensurate or incommensurate spin-density waves (SDW), stripe order (combination of SDW and charge-density wave (CDW)), 1D-CDW, biaxial CDW, or charge current loops which either break or do not break the translational symmetry [80, 81].

There is plenty of experimental evidence supporting both scenarios, with the more recent experimental results pointing towards the second scenario. The Knight shift decrease in the NMR measurements could be understood in the context of a singlet preformation before the phase coherence of the superconducting state and the ARPES Fermi arcs could be understood as a precursor to the superconducting nodes in the Fermi surface. On the other hand, in favor of a competing state scenario are several experiments suggesting that T^* marks the onset of a phase with broken symmetry. The polar Kerr effect and the Nernst effect measurements indicate a broken rotational symmetry in the pseudogap phase, while polarized neutron diffraction data indicate a novel magnetic order at Q=0 in underdoped cuprates [82, 83]. Recent resonant ultrasound spectroscopy measurements suggest that the doping dependence of the pseudogap line is such that it terminates at zero temperature inside the superconducting dome, as expected in a picture of quantum criticality [84].

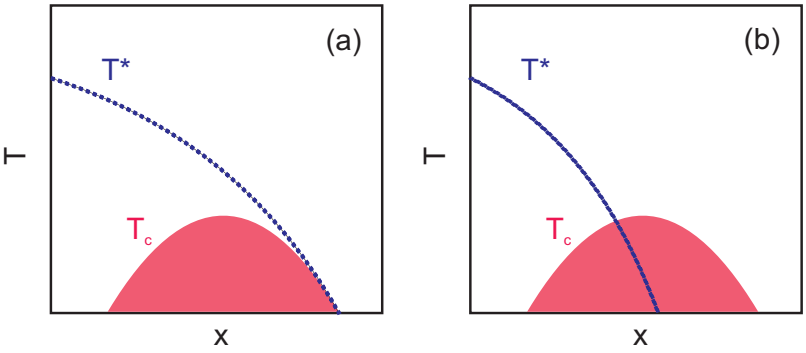

Figure 1.12: The two possible phase diagrams of the cuprates. The blue line is the pseudogap phase line and the red area is the superconducting regime. Panel (a) corresponds to the preformed Cooper pairs scenario and panel (b) to the competing phase scenario. The figure is based on [65].

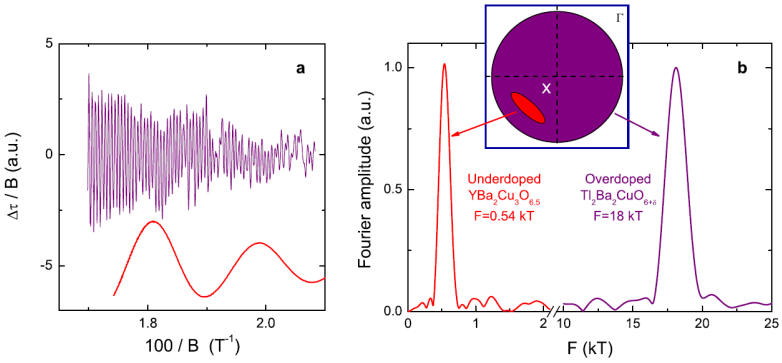

Figure 1.13: Quantum oscillations data on underdoped and overdoped cuprates. (a) Oscillatory part of the magnetization versus 1/B for overdoped $Tl_2Ba_2CuO_{6+\delta}$ (magenta) and underdoped $YBa_2Cu_3O_{6.5}$ (red). (b) Fourier analysis of the raw data of (a). Each dataset reveals a single frequency, but with vastly different values. The inset is a sketch of the size of the Fermi pocket in the first Brillouin zone deduced from the frequency of the quantum oscillations for $Tl_2Ba_2CuO_{6+\delta}$ (magenta) and $YBa_2Cu_3O_{6.5}$ (red). The position in the Brillouin zone and the shape of the Fermi surfaces are arbitrary. The figure is taken from [85]

Recent quantum oscillation experiments on underdoped cuprates are also in line with the competing order scenario. Quantum oscillations result from the Landau quantization of states in a magnetic field and the orbiting motion of quasiparticles around the various pockets of the Fermi surface in a metal. Their very observation confirms the existence of a coherent closed Fermi surface and their frequency is a direct measure of the Fermi surface area [86]. These experiments have revealed a very different Fermi surface topology between the overdoped and the underdoped part of the phase diagram. For the overdoped cuprates they suggest a large quasi-two-dimensional Fermi cylinder, in line with the Fermi liquid behavior described previously [87]. For the underdoped cuprates quantum oscillation experiments on $YBa_2Cu_3O_{6.5}$ and $YBa_2Cu_4O_8$ samples have revealed the existence of small Fermi surface pockets [85, 88, 89, 90, 91]. This is schematically illustrated in Fig. 1.13. There have been some doubts concerning a possible non-universal origin of the Fermi surface pockets related to peculiarities of the $YBa_2Cu_3O_{6.5}$ and $YBa_2Cu_4O_8$ structures and more specifically to the presence of Cu-O chains, which were recently cleared out by the observation of quantum oscillations in underdoped $HgBa_2CuO_{4+\delta}$ which is a model tetragonal cuprate superconductor with individual CuO_2 layers and no Cu-O chains [92]. These universal quantum oscillations in underdoped cuprate superconductors offer strong evidence that below a critical doping level within the superconducting dome the cuprates undergo a Fermi surface reconstruction where the large hole-like Fermi surface reconstructs into small pockets [85]. The

standard mechanism for such a reconstruction is the onset of an ordered phase at Q≠0 that breaks the translational symmetry of the lattice. This is further sustained by NMR results in $YBa_2Cu_3O_{6.5}$, which have revealed signatures of magnetic field-induced charge modulations [93, 94].

The case of the competing order phase with broken symmetry has been significantly invigorated by the discovery of the charge density wave state in underdoped cuprates. Until recently the only directly probed periodic modulation of the charge density in the CuO_2 planes of high-T_c cuprates was the so-called *stripe phase*. Static spin and charge type order has been observed in $La_{1.6-x}Nd_{0.4}Sr_xCuO_4$ and $La_{2-x}Ba_xCuO_4$ in both cases at a doping level p∼1/8 per planar Cu atom [95, 96, 97]. It involves a combination of uniaxial spin and charge density wave orders in the CuO_2 planes with a commensurate charge modulation of period ∼4a (where lattice unit a is the distance between neighboring Cu atoms in the CuO_2 planes). The stripe phase has been invoked to explain the observed "1/8 T_c-anomaly", i.e the strong drop of T_c in materials of the "214" family at p∼1/8. For many years, the question of the stripe order universality in the cuprates was debated and questions have arisen on whether stripe order is a generic feature of the copper oxides and whether stripe fluctuations are essential for superconductivity.

Recently an incipient CDW state was discovered in underdoped cuprates initially for compounds with composition $(Y,Nd)Ba_2Cu_3O_{6+x}$ belonging in the so-called "123" family and most newly for Bi-based cuprate superconductors [1, 2, 98, 99].

More specifically for the case of "123" cuprates, which are relevant to the results of the current thesis, at low oxygen content (0.3≤x≤0.45) a uniaxial, static, incommensurate magnetic order is formed. The observed ordering vector is q_{SDW}=(0.5+δ, 0.5) and the incommensurability δ is found to increase monotonically with p. Unlike the case of the "214" family, the magnetic ordering is not accompanied by a corresponding charge modulation [47]. At higher oxygen content (0.5≤x≤0.75) static magnetism disappears and a gap that increases smoothly with p opens in the spin excitation spectrum, whereas low-energy fluctuations of the charge density in the CuO_2 planes appear [100, 101].

The CDW state has been directly observed through resonant and non-resonant x-ray diffraction for 0.5≤x≤0.75 (see Fig. 1.14, panel a) [1, 2, 102, 103, 104]. Charge order appears well above T_c and survives in the superconducting state, with an onset temperature ∼150K, depending on the doping level and on the experimental probe, as will be discussed later on. The CDW fluctuations are biaxial and incommensurate with in-plane ordering wavevectors q_{CDW}=(∼0.31,0) and (0,∼0.31). The ordering wavevector exhibits a weak doping dependence and a small anisotropy between the a- and b-axis directions, as observed in the case of *ortho*-II $YBa_2Cu_3O_{6.5}$ [104]. The CDW wavevector q_{CDW} appears unrelated to the magnetic wavevector q_{SDW}=(0.5+δ, 0.5) of the spin density wave state immediately adjacent in the phase diagram for lower doping levels (x≤0.45). The charge order appears well separated from any magnetic order, in sharp contrast to the "214" family where charge and spin orders coexist microscopically in the stripe phase. Furthermore, substitution of spinless Zn impurities for planar Cu2 in $YBa_2Cu_3O_{6.6}$ has

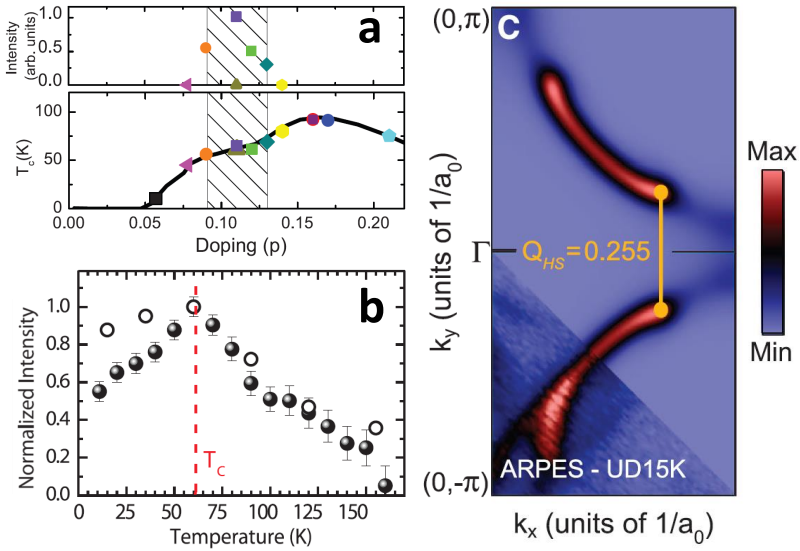

Figure 1.14: (a) Doping dependence of the normalized intensity of the CDW peak, I_{CDW}, and of the superconducting transitions temperature T_c. The shaded region where the CDW peak appears in the resonant elastic x-rays scattering (REXS) data coincides with the plateau of T_c. (b) T-dependence of the CDW normalized intensity derived from the energy-resolved (open circles) and the energy-integrated (solid circles) x-ray data. The CDW intensity is maximized at T_c. The figures are taken from [1]. (c) ARPES experimental data and theory comparison on $Bi_2Sr_{2-x}La_xCuO_{6+\delta}$. The q_{HS} wavevector associated with the tips of the Fermi arcs (hot spots) is marked by the gold line and is in good agreement with the q_{CDW} deduced by REXS and STM data. The figure is taken from [99].

revealed that spin and charge order are strongly competing in the "123" family [104].

On the other hand, soft and hard x-ray scattering measurements show that the intensity of the CDW-superlattice reflections is maximized at T_c and suppressed in the superconducting state, as shown in Fig. 1.14 [1, 2]. In addition to this, the doping range where the CDW state appears coincides with the well-known plateau in the doping dependence of T_c shown in Fig. 1.6, suggesting a strong competition between the CDW and the superconducting state and providing an interpretation for the anomalously low T_c in this doping range [1]. The competition between the CDW order and superconductivity is further corroborated by measurements under high magnetic fields which were proven to suppress superconductivity and enhance the CDW correlations [2, 104]. These observations are furthermore suggestive of a possible CDW ground state in magnetic fields high enough to completely suppress superconductivity.

Soon after the discovery of the CDW is has been proposed that the observed charge

ordering wavevector q_{CDW} connects bonding bands at the anti-nodal region of the high-temperature Fermi surface, where the pseudogap is maximized [1, 2]. More recent combined ARPES, x-ray scattering and STM results on Bi-based cuprates though, suggest that the charge-ordering wave vector connects the Fermi arc tips, the so-called "hot spots" (HS), and not the antinodal Fermi surface sections (Fig. 1.14, panel c) [99]. Both the magnitude of the hot spots nesting wave vector q_{HS} and the slope of its doping-dependence (dq_{HS}/dp) agree with the experimental data on the q_{CDW}, forming a direct connection between charge order and scattering through the hot spots nesting wavevector.

1.1.4 The $YBa_2Cu_3O_{6+x}$ and $YBa_2Cu_4O_8$ systems

For the current thesis two members of the cuprate family of superconductors have been studied: $YBa_2Cu_3O_{6+x}$ and $YBa_2Cu_4O_8$. In this section some details concerning the structure, doping mechanisms and sample preparation of these specific compounds will be given in order to facilitate the later discussion of the experimental results.

The structures of $YBa_2Cu_3O_{6+x}$ and $YBa_2Cu_4O_8$: Cu-O chains

The structure of $YBa_2Cu_3O_{6+x}$ is plotted in Fig. 1.15 for the two extreme cases of oxygen content: x=0 and x=1. In the structures of Fig. 1.15 there are two non-equivalent Cu sites easily distinguished by their different oxygen environment: the planar copper site, Cu2, and the chain copper site, Cu1. The planar copper, Cu2, is pyramidally coordinated by the four planar oxygen atoms, O2, and the apical oxygen atom of the BaO layer, O4, whereas the chain copper, Cu1 is linearly coordinated by the chain oxygen atoms, O1.

The CuO_x chains along the crystallographic *b*-direction act as the charge reservoir where the excess oxygen content *x* is positioned. The excess oxygen content can be continuously tuned between x=0 and x=1. In the case of $YBa_2Cu_3O_6$ with entirely empty chains and no excess oxygen (x=0, left panel in Fig. 1.15) the structure is tetragonal (space group *P*4/*mmm*). When excess oxygen atoms are introduced in the structure finite length Cu-O chain fragments are formed, growing longer as the oxygen content is increased [106, 107]. For low oxygen content ($x \lesssim 0.3$) the Cu-O chain fragments do not have a preferred orientation and the structure remains tetragonal, but for higher oxygen contents the Cu-O fragments align in the crystallographic *b*-direction leading to an orthorhombic distortion (space group *Pmmm*). The structural orthorhombicity is enhanced as the oxygen content is increased, until the chain oxygen sites are fully occupied for the case of $YBa_2Cu_3O_7$ (x=1, right panel in Fig. 1.15) [107, 108]. The doping dependence of the in-plane lattice parameters *a* and *b* across the tetragonal to orthorhombic transition is plotted in Fig. 1.16 [107].

The CuO_x chains tend to grow in length and to order in superstructures with different sequences of full Cu-O and empty Cu-vacancy chains along the *a*-axis depending on their oxygen content [109]. The different superstructures are grouped based on their periodicity along the crystallographic *a* direction and labeled accordingly in units of the *a*-axis

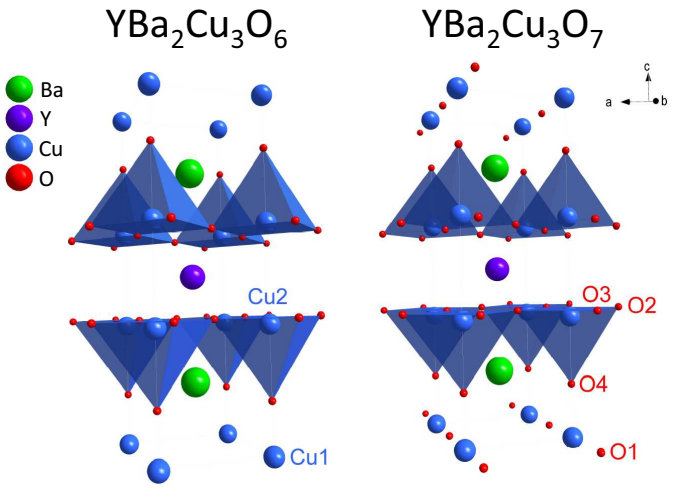

Figure 1.15: Crystal structure of $YBa_2Cu_3O_{6+x}$ for the two extreme cases: $YBa_2Cu_3O_6$ for x=0 (left) and $YBa_2Cu_3O_7$ for x=1 (right). The two non-equivalent Cu sites, in the CuO_2 planes and the CuO_x chains can be distinguished. The excess oxygen of the structure is accommodated in the CuO_x chains running along the crystallographic b-direction. The figure was prepared based on the data of [105].

lattice parameter using roman enumeration [109, 110]. When all the CuO chains are filled with oxygen atoms, the corresponding periodicity is 1a and the *ortho*-I phase, plotted on the right panel of Fig. 1.15, is formed. The *ortho*-I phase appears also for all low oxygen contents $x \lesssim 0.3$, below the tetragonal to orthorhombic phase transition, as alignment of finite length chain fragments. In Fig. 1.17 are plotted schematically some superstructures appearing for oxygen contents between the tetragonal $YBa_2Cu_3O_6$ and the *ortho*-I structure of $YBa_2Cu_3O_7$: the *ortho*-II, *ortho*-III, *ortho*-V and *ortho*-VIII phases with 2a, 3a, 5a and 8a periodicity of the oxygen superstructure along the a-axis respectively. In neutron and x-rays scattering experiments the corresponding superstructure peaks appear in reduced lattice units at modulation vectors: Q=(nh_m,0,0) where n is an integer and h_m=1/m for m=2, 3, 5 and 8 respectively [109, 110, 111, 112, 113]. These superstructures have also been observed by electron microscopy [114, 115, 116]. In the right panel of Fig. 1.17 is plotted the structural phase diagram of the oxygen superstructures in $YBa_2Cu_3O_{6+x}$ as a function of oxygen content x.

The correlation length ξ of the different oxygen superstructures can be estimated by the width Γ_m of the respective superstructure peaks ($\xi = 1/\Gamma_m$) measured in a scattering experiment. The biggest correlation lengths, of the order of a few hundred Angstroms, are observed for the *ortho*-II phase of $YBa_2Cu_3O_{6.5}$, for which filled and empty CuO

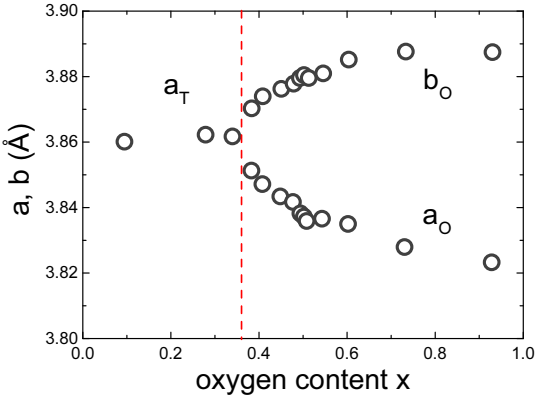

Figure 1.16: Doping dependence of the in-plane lattice parameters a and b in $YBa_2Cu_3O_{6+x}$. The dashed vertical line marks the tetragonal to orthorhombic transition upon increasing the oxygen content x. The plotted structural data are taken from [107].

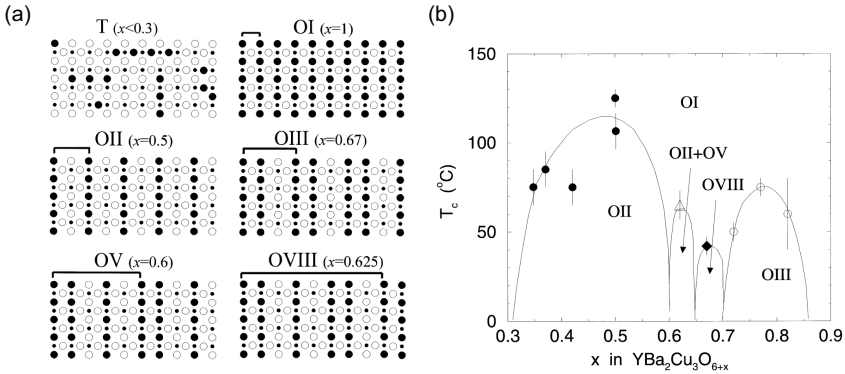

Figure 1.17: (a) Schematic representation of the CuO_x chain layer for the different $YBa_2Cu_3O_{6+x}$ structural phases: T is the tetragonal disordered phase with Cu-O chain fragments, and OI-OVIII are the orthorhombic *ortho*-I-*ortho*-VIII phases. The optimal oxygen stoichiometries for which the superstructure phases are expected are given in parenthesis. (b) Structural phase diagram for the oxygen superstructures in $YBa_2Cu_3O_{6+x}$ as a function of oxygen content. An additional *ortho*-IV phase in optimally doped $YBa_2Cu_3O_{6.92}$ is not shown [113, 117]. The figure is taken from [109].

chains are alternating each other [118]. As the order of the oxygen superstructure increases (from *ortho*-II towards *ortho*-VIII) the correlation lengths decrease and shorter range order is established [110]. For this reason $YBa_2Cu_3O_{6.5}$, together with the stoi-

chiometric underdoped $YBa_2Cu_4O_8$ which will be presented next, are considered to be the underdoped cuprates with the lowest disorder arising from oxygen vacancies.

$YBa_2Cu_4O_8$ was first detected through electron microscopy as a lattice defect in powders of $YBa_2Cu_3O_{6+x}$ and was soon after synthesized in bulk form at high and ambient oxygen pressure [120, 121, 122]. In the structure of $YBa_2Cu_4O_8$ the single Cu-O chain of $YBa_2Cu_3O_{6+x}$ is replaced by a double Cu-O chain forming an edge-sharing square planar network (space group *Cmmm*) [123, 124]. The structure is schematically illustrated in Fig. 1.18. In this coordination, the chain oxygen atoms are bonded to copper atoms both along the *b*- and the *c*-axis directions. Each oxygen of the chain is therefore bonded to three copper atoms rather than two like in $YBa_2Cu_3O_{6+x}$, offering an enhanced stability of the oxygen content and preventing oxygen losses from the system. Moreover, $YBa_2Cu_4O_8$ is fully stoichiometric, containing no oxygen vacancies and exhibiting no superstructures like the ones of the $YBa_2Cu_3O_{6+x}$ system. These characteristics render this compound uniquely chemically stable and defect-free in the whole family of underdoped cuprates.

Tuning the hole doping: sample annealing and detwinning

As already mentioned, in the $YBa_2Cu_3O_{6+x}$ family the hole doping is chemically performed through the introduction of extra oxygen atoms in the CuO_x chains. Determining the hole doping *p* from the oxygen content *x* (as given in the chemical formula) is not a straightforward task due to the presence of two non-equivalent copper sites, Cu1 and Cu2. The dependence of the doping level on the oxygen stoichiometry in $YBa_2Cu_3O_{6+x}$

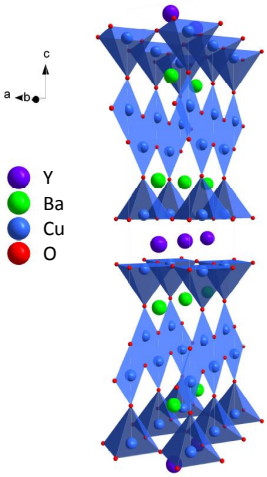

Figure 1.18: Schematic representation of the crystal structure of $YBa_2Cu_4O_8$. The single Cu-O chain of $YBa_2Cu_3O_{6+x}$ is replaced by a double Cu-O chain. The edge sharing network in the Cu-O chains stabilizes the oxygen content and makes the compound chemically less fragile. The structure is plotted based on the structural data of reference [119].

is plotted in Fig. 1.19, with data taken from reference [34], in which the dependence was derived through an empirical relationship between p and the c-axis lattice parameter. Since the hole doping does not depend only on the oxygen content but also on the level of oxygen ordering in the chains, the dependence is not unique (indicated by the two lines for $0.3 \lesssim x \lesssim 0.5$ in Fig. 1.19).

For low oxygen content ($x \lesssim 0.3$), $YBa_2Cu_3O_{6+x}$ is in the tetragonal phase and the chain oxygen atoms are far apart from one another and only a small fraction of them are in chain fragments. For fragment lengths smaller than a critical length of three Cu atoms (with two oxygen atoms in between), the chains do not act as dopants, holes can not be promoted towards the CuO_2 planes [125] and the system is in the *undoped regime* of the phase diagram. When the length of the chain fragments exceeds the critical value, for oxygen contents $x \gtrsim 0.3$, charge transfer occurs from the chains to the CuO_2 planes and superconductivity emerges. For $YBa_2Cu_3O_{6+x}$ the upper limit for hole doping is $x=1$, which corresponds to a hole doping $p \sim 0.19$, where the system is slightly overdoped. Therefore, in order to reach the highly overdoped and the metallic regimes in the $YBa_2Cu_3O_{6+x}$ family, a chemical substitution of Y^{3+} for a divalent cation, e.g. Ca^{2+}, is required [126, 127].

Given the very sensitive dependence of the superconducting properties of $YBa_2Cu_3O_{6+x}$ on the doping level, it becomes clear that an accurate control of the oxygen content in the CuO_x chains is of pivotal importance. This can be achieved through an appropriate heat treatment during the sample preparation, a procedure commonly referred as "annealing". The chemical diffusion of the oxygen atoms during the annealing procedure depends on the annealing temperature and on the conditions of the oxygen partial pressure [107, 128, 129]. After choosing the appropriate annealing conditions and taking into account the oxygen diffusion times, the samples are kept in those conditions for the appropriate period of time and are then quenched in order to stabilize the equilibrium oxygen content at room temperature. The resulting stoichiometry and the homogeneity of the oxygen content are commonly tested by measuring the superconducting transition temperature T_c and the c-axis lattice parameter, which have a known dependence on the oxygen content of the system (plotted in Fig. 1.2 and Fig. 1.20 respectively [34]).

In orthorhombic $YBa_2Cu_3O_{6+x}$ the crystals tend to form a twinned microstructure due to the small difference in the in plane a and b lattice parameters. The twinned microstruc-

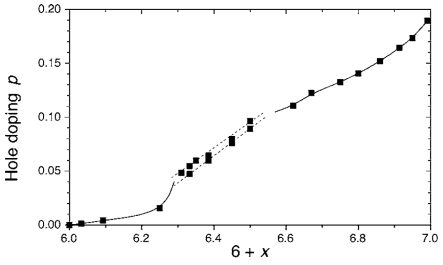

Figure 1.19: Hole doping p per planar Cu ion as a function of the oxygen content x in $YBa_2Cu_3O_{6+x}$. The dependence is not unique because the hole doping is also dependant on the degree of oxygen chain ordering. This is particularly obvious for $0.3 \lesssim x \lesssim 0.5$ (marked by the two dashed lines). Data are taken from reference [34].

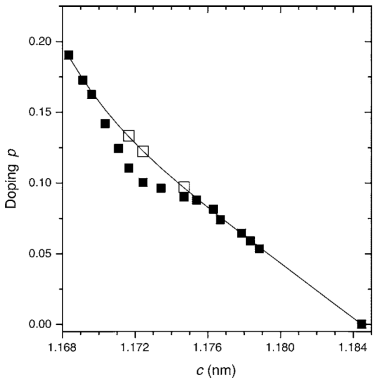

Figure 1.20: Doping dependence of the c-axis lattice parameter in $YBa_2Cu_3O_{6+x}$. Solid squares represent p values obtained based on the doping dependence of T_c given by Eq. 1.1. Open squares are p values estimated for the chain oxygen ordered phases (for more details see reference [34]). The figure is taken from [34].

ture starts as a result of local thermal strains during the transformation of the high temperature tetragonal phase into the low temperature orthorhombic phase, during the annealing and quenching procedure previously described [130]. The twin domains are described as regions of mutually nearly perpendicular directions of the in-plane a- and b- axis, with domain walls along the 110 crystallographic planes [131]. The domain size varies from tens or hundreds of angstroms to fractions of a millimeter, depending on the conditions of the sample growth and the subsequent thermal treatment. The twin domains arrangement can be easily observed under a polarized light microscope as a pattern of bright and dark fringes, like the one shown in Fig. 1.21 [132]. The presence of the Cu-O chains along the b crystallographic axis leads to a strong in plane anisotropy of the optical conductivity. As a result, upon illumination with the linearly polarized light of a polarized microscope the reflectivity of neighboring twin domains is very different, creating this color contrast which can be reversed by a 90° rotation of the sample around the microscope axis (or equivalently by a 90° rotation of the light polarization with the use of a polarization analyzer).

The presence of twin domains is a problem in the study of $YBa_2Cu_3O_{6+x}$ samples since the ab anisotropy of their physical properties cannot be probed. Using a bulk sensitive probe, like for example in an x-ray scattering experiment, both twin domains would contribute equally and would not allow observing the anisotropy of the electronic system. In order to overcome this problem it is necessary to prepare twin-free crystals through an appropriate "detwinning procedure". What is usually employed is a thermomechanical method in which uniaxial stress is applied along one of the tetragonal 100 crystallographic axis of the twinned crystal at elevated temperatures [131, 133]. This leads to a reorientation of the ferroelastic domains and thereby to an elimination of the twinning.

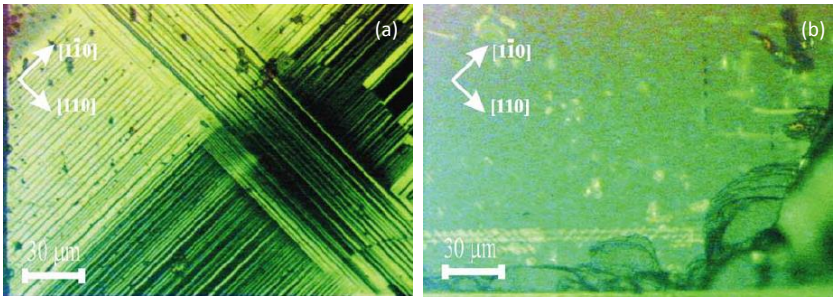

Figure 1.21: Polarizing optical micrographs of the *ab* plane of a $YBa_2Cu_3O_{6+x}$ crystal before (a) and after (b) the detwinning procedure. The bright and dark fringes in (a) correspond to different twin domains with perpendicular directions of the in-plane axis. The figure is taken from [133].

1.1.5 High Pressure Effects

A major part of the current thesis concerns experiments performed under high pressure conditions, therefore a short summary of the effect of pressure on high-T_c cuprates will be included. For a detailed description one can refer to the available reviews [22, 134, 135].

From the early days of high-T_c cuprates high pressures have been extensively used as a valuable tool for their investigation [134, 136]. External pressure offers a "clean" route to explore the complex phase diagram of copper oxide superconductors, avoiding the complexity introduced by chemical doping. High pressure experiments contributed not only to the better understanding of the superconducting mechanism, but have also led to world record values of T_c (164K in $HgBa_2Ca_2Cu_3O_{8+\delta}$ under external pressure P≃30GPa) [24, 25][ii]. It is worth mentioning that the observation of a large pressure enhancement of T_c on the $La_{2-x}Ba_xCuO_4$ cuprate has motivated the substitution of the smaller Y^{3+} cation for La^{3+} which gave rise to the discovery of the famous $YBa_2Cu_3O_{6+x}$ family, which is studied in the current thesis.

While for the majority of conventional simple metal and transition metal superconductors T_c decreases with pressure, copper oxides do not follow this trend. The pressure-induced increase of T_c has attracted a lot of attention and numerous high pressure transport studies on superconducting cuprates have been performed. The main aim of these investigations was to obtain higher superconducting transition temperatures and to offer insights into the parameters controlling the T_c enhancement. Pressure application leads to changes of the structural parameters and subsequently of the electronic properties of the studied system. The superconducting transition temperature depends on many different parameters that are effectively changed by pressure including the carrier concentration in

[ii] More recently a slightly higher T_c=166 K was obtained at P≃23GPa at fluorinated samples of $HgBa_2Ca_2Cu_3O_{8+\delta}$ near the optimum doping level [137].

the superconducting CuO_2 planes, the area of the CuO_2 planes, the separation and the flatness of the CuO_2 planes, the position of the apical oxygen, and the *c/a* ratio of the lattice constants [138]. A major question that the high pressure experiments intended to answer was whether the most important interactions for high temperature superconductivity were taking place within the CuO_2 planes or between them.

Since in copper oxide superconductors T_c strongly depends on the density of charge carriers, the effect of pressure on T_c is usually divided in two main categories: the pressure-induced charge transfer effect and the "intrinsic" pressure effect [139, 140], and can be written as:

$$\frac{dT_c}{dP} = \left(\frac{\partial T_c}{\partial n}\right)\left(\frac{\partial n}{\partial P}\right) + \frac{dT_c^{int}}{dP} \tag{1.4}$$

The first term on Eq. 1.4 represents the pressure-induced charge transfer effect. Focusing on the $YBa_2Cu_3O_{6+x}$ family, the *c*-axis compressibility is relatively high and therefore the application of high pressures results in an increase of the covalent bonding between the CuO_2 planes and the neighboring Cu-O chains. This leads to a pressure-induced charge transfer from the Cu-O chains to the superconducting CuO_2 planes and thus to an effective hole doping of the system. In this framework the effect of pressure on high-T_c cuprates is described as an effective doping of the system and the T_c dependence is understood as the result of the doping variation, following what is expected from the universal expression given in Eq. 1.1. The charge redistribution and the increase of the hole concentration in the CuO_2 planes has been experimentally verified by Hall measurements under high pressure conditions [141, 142, 143] and by high pressure structural data obtained by neutron scattering in combination with a bond valence sum analysis [144]. Phenomenological models have also been suggested to describe the effect quantitatively [140, 145, 146].

The second term on Eq. 1.4 represents the "intrinsic" pressure effect, which is described as the effect of pressure on T_c neglecting the carrier concentration and the charge transfer. The intrinsic pressure effect is better described with the help of Fig. 1.22 which shows the pressure coefficient of T_c for the different doping regions of the phase diagram. If pressure were purely a charge transfer effect then the application of pressure on optimally doped samples would lead the system to the overdoped regime of the phase diagram and to the reduction of its T_c. As simple and appealing the pure charge transfer scenario is, experimental data reveal the pressure-induced increase of T_c for optimally doped systems, and suggest that the charge transfer mechanism alone cannot account for the pressure dependence of T_c [5, 147, 148, 149]. An additional pressure contribution has been suggested to arise from changes in the intraplanar hoping integral deriving from the pressure-induced in-plane compression [134, 150, 151], but in general the origin of the intrinsic pressure effect remains still a subject of scientific research.

A side effect of the high pressure application on oxygen deficient high-T_c cuprates is the so-called pressure-induced "relaxation effect". High oxygen mobility in $YBa_2Cu_3O_{6+x}$ not only imposes complications to the synthesis of a system with a given oxygen stoichiometry but also renders the system susceptible to changes of the oxygen sublattice

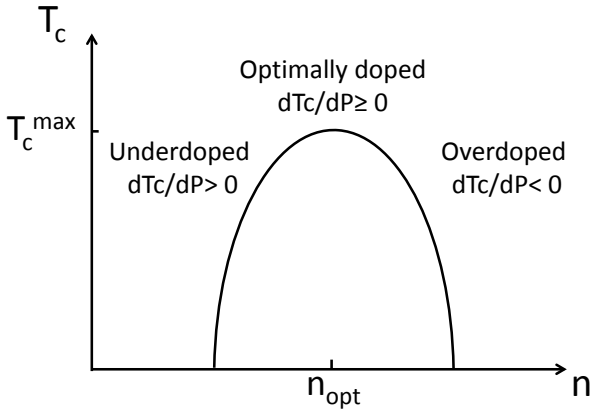

Figure 1.22: The pressure coefficient of T_c in the underdoped, optimally doped and overdoped parts of the phase diagram.

as a function of temperature or pressure. Oxygen atoms residing in the Cu-O chains tend to reorder under pressure application, changing the original oxygen superstructures of the Cu-O chains. On a number of underdoped and overdoped high-temperature superconductors, including $YBa_2Cu_3O_{6+x}$, $Tl_2Ba_2CuO_{6+\delta}$ and $HgBa_2CuO_{4+\delta}$, the transition temperature T_c has been found to change with time in a manner depending on the sample's detailed temperature and pressure history [5, 148, 152, 153]. The first experiments carried out by Sieburger *et al.* [149] on $Tl_2Ba_2CuO_{6+\delta}$ revealed that the pressure dependence of T_c changes significantly depending on the temperature at which the pressure is varied. This anomalous behavior was shown to be a sensitive function of the concentration of the oxygen composition in $Tl_2Ba_2CuO_{6+\delta}$ and it has therefore been attributed to relaxation effects within the oxygen sublattice. Temperature-quench experiments on strongly underdoped $YBa_2Cu_3O_{6+x}$ indeed evidenced strong relaxation effects in T_c from oxygen ordering effects [154]. Sadewasser *et al* [5] have suggested the following time dependence for T_c due to relaxation effects:

$$T_c(t) = T_c(\infty) - [T_c(\infty) - T_c(0)]exp\left\{-\left(\frac{t}{\tau}\right)^{\alpha}\right\} \tag{1.5}$$

where $T_c(\infty)$ is the transition temperature at a given pressure after infinite time, $T_c(0)$ is the initial value of the transition temperature at a given pressure before relaxation begins, α is the stretched exponent and τ is the temperature dependent relaxation time which is

related to the activation energy barrier E_A by the Arrhenius law:

$$\tau(T,P) = \tau_0 exp\left(\frac{E_A(T,P)}{k_\beta T}\right) \tag{1.6}$$

where τ_0 is the attempt period. If the pressure is changed at low temperatures and the entire experiment is also performed at low temperatures then there is insufficient thermal energy for oxygen atoms to rearrange and no relaxation effects are practically observed for T_c. An alternative way to minimize the relaxation effects is to work under pressure on highly ordered samples, ideally fully oxygenated. This will be further discussed later on when the high pressure measurements of the current thesis will be presented.

The fact that the pressure-induced T_c change depends on the temperature at which the pressure is varied was not recognized in the early high pressure experiments, and therefore large discrepancies in the measured pressure coefficients of T_c appear in the literature. An additional factor contributing to the reported experimental discrepancies derives from the very different conditions under which the experiments were performed. Results of different experimental groups may vary substantially because of differences in the studied samples, or in the method used to determine T_c or more commonly in the pressure medium used to ensure hydrostatic conditions. Especially for the case of high pressure resistivity measurements, for which a very delicate wire bonding procedure has to be followed, the majority of the reported data are recorded under strongly non-hydrostatic conditions, with the use of solid high pressure media or no pressure media at all. Although this may significantly simplify the experimentation, the data obtained under such conditions are subjected to non-hydrostatic shear stresses and do not allow for a direct comparison or for reliable quantitative results for which fluid pressure media, particularly helium, should be employed.

1.2 Iron-based Superconductors

1.2.1 Crystal Structure and Superconductivity

Almost 20 years after the first observation of high-T_c superconductivity in copper oxides, a new era of fresh scientific excitement began in 2006 with the discovery of superconductivity in iron-based compounds. Soon after the initial report of superconductivity in LaFePO with a modest T_c of ~4 K [21], fluorine doped $LaFeAsO_{1-x}F_x$ was found to be superconducting with T_c=26 K [155]. An immediate quest for similar compounds with higher T_c followed this discovery, leading to an unprecedentedly fast progress and to the discovery of several new compounds belonging in the iron-based superconductors family. To this purpose, not only chemical substitutions but also external pressure application was extensively implemented (see section 1.2.5).

The members of the iron-based superconductors are classified by their crystal structure. Each structural family is typically named with reference to the stoichiometry of its parent undoped member, for instance "1111" commonly refers to the *Ln*FeAsO family (where *Ln*=lanthanides), whereas "122" refers to the AFe_2As_2 family (where *A*=alkaline-earth). The structures of the most extensively studied families are shown in Fig. 1.23.

Similar to the cuprates, all iron-based superconductors display a layered structure with a layer of iron-pnictogen atoms (or iron-chalcogen atoms in the case of the "11" family) being the common structural element present in all of them and believed to be associated with the emergence of superconductivity [i]. In this square lattice layer the Fe atoms are

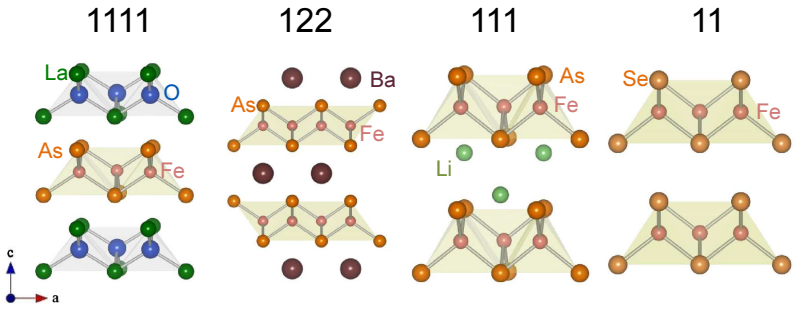

Figure 1.23: Crystal structures of four members of the main structural families of iron-based superconductors: LaFeAsO ("1111" family), $BaFe_2As_2$ ("122" family), LiFeAs ("111" family) and FeSe ("11" family). The common structural unit of all iron-based compounds is the iron-pnictogen/chalcogen tetrahedral layer, highlighted in beige. The figure is adapted from [156].

[i] In most cases the common layer is an Fe-As layer because chemical substitutions are usually performed on chemical sites outside the superconducting layers. Nevertheless, sometimes P replaces As, and/or Co, Ni or other transition metals replace Fe partially or fully for the purpose of electron doping.

at the centers of As tetrahedra (or in general pnictogen/chalcogen tetrahedra), which are usually distorted with respect to the canonical tetrahedron. The iron-pnictogen layers alternate with charge reservoirs along the *c*-axis. The diversity among the different families lies in the structure of the blocking layers, which could be layers of alkali and alkali-earth cations, *Ln*O layers or even more complicated transition metal perovskite-related layers. For the structures plotted in Fig. 1.23 the blocking layers are: LaO layers in the case of LaFeAsO, Ba layers in the case of $BaFe_2As_2$, Li layers in the case of LiFeAs, while no charge donation layer is present in the "11" structure. The room temperature structures of the Fe-based superconductors parent compounds are tetragonal whereas very often an orthorhombic distortion takes place upon cooling at lower temperatures.

The undoped "parent" compounds of Fe-based superconductors are generally non- superconducting. Superconductivity emerges either by chemical doping (heterovalent doping or isovalent substitution) or by application of external pressure [ii]. This is illustrated in their generic phase diagram plotted in Fig. 1.24. In the case of isovalent substitution and application of external pressure the crystallographic structure is modified, whereas in the case of heterovalent doping, in addition to the applied internal chemical pressure, charge carriers are introduced to the structure. A general characteristic of Fe-based superconductivity, linking them to the cuprates case, is the proximity to a magnetic phase. The parent

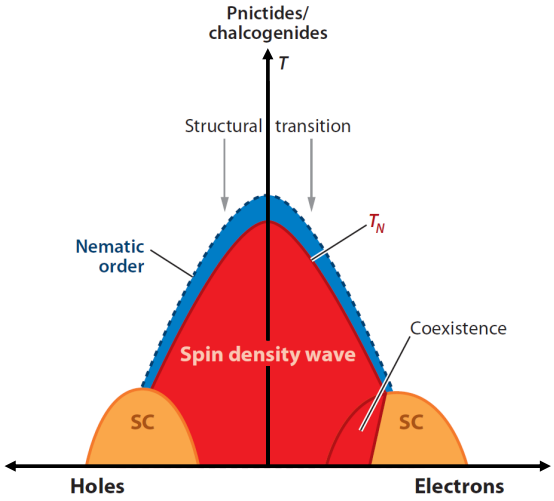

Figure 1.24: Schematic phase diagram of Fe-based superconductors on hole or electron doping. The figure is adapted from [157].

[ii] Some systems, for instance LiFeAs, exhibit superconductivity already at zero doping.

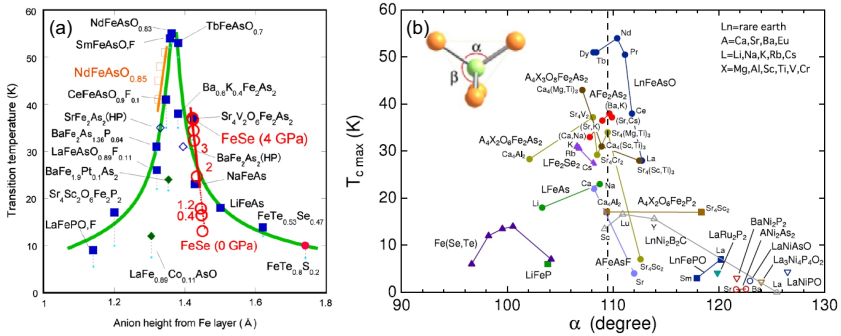

Figure 1.25: T_c dependence on the (a) Pn height from the Fe layer and (b) bond angle α among the Fe and As atoms for a variety of Fe-based superconductors. The graphs are taken from references [158, 159].

compounds are generally antiferromagnetically ordered in a spin density wave (SDW) state (see Fig. 1.24). Moreover, in contrast to the parent compounds of the cuprates superconductors, the undoped members of the Fe-based superconductors are metallic (or more precisely semimetallic). Superconductivity emerges as antiferromagnetism (often accompanied by a structural transition) is suppressed by a tuning parameter (doping/pressure), indicating a certain competition between the two phases as will be discussed later on (see section 1.2.3).

There exists a certain correlation between the crystal structure and superconductivity in iron pnictides. More specifically, the superconducting transition temperature T_c displays a dependence on the structural characteristics of the $FeAs_4$ tetrahedra, namely on the bond angle $\theta_{As-Fe-As}$ among the Fe and As atoms (reflecting the distortion of the $FeAs_4$ tetrahedra) and on the distance h between the Fe layer and the adjacent As layer. As shown in Fig. 1.25 for a variety of Fe-based superconductors, although there is no unique correlation between T_c and bond angle there is a tendency of maximizing T_c when the tetrahedra approach their canonical shape, i.e. for $\theta_{As-Fe-As}$ approaching 109.47°, or for h~1.38 Å (see references [158, 159, 160, 161, 162] and references therein). Similar trends have also been observed under high pressure conditions, verifying that this truly a structural and not a carrier doping effect and highlighting the significance of high pressure studies of these materials [163, 164, 165].

1.2.2 Electronic Structure

The electronic structure of Fe-based superconductors has been studied extensively both experimentally as well as theoretically by first-principles calculations. All the different studies in the various families, regardless of their structural differences, agree on the

multiband character of their electronic structure, contrasting the relatively simple one-band picture of the high-T_c cuprates (Cu-$d_{x^2-y^2}$ valence orbital).

Fig. 1.26 shows the calculated electronic band structure and Fermi surface of the parent LaFeAsO, which incorporates the general characteristics present in all Fe-based superconductors. The calculation was performed within the local-density approximation (LDA) in the density functional theory (DFT) [166]. Close to the Fermi energy (between -2.2 and 2 eV, assigning zero energy to the Fermi level) the electronic bands have a Fe-d character, whereas lower in energy (between -3.2 and -2.2 eV) are positioned the As-p bands (partly hybridized with Fe-d) and the O-p bands. La states occur at energies higher than 2 eV.

Therefore the five bands shown in Fig. 1.26 crossing the Fermi level and participating in the low energy electronic excitations are mainly of Fe-d character. The resulting five sheets of the Fermi surface are two quasi-cylindrical electron pockets centered at the corners of the Brillouin zone (M-A line in Fig. 1.26), two quasi-cylindrical hole pockets centered at the center of the Brillouin zone (Γ-point) and a third heavy hole pocket centered at the Z-point and intersecting the hole cylinders. The third hole pocket is related to the specific details of the "1111" structure and is not generally present in all Fe-based superconductors unlike the rest hole and electron pockets. The two-dimensional character of the layered crystallographic structure is directly reflected in the electronic structure of iron pnictides, which presents only a very moderate k_z dispersion (especially in the case of the "1111" family shown in Fig. 1.26).

Experimental evidence regarding the band structure and fermiology of these materials

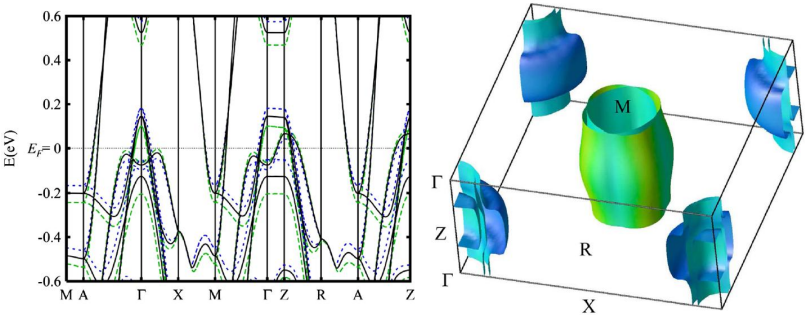

Figure 1.26: DFT calculated band structure (left) and Fermi surface (right) of LaFeAsO. In the band structure the effect of the As height is indicated: the unshifted band structure is given by the solid black line, whereas the one shifted away (towards) the Fe layer is given by the blue dotted (green dashed) line. The Fermi surface is shaded according to the band velocity (blue denotes low velocity). The symmetry points on the Fermi surface are: Γ=(0,0,0), Z=(0,0,1/2), X=(1/2,0,0), R=(1/2,0,1/2), M=(1/2,1/2,0) and A=(1/2,1/2,1/2). The figures are taken from [166].

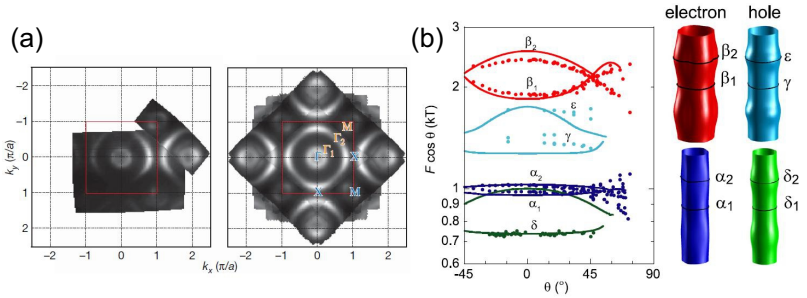

Figure 1.27: (a) Fermi surface maps of LaOFeP. The left panel shows an overlay of two sets of Fermi surface maps (unsymmetrized raw data). The right panel shows the symmetrized Fermi surface map obtained by flipping and rotating the raw data along the high-symmetry lines. The figure is taken from [167]. (b) Observed de Haas-van Alphen oscillation frequencies in LaFePO (solid symbols) versus field angle as the field is rotated from parallel to the *c*-axis towards the *ab*-plane of the crystal. The solid lines correspond to the values derived from DFT calculations, after appropriately shifting the band energies. The right panel shows the Fermi surfaces as predicted by theory using the experimental frequencies of the left panel. The figure is taken from [168].

is qualitatively in very good agrement with the predictions of electronic structure calculations. The Fermi surface has been investigated mainly by two different methods, ARPES and quantum oscillation experiments, which are considered complementary techniques for the study of the electronic structure [169]. As already pointed out for the case of high-T_c cuprates, while ARPES experiments allow a direct mapping of the Fermi surface in the k-space, they are limited by their extreme surface sensitivity and by their relatively low resolution. Quantum oscillations provide accurate information about the cross-sections of the Fermi surface based on the measured variation of the magnetization as function of the magnetic field. Despite their high accuracy, these experiments on one side are limited by the very high magnetic fields needed for the complete suppression of superconductivity and on the other side provide only partial information since they can not determine the position of the measured Fermi surface cross-section in the reciprocal space.

Fig. 1.27 shows the experimental results of ARPES and quantum oscillations experiments on "1111" Fe-based superconductors for a direct comparison with the theoretical results of Fig. 1.26 [167, 168]. The measured ARPES spectra of a LaOFeP single crystal are in reasonable agreement with first principles calculations: two hole pockets (Γ_1 and Γ_2 labeled in Fig. 1.27) are centered at the Γ-point and one electron pocket (M) is centred at the M-point. Given the limited resolution of the measurements and the nearly degenerate sheets under the Γ_1 and M pockets, the observed Fermi surface is qualitatively consistent with the five sheets of Fermi surfaces theoretically predicted (see Fig. 1.26). Quantum oscillation measurements on LaOFeP have determined multiple frequencies through the

Fourier transform spectra of the oscillatory data, in line with the multiband character of the system. The schematic partial Fermi surfaces shown in Fig. 1.27 attempt an assignment of the experimentally observed frequencies to hole and electron Fermi pockets of the theoretically predicted band structure.

A particular characteristic of the electronic structure that was highlighted already in the very early days by theoretical calculations is the shape and size matching of the hole pockets at the Γ-point and the well-separated electron pocket at the M-point (see Fig. 1.26). It was therefore suggested that significant interband scattering takes place at the nesting vector $Q_{nesting}=(\pi,0)$ which maps one of them to the other [170]. Such a nesting instability has also received wide experimental support and is believed to be associated both with the observed SDW magnetic state, as well as with the emergence of superconductivity, as will be discussed next.

Finally regarding the doping evolution of the Fermi surface, as charge carriers are introduced to the parent compounds the basic topology remains unchanged and the chemical potential is suitably shifted depending on the doping type (electron/hole). The effect can be described within the picture of a rigid band shift: as the electron (hole) doping increases the hole (electron) pockets shrink whereas the electron (hole) pockets become larger [171, 172, 173].

1.2.3 Phase Diagram

The generic phase diagram of Fe-based superconductors is presented in Fig. 1.24. The undoped parent compounds are semimetals and undergo at low temperatures a transition towards an antiferromagnetic spin density wave (SDW) state, often accompanied by an almost simultaneous tetragonal-to-orthorhombic phase transition. An electronic nematic phase is suggested to be related to the structural transition [iii]. Upon doping the parent compounds, the magnetic and structural transitions are rapidly suppressed and superconductivity emerges, with the superconducting transition temperature T_c exhibiting a dome-like dependence on doping [iv]. All together the resulting phase diagram resembles strongly the one of high-T_c cuprates, with the most important similarity being the proximity of the superconducting to an antiferromagnetic state (even though the nature of antiferromagnetism is different in the two classes of superconductors, as will be discussed next).

[iii] It is worth mentioning that although the pseudogap phase is still not completely established in the phase diagrams, many scientific reports have indicated the a pseudogap formation also for the Fe-based superconductors and often associated it with the presence of nematicity (see reference [174] and references therein).

[iv] For the sake of completeness it should be noted that in some Fe-based superconductors a second superconducting dome appears at high pressures [175]. Additionally, a double-dome T_c dependence is also obtained for H-doped $LaFeAsO_{1-x}H_x$ [176].

The Antiferromagnetic Phase

The proximity of magnetism and superconductivity in the phase diagram of Fe-based superconductors has not only suggested a possible pairing mechanism of magnetic origin but has also directed a major scientific effort towards the detailed investigation of their magnetic properties. The antiferromagnetic (AF) structure and spin dynamics of all the different families have been studied in detail and reviewed in references [160, 177, 178, 179].

The magnetic structure realized in the parent compounds of different Fe-based superconductors families is shown in Fig. 1.28 [178]. The parent members of the "1111", "122" and "11" families display a collinear antiferromagnetic structure in which the Fe magnetic moments are aligned in-plane with an ordering wavevector Q_{AF}=(1,0) , or (0,1) due to twinning, in the notation of the low temperature orthorhombic unit cell [v]. The $\Gamma(0,0)\leftrightarrow M(1,0)/(0,1)$ nesting wave vector connecting the hole and electron Fermi surface pockets described earlier coincides with the commensurate ordering wavevector, suggesting that the antiferromagnetic ordering is a SDW due to Fermi surface nesting of itinerant electrons. The Fermi surface nesting picture in combination with the small value of the measured magnetic moments (<1 μ_B per Fe) and the weak electronic correlations in iron pnictides have initially pointed towards an itinerant electron character of magnetism (in-

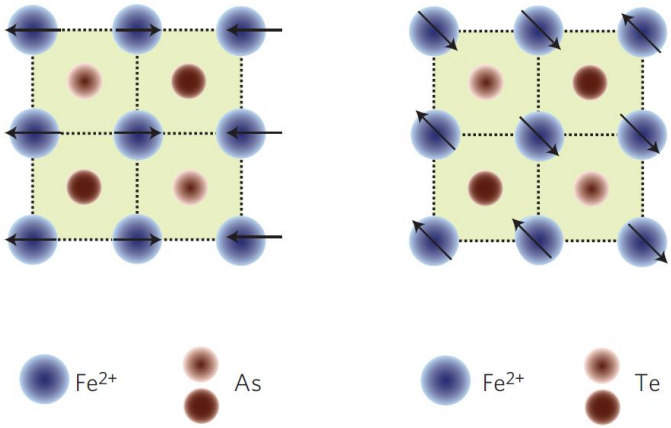

Figure 1.28: The antiferromagnetic structure realized in the parent compounds of the (a) "111", "1111", "122" and (b) "11" families of iron-based superconductors. The dark (light) brown As/Te atoms indicate their vertical positions above (below) the Fe layer. The figure is adapted from [178].

[v] In the out-of-plane direction, the coupling of neighboring planes is for the REFeAsO materials either ferromagnetic or antiferromagnetic depending on the rare earth element, and antiferromagnetic for the "122" materials.

stead of a local moment character).

Unlike the rest of Fe-based superconductors, the spin structure of the "11" materials is collinear with in-plane ordering wavevector Q_{AF}=(1/2,1/2) (see Fig. 1.28). Surprisingly this happens despite the fact that their Fermi surface is very similar to the rest of the families [180], according to which the "11" materials are susceptible to the same nesting instability. In view of the failure of a Fermi surface nesting picture in this case, attention was partly oriented towards local moment approaches in order to understand the magnetic ordering. This is further supported by multiple experimental observations inconsistent with the itinerant electrons picture including the observation of local magnetic moments in the room temperature paramagnetic state [181] and the cases of compounds, such as LaFePO, for which no magnetic order is observed in spite of the well nested Fermi surface [182].

The overall experimental observations suggests that despite earlier views, solely itinerant electron approaches are not sufficient to explain magnetism in these compounds. Magnetism in Fe-based superconductors embodies a dual nature with expressions of both local magnetic moments and itinerant electrons.

Concerning the doping evolution of the magnetic ordering, according to the phase diagram of Fig. 1.24 while the antiferromagnetic transition is suppressed as superconductivity emerges, there exists a doping range in which the magnetic and superconducting phases overlap [vi]. This region has been extensively studied in the literature especially in the "122" family (earlier in electron-doped $Ba(Fe_{1-x}Co_x)_2As_2$ and more recently in hole-doped $Ba_{1-x}K_xFe_2As_2$) [183]. In order to understand this overlap, two different approaches have been proposed: phase separation and microscopic phase coexistence. The former case is supported by early muon spin rotation results [184] according to which only part of the system orders magnetically while the rest of the compound remains paramagnetic and hosts superconductivity. In the latter case, SDW and superconductivity microscopically coexist below T_c. Very recent STM and ARPES studies have provided strong supporting evidence for the microscopic coexistence of the two phases and their dynamic competition, suggesting that the phase separation is a non-intrinsic but sample quality related effect [185, 186].

The Structural Transition and the Nematic Phase

In the "1111" and "122" Fe-based superconductors very often a tetragonal-to-orthorhombic transition takes place at temperatures very close to the antiferromagnetic transition (usually the structural transition precedes). It was therefore suggested that the two transitions are connected and that the observed structural transition is not lattice-driven but electronically-driven and related to the so-called electronic nematic phase [187, 188].

In this case, nematicity refers to a spontaneously broken rotational symmetry without a broken translational and time-reversal symmetry and is observed as an anisotropy in an

[vi] This holds for the "111" and especially the "122" materials.

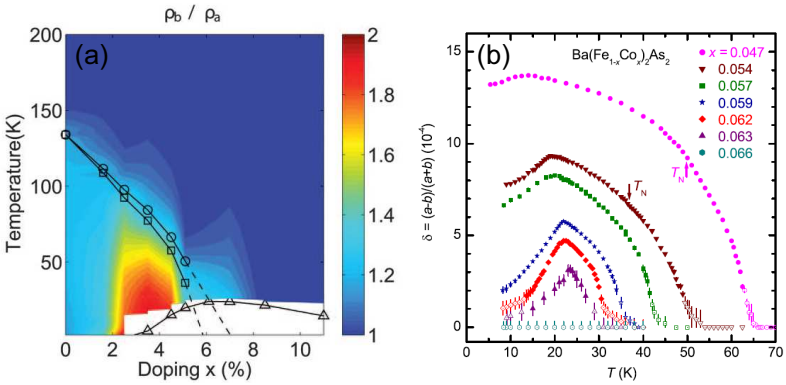

Figure 1.29: (a) Resistivity ration ρ_b/ρ_a as a function of temperature and doping. The structural, magnetic and superconducting transition temperatures are shown as circles, squares, and triangles, respectively. The resistivity ratio deviates from unity at a considerably higher temperature than T_{str} indicating the presence of nematic fluctuations. The figure is taken from [189]. (b) Orthorhombic distortion δ in $Ba(Fe_{1-x}Co_x)_2As_2$ single crystals as a function of temperature and doping. The magnetic transition temperature is indicated by the arrows. The figure is taken from [190].

electronic property that locally breaks the lattice symmetry [189, 191]. In systems for which the rotational symmetry of the crystal lattice is also broken, like in the orthorhombic phase of the iron pnictides, the observed electronic anisotropy is much more pronounced than the anisotropy of the crystal lattice alone would suggest. While the first indications of electronic nematicity in iron pnictides came from resistivity anisotropy measurements, several other probes including ARPES, NMR and STM reported anisotropies in charge or spin related observable properties both in the orthorhombic as well as in the tetragonal phase (for a recent review of the experimental studies see reference [187]). An example is given in Fig. 1.29 which shows the resistivity anisotropy in $Ba(Fe_{1-x}Co_x)_2As_2$ single crystals starting at temperatures greater than the structural transition temperature [189]. In the same figure is also plotted the measured orthorhombic distortion for the same system, which shows a pronounced suppression in the superconducting state, suggesting the competition for the same electronic states between two electronically driven orders [190].

Considering nematicity as an integral part of the phase diagram, the idea that nematicity, magnetism and superconductivity have the same driving force has been put forward. Theories including either anisotropic magnetic fluctuations or charge/orbital fluctuations have been proposed, however up to now there has been no definite determination of the origin of nematicity and its interplay with superconductivity.

The Superconducting Phase

The main points of interest to be determined in the superconducting state of Fe-based superconductors are the pairing symmetry and ultimately the pairing mechanism (for recent reviews see references [172, 192, 193, 194, 195]). Very early it was realized that the strength of the electron-phonon coupling is not sufficient to explain superconductivity in these compounds [196] and the attention was oriented towards unconventional pairing mechanisms, while the proximity of magnetism and superconductivity in the phase diagram have positioned spin fluctuations on top of the list [vii].

Even though a consensus on the pairing mechanism is lacking, several measurements have been carried out aiming to determine experimentally the pairing symmetry. Early NMR measurements have shown that the Knight shift decreases in all crystallographic directions, therefore indicating that the spin symmetry of the superconducting state is a singlet [197] and that consequently the orbital pairing symmetry is even. Similar to the cuprates case, the singlet pairing possibilities are limited by the tetragonal D_{4h} crystallographic symmetry of the superconducting layers [53]. In the case of iron pnictides though, the situation gets further complicated by additional "sub-symmetries" arising from the multiband electronic structure. The best way to determine experimentally the orbital symmetry would be through phase sensitive measurements, but in addition to technical obstacles, the multiband character of iron pnictides imposes considerable difficulties in interpreting Josephson based experiments. Multiple ARPES measurements on different compounds have shown the opening of nodeless superconducting gaps of different magnitudes at the hole and electron Fermi pockets. This is illustrated in the ARPES data shown in Fig. 1.30 for the case of $Ba_{0.6}K_{0.4}Fe_2As_2$ [198]. Moreover, the ARPES determined gap magnitudes can generally be classified in two groups: a small gap in the outer hole pocket and larger gaps on the rest Fermi sheets [199].

Such a symmetric superconducting gap with the additional characteristic of a sign change between different Fermi sheets in the multiband electronic structure was theoretically predicted in the context of a spin fluctuations mediated pairing [170, 202]. This is the so-called $s_{\pm}$-wave symmetry and constitutes the most discussed pairing symmetry in the Fe-based superconductors literature. The sign change is a crucial requirement for a superconducting mechanism including spin fluctuations, in order to obtain an effective attractive pairing interaction from the repulsive screened Coulomb interaction [193, 203]. Strong experimental support for this pairing scenario is provided by the observation of the magnetic resonant mode in the spin-excitation spectra below T_c, which is generally expected to appear only in the case that the superconducting gap changes sign on the different Fermi sheets (see Fig. 1.29) [200, 204]. Sub-gap bound states at single impurities seen by STM, as well as the observed variation of the quasiparticle interference pattern in a magnetic field are also consistent with an $s_{\pm}$ symmetry picture [194, 205]. An alterna-

[vii] In view of the phononic Raman study of the current thesis, it should be mentioned that including the effects of magnetism increases the electron-coupling constant by as much as 50%, which even though is still not enough to explain the observed values of T_c, may however have a significant effect on superconductivity [201].

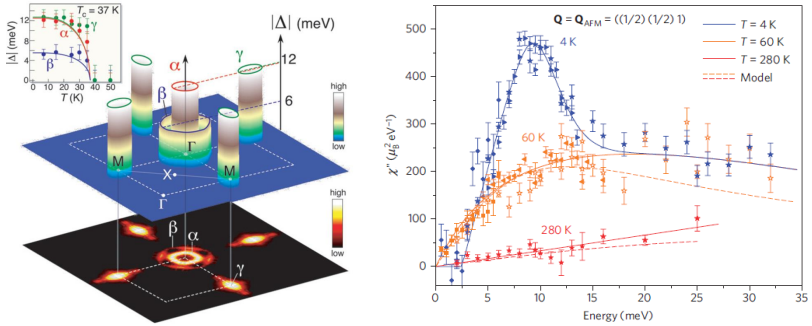

Figure 1.30: (a) 3-D plot of the superconducting-gap magnitude Δ measured at 15 K on the three observed Fermi surface sheets (shown at the bottom as an intensity plot) and their temperature evolutions (inset). (b) Experimental neutron data showing the appearance of the spin resonance in $BaFe_{1.85}Co_{0.15}As_2$ below T_c=25 K. The figure is taken from [200].

tive theoretical proposal involves an orbital-fluctuations pairing mechanism and suggests a symmetric *s*-wave gap but in this case without sign change (the so-called s_{++} symmetry) [206]. The observed robustness of superconductivity against impurities appears in favor of such a scenario, together with the suggested alternative explanation for the spin resonance mode that does not involve a sign change of the order parameter [207].

While the issue of the pairing mechanism in iron pnictides has not been settled, it appears that the majority of the experimental studies are in favor of a sign changing $s_{\pm}$-wave symmetry of the superconducting gap and the accompanying magnetic-fluctuation mediated Cooper pairing scenario [193].

1.2.4 The REFeAsO "1111" family

The current thesis includes an experimental study of the structure and lattice dynamics of the *Ln*FeAsO "1111" family, and more specifically of the SmFeAsO compound. This was the first family for which Fe-based superconductivity was observed and the one with the highest reported T_c (55 K for $SmFeAsO_{1-x}F_x$ with x=0.12 [209]). Yet, the scientific attention was soon shifted towards other families, especially the "122" and "11" families, due to the difficulties encountered in synthesizing "1111" single crystals of considerable volume. Up to date, the available "1111" single crystals have in-plane dimensions in the range of 150-300 μm, while more recently the growth of epitaxial "1111" thin films by molecular beam epitaxy (MBE) was reported. Superconductivity is induced to the initial non-superconducting films through subsequent F diffusion from an overlayer of SmF_3 [210, 211, 212].

The crystal structure of parent *Ln*FeAsO at ambient conditions is tetragonal (space group *P*4/*nmm*) with alternating layers of *Ln*O and FeAs, stacked along the *c*-axis, as

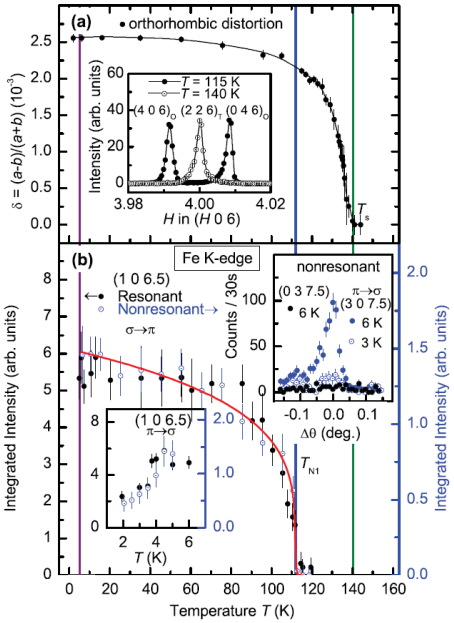

Figure 1.31: (a) Temperature dependence of the orthorhombic distortion. The inset shows (ξ 0 0) scans through the (4 0 6) reflection in the tetragonal and orthorhombic phases. (b) Temperature dependence of the integrated intensity of the magnetic (1 0 6.5) reflection in resonant (left) and non-resonant (right) conditions. The figure is taken from [208].

shown in Fig. 1.23. A structural transition to an orthorhombic phase (space group *Cmma*) occurs at temperatures located between 130-180 K (depending on the compound), very close in temperature to the SDW transition. For the parent compounds with magnetic rare earth ions, as is the SmFeAsO compound, in addition to the iron magnetic moments also the rare earth moments order at very low temperatures (5-15 K). Moreover, a coupling between the rare earth and Fe moments has been reported which in most case leads to the enhancement of the Fe moment [177].

An example is shown in the x-ray scattering data of Fig. 1.31 for the case of the SmFeAsO compound. The transition to the orthorhombic structure occurs at ~140 K. Upon further cooling, the orthorhombicity increases while a magnetic signal appears below ~110 K [208].

As in all Fe-based superconductors, superconductivity in the "1111" family is induced through appropriate carrier doping (with electrons or holes) of the superconducting FeAs layers or through the application of external pressure. The most common and practical way of chemically doping the "1111" family is though the substitution of divalent oxygen ions with monovalent fluorine ions (F-doping), a procedure which promotes extra electrons towards the FeAs layer (electron doping) [155]. However, in $REFeAsO_{1-x}F_x$ the small solubility of fluorine limits the accessible doping region to x≃0.2. In order to

reach higher doping levels, REFeAsO has been later on doped with hydrogen, permitting the study of the entire phase diagram of $REFeAsO_{1-x}H_x$ [176, 213, 214]. Electron doping has also been achieved though the introduction of oxygen deficiencies in the REO layer [215]. Hole doping has been implemented through substituting the trivalent rare earth atoms by divalent atoms, e.g. substituting La^{3+} by Sr^{2+} atoms [216]. Finally, substitutions of the Fe ions of the superconducting FeAs planes with different transition metals (Co or Ni) have also yielded similar results [217].

The emergence of superconductivity in the "1111" family is accompanied by the suppression of the magnetic and structural transitions. In some cases, as in $LaFeAsO_{1-x}F_x$ and $PrFeAsO_{1-x}F_x$, magnetism abruptly disappears as a function of doping, whereas in others, like in $CeFeAsO_{1-x}F_x$, the magnetic transition is continuously suppressed and there exists an overlap range between superconductivity and magnetism. The phase diagram of $SmFeAsO_{1-x}F_x$ will be discussed in more detail later on with respect to the experimental results of the current thesis.

1.2.5 High Pressure Effects

Following the wealth of information offered by high pressure experiments on high-T_c cuprates, high pressure application was implemented for the study of Fe-based superconductors almost immediately after their discovery. Some reviews of the high pressure investigations on iron pnictides are given in references [218, 219, 220].

Similar to the cuprates, the main motivation behind these studies was to gain further insights in the parameters controlling superconductivity as well as to maximize the T_c reported at ambient pressure. This is not very surprising given the significant dependence of T_c on the structural characteristics of the $FeAs_4$ tetrahedra (see Fig. 1.25) in combination with the drastic changes in the bond lengths and bond angles induced by the application of pressure. As already shown in Fig. 1.26, the electronic band structure and the density of states at the Fermi level are sensitively dependent on the spacing between the pnictogen/chalcogen layer and the iron layer and therefore on the applied external pressure. Moreover, the lattice compression can induce changes of the carrier concentration through the increase of the inter- or intraplane charge transfer. However, Hall measurements under comparatively high pressure and chemical doping conditions are still needed to provide a clear quantitative understanding of the effect of pressure on the carrier concentration.

As in the case of high-T_c cuprates, the resulting pressure dependence of T_c generally exhibits a dome-like shape (although this depends also on the doping level of the compound under pressure [11]) resembling strongly the doping dependence of T_c and suggesting the role of external pressure in leading the system towards the optimal doping conditions. Unlike the case of cuprates though, for which pressure is mostly used to enhance the existing superconducting properties, pressure application has often led to the emergence of superconductivity in the non-superconducting parent compounds of Fe-based superconductors. For example, superconductivity appears at ~2 GPa in LaFeAsO

(T_c^{max}≃20 K at 12 GPa) [221] and at ~3 GPa in $BaFe_2As_2$ (T_c^{max}≃30 K at 3.8 GPa) [222].

The experimentally determined phase diagrams under chemical doping and under external pressure are very similar, as illustrated in Fig. 1.32 for the case of $BaFe_2As_2$ [172]. Note that together with the enhancement of T_c, pressure simultaneously suppresses the magnetic and structural transitions in a similar manner as chemical substitutions. However, the exact pressure under which superconductivity (magnetism) appears (disappears), the obtained value of T_c and the pressure under which it occurs vary considerably among the results of different experimental studies, depending both on the pressure conditions and on the sample quality.

The importance of the degree of hydrostaticity in high pressure investigations was already highlighted for the respective studies in copper oxides. For Fe-based materials this is particularly important, since they appear to be extremely sensitive to uniaxial pressure components. High pressure studies on the same compounds have yielded substantially different results when using different pressure transmitting media [223, 224]. This enhanced sensitivity to shear stresses was suggested to account not only for the reported experimental discrepancies, but also for the pressure-temperature history effects observed in iron pnictides [225]. Surprisingly though, many studies have shown that the deviation from hydrostaticity and the presence of shear stresses act in favor of superconductivity, reducing the required pressure applied in order to suppress magnetism (see reference [220] and references therein). In any case, the contribution of the distinct parameters on the emergence of superconductivity can only be determined through well-controlled purely hydrostatic (under helium pressure transmitting medium) or purely uniaxial experiments. Additionally, the dependence of the pressure effect on the applied stress/strain conditions

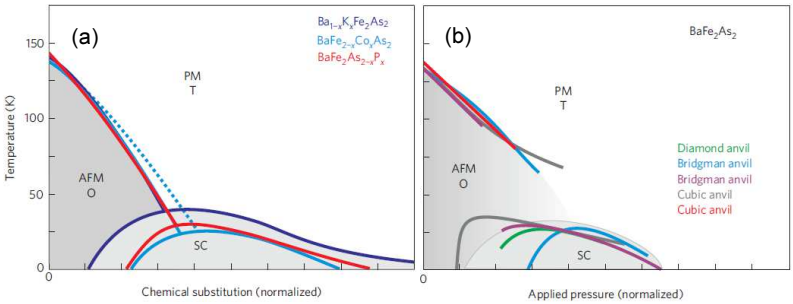

Figure 1.32: (a) Phase diagram of the $BaFe_2As_2$ system obtained under K, Co and P doping. The chemical doping is normalized such that the slope of the magnetic transition overlaps for the different dopants in order to facilitate the comparison of T_c. The dotted line indicates the structural transition form the tetragonal (T) to the orthorhombic (O) phase. (b) Phase diagram of parent $BaFe_2As_2$ as a function of external pressure using different pressure application devices. The applied pressure for the different devices is again normalized as in panel (a). The figure is taken from [172].

in combination with the anisotropic compressibility of Fe-based superconductors, highlight the need to perform high-pressure studies on high quality single crystals, instead of the polycrystalline and powder samples that were often used in the early experiments.

Finally, it is worth to mention that several structural studies have indicated the emergence of a new structure under high pressure conditions, the so-called "collapsed-tetragonal structure", suggesting that it is a common feature in the phase diagrams of Fe-based superconductors. The initial tetragonal structure collapses along the c-axis direction, with a simultaneous increase of the a-axis, resulting in a big decrease of the unit cell volume and of the c/a ratio. The collapsed tetragonal structure has often been observed in the "122" family [226, 227, 228, 229], but also in "1111" compounds [230, 231]. The pressure under which the structural transition occurs, as well as its coexistence with superconductivity vary depending on the exact compound and on the experimental conditions (see for example the case of $CaFe_2As_2$ in references [232, 233, 234]). As a general trend, the pressure under which the transition occurs scales linearly with the ambient conditions unit cell volume [235] and a decrease of T_c (or even a disappearance of superconductivity in some cases) takes place in the collapsed tetragonal phase.

Chapter 2

Raman scattering

2.1 Overview of Inelastic Light Scattering

Most of the incident light on a solid sample is reflected, transmitted or absorbed following the standard laws of reflection and refraction, while a small part of it is scattered towards different directions. In the case of monochromatic irradiation of the sample in the visible range, the scattered light can be of the same wavelength as the incident through a procedure known as elastic or *Rayleigh scattering*, or of different wavelength through a procedure known as inelastic or *Raman scattering*. During the scattering process, energy and momentum are exchanged between the probe (incident photon) and the investigated system, creating or annihilating elementary excitations [i].

The incident (i) and scattered (s) light is typically described by plane waves of frequency ω_i, ω_s and wave vectors $\mathbf{k}_s$, $\mathbf{k}_s$ respectively. Following the energy and momentum conservation rules it applies that:

$$\hbar\omega_s = \hbar\omega_i \pm \hbar\omega, \quad \mathbf{k}_s = \mathbf{k}_i \pm \mathbf{q} \tag{2.1}$$

where ω and $\mathbf{q}$ are respectively the energy and the momentum transferred to the system. A minus sign in Eq. 2.1 corresponds to the creation of an elementary excitation and to an outgoing photon of smaller energy than the incident photon (*Stokes process*), whereas a plus sign corresponds to the annihilation of an elementary excitation and to a scattered photon of higher energy than the incident photon (*anti-Stokes process*).

The energy of the scattered light is analyzed by a Raman spectrometer (more details can be found in the "Experimental Techniques" chapter). The resulting Raman spectrum presents the intensity of the scattered light as a function of the *Raman shift*, i.e the energy shift (or equivalently the frequency shift) of the scattered light with respect to the incident

[i] To be exact, Raman scattering refers to inelastic light scattering in the visible range by any type of excitation except for acoustical phonons. Inelastic scattering by acoustical phonons is known as *Brillouin scattering*.

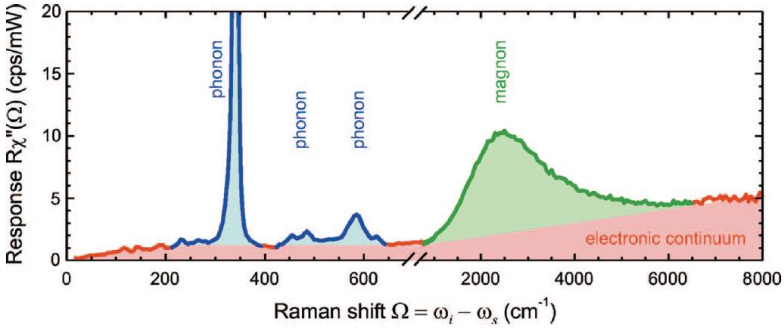

Figure 2.1: Characteristic Raman spectrum of $Y_{0.92}Ca_{0.08}Ba_2Cu_3O_{6.3}$. Light scattering contributions from phonons, magnons, and electrons are plotted in blue, green, and red, respectively. The figure is taken from reference [236].

light. The energy of the incident light, and correspondingly of the elastically scattered light, determines the origin of the energy axis. The energies of the elementary excitations involved in a Stokes or an anti-Stokes process have positive and negative energy values respectively. Typically the Raman shift ω is expressed in spectroscopic wavenumber units of cm^{-1}, which are connected to the wavelength through: $\omega = \frac{1}{\lambda_0} \pm \frac{1}{\lambda_1}$, where λ_0 is the excitation wavelength, and λ_1 is the Raman spectrum wavelength. An approximate conversion of the energy units is 1 $cm^{-1} \simeq$ 29.98 GHz$\simeq$ 0.124 meV.

The elastically scattered light is typically $\sim 10^6$-10^8 times stronger than the inelastically scattered light, rendering highly important the use of an intense excitation light source. Raman scattering experiments are typically carried out with the incident light coming from a laser source and with energy in the visible range. Using optical photons of such energy (~1-2 eV), the study of low energy excitations like phonons (~10-20 meV) requires a good resolution and an effective rejection of the elastically scattered light. According to the light dispersion relation, photons of this energy range (~1-2 eV) have wave vectors $|\mathbf{k}_i| \sim 10^{-3}$ Å. Subsequently the maximum momentum transfer to the system is very small compared to the size of the first Brillouin zone $|\mathbf{k}_{BZ}| = 2\pi/a \sim$ Å. First order Raman scattering is therefore limited to probe excitations only very close to the Brillouin zone center (Γ-point).

Light can be inelastically scattered from many types of excitations, including electronic excitations, phonons, magnons etc. A typical Raman spectrum of $YBa_2Cu_3O_{6+x}$, a member of the high-T_c cuprates family studied here, is shown in Fig. 2.1 where the light scattering contributions from the different types of excitations are separately highlighted. Reviews of electronic and magnetic Raman scattering in solids, and specifically in high-T_c superconductors, can be found in references [236, 237, 238, 239]. From now on for

the current description we will focus on phononic Raman scattering which is relevant to the results of the thesis.

2.2 Phononic Raman scattering

2.2.1 Classical description of phononic Raman scattering

We now consider an approach to the theory of phononic Raman scattering in which both the electromagnetic radiation and the solid system are treated classically. The electric field of the incident monochromatic light is described by a plane wave $\mathbf{E}_i(\mathbf{k}_i, \omega_i) = \mathbf{E}_0 \cos(\mathbf{k}_i \cdot \mathbf{r} - \omega_i t)$ with frequency ω_i and wave vector $\mathbf{k}_i$. Upon incidence to the solid material the electric field induces a polarization given by:

$$\mathbf{P} = \varepsilon_0 \overleftrightarrow{\chi}\, \mathbf{E}_i \tag{2.2}$$

where ε_0 is the electric permittivity of free space and $\overleftrightarrow{\chi}$ is the electric susceptibility of the material, which is in general a second-rank tensor. For the rest of the discussion we will assume an isotropic medium, in which case χ can be represented by a scalar.

The electronic susceptibility χ describes the ability of the system to polarize in response to the electric field and is in general a function of the atomic coordinates. Consequently at a finite temperature the presence of thermally excited lattice vibrations induces fluctuations of χ. Within the classical theory of harmonic crystals the atomic vibrations are treated as coupled classical harmonic oscillators [ii]. The atomic displacements $\mathbf{u}$ from their equilibrium positions are given by $\mathbf{u}(\omega, \mathbf{q}) = \mathbf{u}_0 \cos(\mathbf{q}\cdot\mathbf{r} - \omega t)$ (for a complete description see references [240, 241]). These are lattice waves with frequency ω and wavevector $\mathbf{q}$ and represent independent vibrational modes of the lattice, the so-called *normal modes*, with a suitable dispersion relation between ω and $\mathbf{q}$. In the Born-Oppenheimer or adiabatic approximation the much lighter electrons move more rapidly than the nuclei and follow instantaneously the slow motion of the heavy atomic nuclei. We assume thus that the characteristic electronic frequencies which determine χ are much larger than ω and hence χ can be described as a function of $\mathbf{u}$. Expanding the electronic susceptibility χ in a Taylor series with respect to the atomic displacements from their equilibrium position

[ii] In the harmonic approximation the atomic displacements $\mathbf{u}$ from their equilibrium positions $\mathbf{R}_0$ are assumed to be small compared to the interionic spacing. The instantaneous position of the ions is given by $\mathbf{R}=\mathbf{R}_0+\mathbf{u}$. The total potential energy of the crystal V can therefore be expanded in a Taylor series around the equilibrium positions:

$$V(\mathbf{R}) = V(\mathbf{R}_0) + \left.\frac{\partial V(\mathbf{R})}{\partial \mathbf{u}}\right|_0 \mathbf{u} + \frac{1}{2}\left.\frac{\partial^2 V(\mathbf{R})}{\partial \mathbf{u}^2}\right|_0 \mathbf{u}^2 + \frac{1}{3}\left.\frac{\partial^3 V(\mathbf{R})}{\partial \mathbf{u}^3}\right|_0 \mathbf{u}^3 + \ldots \tag{2.3}$$

The subscript "0" on the derivatives indicates that these are to be taken at the equilibrium positions. The linear term vanishes in the equilibrium position, leaving the quadratic terms as the first non-vanishing correction to the equilibrium potential $V(\mathbf{R}_0)$. The harmonic approximation consists of considering only the quadratic term and neglecting the third and higher order terms in this expansion.

u we get:

$$\chi(\mathbf{u}) = \chi_0 + \left.\frac{\partial\chi}{\partial\mathbf{u}}\right|_0 \mathbf{u} + \frac{1}{2}\left.\frac{\partial^2\chi}{\partial\mathbf{u}^2}\right|_0 \mathbf{u}^2 + ... \tag{2.4}$$

where the first term χ_0 describes the electronic susceptibility of the crystal in the absence of lattice vibrations (static electronic susceptibility), whereas the rest of the terms describe the modulation of the electrical susceptibility by the lattice vibrations. The subscript "0" on the derivatives indicates that these are to be taken at the equilibrium configuration. If we take into account only the first two terms of Eq. 2.4 and ignore the higher order terms, then combining Eq. 2.2 and Eq. 2.4 (neglecting the ε_0 multiplier factor), we can express the induced polarization of the system in the presence of lattice vibrations:

$$\begin{aligned}
\mathbf{P} &= \chi_0\mathbf{E}_i(\mathbf{k_i},\omega_i) + \left.\frac{\partial\chi}{\partial u}\right|_0 \mathbf{u}(\omega,\mathbf{q})\cdot\mathbf{E}_i(\mathbf{k_i},\omega_i) \\
&= \mathbf{P}_0(\mathbf{k_i},\omega_i) + \left.\frac{\partial\chi}{\partial u}\right|_0 \mathbf{u}_0\cos(\mathbf{q}\cdot\mathbf{r}-\omega t)\cdot\mathbf{E}_0\cos(\mathbf{k_i}\cdot\mathbf{r}-\omega_i t) \\
&= \mathbf{P}_0(\mathbf{k_i},\omega_i) + \frac{1}{2}\left.\frac{\partial\chi}{\partial u}\right|_0 \mathbf{u}_0\mathbf{E}_0\cos[(\mathbf{k_i}+\mathbf{q})\cdot\mathbf{r}-(\omega_i+\omega)t] \\
&+ \frac{1}{2}\left.\frac{\partial\chi}{\partial u}\right|_0 \mathbf{u}_0\mathbf{E}_0\cos[(\mathbf{k_i}-\mathbf{q})\cdot\mathbf{r}-(\omega_i-\omega)t] \\
&= \mathbf{P}_0(\mathbf{k_i},\omega_i) + \mathbf{P}_{ind}[(\mathbf{k_i}-\mathbf{q}),(\omega_i-\omega)] + \mathbf{P}_{ind}[(\mathbf{k_i}+\mathbf{q}),(\omega_i+\omega)]
\end{aligned} \tag{2.5}$$

This oscillating polarization vector generates scattered radiation of the respective frequency and wave vector. The electric field of the scattered light will therefore be of the form:

$$\mathbf{E}_s(\mathbf{k_s},\omega_s) = \mathbf{E}_i(\mathbf{k_i},\omega_i) + \mathbf{E}_i[(\mathbf{k_i}-\mathbf{q}),(\omega_i-\omega)] + \mathbf{E}_i[(\mathbf{k_i}+\mathbf{q}),(\omega_i+\omega)] \tag{2.6}$$

The first term of Eq. 2.6 is the elastic term which describes scattered light of the same frequency and wave vector as the incident light. The last terms are the ones of Raman scattering, which describe scattered radiation in frequencies and wave numbers shifted with respect to the ones of the incident radiation. The second term corresponds to the Stokes process (ω_s=ω_i-ω) while the third term corresponds to the anti-Stokes process (ω_s=ω_i+ω), belonging both in a first order Raman scattering process. If we take into account also higher order terms of the electronic susceptibility Taylor series of Eq. 2.3 this would give rise to higher-order Raman scattering terms. For instance, the third term of Eq. 2.3 ($\frac{1}{2}\left.\frac{\partial^2\chi}{\partial u^2}\right|_0 u^2$) governs the second order Raman scattering process in which the scattered light frequency ω_s is shifted from the laser frequency ω_i by ($\pm\omega_1 \pm \omega_2$), where ω_1 and ω_2 are the frequencies of two different vibrational modes of the lattice. The momentum conservation principle in this case requires that $q_1 \pm q_2 \simeq 0$, offering therefore the possibility to study lattice vibrations with $q\neq0$ through higher order Raman scattering processes.

Using the standard procedures of electromagnetic theory, the electric and magnetic field produced by an harmonically oscillating electric dipole can be calculated as a function of time and position (for a detailed description of the calculation see reference [242]). The energy flux density Φ_s of the scattered electromagnetic radiation is given by:

$$d\Phi_s = \frac{\omega_s^4}{16\pi^2 c^3} |\hat{e}_s \cdot \mathbf{P}|^2 d\Omega \tag{2.7}$$

where $d\Omega$ is the solid angle. Replacing $\mathbf{P}$ from Eq. 2.2, we obtain:

$$\frac{d\Phi_s}{d\Omega} = \Phi_i \frac{\omega_s^4}{16\pi^2 c^4} |\hat{e}_s \cdot \chi \cdot \hat{e}_i|^2 \tag{2.8}$$

where $\Phi_i = \varepsilon_0 c E_i^2$ is the energy flux density of the incident radiation. For the case of first order Raman scattering, replacing χ from Eq. 2.4 it follows that:

$$\frac{d\Phi_s}{d\Omega} = \Phi_i \frac{\omega_s^4}{16\pi^2 c^4} \left| \hat{e}_s \cdot \left[\frac{\partial \chi}{\partial \mathbf{u}} \Big|_0 \mathbf{u} \right] \cdot \hat{e}_i \right|^2 \tag{2.9}$$

The term in square brackets in Eq. 2.9 is the so-called *Raman tensor* $\overleftrightarrow{R} = \frac{\partial \chi}{\partial \mathbf{u}}\big|_0 \mathbf{u}$. The differential *scattering cross section*, $\partial^2\sigma/\partial\Omega\partial\omega$, which represents the probability of an incident photon to be inelastically scattered in a solid angle $d\Omega$ with energy between ω and $\omega+d\omega$, is obtained by dividing Eq. 2.9 by Φ_i:

$$\frac{\partial^2\sigma}{\partial\Omega\partial\omega} = \frac{\omega_s^4}{16\pi^2 c^4} \left| \hat{e}_s \cdot \overleftrightarrow{R} \cdot \hat{e}_i \right|^2 \delta(\omega - \Delta\omega) \tag{2.10}$$

where δ is the δ-function centered at the Raman shift ω.

The intensity of the scattered light is proportional to the differential scattering cross-section $\partial^2\sigma/\partial\Omega\partial\omega$ and therefore according to Eq. 2.10:

$$I \propto \left| \hat{e}_s \cdot \overleftrightarrow{R} \cdot \hat{e}_i \right|^2 \tag{2.11}$$

Hence, it follows that in certain choices of the incident and scattered light polarizations the intensity of the scattered light can vanish even if the components of the Raman tensor are not zero. This defines the so-called *selection rules* which can be derived for each crystal symmetry via group-theoretical considerations. A detailed description for the crystal symmetries relevant to the studied systems of the current thesis will be given in section 2.4.

2.2.2 Quantum mechanical description of phononic Raman scattering

The classical description can clearly not highlight fully the Raman scattering process. Several experimental observations, including the resonance Raman scattering effect and the intensity ratio between Stokes and anti-Stokes scattering, cannot be explained in the classical framework. The complete description of Raman scattering is possible through the quantum mechanical treatment by third-order time-dependent perturbation theory. A full description can be found in reference [243], where this short summary will be based on.

The Hamiltonian of the system consists of two parts, one part describing the unperturbed system, that is, of the investigated material in the absence of electromagnetic field, and another including perturbation terms:

$$H = H_0 + H_{el-phot} + H_{el-phon} \tag{2.12}$$

where H_0 is the Hamiltonian of the unperturbed system, $H_{el-phot}$ describes the electron-photon interaction and $H_{el-phon}$ describes the electron-phonon interaction [iii]. In the quantum mechanical treatment, a *phonon* is a quantum of lattice vibration (a detailed description of the quantization of the classical lattice waves in the second quantization formalism can be found in [241, 244]). The electron-photon interaction term of Eq. 2.12 is given in the Coulomb gauge ($\nabla \cdot \mathbf{A}(\mathbf{r})$=0) by:

$$H_{el-phot} = \sum_i \left(-\frac{e}{mc} \mathbf{p}_i \cdot \mathbf{A}(\mathbf{r}_i) + \frac{e^2}{2mc^2} \mathbf{A}(\mathbf{r}_i)^2 \right) \tag{2.13}$$

where $\boldsymbol{p}$ is the momentum operator of the electron and $\boldsymbol{A}$ is the vector potential of the electromagnetic field [iv], whereas the electron-phonon interaction term is given by:

$$H_{el-phon} = e \left[\left(\frac{1}{\varepsilon_\infty} - \frac{1}{\varepsilon_0} \right) \left(\frac{2\pi\hbar\omega}{V} \right) \right]^{1/2} \sum_q \frac{1}{q} e^{i\mathbf{q}\cdot\mathbf{r}} (b_{\mathbf{q}} + b^+_{-\mathbf{q}}) \tag{2.15}$$

where ε_∞ and ε_0 are the high and low frequency dielectric constants respectively, ω is the frequency of longitudinal optical phonons and $b_{\mathbf{q}}$ and $b^+_{\mathbf{q}}$ are the annihilation and creation

[iii] Since the incident/scattered photon energy is much larger than the energy of the phonon, the direct coupling between the photons and the lattice vibrations is negligible, and therefore no photon-phonon coupling term is included in the Hamiltonian.

[iv] The quantized vector potential of the electromagnetic field is given by

$$\mathbf{A}(\mathbf{r}_i) = \sqrt{\frac{2\pi\hbar c^2}{V}} \sum_{i,q} \frac{1}{\sqrt{\omega_q}} \mathbf{e}_i (a_{\mathbf{q}} e^{iq\mathbf{r}} + a^+_{-\mathbf{q}} e^{-iq\mathbf{r}}) \tag{2.14}$$

where the operators $a^+_{-\mathbf{q}}$ and $a_{\mathbf{q}}$ respectively create and annihilate a photon with wave vector $\mathbf{q}$ having a polarization direction denoted by the unit vector $\mathbf{e}_i$.

operators of phonons with wave vector $\mathbf{q}$ [v].

The different steps involved in the microscopic description of first-order Raman scattering are schematically depicted in Fig. 2.2 for phonon creation and annihilation. In the case of the creation of one phonon the scattering process can be described as follows:

- An electron is excited from an initial electronic state $|i\rangle$ to a virtual or real intermediate state $|\alpha\rangle$, creating an electron-hole pair. The transition to the excited state is realized through the interaction of the electron with the incident photon $(\omega_i, \mathbf{k_i})$, described by the operator H_{e-phot}.
- The excited electron-hole pair is scattered by a phonon $(\omega, \mathbf{q})$, through electron-phonon interaction described by the operator H_{e-phon}, leaving the system to another virtual or real intermediate state $|\beta\rangle$.
- The electron-hole pair recombines emitting a scattered photon $(\omega_s, \mathbf{k_s})$, and the system decays into the final ground state $|f\rangle$ through electron-photon coupling (H_{e-phot}).

In each of the three steps the wave vector must be conserved, whereas the energy should be conserved in the total process. Phononic processes are symmetric under time reversal and therefore the three described steps can take place in arbitrary order, leading to 3! = 6 possible permutations. The Feynman diagrams for the 6 different permutations are

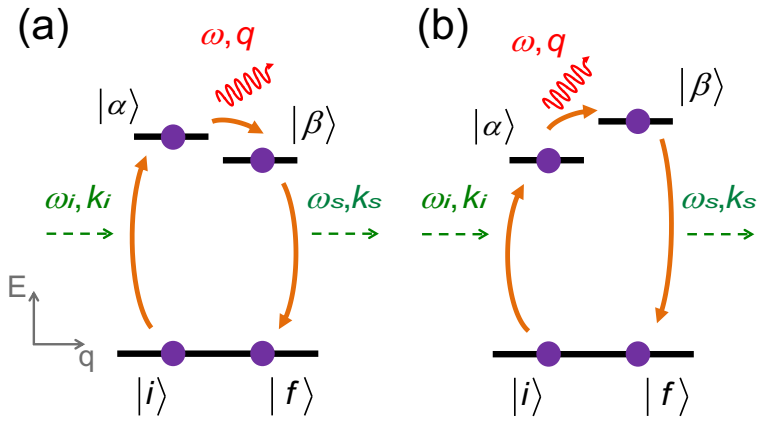

Figure 2.2: Schematic illustration of the steps included in a first order Raman scattering process for phonon creation (left) and annihilation (right). The intermediate states $|\alpha\rangle$ and $|\beta\rangle$ could be real or virtual states.

[v] Here is given the Fröhlich electron-phonon interaction Hamiltonian for polar coupling between electrons and optical phonons.

shown in Fig. 2.3. The scattering probability can be calculated by third-order perturbation theory with the help of the Feynman diagrams using Fermi's golden rule. Application of Fermi's golden rule for every vertex of the first Feynman diagram of Fig. 2.3 results in [vi]:

$$\Gamma_{i\to f} = \left(\frac{2\pi}{\hbar}\right)\left|\sum \frac{\langle f|H_{e-phot}|\beta\rangle\langle\beta|H_{e-phon}|\alpha\rangle\langle\alpha|H_{e-phot}|i\rangle}{[\hbar\omega_i - (E_\alpha - E_i)][\hbar\omega_i - \hbar\omega - (E_\beta - E_i)]}\right|^2 \times \delta(\hbar\omega_i - \hbar\omega - \hbar\omega_s) \quad (2.16)$$

where $\hbar\omega_i$, $\hbar\omega_s$, $\hbar\omega$ is the energy of the incident photon, scattered photon and phonon respectively, E_i is the energy of the initial state $|i\rangle$, E_α is the energy of the first intermediate state $|\alpha\rangle$, E_β is the energy of the second intermediate state $|\beta\rangle$. It is assumed that the final state $|f\rangle$ coincides with the initial state $|i\rangle$. All the individual contributions due to all six diagrams of Fig. 2.3, like the one given in Eq. 2.16 for the first diagram, have to be taken into account.

In order to obtain the scattering probability the thermal average of the transition probability $\Gamma = \langle\Gamma_{i\to f}\rangle$ is multiplied by the number of scattered photon states in a solid angle $d\Omega$ and a frequency interval $d\omega$ and then divided by the flux of incident photons and by the illuminated area giving a final result (the detailed calculation can be found in refer-

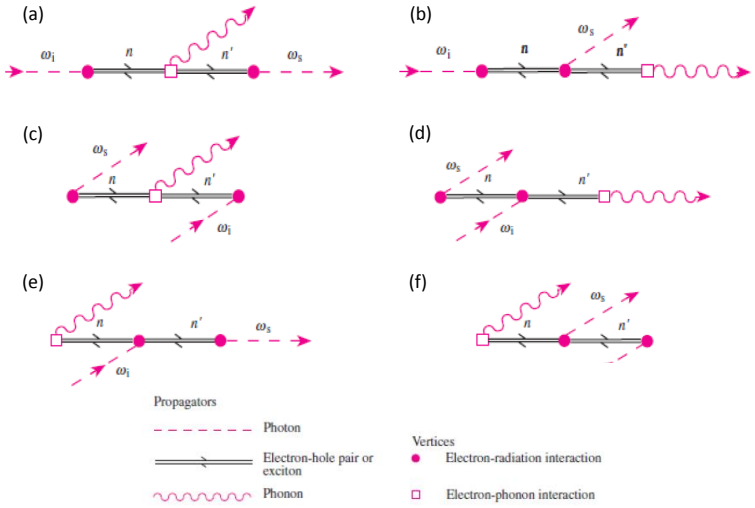

Figure 2.3: Feynman diagrams for the six scattering processes that contribute to one-phonon (Stokes) Raman scattering. The figure is taken from reference [245].

[vi] Here only the first term of the Hamiltonian of Eq. 2.13 is considered, whereas the detailed calculation including both interband and intraband scattering can be found in references [237, 243, 245].

ences [243, 246]):

$$I \propto \frac{\partial^2\sigma}{\partial\Omega\partial\omega} = \frac{V\omega_s^2 A}{8\pi^3 c^3 \Phi}\Gamma \tag{2.17}$$

where, A is the illuminated area and Φ is the incident photon flux.

A special case occurs if the energy of the incident or the scattered photon matches an energy gap between the initial/final ground state and an unoccupied excited state. Then electrons are excited into real electronic states and the denominator in Eq. 2.16 becomes zero. This is the case of *resonant Raman scattering*, which results in an enhanced intensity at these particular incident/scattered photon energies.

2.2.3 Phonon Interactions

Within the harmonic approximation phonons are treated as independent and non-interacting, having infinite lifetimes as described by the δ-function in Eq. 2.16. In real solids however phonons are interacting with electrons, other phonons, magnons, other electronic excitations etc. leading to finite phonon lifetimes. In order to describe quantitatively the phonon interactions one has to go beyond the harmonic approximation and to take into account anharmonic terms of the potential energy (power terms ≥3, see Eq. 2.3, details can be found in reference [247]) and interaction terms.

This can be treated in the framework of perturbation theory, introducing perturbation terms, such as anharmonicity or electron-phonon interaction, to the Hamiltonian of the harmonic oscillator[vii]. Correlation functions describing the response of a system to an imposed perturbation are expressed within the mathematical formalism of Green's functions (for a detailed description see references [243, 248]. The zero temperature unperturbed phonon Green's function is given by [viii]: :

$$D^{(0)}(q, t - t') = -i\left\langle 0 \mid T\{A_q(t)A_{-q}(t')\} \mid 0\right\rangle \tag{2.19}$$

where $A_q(t)=b_q e^{-i\omega t}+b_{-q}^{+}e^{i\omega t}$, b_q and b_q^{+} are the annihilation and creation operators for a phonon of momentum q, $|0\rangle$ denotes the ground state of the harmonic hamiltonian at zero temperature and T is the time-ordering operator (given two or more time-dependent operators, it orders these in such a way that the operators with later times are left). The Fourier transform of $D^{(0)}(q, t - t')$ gives the bare phonon Green's function in the frequency

[vii] In the harmonic oscillator treatment, the atomic displacement **u** form the equilibrium positions **R** is related to the phonon annihilation and creation operators b_q and b_q^{+} by:

$$\mathbf{u} = \sum_{\mathbf{q}}\left(\frac{\hbar}{2m\omega_{\mathbf{q}}}\right)^{1/2} e^{i\mathbf{q}\cdot\mathbf{R}}\xi_{\mathbf{q}}(b_{\mathbf{q}} + b_{\mathbf{q}}^{+}) \tag{2.18}$$

where $\xi_{\mathbf{q}}$ is the phonon polarization vector.

[viii] In the present short description, only the the zero temperature Green's functions will be described. The formalism introduced by Matsubara to treat Green's functions at finite temperature can be found in reference [248].

space:

$$D^{(0)}(q,\omega) = \frac{1}{\omega - \omega_q + i\delta} - \frac{1}{\omega + \omega_q - i\delta} = \frac{2\omega_q}{\omega^2 - \omega_q^2 + i\delta} \tag{2.20}$$

where δ is a positive quantity of infinitely small value. The unperturbed phonon Green's function has two poles where Eq. 2.20 diverges: one at the frequency ω=ω_q (infinitesimally shifted towards lower frequencies) and the other one at ω=-ω_q (infinitesimally shifted towards higher frequencies). Therefore in the bare phonon Green's function the poles identify with the unperturbed phonon energies ω_q of the non-interacting harmonic system. The measured spectral function of the phonon is the imaginary part of the phonon Green's function (which is a δ-function in the case of no interaction).

The unperturbed phonon energies and lifetimes are only valid if the perturbation is either localized or limited to a small number of particles.If the propagating phonon interacts with its environment, its Green's function is renormalized. The new, "dressed" Green's function obeys Dyson's equation:

$$\begin{aligned} D(q,\omega) &= D^{(0)}(q,\omega) + D^{(0)}(q,\omega)\Pi(q,\omega)D(q,\omega) \\ &= \frac{D^{(0)}(q,\omega)}{1 - D^{(0)}(q,\omega)\Pi(q,\omega)} \\ &= \frac{2\omega_q}{\omega^2 - \omega_q^2 - 2\omega_q\Pi(q,\omega) + i\delta} \end{aligned} \tag{2.21}$$

where Π(q,ω) is the *phonon self-energy* [249]. The self-energy incorporates the different perturbation terms which contribute to the renormalization of the phonon frequency and lifetime. The renormalization is mirrored in Eq. 2.21 which has poles at frequencies different than the ω_q of the harmonic oscillator. The phonon self-energy is a complex function, $\Pi(q,\omega) = \Delta(\omega) + i\Gamma(\omega)$, where the real part $\Delta(\omega)$ describes the shift in the phonon frequency and the imaginary part $\Gamma(\omega)$ describes the induced broadening of the phonon linewidth. $\Delta(\Omega)$ and $\Gamma(\Omega)$ are Kramers-Kronig related. The calculation of the phonon self-energy is performed taking into account the respective interaction Hamiltonian terms, e.g. the electron-phonon interaction term.

The phonon interactions are very often studied through the temperature dependence of the phononic Raman spectrum. Here we will shortly discuss two types of interactions which are relevant for the study of superconductors: the phonon-phonon interaction and the electron-phonon interaction.

Phonon-Phonon Interaction

The main reason for non-infinite phonon lifetimes is the decay of a phonon into other phonons, rendering highly important the quantitative understanding of phonon-phonon interactions [247]. The anharmonic terms of the phonon interactions are very complicated to evaluate even if the potential functions (see Eq. 2.3) are known, which has led to

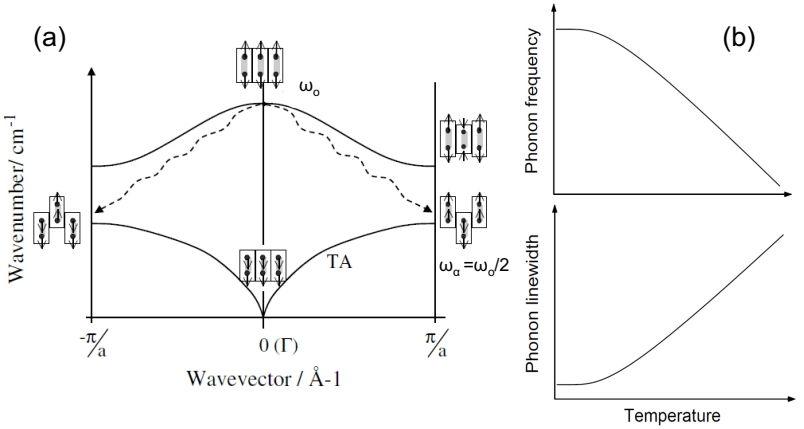

Figure 2.4: Anharmonic decay of optical phonons. (a) Schematic illustration of the decay of an optical phonon into two acoustic phonons of opposite momenta. The energy conservation determines the momenta of the acoustic phonons (in the current example they are chosen to be zone boundary phonons but this is not the general case). The figure is taken from reference [250] and it represents phonons of a linear assembly of diatomic molecules in which atoms vibrate perpendicularly to the axis of the chain. (b) The temperature dependence of the phonon frequency and phonon linewidth according to the Klemens decay expressions given in Eq. 2.22.

a number of approximations aiming to simplify them as much as possible and to describe the temperature dependence of the phonon lifetime (the phonon lifetime is inversely proportional to the phonon linewidth: $\Gamma \sim 1/\tau$). An approach that has gained wide acceptance is the one proposed by Klemens, in which it is assumed that the only contribution to the phonon lifetime arises from the decay of an optical phonon into two acoustical phonons of opposite momenta belonging to the same branch of the phonon dispersion curve [251]. The momenta of the acoustic phonons are dictated by the energy conservation. The resulting expressions for the phonon frequency ω_{ph} and linewidth Γ_{ph} (Γ_{ph} is the observed full width at half maximum, FWHF) are:

$$\begin{aligned} \omega_{ph} &= \omega_0 - A\left(1 + \frac{2}{exp(\hbar\omega_0/2k_BT) - 1}\right) \\ \Gamma_{ph} &= \Gamma_0 - C\left(1 + \frac{2}{exp(\hbar\omega_0/2k_BT) - 1}\right) \end{aligned} \tag{2.22}$$

where A and C are positive constants, ω_0 is the bare phonon frequency and Γ_0 is a residual temperature-independent linewidth, arising e.g. from scattering by impurities. A schematic representation of the Klemens decay, together with the graphic representations of the expressions of Eq. 2.22 are given in Fig. 2.4.

Electron-Phonon Interaction

In addition to the phonon decay into other phonons through phonon-phonon interactions, a phonon can also decay into electronic excitations through electron-phonon interactions described by the operator H_{e-phon}. The electron-phonon interaction contributes to the phonon lifetime and subsequently induces a renormalization of the phonon frequency.

A benchmark for strong electron-phonon interaction in the Raman spectra is the appearance of a characteristic distortion of the common Lorenzian lineshape to an asymmetric phonon lineshape described by the *Fano profile*. The asymmetry of the lineshape is the result of the interference between the wavefunctions of discrete phononic $|p\rangle$ and continuous electronic $|e\rangle$ states, coupled through the matrix element $g \propto \langle p|H_{e-phon}|e\rangle$ (more details can be found in [252, 253]). The resulting Fano lineshape is described by:

$$I_F = C_F \frac{(q+e)^2}{1+e^2} \tag{2.23}$$

where I_F is the imaginary part of the phonon Green's function with the phonon self-energy calculated based on the Fröhlich electron-phonon interaction Hamiltonian, $e = (\omega - \omega_{ph})/\Gamma_{ph}$, ω_{ph} is the normalized phonon frequency, Γ_{ph} is the phonon linewidth and q is the Fano asymmetry parameter which reflects the strength of the electron-phonon coupling [254]. In Fig. 2.5 is plotted the Fano lineshape for different values of the asymmetry parameter q [252].

The electron-phonon coupling is qualitatively described by an additional contribution to the phonon self-energy. Any changes occuring in the underlying electronic system, e.g. the opening of the electronic gap upon the transition to the superconducting state that will be relevant for this thesis, will be reflected in the behavior of the phonons through the respective phonon self-energy effects [255, 256]. The superconductivity-induced phonon self energy effects have received massive theoretical and experimental attention and will

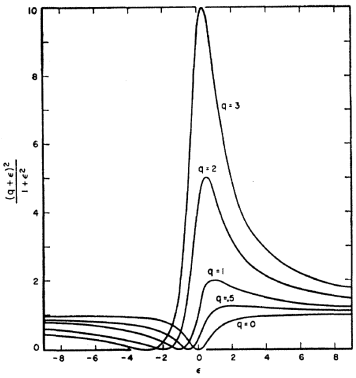

Figure 2.5: Fano lineshape for different values of the asymmetry parameter q. As q increases, a more symmetric lineshape is acquired and for $q \to \infty$ a Lorentzian lineshape is recovered. The figure is taken from [252].

be discussed in detail in a following chapter in parallel with the corresponding experimental results.

2.3 Phononic Raman scattering under high pressure

High pressure Raman spectroscopy offers the unique possibility to study *in situ* the effect of external pressure in the big variety of phenomena and of elementary excitations studied by inelastic light scattering, including phase transitions, lattice dynamics, magnetic and electronic excitations etc. A general overview of Raman scattering studies under high pressure conditions can be found in references [250, 257, 258, 259, 260], whereas here we will mainly focus on high pressure phononic Raman scattering.

In addition to temperature, which constitutes the most commonly used thermodynamic variable in Raman experiments, hydrostatic pressure is generally considered a clean external tuning parameter. The basic microscopic effect of pressure application on solids is to decrease the interatomic distances and to change the bond angles, leading to changes in the electronic system far more substantial than those induced by temperature. In the Raman scattering studies which are relevant for the current thesis, variations of both pressure and temperature induce changes in the phononic spectrum. The temperature dependence is in general more complicated than the pressure dependence, since while pressure generates solely a volume change, temperature has a simultaneous effect on the phonon population.

As it is pointed out in reference [257] there are four principal pressure-induced effects in the Raman spectra: frequency shifts of the elementary excitations, changes of the Raman linewidths and lineshapes, changes in the Raman selection rules and tuning of the resonance conditions.

The pressure induced changes in the frequencies of the elementary excitations, and more specifically of the lattice vibrations, are the most commonly studied effects in high pressure Raman experiments. The pressure-induced decrease of the interatomic distances distorts the electronic clouds and changes the effective force constants between the atoms, which in most cases increase upon volume decrease. This induces in turn a subsequent increase in the frequency ω of the respective phononic vibrations. The effect is usually described using the Grüneisen parameter which is defined as:

$$\gamma_i = -\frac{\partial \ln \omega_i}{\partial \ln V} = \frac{1}{\beta}\frac{\partial \ln \omega_i}{\partial P} \tag{2.24}$$

where β is the isothermal volume compressibility [257]. The mode Grüneisen parameter γ_i is essentially an exponent describing how the mode frequency ω_i scales with volume. In the *quasi-harmonic* or *Grüneisen approximation*, γ is assumed to be independent of

volume, therefore integrating Eq. 2.24 results in:

$$\frac{\omega_i(V_1)}{\omega_i(V_2)} = \left(\frac{V_2}{V_1}\right)^{-\gamma_i} \tag{2.25}$$

where $\omega_i(V_1)$ and $\omega_i(V_2)$ are the values of ω_i at volumes V_1 and V_2, respectively [257].

In most of the Raman experiments under high pressure conditions, broadenings of the Raman linewidths are observed. As already mentioned earlier, the phonon linewidth $\Gamma_i/2$ is given by the imaginary part of the phonon self-energy and is inversely proportional to the phonon lifetime. In the framework of the anharmonic decay of an optical phonon into two acoustic phonons, the observed decrease of the phonon lifetime is usually attributed to pressure-induced changes in the density of final states of the two-phonon spectrum [250]. Very often the broadening is caused by non-intrinsic effects such as the presence of a pressure gradient or the emergence of pressure-induced disorder. Therefore special care should be given in determining the intrinsic broadenings of Raman lines under high pressures.

Another usual observation in high pressure Raman measurements is the pressure-induced decrease of the intensity of the Raman modes. From Eq. 2.11 it follows that the Raman intensity is determined by the derivative of the electronic susceptibility at the equilibrium configuration. In the case that the interatomic distances are changed as it happens upon pressure application, a different derivative of the electric susceptibility would emerge for the new configuration, leading to a change in the observed intensity [250]. In addition to that, it is very often the case that the whole Raman spectrum undergoes an intensity decrease under high pressure conditions, an observation that has been attributed to scattering losses due to pressure-induced disorder, or due to changes of the absorption coefficient with pressure [250, 261].

A decrease in the intensity of the Raman modes can also be observed as a pre-transitional effect upon approaching a pressure induced phase transition. Raman spectroscopy has been extensively used to detect pressure-induced structural phase transitions, which are evidenced in the Raman spectra through the appearance and/or disappearance of Raman modes or though changes in their pressure dependence. Additionally, Raman experiments have contributed in the identification of the symmetry of the new phase through the study of the Raman selection rules.

Finally, pressure-induced changes in the Raman intensities can also be a signature of a change in the electronic properties of the studied system, as happens in the case of a pressure induced insulator-to-metal transitions or in the case of pressure-tuned resonance Raman scattering. As mentioned earlier, resonance Raman scattering occurs when the energy of the incident laser light is tuned so as to fit the energy gap between the initial and the final state. Alternatively, instead of tuning the incident energy, one could achieve the resonance conditions by tuning the energy gap through the application of high pressures [257].

2.4 The Raman spectrum of high-T_c cuprate and iron-based superconductors

A mode is *Raman-allowed* (or *Raman-active*) when Eq. 2.11 is different from zero for at least one combination of the incident and the scattered light polarizations ($\hat{e}_i$ and $\hat{e}_s$ respectively) [262]. The dependence of the Raman intensity on the geometry of the incident and scattered light polarizations allows the deduction of the symmetry of the Raman tensor and therefore of the respective Raman modes.

Identifying the number and symmetries of the Raman allowed modes is a straightforward task in the case that the complete crystal structure of the investigated material is known. The procedure that will be described in the following is the site group analysis as discussed in detail in reference [263]. The first step of the analysis is to identify the space group of the studied system as well as the precise position of each atom in the unit cell (atomic sites and site symmetries). The second step is to derive the irreducible representations of the zone center phonons resulting from the occupied atomic sites in the unit cell. Finally the last step of the procedure is to determine the Raman tensors of the irreducible representations that are Raman allowed [262].

2.4.1 Raman modes of $YBa_2Cu_3O_{6+x}$

$YBa_2Cu_3O_{6+x}$ belongs to the centrosymmetric orthorhombic space group *Pmmm*. As discussed in a previous chapter, for oxygen stoichiometry $x \lesssim 0.3$ the structure is tetragonal (point group D_{4h}), whereas for higher oxygen content the presence of oriented Cu-O chains lowers the symmetry to orthorhombic (point group D_{2h}). This orthorhombic distortion is often neglected in the literature and many Raman studies refer to the phonons using the tetragonal notation. For the current description both notations will be given and their differences will be pointed out, based on [239, 253, 264].

Table 2.1 summarizes the symmetries of the occupied atomic sites and the resulting irreducible representations in the orthorhombic and the the tetragonal notation. The fully oxygenated *ortho*-I $YBa_2Cu_3O_7$ and the undoped tetragonal $YBa_2Cu_3O_6$ contain N=13 and N=12 atoms per unit cell respectively, giving rise to 3N-3 optical phonon modes each, so 36 and 33 optical phonon modes respectively, in line with the results of the analysis presented in the previous table. The Raman scattering tensors corresponding to the irreducible representations listed in Table 2.1 which are Raman allowed are given in Table 2.2.

As already mentioned, obtaining the Raman selection rules is done by evaluating Eq. 2.11 for the Raman tensors of Table 2.2 and for all possible polarization configurations of the electric field of the incident and scattered light, $\hat{e}_L$ and $\hat{e}_S$. In polarized Raman experiments the polarization configuration is usually described using the Porto notation. The Porto notation has the *i(kl)j* form, where *i* and *j* correspond to the propagation directions of the incident and the scattered light respectively, whereas *k* and *l* denote the polarizations of their corresponding electric fields. The selection rules for the Raman

		Orthorhombic Notation	Tetragonal Notation
Atom	**Site Symmetry**	**Irreducible Representations**	
Y	D_{2h} / D_{4h}	$B_{1u}+B_{2u}+B_{3u}$	$A_{2u}+E_u$
O1	D_{2h} / -	$B_{1u}+B_{2u}+B_{3u}$	-
Cu1	D_{2h} / D_{4h}	$B_{1u}+B_{2u}+B_{3u}$	$A_{2u}+E_u$
Ba	C_{2v} / C_{4v}	$B_{1u}+B_{2u}+B_{3u}+A_g+B_{2g}+B_{3g}$	$A_{1g}+E_g+A_{2u}+E_u$
Cu2	C_{2v} / C_{4v}	$B_{1u}+B_{2u}+B_{3u}+A_g+B_{2g}+B_{3g}$	$A_{1g}+E_g+A_{2u}+E_u$
O2	C_{2v} / C_{2v}	$B_{1u}+B_{2u}+B_{3u}+A_g+B_{2g}+B_{3g}$	$A_{1g}+2E_g+B_{1g}+A_{2u}+2E_u+B_{2u}$
O3	C_{2v} / C_{2v}	$B_{1u}+B_{2u}+B_{3u}+A_g+B_{2g}+B_{3g}$	$A_{1g}+2E_g+B_{1g}+A_{2u}+2E_u+B_{2u}$
O4	C_{2v} / C_{4v}	$B_{1u}+B_{2u}+B_{3u}+A_g+B_{2g}+B_{3g}$	$A_{1g}+E_g+A_{2u}+E_u$

Table 2.1: Atomic site symmetries and resulting vibrational modes for $YBa_2Cu_3O_{6+x}$ in the orthorhombic and the tetragonal notation.

Orthorhombic notation D_{2h}

$\mathbf{A}_g$	$\mathbf{B}_{2g}$	$\mathbf{B}_{3g}$
$\begin{pmatrix} xx & 0 & 0 \\ 0 & yy & 0 \\ 0 & 0 & zz \end{pmatrix}$	$\begin{pmatrix} 0 & 0 & xz \\ 0 & 0 & 0 \\ xz & 0 & 0 \end{pmatrix}$	$\begin{pmatrix} 0 & 0 & 0 \\ 0 & 0 & yz \\ 0 & zy & 0 \end{pmatrix}$

Tetragonal notation D_{4h}

$\mathbf{A}_{1g}$	$\mathbf{B}_{1g}$	$\mathbf{E}_g$	$\mathbf{E}_g$
$\begin{pmatrix} xx & 0 & 0 \\ 0 & xx & 0 \\ 0 & 0 & zz \end{pmatrix}$	$\begin{pmatrix} xx & 0 & 0 \\ 0 & -xx & 0 \\ 0 & 0 & 0 \end{pmatrix}$	$\begin{pmatrix} 0 & 0 & xz \\ 0 & 0 & 0 \\ zx & 0 & 0 \end{pmatrix}$	$\begin{pmatrix} 0 & 0 & 0 \\ 0 & 0 & xz \\ 0 & zx & 0 \end{pmatrix}$

Table 2.2: Raman tensors for the Raman active phonon modes of $YBa_2Cu_3O_{6+x}$ in the orthorhombic D_{2h} notation and in the tetragonal D_{4h} notation.

active modes of $YBa_2Cu_3O_{7-x}$ in the orthorhombic and the tetragonal notation are given in Table 2.3 using the Porto notation.

Having identified the symmetries of the optical phonons in orthorhombic and tetragonal $YBa_2Cu_3O_{7-y}$, in order to understand properly the observed Raman spectrum it is

Selection rules	D_{2h} notation	D_{4h} notation
xx, yy, zz	A_g	A_{1g}+B_{1g}
xy, yx	B_{1g}	A_{2g}+B_{2g}
xz, zx	B_{2g}	E_g
yz, zy	B_{3g}	E_g
$x'x', y'y'$	A_g+B_{1g}	A_{1g}+B_{2g}
$x'y', y'x'$	A_g	B_{1g}

Table 2.3: Selection rules for the Raman active phonon modes of $YBa_2Cu_3O_{6+x}$ in the orthorhombic D_{2h} and tetragonal D_{4h} notation. The complete set of selection rules is given here, although there are no Raman active phonon modes of all the allowed symmetries, e.g. there is no Raman active mode of the B_{2g} symmetry in $YBa_2Cu_3O_{6+x}$.

important to obtain an estimate of the frequencies of the expected modes. Since the early years of cuprate superconductivity a number of theoretical studies have been performed, including simple spring-mass approaches, shell model calculations and ab *initio* calculations [265, 266, 267, 268, 269, 270]. The resulting frequencies and eigenvectors of the Raman and infrared active phonon modes are presented in figure Fig. 2.6 as derived from shell model calculations [266, 267]. The symmetries are given in the orthorhombic notation. The atomic displacements are shown for the upper part of the unit cell and the corresponding ones for the lower part can be obtained by extending the atomic displacements symmetrically through the inversion center with even parity for the Raman modes an with odd parity for the infrared modes.

The following description of the phonons will be focused only on the Raman active ones which are relevant to the content of the current thesis. Starting from the 5 A_g symmetry phonon modes, the lowest frequency phonon at 115 cm^{-1} corresponds to vibrations of mostly Ba atoms while the next one in frequency at 157 cm^{-1} corresponds to the vibrations of the Cu2 atoms in the Cu-O planes. The following two modes at 353 and 377 cm^{-1} correspond to the in- and out-of-phase vibrations of the O2, O3 atoms of the Cu-O planes. Of particular interest is the buckling phonon mode corresponding to the out-of-phase O2-O3 vibrations. In the orthorhombic notation, this mode has a A_g symmetry, whereas in the tetragonal notation it has a B_{1g} symmetry. As already mentioned, the orthorhombic distortion in $YBa_2Cu_3O_{7-y}$ is small and as a result the out-of-phase O2-O3 mode still holds the character of B_{1g} symmetry, and is often referred as the "B_{1g}-like" mode. The highest frequency A_g symmetry phonon at 509 cm^{-1} is the one of the apical oxygen vibrations along the *c*-axis.

Regarding the B_{2g} and B_{3g} symmetry modes, they appear in the Raman spectra significantly less intense compared to the A_g symmetry modes (over 10 times lower in intensity). Starting from the lowest frequency, they correspond to vibrations of the Ba (70/91 cm^{-1}), Cu2 (142/137 cm^{-1}), O4 (346/490 cm^{-1}), O3 (428/411 cm^{-1}), and O2 (584/545 cm^{-1})

atoms along the *a*- and *b*-axis respectively.

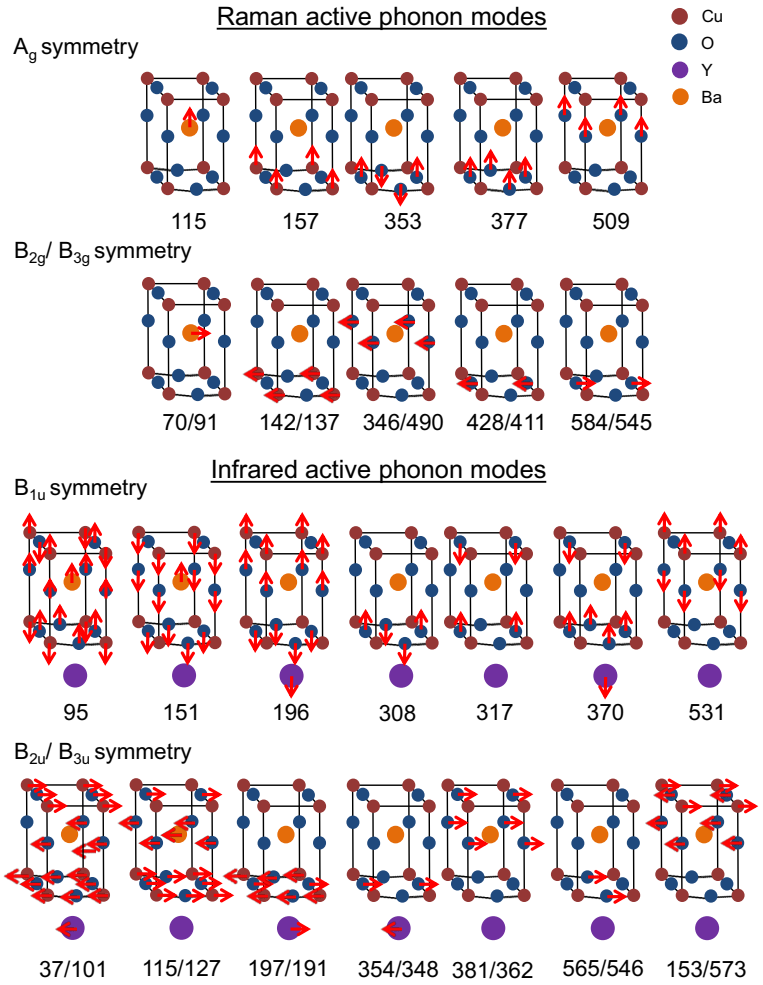

Figure 2.6: Eigenvectors and phonon frequencies (in cm^{-1}) of the Raman and infrared active optical modes of $YBa_2Cu_3O_{6+x}$. The atomic displacements are shown only for the upper half part of the unit cell. The figure is adapted from [266, 267]. The phonon frequencies are the calculated frequencies as obtained from shell modes calculations by Humlíček *et al.* [267].

The calculated frequencies from shell-model calculations [267] and ab *initio* calculations [270] and the experimentally measured frequencies [269] of the Raman active phonon modes of $YBa_2Cu_3O_7$ are summarized in Table 2.4.

In Fig. 2.7 are plotted the room temperature Raman spectra of *ortho*-I $YBa_2Cu_3O_7$ in the *xx*, and *yy* polarization geometries which, according to Table 2.3, probe the A_g symmetry modes (data taken from Bakr [271]). In addition to the already described phonons, two extra phonon modes are observed in the *yy* geometry at ~232 cm^{-1} and ~579 cm^{-1} (the latter one is the most intense of the two). These are defect-induced modes and they correspond to vibrations of the Cu1 and O1 chain atoms along the chains, i.e. along the *b*-axis [272, 273]. These modes have the B_{1u} symmetry and are in principle infrared active, but Raman forbidden. They become observable in the presence of oxygen deficiencies and broken Cu-O chains, leading to the breaking of the translational symmetry [274]. The defect modes are sharply resonant for excitation energies close to ~2.2 eV (yellow line of a Kr^+ laser) [273, 275]. Moreover, the two modes appear only with light polarizations parallel to the Cu-O chains, i.e. in the *yy* geometry, and their absence in the geometry perpendicular to the Cu-O chains, i.e. in the *xx* geometry, is a signature of an excellent detwinning quality of the investigated sample.

As already mentioned, in non-stoichiometric orthorhombic $YBa_2Cu_3O_{6+x}$ the Cu-O

	Phonon	ω_{th} (shell-model)	ω_{th} (ab *initio*)	ω_{exp}
$\mathbf{A}_g$	Ba	115	119	116-123
	Cu2	157	152	145-152
	O2-O3	353	340	335-338
	O2+O3	377	407	435-442
	O4	509	473	493-500
$\mathbf{B}_{2g}$	Ba	70	65	69-79
	Cu2	142	140	140-142
	O4	346	224	209-210
	O3	428	386	370
	O4	584	576	379-385
$\mathbf{B}_{3g}$	Ba	91	79	78-83
	Cu2	137	140	140-141
	O4	490	295	303-307
	O3	411	365	378
	O4	545	526	526

Table 2.4: Calculated and measured frequencies of the Raman active phonon modes of $YBa_2Cu_3O_7$ in cm^{-1}. The calculated frequencies are taken from Humlíček *et al.* (shell-model calculations) [267] and from Bohnen *et al.* (ab *initio* calculations) [270]. The experimental frequencies are taken from Ambrosch *et al.* [269] and references therein.

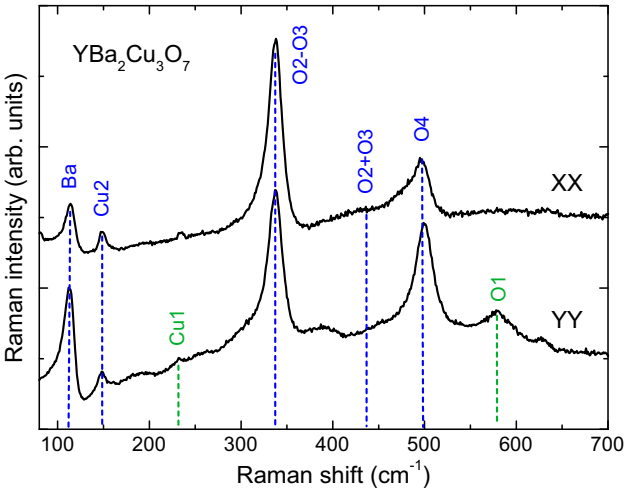

Figure 2.7: Room temperature Raman spectra of *ortho*-I $YBa_2Cu_3O_7$ taken with the Ar^+ laser line (λ=514.5 nm) in the *xx* and *yy* polarization geometries (data taken from Bakr *et al.* [271]).

chains tend to form oxygen superstructures with different periodicity along the *a*-axis depending on the heat treatment and the oxygen content [109, 110]. The resulting supercells lead to an increased number of modes at $\vec{k}$=0 originating from activated Raman-forbidden phonons at the Γ-point or phonons away from the Γ-point [276, 277]. The new Raman modes are connected to the specific oxygen superstructure and are therefore different for the different types of supercells formed at the different doping levels.

A typical example of a highly ordered oxygen superstructure is the case of *ortho*-II $YBa_2Cu_3O_{6.55}$ with alternating full Cu-O and empty Cu-vacancy chains. In this case the resulting unit cell is doubled along the *a*-axis and $2a\times b\times c$ supercells are formed (25 atoms per supercell). The doubling of the unit cell along the *a* direction gives rise to additional phonons. This is caused by the transformation of the X-point of the *ortho*-I unit cell into the Γ-point of the *ortho*-II structure and the appearance of new, non-equivalent groups of ions on the side faces and on the inside of the new unit cell [277]. There are a total of 25 atoms in the supercell giving rise to a total of 75 phonons at the Γ-point, out of which 34 are Raman active. Based on symmetry considerations, the irreducible representations of the Raman active phonon modes are $11A_g+4B_{1g}+11B_{2g}+8B_{3g}$ [279]. In addition to the already described modes of the *ortho*-I structure six A_g, four B_{1g}, six B_{2g} and three B_{3g} extra modes are expected for *ortho*-II $YBa_2Cu_3O_{6.55}$. As already mentioned, the intensities of the B_{2g} and B_{3g} symmetry modes are significantly smaller compared to the ones of the A_g modes, so from now on we will focus on the new *ortho*-II induced A_g

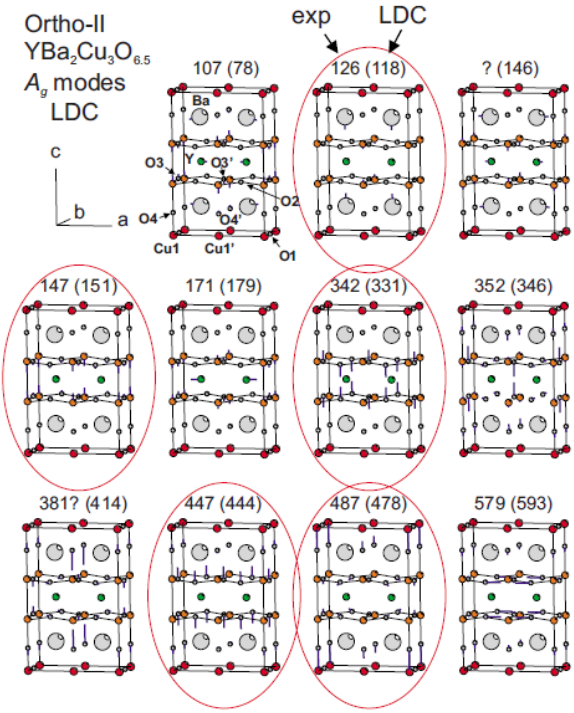

Figure 2.8: Main atomic displacements of the A_g modes of ortho-II $YBa_2Cu_3O_{6.5}$ as obtained by lattice dynamical calculations. The calculated frequencies are given in parenthesis and are compared to the experimentally observed values. The figure is taken from Iliev *et al.* [278].

modes.

Fig. 2.8 shows the eigenvectors of the $11A_g$ Raman-active modes in $YBa_2Cu_3O_{6.55}$ (5 A_g modes of the *ortho*-I structure and 6 additional A_g modes of the *ortho*-II superstructure) as predicted by LDA calculations, together with their theoretically calculated and experimentally measured frequencies [278, 280]. In Fig. 2.9 are plotted the Raman spectra of *ortho*-II $YBa_2Cu_3O_{6.55}$ at 10K in the polarization geometries parallel and perpendicular to the Cu-O planes (*xx* and *yy* respectively). The phonon modes of the *ortho*-I structure are indicated by the blue dashed lines, whereas the red lines correspond to the additional phonons of the *ortho*-II structure. The green dashed line indicates the O1 defect mode of the broken Cu-O chains, which is present only in the *yy* geometry verifying

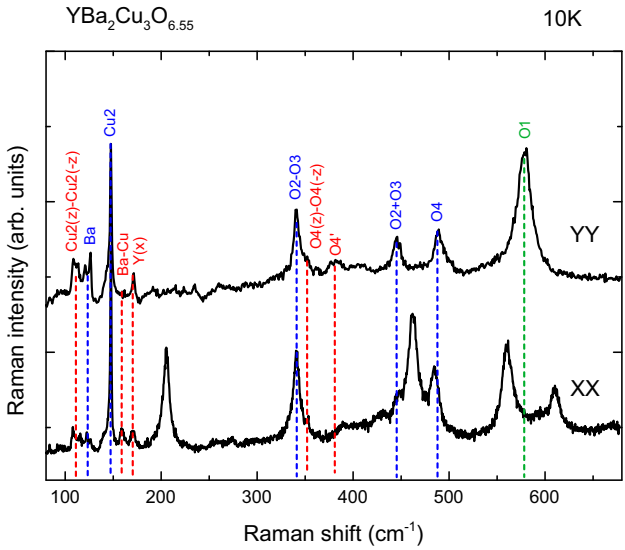

Figure 2.9: Raman spectra of *ortho*-II $YBa_2Cu_3O_{6.5}$ at 10 K taken with a He-Ne laser (λ=632.817 nm) in the *xx* and *yy* polarization geometries. The blue dashed lines indicate the phonon modes of the *ortho*-I structure, the red lines correspond to the additional phonons of the *ortho*-II structure and the green dashed line indicates the O1 defect mode of the broken Cu-O chains (present only in the *yy* geometry).

the excellent detwinning quality of our samples. The intensities of the additional *ortho*-II superlattice induced modes are considerably weaker than those of the *ortho*-I allowed modes. The strong features observed around 205, 470, 560, and 610 cm^{-1} have a different physical origin and will be analyzed in detail in a following chapter (see chapter 4).

2.4.2 Raman modes of $YBa_2Cu_4O_8$

The structural difference between $YBa_2Cu_3O_7$ and $YBa_2Cu_4O_8$ is the doubling of the Cu-O chains stacked up along the *c*-axis. The space group changes from *Pmmm* to *Cmmm* while the point group remains the same [120, 123]. In contrast to the corner-sharing squares of the single chains in $YBa_2Cu_3O_7$, the double chains in $YBa_2Cu_4O_8$ have edge-sharing squares. This leads to a shift of the two chains relative to each other by *b*/2 along the *b*-axis and therefore to an approximate doubling of the orthorhombic unit cell lattice constant *c*. The inversion centers that for $YBa_2Cu_3O_7$ were located at the atomic sites of Cu1 and O1 are in the case of $YBa_2Cu_4O_8$ shifted to the midpoints of the Cu1-Cu1 and O1-O1 atoms in the double chains. Since the chain atoms are no longer located at

Phonon	ω_{th} (cm^{-1})	ω_{exp} (cm^{-1})
Ba	89	103
Cu2	169	150
Cu1	270	247
O2-O3	393	340
O2+O3	426	439
O4	489	502
O1	579	603

Table 2.5: Calculated and measured frequencies of the A_g Raman modes of $YBa_2Cu_4O_8$ in cm^{-1}. The calculated frequencies are taken from reference [239] and references therein (ab *initio* calculations) and the experimental frequencies are taken from Heyen *et al.* [281].

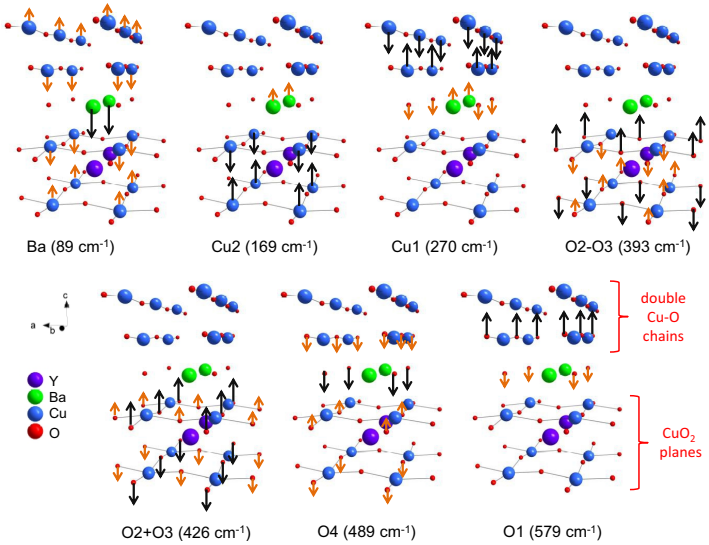

Figure 2.10: Eigenvectors and phonon frequencies (in cm^{-1}) of the A_g symmetry Raman active modes of $YBa_2Cu_4O_8$. The black arrows indicate the main atomic displacements. The phonon frequencies are the calculated frequencies as obtained from shell modes calculations by Trajnerowicz *et al.* [282]. The figure was prepared based on [282].

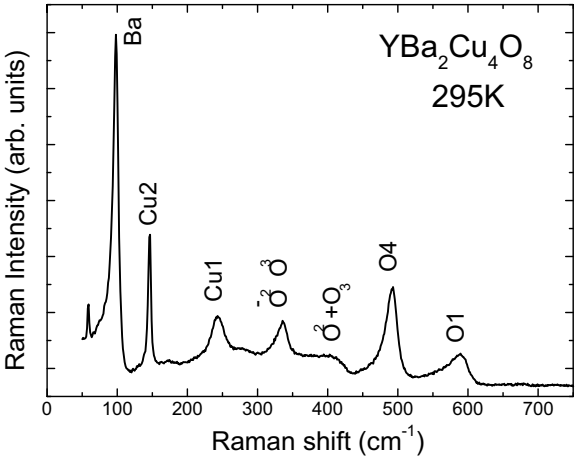

Figure 2.11: Unpolarized Raman spectrum of $YBa_2Cu_4O_8$ at 295K taken with a He-Ne laser (λ=632.817 nm). The phonon modes are labeled according to the corresponding atomic vibrations.

inversion centers their site symmetry changes from D_{2h} to C_{2v}, and therefore each atom contributes B_{1u}+B_{2u}+B_{3u}+A_g+B_{2g}+B_{3g} optical phonons instead of B_{1u}+B_{2u}+B_{3u} as in the case of $YBa_2Cu_3O_7$ [281, 283].

Regarding the expected phonon frequencies, most of the atomic distances do not change significantly with respect to the ones of $YBa_2Cu_3O_7$ and so the frequencies of the phonon modes have very close values to the ones of Table 2.4 [106, 284]. The calculated and experimental frequencies of the A_g symmetry Raman modes are given in Table 2.5 from references [239] and [281], while the eigenvectors of the A_g Raman active phonon modes are presented in figure Fig. 2.10 as derived from *ab initio* calculations within the local density approximation [282]. The Raman spectrum of $YBa_2Cu_4O_8$ under ambient conditions is plotted in Fig. 2.11.

2.4.3 Raman modes of $REFeAsO_{1-x}F_x$

$REFeAsO_{1-x}F_x$ with Re=(Sm, La, Nd, Pr, Ce) crystallizes at room temperature in the tetragonal *P*4/*nmm* structure and undergoes a structural transformation to the orthorhombic *Cmma* structure upon cooling. In the existing literature, the orthorhombic distortion is usually neglected and the Raman reports refer to the phonons using the tetragonal notation. Here both notations will be given, highlighting their differences, while for the rest of the thesis the tetragonal notation will be employed. Following the same procedure as for the case of $YBa_2Cu_3O_{6+x}$, the symmetries of the occupied atomic sites and the resulting irreducible representations are summarized in Table 2.6 for the high temperature

tetragonal and the low temperature orthorhombic phases.

In the tetragonal notation, the atomic vibrations along the x, y and z directions produce three infrared and three Raman active modes per atom: the infrared modes are of E_u and A_{2u} symmetry, whereas the Raman modes are of E_g and A_{1g}/B_{1g} symmetry for atoms with C_{4v}/D_{2d} site symmetry respectively. Focusing on the even vibrational patterns which are relevant for our Raman study, these are usually categorized in two groups: the first one includes the Raman active modes which arise from atomic vibrations along the c-axis (A_{1g}, B_{1g} modes) whereas the second one includes the modes which arise from atomic vibrations in the ab-plane (E_g modes).

The structural transition does not introduce any new Raman-active modes but since in the orthorhombic phase the vibrations along the a- and b-axis are no longer degenerate, the doubly degenerate modes split into non-degenerate ones. Therefore the two E_g modes of the tetragonal phase split into the non-degenerate B_{2g} and B_{3g} modes of the orthorhombic phase which correspond to vibrations along the a- and b-axis respectively, while the c-axis modes are not affected by the distortion [285].

The scattering tensors of the above mentioned Raman modes in the tetragonal and the orthorhombic notation are given in Table 2.7, while the Raman selection rules, obtained through Eq. 2.11, are given in Table 2.8 using the Porto notation.

Several *ab initio* calculations on the lattice dynamics of high-T_c pnictides have appeared very soon after their discovery [196, 286, 287, 288, 289]. The frequencies and eigenvectors of the Raman active phonon modes are presented in figure Fig. 2.12 as derived from the calculations of reference [287] performed in the framework of the density functional perturbation theory. According to the calculations there are 8 Raman active phonon modes at the Brillouin zone center, in line with the previously mentioned group theory considerations. The modes of A_g symmetry derive from atomic vibrations of RE and As atoms along the c-axis: the phonon at $\sim$181cm^{-1} corresponds to vibrations of mainly the rare earth atoms, while the one at $\sim$204cm^{-1} of mainly the As atoms. The B_{1g} phonons at $\sim$218cm^{-1} and $\sim$282cm^{-1} correspond to atomic vibrations of Fe and O/F

	Tetragonal Notation		**Orthorhombic Notation**	
Atom	**Site Symmetry**	**Irreducible Representations**	**Site Symmetry**	**Irreducible Representations**
RE	C_{4v}	$A_{1g}+E_g+A_{2u}+E_u$	C_{2v}	$A_g+B_{2g}+B_{3g}+B_{1u}+B_{2u}+B_{3u}$
Fe	D_{2d}	$B_{1g}+E_g+A_{2u}+E_u$	D_2	$B_{1g}+B_{2g}+B_{3g}+B_{1u}+B_{2u}+B_{3u}$
O/F	D_{2d}	$B_{1g}+E_g+A_{2u}+E_u$	D_2	$B_{1g}+B_{2g}+B_{3g}+B_{1u}+B_{2u}+B_{3u}$
As	C_{4v}	$A_{1g}+E_g+A_{2u}+E_u$	C_{2v}	$A_g+B_{2g}+B_{3g}+B_{1u}+B_{2u}+B_{3u}$

Table 2.6: Atomic site symmetries and resulting vibrational modes for $REFeAsO_{1-x}F_x$ in the tetragonal $P4/nmm$ and the orthorhombic $Cmma$ space group.

tetragonal notation			
$\mathbf{A}_{1g}$	$\mathbf{B}_{1g}$	$\mathbf{E}_g$	$\mathbf{E}_g$
$\begin{pmatrix} xx & 0 & 0 \\ 0 & xx & 0 \\ 0 & 0 & zz \end{pmatrix}$	$\begin{pmatrix} xx & 0 & 0 \\ 0 & -xx & 0 \\ 0 & 0 & 0 \end{pmatrix}$	$\begin{pmatrix} 0 & 0 & -xz \\ 0 & 0 & 0 \\ -zx & 0 & 0 \end{pmatrix}$	$\begin{pmatrix} 0 & 0 & 0 \\ 0 & 0 & xz \\ 0 & zx & 0 \end{pmatrix}$

Orthorhombic notation			
$\mathbf{A}_g$	$\mathbf{B}_{1g}$	$\mathbf{B}_{2g}$	$\mathbf{B}_{3g}$
$\begin{pmatrix} xx & 0 & 0 \\ 0 & yy & 0 \\ 0 & 0 & zz \end{pmatrix}$	$\begin{pmatrix} xy & 0 & 0 \\ 0 & yx & 0 \\ 0 & 0 & 0 \end{pmatrix}$	$\begin{pmatrix} 0 & 0 & xz \\ 0 & 0 & 0 \\ zx & 0 & 0 \end{pmatrix}$	$\begin{pmatrix} 0 & 0 & 0 \\ 0 & 0 & yz \\ 0 & zy & 0 \end{pmatrix}$

Table 2.7: Raman tensors for the Raman active phonon modes of $REFeAsO_{1-x}F_x$ in the tetragonal and the orthorhombic notation.

Selection rules	Tetragonal notation	Orthorhombic notation
xx, yy	A_{1g}, B_{1g}	A_g
zz	A_{1g}	A_g
xz	E_g	B_{2g}
yz	E_g	B_{3g}
xy	B_{2g}	B_{1g}

Table 2.8: Selection rules for the Raman active phonon modes of $REFeAsO_{1-x}F_x$ in the tetragonal notation.

atoms respectively along the *c*-axis. Finally the E_g modes are assigned as follows: the lowest energy one at ~96cm^{-1} derives from vibrations of the rare earth atoms in the *ab*-plane (along the *a*- or *b*-axis), the one at ~138cm^{-1} from vibrations of the Fe and As atoms in the *ab*-plane, the one at ~279cm^{-1} from in-plane vibrations of the Fe atoms and the highest energy mode at ~420cm^{-1} corresponds to vibrations of O atoms along the *a*- or *b*-axis.

The room temperature Raman spectra in the $x'x'$, $y'y'$ and zy' polarization geometries which according to Eq. 2.11, probe the A_{1g}, B_{1g} and E_g symmetry modes are plotted in Fig. 2.13. The phonon assignment and labeling is done based on the previous analysis. It is worth mentioning that the intensity of the E_g phonons is considerably weaker than the

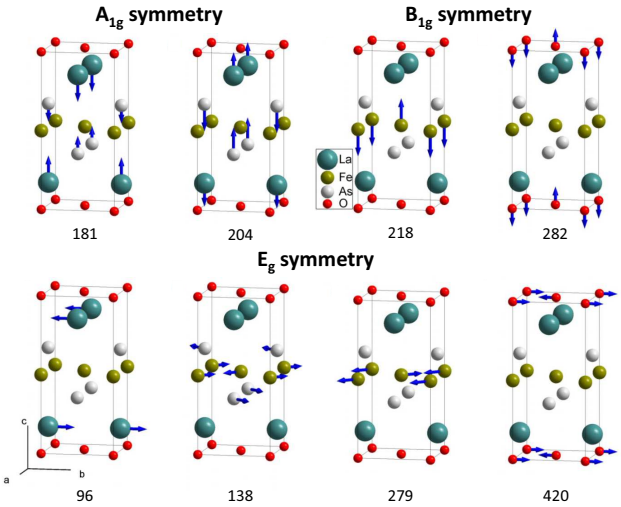

Figure 2.12: Eigenvectors and frequencies (in cm^{-1}) of the Raman modes in $REFeAsO_{1-x}F_x$. The phonon frequencies are the calculated frequencies for parent LaFeAsO. The figure and the values are taken from the calculations of reference [287].

one of the A_{1g} and B_{1g} modes which, in combination with the polarization requirements imposed by the selection rules, renders their study challenging.

2.5 Analysis of the phononic Raman data

The phonon peaks of the recorded Raman spectra were typically fitted using symmetric Voigt lineshapes (this holds in the absence of Fano asymmetries shown in Fig. 2.5). The Voigt profile results from the convolution of a Lorentzian phonon lineshape with the Gaussian lineshape imposed by the instrumental resolution function. The convolution is performed according to:

$$y(x) = \int_{-\infty}^{\infty} L(x-\tau)G(\tau)d\tau \tag{2.26}$$

where y(x) is the Voigt line shape, L(x) is the Lorentzian profile and G(x) is the Gaussian profile. The resulting Voigt line shape is intermediate between a Lorentzian and a Gaussian [290].

The resolution of the spectrometer was determined by measuring the spectrum of a discharge lamp containing a low pressure gas (usually an Argon or a Neon lamp). Given

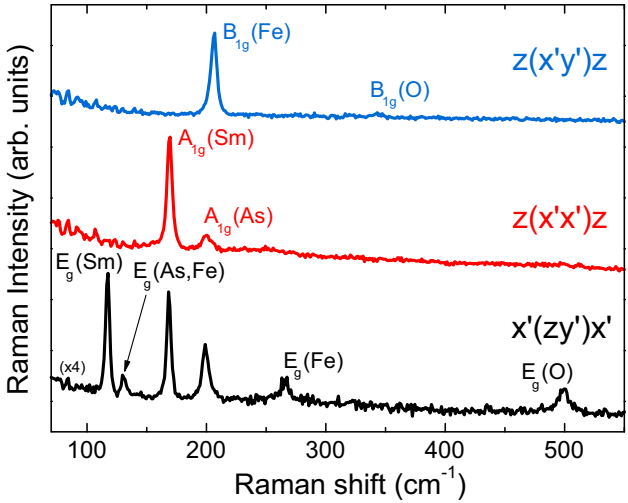

Figure 2.13: Room temperature Raman spectra of parent SmFeAsO taken with a He-Ne laser (λ=632.817 nm) in the $x'x'$, $y'y'$ and zy' polarization geometries, probing respectively the A_{1g}, B_{1g} and E_g symmetries. The spectrum int the zy' polarization is multiplied by 4.

the negligible intrinsic linewidth of these sharp emission lines, their measured linewidth is dominated by the Gaussian broadening of the spectrometer. An example of the experimental data fitting is given in Fig. 2.14 for the case of the SmFeAsO system (see chapter 6). The plotted Raman data were measured at 200 K and 25 K (both under a pressure of 6 GPa) and the shown frequency region is the one of the A_{1g} Sm phonon (the frequencies were suitably shifted so that the peaks are at both temperatures centered at the origin of the frequency axis). The same figure also shows the emission line of an Argon lamp calibration spectrum (bottom spectrum also shifted to the axis origin) fitted with a gaussian lineshape (blue line). The final Voigt fitting of the experimental data (red line) is the result of the convolution of a lorentzian lineshape (green lines) with the gaussian resolution given by the Argon line. The deconvoluted lorentzian linewidth of the phonon modes, labeled as "Γ", is the intrinsic one we will be referring to for the analysis of the experimental data in the following chapters.

The benefit of recording a discharge lamp spectrum is twofold. In addition to determining the resolution of the experimental setup, the emission lines of the calibration lamp serve as a reference for determining the precise frequencies of the measured spectra. The recorded Raman spectra are susceptible to non-intrinsic frequency shifts due to variations of the room temperature or to mechanical drifts in the experimental setup. The sharp emission lines of the discharge lamps are precisely documented in the literature and

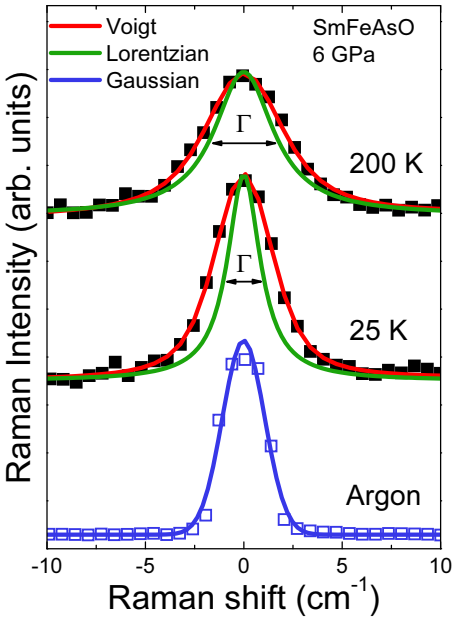

Figure 2.14: Fitting of the A_{1g} Sm phonon to a Voigt profile. The Raman spectra of SmFeAsO (black symbols) are measured at 200 K and 25 K (both at 6 GPa). The spectra are horizontally shifted so that the Sm phonon is centered at the origin of the frequency axis (the original frequencies are 184.85 cm^{-1} and 185.66 cm^{-1} at 200 and 25 K respectively). The calibration spectrum of an Argon lamp (also horizontally shifted so that the 160.14 cm^{-1} line is centered at the origin) is shown with the blue symbols. The blue line is a gaussian fitting to the Argon lineshape. The final Voigt fitting of the Sm phonon (red line) results from the convolution of the lorentzian phonon lineshape (green line) with the gaussian broadening obtained by the Argon spectrum. The deconvoluted lorentzian linewidth (FWHM) is marked as "Γ".

can serve as calibration standards for the measured Raman frequencies. For this reason, a calibration lamp spectrum was recorded before and after every Raman spectrum.

Chapter 3

Experimental Techniques

3.1 High Pressures and Low Temperatures

3.1.1 High Pressure Techniques: The Diamond Anvil Cell

The most extensively used device for optical and x-rays spectroscopic studies under high pressure conditions is the the diamond anvil cell (DAC) [291, 292]. The first attempt to use diamonds for generating high pressures was done in a split bomb configuration for high pressure x-ray diffraction studies by Lawson and Tang in 1950 [293]. Since then, major steps in the evolution of the DAC include the two versions of the DAC introduced

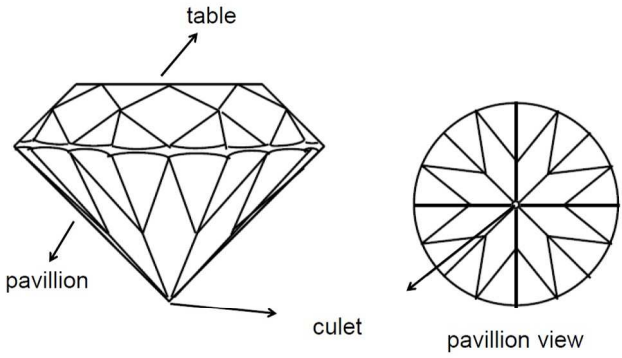

Figure 3.1: The brilliant-cut shape of diamonds. In the case of diamonds used in high pressure DACs the culet is not point-like but polished until the diagonal dimensions of the surface are ~200-600 μm.

by Jamieson *et al.* [294] and by Weir *et al.* [295], the introduction of a metallic gasket for hydrostatic pressure generation [296], the use of the ruby luminescence technique as a versatile tool for the calibration of pressure [297], the introduction of new pressure transmitting media for hydrostatic pressures up to 10 GPa [298] and the many innovative changes in the DAC design.

The use of diamonds as anvils for high pressure cells is justified firstly by the mechanical properties of diamond (the hardest material known, i.e. having the largest bulk modulus), and secondly by the transparency of diamonds to infrared, visible, UV light (up to 5.5 eV) [299, 300], and x-rays (above 10 keV), offering a broad energy spectrum for investigations under pressure. The diamonds used for high pressure DACs should bear some specific characteristics regarding their weight, size and cleanness. The used diamonds weigh typically 0.25-0.5 carats (1 carat=0.2 gr) and have the brilliant-cut shape, illustrated in Fig. 3.1. In the case of high pressure diamonds, the culet is not point-like but it is polished until its surface has diagonal dimensions of typically 0.2-0.6 mm. The cut is such so that both the table and culet are parallel to the (100) crystallographic plane. Natural diamonds contain nitrogen as an impurity, leading to luminescence in the visible spectral range [301]. For Raman experiments, the minimum contribution of the diamonds in the recorded Raman spectra is sought, so diamonds with low luminescence have to be selected (natural type-IIa diamonds). Synthetic diamonds are also available (Almax-easyLab, Sumitomo Electric Industries Ltd.), emitting only minimal luminescence and so presenting, in this respect, superior characteristics to natural type-IIa diamonds.

The basic working principle of the DAC is depicted in figure Fig. 3.2. Two similar sized

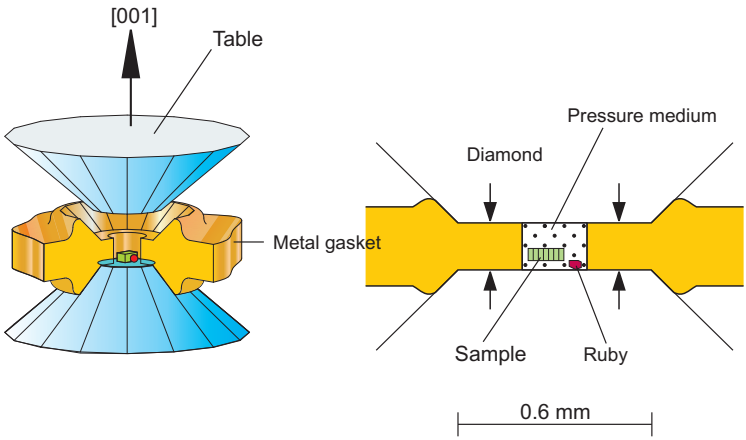

Figure 3.2: Schematic illustration of the basic working principle in a DAC: arrangement of the diamond anvils and the gasket (left), and enlarged view of the sample chamber (right).

diamonds are positioned with their culets facing each other. A metallic gasket (made e.g. by stainless steel) with an initial thickness of ~250 μm is placed between the culets of the two diamonds. By pressing the two diamonds against each other, the center of the gasket is initially thinned down to 60-70 μm and then subsequently a hole is drilled in the middle of its thinned part. The drilling of the gasket hole is performed either mechanically with a micro-drill, or by laser drilling or by electro-erosion. The space created inside the hole of the metallic gasket between the two diamonds serves as the sample chamber. A typical diameter of the gasket hole, and thus of the sample chamber, is 100-250 μm. Inside the sample chamber are placed a small piece of the sample of interest together with a small piece of a ruby crystal, serving for the pressure calibration, as it will be discussed in the following section. Finally the pressure transmitting medium is loaded in the DAC, in order to transform the uniaxial pressure generated by the two anvils to quasi-hydrostatic pressure. The medium is sealed inside the sample space by pressing the two diamonds against each other. Once the medium is sealed, pushing further the two diamonds leads to the plastic deformation of the gasket, thus to the decrease of the volume of the sample chamber, and this way pressure is generated.

Typical dimensions of the sample inside the DAC are 80 μm $\times$ 80 μm $\times$ 30 μm. It is particularly important that the loaded sample is not in touch with the two anvils, in order to prevent the application of uniaxial pressure on the sample or even the breaking of the sample between the anvils. Therefore, before loading the sample thickness must be carefully controlled to be safely smaller than the gasket thickness. The samples studied in the current thesis were all single crystals. In the case that the as-grown single crystals were not in the right dimensions for the high pressure loading, special crystal preparation was conducted, including cutting the initial crystals and polishing them until they were thinned down to ~30 μm. In the case of polarized Raman measurements, special care was taken to obtain the correct orientation of the crystal inside the DAC.

Whereas the main components of the DAC are clearly the diamond anvils, the rest of the cell bears the major task of aligning the diamonds, maintaining the alignment after the loading and sustaining the pressure load. For the current thesis, the high pressure Raman measurements were performed using the Stuttgart type DAC [302]. The force transmission principle of this type of DAC is illustrated in Fig. 3.3. One of the two diamonds is fixed on the bottom plate, which is attached to the main body of the DAC, whereas the second diamond is fixed on a moving piston. Turning the two threaded rods leads to the mechanical movement of the two levers which push the moving piston towards the body of the DAC and thus push the upper diamond towards the bottom one. The turning of the threaded rods is performed with a gear box and a stepping motor (remote control), allowing for a very fine tuning of the mechanical movement and subsequently of the resulting generated pressure. The light entrances needed for spectroscopic measurements are provided through the conical openings in the bottom plate and the upper piston.

For our x-ray diffraction measurements (discussed in a following section) we used a different DAC design, namely a membrane-driven type of DAC based on Le Toullec

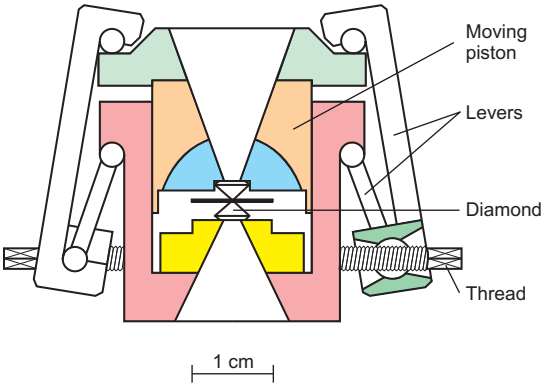

Figure 3.3: Layout of the Stuttgart type DAC. Pressure is generated when the piston, holding the upper diamond, is pressed by the levers towards the main body of the DAC, holding the lower diamond. The mechanical movement of the levers is controlled by turning the threaded rods.

et al. DAC principle [303]. In this case, a pressurized inert gas (e.g. helium, in the case of our experiment) is injected through a thin capillary tube into an expandable membrane causing its inflation. As the membrane expands it pushes the piston of the DAC, moving the upper diamond towards the lower diamond and generating pressure, similar to what was previously described for the Stuttgart type DAC.

Pressure Calibration: The Ruby Luminescence Lines

The most widely used method for the pressure calibration in DAC experiments is based on measuring the pressure-induced frequency shift of the ruby luminescence R_1 line [304].

The origin of the two ruby luminescence lines is illustrated in Fig. 3.4 where the 3*d* electronic levels of Cr^{3+} are plotted. Ruby is Cr-doped α-Al_2O_3 (corundum with trigonal crystal structure). In the 3*d* shell of free Cr^{3+} ions, there are three electrons. In the crystal field environment of the ruby crystal the 3*d* levels of free Cr^{3+} ions are split. The major crystal field induced splittings are caused by the octahedral field component, whereas the trigonal field component in combination with spin-orbit interaction results in additional smaller splittings. The ^2E levels involved in the emission of the luminescence lines are split by ΔE=29 cm^{-1}. Upon laser illumination electrons are excited from the $^4A_2$ ground state to higher electronic levels, e.g. to the U band in the case of green laser illumination or the Y band for violet laser illumination, as shown in Fig. 3.4. Then through phonon-assisted relaxation the electrons populate the lower energy double spit ^2E levels. Finally, the transition from the ^2E levels to the ground state $^4A_2$ produces the two ruby luminescence lines R_1 and R_2. Under ambient conditions R_1 and R_2 are observed at

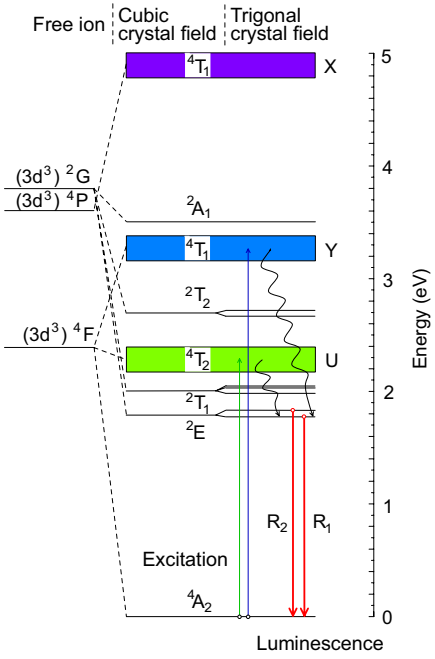

Figure 3.4: The 3*d* levels of Cr^{3+} in the free ion and in the cubic and trigonal crystal field of the ruby crystal α-Al_2O_3 (after Tanabe and Sugano [305, 306]). Optical absorption into the $^4T_2$ and $^2T_2$ levels (the U and Y bands) and the sharp ruby luminescence lines originating from the ^2E level are indicated.

~14404 and 14433 cm^{-1} (separated by 29 cm^{-1} as the involved ^2E levels), whereas their linewidth is ~11.5 and 8.5 cm^{-1} respectively.

Pressure dependence of the ruby luminescence lines

Upon pressure application, the ruby lattice is almost isotropically deformed [307], leading to the decrease of the distances between Cr and O ions and therefore to the increase of the crystal field in the Cr ions. The energies of the ^2E states depend on the difference in crystal field splittings of two different free-ion levels (^4F and ^2G, shown in Fig. 3.4). The increased crystal field changes the energy levels splittings of Cr^{3+}, in such a way that the the energy gap between the ^2E states and the ground state becomes smaller. Therefore, the two ruby luminescence lines R_1 and R_2 are shifted towards lower energies and thus higher wavelengths. This is illustrated in Fig. 3.5 where the luminescence lines are plotted at 1 and 10.7 GPa (at room temperature).

Various calibration scales have been suggested for the frequency shift of the ruby R_1 line under high pressure application [297, 308]. These calibration scales were determined

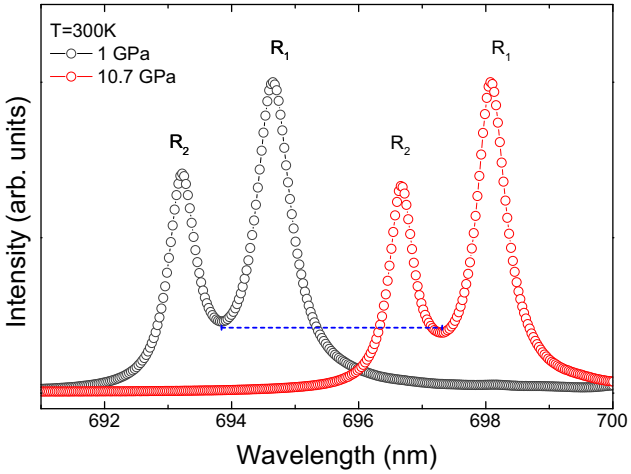

Figure 3.5: Room temperature normalized spectra of the ruby luminescence lines at 1 and 10.7 GPa. The pressure-induced shift is indicated by the dashed blue line.

by measuring simultaneously the pressure-induced shift of the R_1 line and the pressure-induced change in the lattice parameters (using x-ray diffraction) of a reference sample with a known equation of state. A well-known such calibration by Mao *et al.* was based on x-ray diffraction measurements of copper up to 80 GPa [309]. The resulting relation between the position of the R_1 luminescence line and the applied pressure is given by:

$$P = \frac{A}{B}\left[\left(1 + \frac{\Delta\lambda}{\lambda_0}\right)^B - 1\right] \tag{3.1}$$

where A=1904 GPa, B=7.665, λ_0 is the wavelength of the R_1 line at ambient pressure and $\Delta\lambda$ is the observed wavelength shift.

Temperature dependence of the ruby luminescence lines

Fig. 3.6-a shows the ruby luminescence lines recorded under a pressure of 1 GPa upon cooling, while in Fig. 3.6-b are plotted the energies of the R_1 and R_2 lines as a function of temperature at ambient pressure (taken from reference [310]). With decreasing temperature, the R-lines shift to higher energies, their widths decrease, and the R_2/R_1 intensity ratio decreases. The temperature-induced energy shift of the R-lines is caused by the electron-phonon interaction [311]. The shift varies with the phonon occupation number and is related to the change of the mean square displacement of atoms with the change in

temperature. The temperature dependence in Fig. 3.6-b is fitted by:

$$\omega(T) = \omega_0 - \frac{\alpha}{\exp(\beta/T) - 1} \tag{3.2}$$

where $\omega(T)$ and ω_0 are the frequencies of the ruby luminescence lines at T and at 0 K respectively. The fitting parameters for the R_1 line are $\omega(T{=}0){=}14421.8{\pm}0.4$ cm^{-1}, $\alpha{=}76.6{\pm}6.9$ cm^{-1}, and $\beta{=}482{\pm}20$ K.

It is usually assumed, and has to some extent been demonstrated experimentally at moderate pressures [312], that the effects of temperature, and pressure are independent of each other. So, the frequency shift can be expressed as a superposition of the following form:

$$\Delta\omega = \Delta\omega(T) + \Delta\omega(P) \tag{3.3}$$

Since the temperature effects depend on the phonon spectrum, which is a function of the applied pressure, the above assumption of the uncoupled temperature and pressure effects is an approximation.

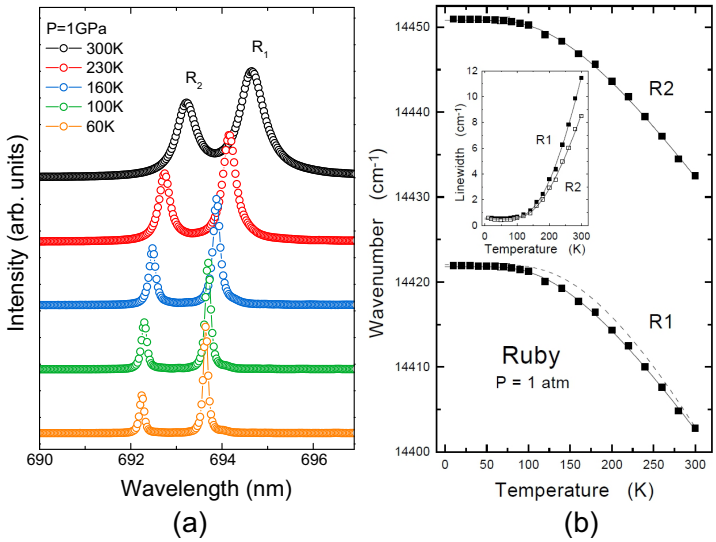

Figure 3.6: (a) Low temperature normalized spectra of the ruby luminescence lines at 1 GPa. The spectra are vertically shifted for clarity. (b) Temperature dependence of the positions of the two ruby lines at ambient pressure, taken from [310].

Hydrostatic Pressures: Pressure Transmitting Media

The aim for hydrostaticity in high pressure experiments derives from the fact that hydrostatic pressure is a thermodynamic parameter and so the results obtained under such conditions are intrinsic properties of the studied sample and can be compared with theory [292, 313]. Additionally, hydrostaticity allows for a direct comparison of various experimental results, avoiding the complications and uncertainties introduced by the differences in the pressure conditions.

Hydrostatic conditions are realized by immersing the sample in a pressure transmitting medium. The main property that the medium should have is low shear strength so that the shear stresses acting on the sample are very small. When choosing a suitable pressure medium, not only the pressure and temperature range to be investigated should be taken into account, but also the special demands of the sample and the experiment. For example, clearly, the investigated sample should not be reacting with the pressure medium and in the case of Raman experiments, the pressure transmitting medium should not have strong Raman features in the spectral range of interest.

The most commonly used pressure transmitting medium for room temperature measurements is a mixture of methanol-ethanol 4:1, which remains hydrostatic up to ~10 GPa [298, 313]. Adding water in a 16:3:1 methanol-ethanol-water mixture increases the hydrostatical limit up to 14.4 GPa [314]. Inert fluid media like paraffin or silicone oil are also used, especially for samples reacting with alcohol. For high pressure transport measurements soft solid pressure media such as KCl, CsCl, NaCl are preferred since they facilitate the loading procedure.

The melting line of fluids increases in temperature upon pressure application and solidification of the medium inevitably occurs at some pressure, leading to loss of hydrostaticity. This is a particularly challenging problem for low temperature measurements under high pressure coonditions. The best choice is then the use of condensed gases, such as nitrogen, argon, and helium as pressure media. The ultimate hydrostatic pressure medium is generally considered to be condensed helium, which at ambient pressure remains liquid even at temperatures close to ~0 K. At room temperature helium solidifies above 12 GPa [315, 316], but still remains the softest material known [317]. Loading a DAC with helium is done either by loading helium as a cryogenic liquid in a cryostat (as was performed in the helium loadings for the high pressure Raman measurements of the current thesis) or as compressed gas with a gas loading system including a compressor and a high pressure vessel (as was performed in the helium loadings for the high pressure x-ray diffraction measurements of the current thesis).

3.1.2 Low Temperature Techniques: The Cryostat

Low temperature measurements were performed both at ambient pressure conditions (Raman measurements) and under, far more demanding, high pressure conditions (Raman and x-ray diffraction measurements). Different designs of cryostats have been employed

for the different types of measurements and will be described separately in the following sections.

Low temperatures at ambient pressure

For the low temperature measurements at ambient pressure conditions we used a horizontal helium flow cryostat (Konti-Cryostat-Mikro, Cryovac) with a suprasil glass window, positioned under the microscope objective of a single stage micro-Raman spectrometer (the micro-Raman setup is described in section 3.2.1). The cryostat has a small and compact design and can achieve temperatures down to ~4 K. In order to ensure a good thermal contact the samples are mounted on the copper cold finger of the cryostat with a silver paste or with an adhesive copper tape. The temperature is controlled with an accuracy of ~0.1 K with the help of a temperature controller (LakeShore, Cryogenic Temperature Controller) and a heater. Due to the horizontal orientation of the cryostat under the microscope, the temperature-induced contraction/expansion of the sample holder leads to shifts of the sample along the laser beam direction and thus the focusing height needs frequent readjustment. The horizontal geometry and the compact size of the cryostat offer the possibility of selecting the measuring geometry by simply rotating the cryostat under the microscope objective.

Low temperatures at high pressures

For the combined high pressure and low temperature Raman measurements a helium bath cryostat (Konti-IT, Cryovac) was employed. A schematic illustration of the high pressure DAC inside the cryostat is shown in figure Fig. 3.7. The cryostat is divided in four different chambers, one inside the other. The outer chamber is the a vacuum chamber isolating the cryostat from the room temperature environment of the laboratory. The second chamber is the liquid nitrogen chamber, serving in pre-cooling the cryostat down to ~80 K, and the third chamber is the helium reservoir (between the nitrogen and the helium chamber there is also vacuum isolation). The helium reservoir is connected to the fourth chamber, the sample chamber, through a needle valve which allows and controls the helium flow through the sample chamber. An electrical heater installed near the DAC, together with two silicon-diode thermometers and a temperature measurement and control unit (LakeShore, Cryogenic Temperature Controller) can stabilize the temperature within ~0.1 K. Temperatures as low as 2 K can be reached with this setup. Two steel rods designed to fit the threaded rods of the DAC inside the cryostat allow the pressure tuning without removing the DAC from the cryostat.

The same cryostat also served for the helium loading of the high pressure DAC. For this purpose, the DAC was fully prepared (gasket preparation, sample and ruby loading at the sample chamber) and inserted in the bath cryostat without being completely closed. The cryostat was then filled with liquid helium and the needle connecting the helium reservoir and the sample chamber was fully opened, so that the DAC was fully immersed

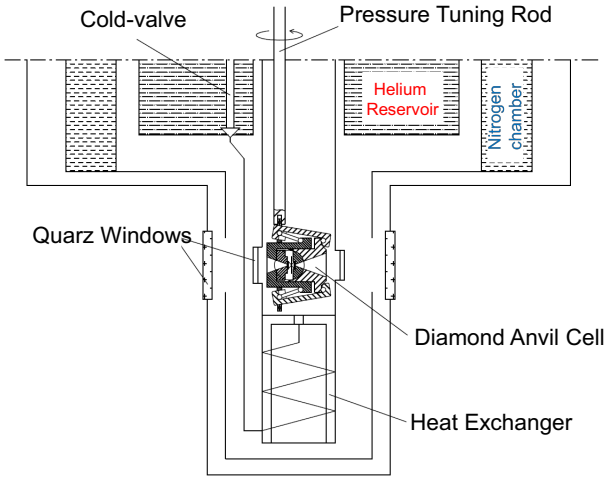

Figure 3.7: Layout of the DAC in the helium-bath cryostat. Pressure can be tuned by the pressure tuning rode without removing the DAC from the cryostat.

in helium. To prevent bubble formation inside the gasket hole, helium was pumped below its λ point (2.17 K), and so superfluid helium filled the sample chamber. After waiting for several minutes, the DAC was slowly closed by turning the pressure rod. Since the helium loading is performed at ~2 K, pressure inevitably increases as temperature is increased, resulting in an starting pressure of 1-2 GPa at room temperature.

For our high pressure x-ray diffraction measurements we used a helium flow cryostat accommodating the membrane-driven DAC previously described. The cryostat was designed and manufactured at the European Synchrotron Radiation Facility and can reach temperatures down to ~2.3 K with a thermal stability $\Delta T/T \leq 10^{-3}$.

3.2 Raman and x-ray Diffraction Setups

3.2.1 Raman Scattering Setups

For the Raman measurements two different setups were used depending on the pressure and temperature measuring conditions. For the low temperature measurements at ambient pressure conditions and for the high pressure measurements at room temperature conditions a single-grating micro-Raman setup was employed (in combination, respectively, with the helium flow cryostat and with the DAC as described previously). For the combined high pressure and low temperature measurements a single/triple-grating

macro-Raman setup was used together with the helium bath high pressure cryostat of Fig. 3.7.

A Jobin Yvon Typ V 010 LabRam single grating spectrometer was employed for the micro-Raman measurements. Pictures of the micro-Raman setup with the cryostat and the high pressure cell are shown in Fig. 3.8. The full optical setup is placed on a vibration-damped optical table. The linearly polarized laser light lines of Table 3.1 are used for excitation. The incident laser light is focused through an appropriate microscope objective (10x, 20x, 50x) on the sample surface. For the low temperature measurements the 50x objective is routinely used (Fig. 3.8, left), whereas for the high pressure measurements a long distance 20x objective is used due to geometrical limitations imposed by the DAC (Fig. 3.8, right). In the case of polarized Raman measurements, a polarizer is inserted in the incident laser light optical path and an analyzer on the scattered light optical path. The spectra are taken in the backscattering geometry with the incident and the reflected light parallel to the direction normal to the sample surface. The same objective that focuses the laser light on the sample is also used to collect the scattered light from the sample. The reflected and elastically scattered light is suppressed by a razor edge filter, which cuts the measured Raman spectra below ~50 cm^{-1}, not allowing a detailed study of the low energy excitation range. The scattered light goes through the entrance slit of the spectrograph and gets dispersed by a 1800 lines/mm holographic grating. For the detection of the Raman signal a Peltier-cooled CCD detector is used. The resolution of the spectrometer is ~1 cm^{-1} (1800 grating).

In Fig. 3.9 is presented schematically the experimental macro-Raman setup employed for measurements under combined low temperature and high pressure conditions. The full optical setup is again positioned on a vibration-damped optical table. Ar^+ and Kr^+ mixed gas lasers providing laser lines between 450-750 nm are used for excitation. Beyond the major amplified laser line, a laser emits also additional weaker plasma lines

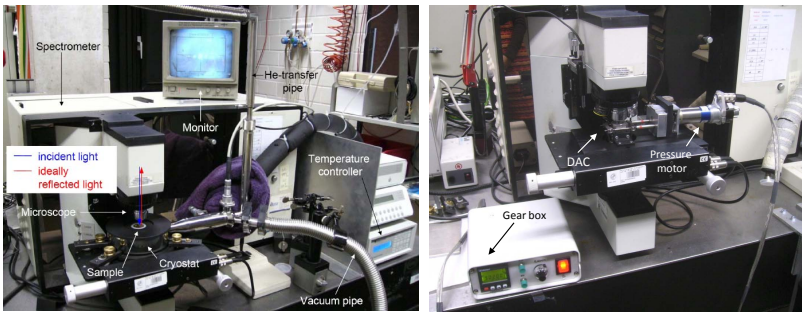

Figure 3.8: The helium flow cryostat (left) and the high pressure DAC (right) in the micro-Raman setup.

Laser	Wavelength
He^+/Ne^+	632.8 nm
Nd:YAG	532 nm
diode laser	488 nm

Table 3.1: Laser light lines used as excitation in the micro-Raman setup.

at slightly different wavelengths. In order to suppress these plasma lines a small fore-monochromator or a plasma filter with small transmitting bandwidth are used. The laser beam is directed towards the sample with the help of small mirrors. Along the optical path, the laser light spreads out, due to e.g non-ideal reflection at the mirrors. Pinholes are therefore used to suppress stray light and contract laterally the beam diameter. In the case of polarized Raman measurements, a polarization rotator together with a polarizer are used to control and select the polarization of the incident laser light. Finally, the laser beam is focused on the sample with the help of a photographic objective to a $\sim$50 μm spot on the sample surface.

The same objective is also used for the collection of the scattered light. A pinhole is placed in the image plane of the sample in order to block scattered light that is not coming from the sample (e.g. scattered light from the free space in the DAC or beam reflections on the diamond). The image plane also serves for the observation of the sample in the gasket hole, with the help of a mirror and an additional objective. In the case of polarized Raman measurements, an analyzer selects the polarization of the scattered light. Finally, the scattered light is focused by a lens in the entrance slit of a Jobin-Yvon triple- or single-grating spectrometer. The spectrometer is equipped with a nitrogen-cooled CCD detector (Jobin-Yvon Symphony) for the detection of the Raman signal.

The spectrometer consists of a series of three holographic gratings (1800 lines/mm) and can operate either in the additive or in the subtractive mode. In the additive configuration the three gratings work as three coupled spectrographs, adding up their dispersions and leading to an enhanced resolution for a narrow energy range. In the subtractive configuration the pre-monochromator works as a bandpass filter. The incoming scattered light is dispersed by the first grating and then sent to the first intermediate slit. This slit allows light in the spectral range between λ_1 and λ_2 to pass and cuts the rest. This way the major part of the elastically scattered light is also cut off and the inelastically scattered Raman signal can be analyzed down to $\sim$5 cm^{-1} (depending also on the quality/roughness of the sample surface). Then the second grating recombines the scattered light (now limited only in the spectral range between λ_1 and λ_2) and sends it through the second intermediate slit to the final grating. The last grating acts as a spectrograph, dispersing and focusing the scattered light on the CCD detector.

In order to gain more signal the scattered light can be directly sent through a second

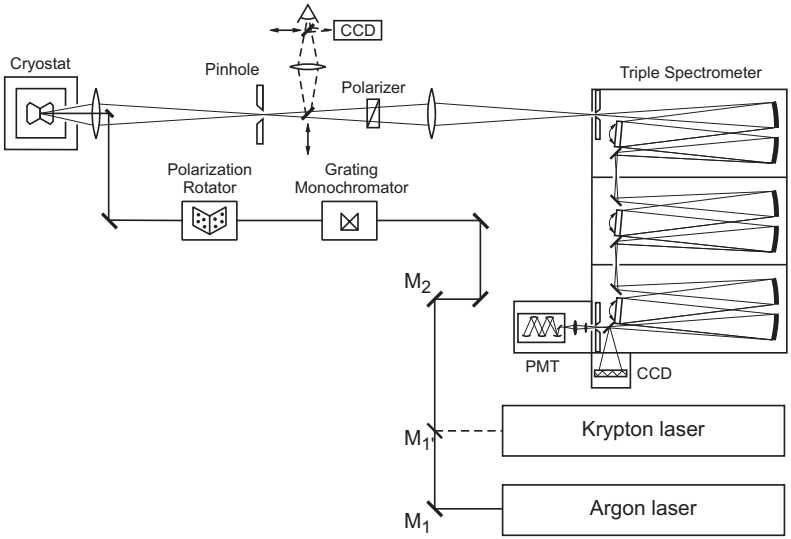

Figure 3.9: Optical path in the macro-Raman setup.

entrance slit to the final grating, without going through the two first gratings of the pre-monochromator. In this case the spectrometer performs as a single stage spectrometer (like the one of the micro-Raman setup) and a razor edge or a notch filter are needed to suppress the elastically scattered light. Due to the use of the razor edge/notch filter though, the measured Raman spectra were cut below ~50 cm^{-1} for the 514.53 nm excitation and below ~90 cm^{-1} for the 647 nm excitation, not allowing a detailed study of the low energy excitation range. For the results of the current thesis, due to the very limited Raman signal of the studied materials the spectrometer was extensively used in the single stage configuration.

Finally, variations of the room temperature or mechanical drifts lead to non-intrinsic shifts of the measured frequencies. To overcome this problem, for every Raman spectrum, taken at either of the two setups, an additional calibration spectrum was recorded using a discharge lamp containing a low pressure gas such as argon, neon, krypton etc (this was analyzed in detail in section 2.5).

3.2.2 X-ray Diffraction Setup

Fig. 3.10 shows the layout of the ID09A beamline in the European Synchrotron Radiation Facility (ESRF) in Grenoble, where our high pressure x-ray diffraction measure-

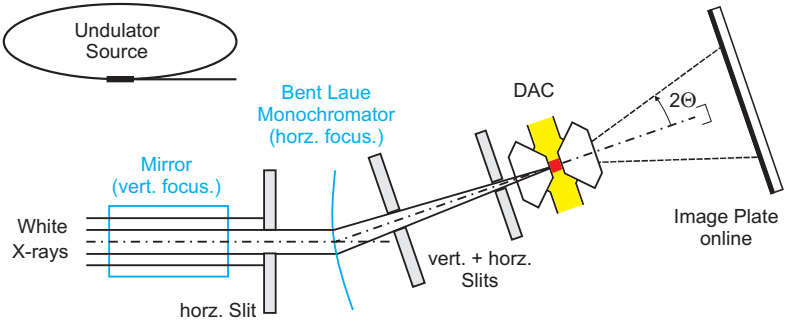

Figure 3.10: Layout of the ID09A beamline in the European Synchrotron Radiation Facility.

ments were performed. The polychromatic x-ray beam is vertically focused by a mirror and horizontally focused and monochromatized by a bent-Laue monochromator. After passing through a number of slits the final beam spot size focused on the sample surface in the DAC is ~10-30 μm. Our measurements were performed in the angle dispersive configuration, in which the energy (wavelength) of the incident beam is kept fixed and the diffraction angle is varied by rotating the DAC. The opening of the DAC imposes limits on the accessible angle range, which are though overcome by the high energy of the incident x-rays (λ~0.415 Å, $\hbar\omega$~30 keV for our measurements) so that, according to Bragg's law, also small d values can be probed.

The x-ray diffraction pattern is recorded on a MAR555 image plate x-ray detector. Conventional x-ray detectors, like e.g. the image plate, count visible light photons and therefore require a phosphor layer to convert x-rays photons into visible photons. MAR555 consists of a thin film transistor (TFT) frame coated with a selenium layer. X-rays directly produce charges on the Se-layer which are directly collected by the individual TFT pixel electrodes. This direct conversion procedure offers an enhanced angular resolution and a superior signal-to-noise ratio. The two-dimensional recorded diffraction patterns are afterwards integrated using the FIT2D software. The final output are intensity vs 2θ diagrams.

Chapter 4

Raman study of $YBa_2Cu_3O_{6+x}$

4.1 Ambient Pressure Results

4.1.1 Introduction

Soon after the discovery of the CDW order in underdoped cuprates, inelastic x-ray scattering (IXS) was implemented to investigate the low energy lattice dynamics in the charge-ordered systems. As already well-studied in classic CDW systems, such as the transition metal dichalcogenides 2*H*-$NbSe_2$ and $TaSe_2$, the periodic modulation of the electron density in the CDW state is reflected in the behavior of the lattice vibrations, via the electron-phonon interaction [318]. IXS experiments in underdoped $YBa_2Cu_3O_{6+x}$ have revealed pronounced phonon anomalies close to q=q_{CDW}, implying a strong electron-phonon interaction sharply concentrated in momentum space around the CDW ordering wavevector [319, 320].

Regarding the phonons in the center of the Brillouin zone though, previous Raman scattering experiments in underdoped $YBa_2Cu_3O_{6+x}$ have not revealed any ordering-related features. This comes in contrast to the case of stripe ordered $La_{2-x}Sr_xCuO_4$ for which clear signatures of the charge order have been identified in the Raman spectra, such as CDW modes, phason and amplitudon, as well as low energy electronic excitations attributed to fluctuations of the charge density [321, 322, 323].

In view of the quasistatic nature of the CDW fluctuations in $YBa_2Cu_3O_{6+x}$, as revealed by the high resolution IXS measurements [319, 320], we have looked for signatures of the CDW order in the zone center lattice dynamics of underdoped $YBa_2Cu_3O_{6+x}$ by means of Raman spectroscopy. Moreover, the pressure evolution of the CDW has been investigated by high pressure Raman measurements and will be presented in section 4.2.

In Fig. 4.1 is plotted the Raman spectrum of an untwinned $YBa_2Cu_3O_{6.55}$ single crystal (T_c= 61 K, $T_{CDW}\simeq$130 K) in the xx scattering configuration recorded at T=80 K therefore in the charge ordered state. The Raman modes of the *ortho*-I structure are marked with

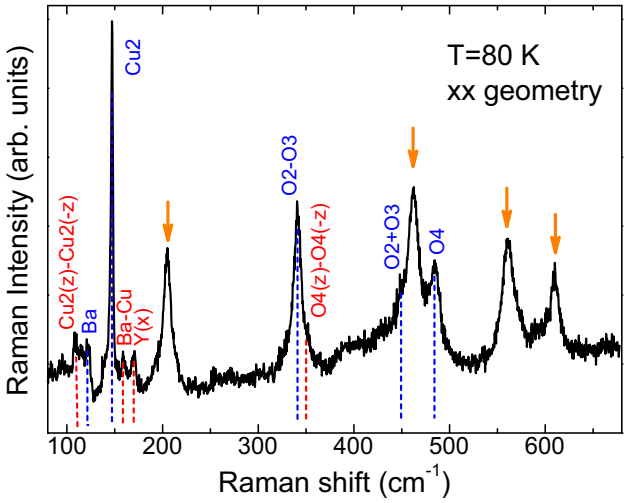

Figure 4.1: Raman spectrum of an *ortho*-II $YBa_2Cu_3O_{6.55}$ detwinned single crystal recorded at 80 K in the xx geometry with a He^+/Ne^+ laser line (λ=632.8 nm). The blue dashed lines indicate the *ortho*-I phonons, whereas the red ones the phonons of the *ortho*-II oxygen superstructure, assigned according to the analysis presented in chapter 2. The new Raman features are marked with the orange arrows.

the dashed blue lines whereas the modes related to the *ortho*-II oxygen superstructures are marked with the red lines. In addition to those modes expected from group theory considerations, new intense Raman active phonon modes appear, pinpointed by the orange arrows. The origin of these new modes has been studied in detail through Raman measurements as a function of doping, excitation energy, temperature and pressure, as described in the following sections.

4.1.2 Experimental Details

The Raman experiments were performed on high-quality detwinned $YBa_2Cu_3O_{6+x}$ single crystals with doping levels ranging from optimally doped (x=0.99) to very underdoped (x=0.45). The stoichiometries, doping levels and T_c of the $YBa_2Cu_3O_{6+x}$ samples studied here are summarized in Table 4.1. The doping levels were stabilized through a suitable annealing procedure. Details on the synthesis are given in references [34, 324]. The samples were individually detwinned under uniaxial pressure upon observation through a polarized microscope, as described in section 1.1.4 [131, 133]. Information on the low temperature Raman scattering experiments presented here has been presented in chapter 3. Special care has been taken in order to avoid laser heating effects, as will be

discussed later on.

4.1.3 Doping Dependence

In Fig. 4.2 are plotted the xx Raman spectra of untwinned $YBa_2Cu_3O_{6+x}$ single crystals for the five studied doping levels, corresponding to stoichiometries: x=0.99, 0.75, 0.6, 0.55, 0.45 (the data for x=0.99 and x=0.6 were taken from [271]). On the left panel of Fig. 4.2 are plotted the room temperature spectra and on the right panel are plotted the equivalent spectra at T=T_c.

At room temperature, the xx Raman spectra are composed of a flat electronic continuum on top of which phonons are superimposed. The 5 A_g symmetry phonons of the *ortho*-I structure are clearly observable in all the doping levels as indicated by the vertical dashed blue lines and their positions are in line with previous Raman studies [264, 268, 280, 325, 326, 327]. The black arrow indicates the softening of the apical oxygen phonon upon decreasing the oxygen content, in accordance with earlier reported results [328].

For the optimally doped sample $YBa_2Cu_3O_{6.99}$ no significant changes are observed upon cooling from room temperature to T_c except for the phonon sharpening as expected from the anharmonic decay of optical phonons, as well as changes in the relative phonon intensities. The overall Raman spectrum at T_c is otherwise very similar to the one at room temperature.

Contrary to that, the spectra of the underdoped samples at T_c look significantly different to the ones at room temperature. At low temperatures, weak features associated with the formation of oxygen superstructures (marked with asterisks in Fig. 4.2) are observed at energies depending on the formed oxygen superstructure and therefore on the doping level of each sample. In addition to those low intensity phonon modes, a very large

sample	**doping level p**	**T_c (K)**
$YBa_2Cu_3O_{6.99}$	0.16	90
$YBa_2Cu_3O_{6.75}$	0.135	75
$YBa_2Cu_3O_{6.6}$	0.12	61
$YBa_2Cu_3O_{6.55}$	0.10	61
$YBa_2Cu_3O_{6.45}$	0.08	35

Table 4.1: List of the $YBa_2Cu_3O_{6+x}$ single crystals investigated here. The hole doping level p was determined from the dependence of the c-axis lattice parameter and of T_c on p. Measurements of the superconducting transition temperatures were done using a superconducting quantum interference device (SQUID).

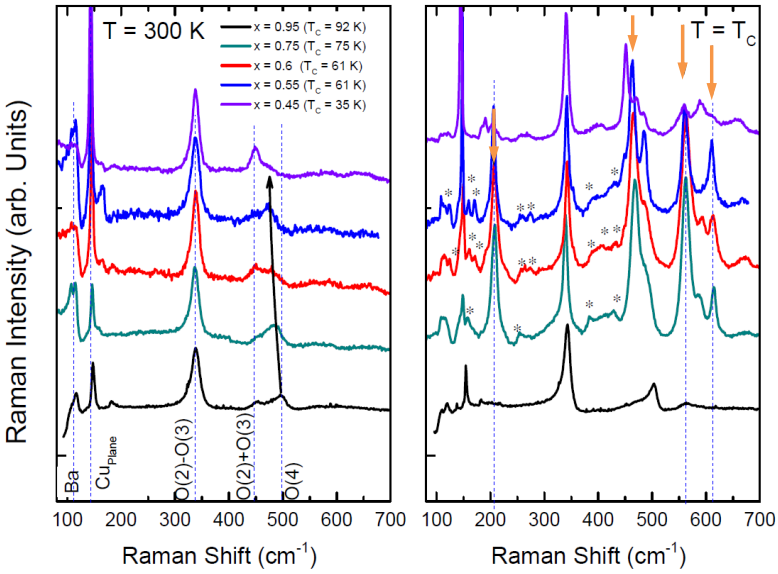

Figure 4.2: Raman spectra of optimally doped $YBa_2Cu_3O_{6.99}$ and underdoped $YBa_2Cu_3O_{6.75}$, $YBa_2Cu_3O_{6.6}$, $YBa_2Cu_3O_{6.55}$ and $YBa_2Cu_3O_{6.45}$ detwinned single crystals in the xx geometry taken with a He^+/Ne^+ laser line (λ=632.8 nm) at room temperature (left) and T_c (right). The blue dashed lines on the left panel indicate the *ortho*-I phonons assigned according to the analysis presented in chapter 2, whereas on the right panel indicate the position of the new phonons. The spectra of different doping levels have been vertically shifted for clarity.

scattering intensity is observed for all the underdoped samples around 205, 465, 560, and 610 cm^{-1}, as already pointed out in Fig. 4.1 for the case of the *ortho*-II sample.

The feature observed at ~465 cm^{-1} is in close proximity to the O2+O3 and O4 phonons of the *ortho*-I structure (observed at ~450 cm^{-1} and ~485 cm^{-1} respectively), leading to a spectral overlap, especially in the case of the $YBa_2Cu_3O_{6.75}$ and $YBa_2Cu_3O_{6.6}$ doping levels (right panel of Fig. 4.2). In the case of *ortho*-II $YBa_2Cu_3O_{6.55}$ the higher oxygen order, compared to the one of the rest underdoped samples, leads to sharper phonons in the Raman spectra. A closer look in the Raman spectrum of $YBa_2Cu_3O_{6.55}$ at T_c is given in Fig. 4.3, in which it is clearly demonstrated that the feature at ~465 cm^{-1} (orange arrow in Fig. 4.3) appears close in energy but is distinct from the neighboring *ortho*-I phonons (dashed blue lines in Fig. 4.3) and is therefore truly a new phonon.

For x=0.55, 0.6 and 0.75 the newly observed features are comparably high in intensity to the strongest A_g symmetry phonons of the *ortho*-I structure, like e.g. the O2-O3 phonon mode at ~340 cm^{-1}. In the most underdoped sample investigated here,

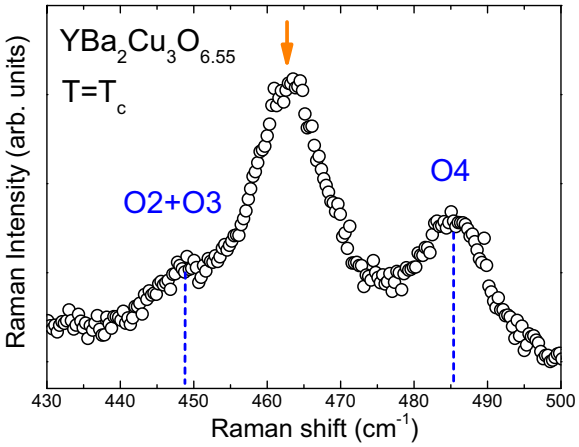

Figure 4.3: Detailed view of the xx Raman spectrum of $YBa_2Cu_3O_{6.55}$ at T_c=61K. The two blue dashed lines indicate the O2+O3 and the O4 modes, while the orange arrow indicates the new feature appearing at ~465 cm^{-1}.

$YBa_2Cu_3O_{6.45}$, these features are very weak in intensity but still observable (at least the ones at 205 and 560 cm^{-1}). Furthermore, they appear for all the studied underdoped samples essentially at the same frequencies. This doping independence of the energies suggests a common physical origin of the new phonons.

A possible connection of the new intense Raman modes to the formation of oxygen superstructures could be considered highly unlikely already in view of the doping dependence of the Raman spectra (in the followings this will be further corroborated). As already explained, the oxygen superstructures give rise to new phonons at the Γ point which are sample dependent and different for the different types of oxygen supercells [277, 278, 280]. This clearly does non apply in the case of the new Raman modes, which contrary to that present a remarkable doping independence. Additionally, the oxygen superstructure related phonons are much lower in intensity compared to the A_g symmetry phonons of the *ortho*-I structure, unlike the strong new Raman features. Taking into account the decreasing correlation length (100 Å for the highly ordered *ortho*-II $YBa_2Cu_3O_{6.55}$, 37 Å for *ortho*-III $YBa_2Cu_3O_{6.75}$ and 16 Å for *ortho*-VIII $YBa_2Cu_3O_{6.6}$, as derived from x-ray scattering measurements on the samples studied here) the corresponding oxygen superstructure modes are expected to be accordingly weak, a behavior which is certainly not encountered in the new Raman features.

4.1.4 Scattering Geometry Dependence

The spectra shown in the previous figures are all recorded in the xx polarization geometry. The symmetry of the newly observed modes can be determined via a detailed polarized Raman study using the selection rules described in section 2.4.

The Raman spectra of $YBa_2Cu_3O_{6.75}$ at T_c=75 K recorded in various geometries of the incident and scattered light polarization (given in the Porto notation) are plotted in Fig. 4.4. The position of the new features is marked by the dashed orange lines. The new modes are observed only in the xx, $x'x'$ and $x'y'$ polarization geometries, therefore according to the selection rules (see 2.4) they have the A_g symmetry.

It is worth commenting that according to the selection rules the A_g symmetry phonon modes are also probed in the yy scattering polarization geometry. In this geometry, the broken chain related Raman modes are observed [273, 275], as indicated by the black arrows in Fig. 4.4. The O1 defect mode at ~580 cm^{-1} is significantly stronger than the Cu1 defect mode at ~230 cm^{-1} and dominates the spectral region close to it. No new features are observed in the yy channel, not only in the spectral region close to ~580 cm^{-1}, where an overlap with the strong O1 defect mode would potentially screen any enhanced Raman intensity of different origin, but also close to 205 cm^{-1} where no chain-related features are present. It is worth emphasizing that the chain modes are only observed in the yy geometry and are absent in the xx geometry, verifying the excellent detwinning

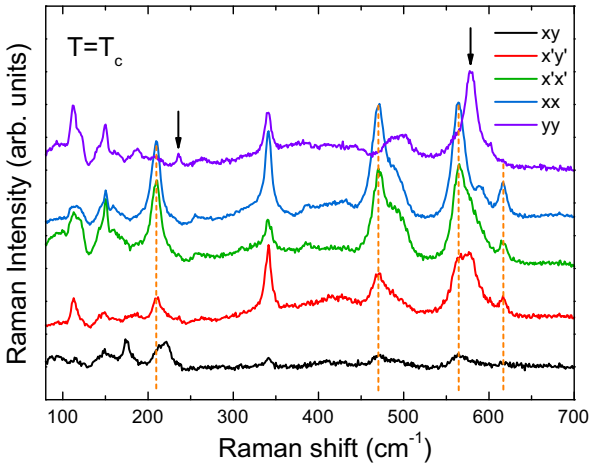

Figure 4.4: Normalized Raman spectra of a detwinned $YBa_2Cu_3O_{6.75}$ single crystal recorded at T_c in the xy, $x'y'$, $x'x'$, xx and yy polarization geometries. The spectra are vertically shifted for clarity. The positions of the new modes are marked by the dashed orange lines, whereas the two black arrows point on the broken chain related modes.

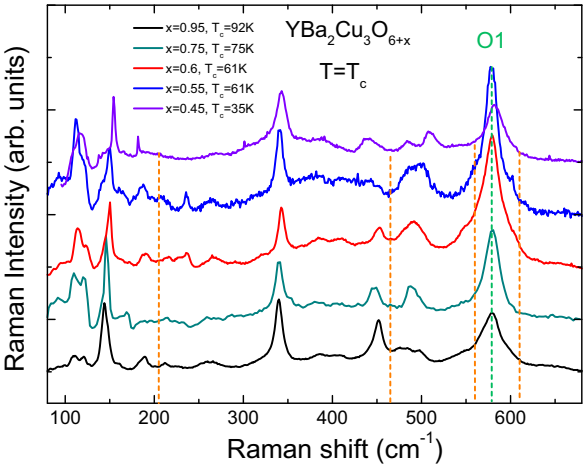

Figure 4.5: Doping dependence of the yy Raman spectra of $YBa_2Cu_3O_{6+x}$ for x=0.95, 0.75, 0.6, 0.55 and 0.45 taken with a He^+/Ne^+ laser line (λ=632.8 nm) at T=T_c. The orange dashed lines indicate the positions were the new phonons appear in the xx scattering geometry and the green line marks the position of the O1 defect mode. The spectra of different doping levels are vertically shifted for clarity.

quality of our samples.

The doping dependence of the yy Raman spectra at T_c is shown in Fig. 4.5. The O1 mode is visible in the yy geometry at all doping levels (green dashed line), including the optimally doped sample for which the new Raman features (orange dashed lines) have not been observed. Therefore a chain-related origin of the newly observed phonons appears improbable. Moreover, the chain modes are visible already at room temperature, contrary to the new Raman modes which appear at lower temperatures, as will be discussed in detail later on.

In order to investigate a potential assignment of the new features to phonons already observed in the out-of-plane scattering geometry, we have also recorded Raman spectra with the light polarization in the *ac* plane. The collected spectra for $YBa_2Cu_3O_{6.55}$ at room temperature and at T_c are plotted on Fig. 4.6. Our data are in good agreement with previous reports [268, 278, 329] and in contrast to the data taken with in-plane polarization geometries, no new features are observed at T_c in the xz and zz geometries, even though the latter also probes the A_g symmetry modes. In the xz spectra, which according to the selection rules probe the B_{2g} symmetry modes, a mode observed at 203 cm^{-1} is in close proximity to the new mode observed at low temperatures at 205 cm^{-1}. The 203 cm^{-1} phonon according to previous reports has been attributed to planar vibrations of the apical O4 atoms. This B_{2g} O4 phonon however is visible already at

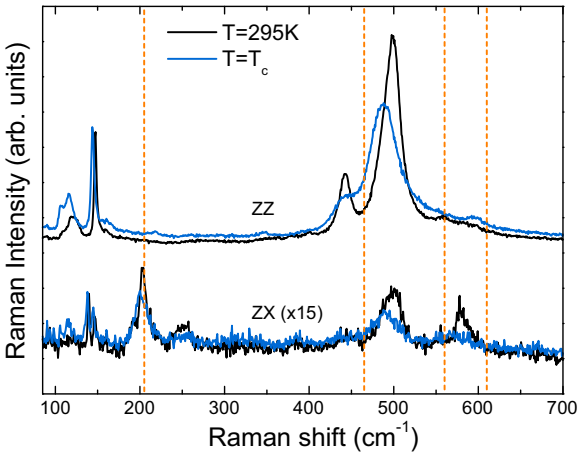

Figure 4.6: Raman spectra of $YBa_2Cu_3O_{6.55}$ in the xz and zz scattering geometries taken with a He^+/Ne^+ laser line (λ=632.8 nm) at room temperature and at T=T_c. The intensity of the xz spectra has been multiplied by 15. The orange dashed lines indicate the positions were the new phonons appear in the xx scattering geometry. The spectra of different doping levels are vertically shifted for clarity.

the room temperature Raman spectrum, unlike the newly observed mode at 205 cm^{-1}. Additionally, none of the other new modes seen in the xx geometry at 465, 560, and 610 cm^{-1} appear in the xz spectra, suggesting a coincidental energy proximity of the two phonons. All together our polarization dependent measurements reveal a very anisotropic A_g Raman tensor associated with the new modes.

4.1.5 Resonance effects

The Raman spectra presented on the previous figures were all recorded using the λ=632.8 nm line of a He^+/Ne^+ laser. After determining the symmetry of the new modes, we looked into resonance effects, i.e. the dependence of the intensity of the new modes on the excitation energy. Resonance effects not only allow for the investigation of otherwise weak Raman signals, but also provide useful information for the intermediate states involved in the scattering process and have been for this purpose widely used for the study of excitations in high-T_c cuprates [273, 330].

In Fig. 4.7 are plotted the xx Raman spectra of $YBa_2Cu_3O_{6.75}$ recorded at T_c using three different excitation energies: 1.96, 2.33 and 2.54 eV. As already shown in previous figures, using the red line of a He^+/Ne^+ laser (1.96 eV), the new modes have at T_c a comparable intensity to the strongest A_g modes of the *ortho*-I structure. Using green

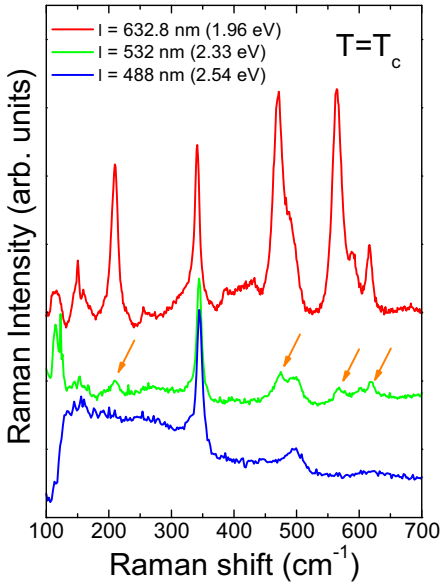

Figure 4.7: Raman spectra of $YBa_2Cu_3O_{6.75}$ at T_c in the xx geometry taken with red (λ=632.8 nm), green (λ=514.5/532 nm) and blue (λ=488 nm) incident laser lights. The orange arrows indicate the new phonon modes. For clarity, the intensities of the spectra have been normalized to the one of the buckling phonon.

laser light (2.33 eV) the new modes are still clearly visible, as indicated by the orange arrows in Fig. 4.7, but they are much lower in intensity compared to the rest of the A_g phonons. Finally, using the blue laser light as an excitation the new modes disappear completely.

This resonance effect with the red laser light does not follow the reported behavior neither of the A_g modes of the *ortho*-I structure, nor of the defect modes of the broken Cu-O chains which exhibit a maximum intensity for green and yellow incident laser light respectively [273, 275, 330]. This observation further supports the scenario of a different physical origin of the new modes.

Surprising as it may be, this resonance behavior might account for the fact that the new modes have not been reported in previous Raman studies, since most of them have been performed using green laser light as an excitation. However, it should be mentioned that some of the new modes are actually present in the reported Raman spectra of at least two previous studies: the 205, 560 and 610 cm^{-1} modes are visible in the *ortho*-II Raman data of Iliev *et al.* [278] taken in the xx geometry with the green laser light, while the 205 and 465 cm^{-1} modes are visible in the data of Panfilov *et al.* [273] taken in an underdoped sample (T_c=70 K) with the λ=647.1 nm line of a Kr^+ laser.

4.1.6 Temperature Dependence

In Fig. 4.8 are plotted the colormaps of the temperature dependence of the xx Raman intensity for all the studied doping levels, together with the corresponding Raman spectra at selected temperatures. For optimally doped $YBa_2Cu_3O_{6.99}$ the opening of the superconducting gap in the electronic density of states leads to a redistribution of the low energy electronic continuum below T_c, most clearly demonstrated on the lower left panel of Fig. 4.8. Moreover, pronounced renormalizations of the energies and linewidths of the phonon modes that are most strongly coupled to the electronic continuum, e.g. the buckling phonon mode O2-O3 at ~340 cm^{-1}, take place upon cooling below T_c, in accordance with previous Raman studies. In the Raman spectra of the underdoped samples, the superconductivity-induced phonon renormalizations are also present though reduced in amplitude. The phonon renormalization effects seen in our data will be described in detail later on.

The most prominent effect shown in the intensity maps of Fig. 4.8 is that the new phonon modes appear for all underdoped samples in the normal state, well above their respective T_c. This is more clear for the cases of $YBa_2Cu_3O_{6.75}$, $YBa_2Cu_3O_{6.6}$ and $YBa_2Cu_3O_{6.55}$ for which the new modes present the highest intensity and less clear for the case of $YBa_2Cu_3O_{6.45}$ for which the new modes are weaker.

The effect is best illustrated in Fig. 4.9 in which the integrated intensities of the modes appearing at 205, 560, and 610 cm^{-1} are plotted as a function of temperature. The intensity of the new phonon at 465 cm^{-1} is not included in this plot, since a possible contribution of the neighboring O2+O3 and/or O4 Raman modes in its intensity

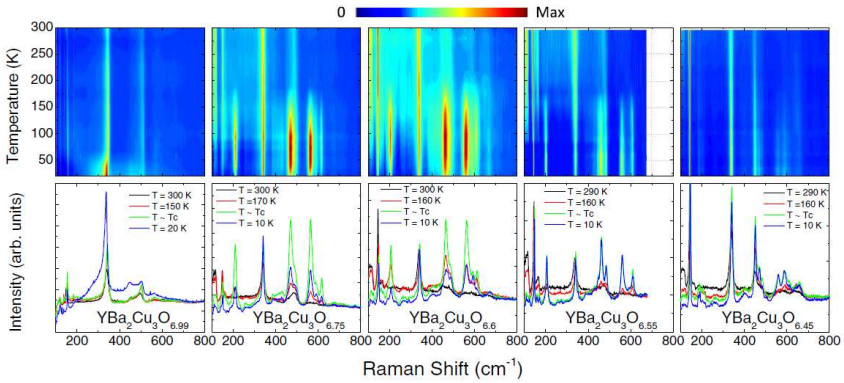

Figure 4.8: Upper panel: Colormap representation of the temperature dependence of the xx Raman intensity measured with λ=632.8 nm for optimally doped $YBa_2Cu_3O_{6.99}$, and underdoped $YBa_2Cu_3O_{6.75}$, $YBa_2Cu_3O_{6.6}$, $YBa_2Cu_3O_{6.55}$, and $YBa_2Cu_3O_{6.45}$. Lower panel: Corresponding Raman spectra recorded at selected temperatures.

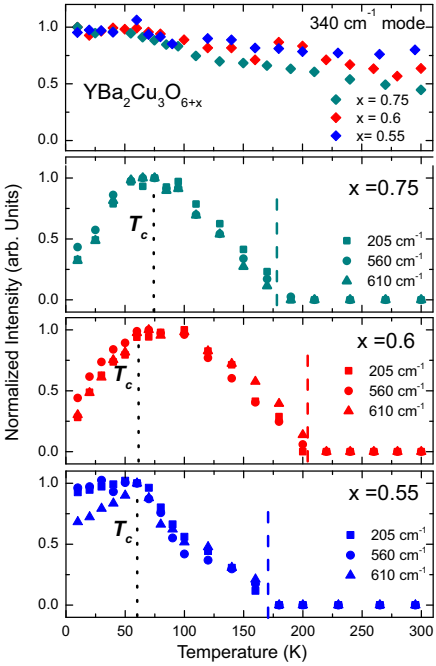

Figure 4.9: Temperature dependence of the integrated intensity of the buckling mode at 340 cm^{-1} (upper panel) and the new phonon modes at 205, 560, and 610 cm^{-1} (lower panels) in $YBa_2Cu_3O_{6.75}$ (green symbols), $YBa_2Cu_3O_{6.6}$ (red symbols), and $YBa_2Cu_3O_{6.55}$ (blue symbols). The black vertical lines denote the respective T_c, whereas the colored dashed lines indicate the onset temperature of the new modes for the different doping levels studied here.

cannot be excluded. In the same plot is included as a reference the temperature dependence of the intensity for the buckling phonon mode. The temperature at which the new modes appear does not have a monotonic doping dependence: ~175 K for $YBa_2Cu_3O_{6.75}$ and $YBa_2Cu_3O_{6.55}$ and ~200 K for $YBa_2Cu_3O_{6.6}$ (their low intensity in the case of $YBa_2Cu_3O_{6.45}$ does not allow for a definite determination of the onset temperature). In addition, in the cases of the $YBa_2Cu_3O_{6.75}$ and $YBa_2Cu_3O_{6.6}$ compounds the temperature dependence of the intensity appears to be non-monotonic (see Fig. 4.9) [i].

4.1.7 Discussion

Before summarizing the experimental data and addressing the possible origin of the new modes, it is worth commenting on the already mentioned superconductivity-induced renormalizations of the phonon frequencies and linewidths.

[i] Even though for all doping levels the onset temperature of the new Raman modes is undoubtedly significantly higher than the respective T_c (~175-200 K), a certain laser-induced bleaching effect appears to influence the temperature dependence of their intensities. This presumably also leads to the observed difference in the temperature dependence of the $YBa_2Cu_3O_{6.55}$ and the rest of the doping levels (see Fig. 4.9). This requires further experimental studies and will not be discussed further more.

The most well-studied superconductivity-induced phonon renormalization in the cuprates concerns the O2-O3 buckling mode. Fig. 4.10 shows the Raman spectra of $YBa_2Cu_3O_{6.75}$ (T_c=75 K) in the frequency region of the buckling mode, for which a clear softening is observed in the superconducting state. In the same figure is plotted the doping evolution of its frequency and linewidth temperature dependence. While in the normal state the temperature dependence of the phonon energy and linewidth follow the expected hardening and narrowing arising from anharmonic phonon-phonon interactions, in the superconducting state both of these quantities deviate strongly from the expected behavior.

As described earlier, although the finite phonon lifetimes mainly originate from the decay of a phonon into other phonons via the phonon-phonon interaction, the decay of a phonon into electronic excitations through the electron-phonon interaction constitutes an additional contribution. In the superconducting state, the opening of the superconducting gap and the redistribution of the electronic density of states strongly influences the available electronic decay channels and therefore the phonon lifetime. The superconductivity-induced renormalization of the phonon self-energy was theoretically investigated by Zeyher and Zwicknagl for an *s*-wave gap and was later on expanded for the *d*-wave case by Nicol *et al.* [255, 256]. The frequency and linewidth changes are related to changes in the real and the imaginary part of the phonon self-energy respectively and are given by [255, 256, 327]:

$$\begin{aligned} \frac{\Delta\omega}{\omega_0} &= \frac{1}{N}\lambda_{e-ph} Re\Pi(\omega_0) \\ \frac{\Delta\Gamma}{\Gamma_0} &= \frac{1}{N}\lambda_{e-ph} Im\Pi(\omega_0) \end{aligned} \tag{4.1}$$

where N is the the electronic density of states at the Fermi level, λ_{e-ph} is the electron-phonon coupling constant and ReΠ/ImΠ is the real/imaginary part of the phonon self-energy. In a qualitative description, phonons with energies lower than the superconducting gap energy do not contribute to pair breaking and cannot decay through the electron-phonon interaction, resulting in longer lifetimes and therefore in the narrowing and softening of the phonon. Contrary to that, phonons with energies higher than the superconducting gap have a higher decay probability due to the increased density of electronic states above the gap and therefore their lifetime decreases and the phonons broaden and harden. The most drastic effects are expected for phonon energies close to the energy of the superconducting gap.

The buckling phonon mode at ~340 cm^{-1} mode is for T$\ll T_c$ below the superconducting gap energy and therefore a softening is observed in the superconducting state (Fig. 4.10) in accordance with the calculations of the self-energy effects as well as with previous Raman studies [327, 328, 331]. Starting from the optimally doped $YBa_2Cu_3O_{6.99}$, the observed softening from T_c=90 K to 10 K is ~5 cm^{-1}, whereas a linewidth increase is seen at 75 K. This has been attributed to the fact that with increasing temperature towards T_c the gap energy shifts to lower energies and moves through the energy of the buckling

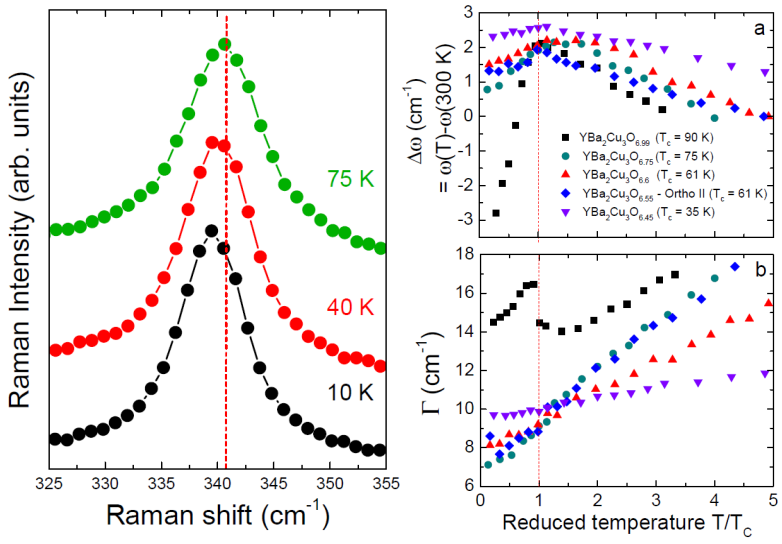

Figure 4.10: (a) xx Raman spectra of $YBa_2Cu_3O_{6.75}$ in the frequency regime of the 340 cm^{-1} buckling phonon mode recorded at 75 K (T_c), 40 K and 10 K with the red (λ=632.8 nm) laser light. The dashed vertical line highlights the phonon softening in the superconducting state. (b,c) Renormalization of the energy and linewidth of the buckling phonon mode through T_c for the different studied doping levels.

mode leading to the an abrupt change of the linewidth [327].

Regarding the doping evolution of the effect, according to Fig. 4.10 as the doping level is decreased the amplitude of the renormalization is strongly reduced. This observation agrees well with previous Raman reports and is the result of the increase of the gap amplitude as doping is decreased, and of the opening of the normal-state pseudogap that suppresses the electronic density of states at the Fermi level. Moreover, the asymmetric lineshape of the buckling phonon mode becomes more and more symmetric as doping is reduced, indicating a decrease of the electron-phonon coupling in line with the observed suppression of the renormalization amplitude.

Similar renormalization effects are also observed for other *ortho*-I modes, e.g. the in phase O2+O3 and the O4 phonon modes at ~450 cm^{-1} and ~500 cm^{-1} respectively, in accordance with previous Raman studies. It is worth commenting that the the onset temperature for the superconductivity-induced renormalizations is found for all studied samples at T_c, confirming that the laser heating on the sample surface was not higher than

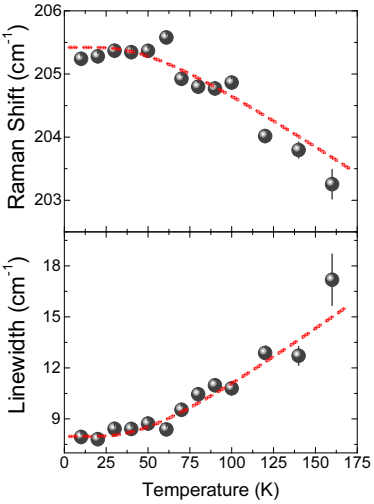

Figure 4.11: Temperature dependence of the frequency and the linewidth of the newly observed mode at 205 cm^{-1} in $YBa_2Cu_3O_{6.55}$. No renormalization is observed upon cooling below T_c.

~5 K.

Unlike the cases of these strongly coupled *ortho*-I modes, the frequencies and linewidths of the newly observed modes do not display any significant renormalization upon cooling below T_c, as shown in Fig. 4.11 for the 250 cm^{-1} mode of $YBa_2Cu_3O_{6.55}$. The modes harden and narrow slightly upon cooling, as expected from the anharmonic decay.

Summarizing the experimental observations, new Raman active phonon modes of A_g symmetry are detected in underdoped $YBa_2Cu_3O_{6+x}$ samples at temperatures well above T_c. The new modes are not detected for optimal doping (x=0.99) and are very weak for the most underdoped sample (x=0.45). They exhibit a strong resonance with the red laser light, unlike the A_g symmetry modes of the *ortho*-I structure, which are resonant with the green laser light, and the chain-related defect modes which have the maximum intensity with the yellow light. The red resonance together with the doping, temperature and polarization dependence rule out a possible chain-related origin of the new features. This is further corroborated by the doping independence of their positions which is incompatible with the structure dependent chain features and suggests that the new modes derive from the same physical origin. The onset temperature of the new modes is ~200 K (doping dependent), whereas their intensity increases upon cooling until T_c and decreases in the superconducting state.

Since the number of the Γ-point Raman active phonon modes is determined by the lattice symmetry (as analyzed in a previous chapter) any possible origin of the new modes would be associated with a symmetry lowering. In this framework, the new modes could be the result of a degeneracy lift or of the breaking of translational or inversion symmetry

which would change the Raman/infrared selection rules (as in the case of the chain-related defect modes). Both scenarios appear highly unlikely in this case since on one hand the new modes are non-degenerate A_g symmetry modes and on the other hand their energies do not match the ones of any of the known infrared active phonon modes.

An alternative scenario explaining the appearance of new Raman active phonon modes at the Γ-point includes the folding of the phonon dispersion, as would happen in the occasion of an increase of the initial unit cell. In view of the recently discovered CDW fluctuations in underdoped $YBa_2Cu_3O_{6+x}$, this provides a natural explanation for our observations: the original $YBa_2Cu_3O_{6+x}$ phonon dispersion would backfold in the new Brillouin zone of the CDW state, bringing new optical modes at the Γ point and rendering them observable in the Raman spectra. Similar CDW-related phonon modes have been extensively reported for the case of "classic" CDW systems, like the transition metal dichalcogenides [332].

The temperature and doping dependence of the new Raman modes is strongly reminiscent of the CDW, strengthening further the connection between the two. Regarding firstly the doping dependence, the CDW state has been observed for underdoped samples and has not been detected for samples of optimal doping, in agreement with what was found for the new phonons. Secondly, the CDW signal appears well above T_c, as is also the case

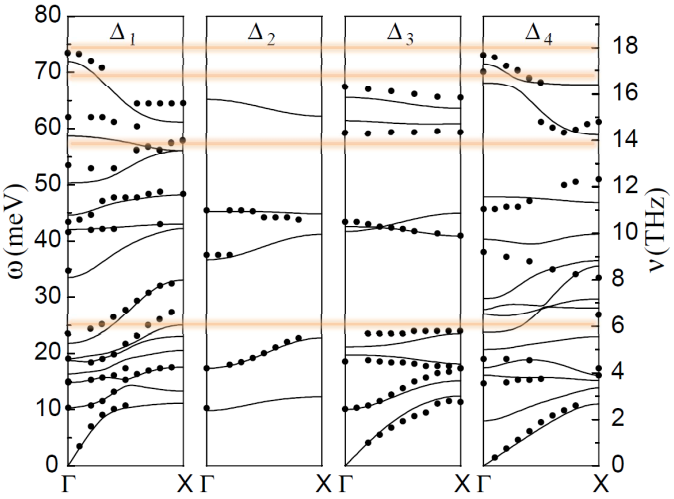

Figure 4.12: Phonon dispersions for $YBa_2Cu_3O_7$ along the [100] direction (the modes are classified according to symmetry). The black lines represent theoretical results, while the dots are neutron scattering experimental data from reference [270] and references therein. The horizontal orange lines mark the positions of the new Raman modes.

for the new Raman phonons. Additionally, the incommensurability of the CDW is found to be only slightly doping dependent decreasing from $\delta \sim 0.32$ to 0.3 upon doping from x = 0.55 to x = 0.75, in line with the doping independence of the positions of the new phonons.

In the case of a commensurate CDW ordering, the new modes can be easily assigned based on group symmetry considerations: the phonon dispersion folding in the new CDW Brillouin zone would bring the zone-boundary phonons of the original phase to the zone center of the CDW ordered phase. In the incommensurate case of underdoped $YBa_2Cu_3O_{6+x}$, assigning the CDW-related phonons is a non-trivial task which is further perplexed by the complicated structure factor revealed by x-ray diffuse scattering measurements [319]. Moreover, already the phonon dispersion of the high-temperature phase is not fully known due to the complexities introduced by the oxygen superstructures. Attempting an assignment of the new phonons to atomic displacement patterns is possible only on the basis of the reported phonon dispersion of fully oxygenated $YBa_2Cu_3O_7$, like the one plotted in Fig. 4.12 for the [100] direction (the positions of the new Raman modes are indicated by the horizontal orange lines) [270]. The modes at 560 cm^{-1} and 610 cm^{-1} could originate from branches of the in-plane vibrations of the plane oxygen atoms, while the one at 465 cm^{-1} could originate from the backfolding of the O2+O3 Raman active mode. The new mode at 205 cm^{-1} is located in a dense phononic region impeding a possible assignment.

The new phonons clearly offer a new complementary sensitive tool for the detailed study of the CDW state. The presence of the new Raman modes serves as a signature of the charge ordered state. The schematic phase diagram of the $YBa_2Cu_3O_{6+x}$ family is given in Fig. 4.13, in which are included the CDW onset temperatures as derived from the new Raman modes. Determining the charge ordering temperature based on the appearance of the CDW modes in the Raman spectra is more straightforward than based on the weak x-ray CDW signal. As shown in Fig. 4.13 the onset temperatures derived from the Raman signal are always significantly higher than the ones of the x-rays signal. This is probably related to the frequencies of the two different probes. On one hand, recent high resolution hard x-ray experiments have set an upper limit of ~100 μeV to the intrinsic energy width of the quasi-elastic CDW signal, corresponding therefore to slow (~13 ps) quasi-static fluctuations of the CDW [319, 320]. On the other hand, phonons are higher frequency probes (~0.1 ps) of the charge dynamics and are therefore able to detect faster fluctuations. The observation of the new modes up to temperatures as high as ~220 K (in the case of $YBa_2Cu_3O_{6.6}$) could thus be regarded as a result of the survival of fast CDW fluctuations up to this temperature.

What is also clear from the phase diagram is that the onset temperature of the CDW, derived either from x-ray or from Raman measurements, is considerably lower and does not follow the same monotonic doping dependence as the temperature where the pseudogap appears [ii]. It is therefore clear that the CDW state should not be identified with the pseudogap phase, but might be better described as an instability in the within the

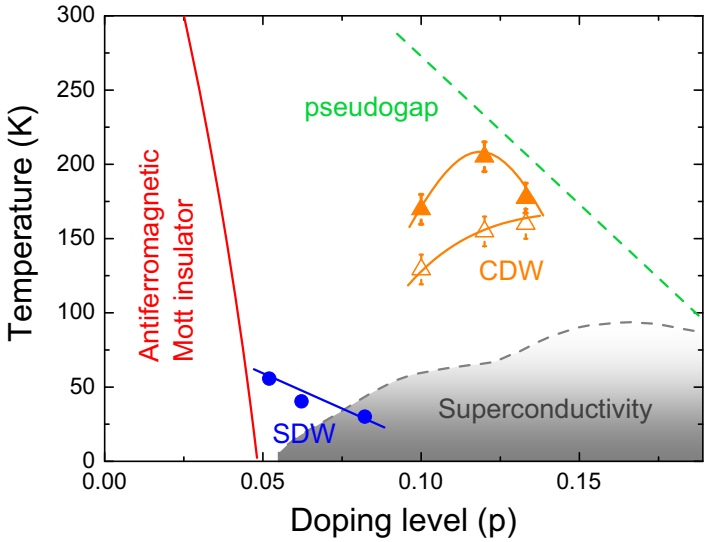

Figure 4.13: Schematic phase diagram of the $YBa_2Cu_3O_{6+x}$ family. The full orange triangles correspond to the appearance temperature of the new CDW modes at the Raman spectra, whereas the open orange triangles correspond to the onset temperature of the CDW peak seen in soft x-ray scattering measurements [1, 102, 104]. The blue symbols correspond to the onset temperature of static incommensurate magnetic order as detected by neutron scattering measurements [47].

pseudogap state.

Finally, it should be noted that for $YBa_2Cu_3O_{6.45}$, the most underdoped sample studied here, while no CDW fluctuations have been observed using x-rays scattering, the new Raman modes at 205 cm^{-1} and 560 cm^{-1} are visible though substantially weakened in intensity compared to the higher doping levels [iii]. In the same doping level, low temperature neutron scattering and NMR measurements have detected quasistatic incommensurate magnetism, confirming the competition between the charge and spin modulations, as also demonstrated through x-rays scattering for the case of magnetically doped $YBa_2Cu_3O_{6.6}$ [104].

[ii] As already mentioned, there is no experimental consensus in the literature regarding the exact temperature T^* below which the pseudogap appears. Deviations up to ~100 K exist at some doping levels between results obtained with different experimental techniques. In references [84, 333] the pseudogap temperatures are grouped in two categories and more details are given.

[iii] Very recently and during writing the current thesis, more detailed x-ray scattering studies of the doping dependence of the CDW have been reported. According to these, x-ray signatures of the CDW formation are also seen in the case of $YBa_2Cu_3O_{6.45}$, albeit very weakened [334, 335].

4.2 High Pressure Results

4.2.1 Introduction

The observation of the CDW-related features in the Raman spectra offers a valuable tool for the systematic study of the newly observed CDW phase and a complementary route to investigate the charge ordering through its effect on the lattice dynamics. Moreover, owing to the versatility of the technique, it is possible using Raman spectroscopy to expand the investigations of the charge ordered state under extreme conditions, e.g. high pressure conditions or high magnetic field conditions, which are typically more complicated to combine with x-rays measurements.

Up to date there has been no x-rays study of the effect of pressure on the CDW phase. This is not surprising taking into account the geometric limitations imposed by the use of the diamond anvil cell (DAC) together with the very weak CDW x-rays signal which is expected to be further weakened through the DAC. X-rays scattering measurements have established the competition between the CDW and the superconducting state through the the doping and magnetic field dependencies [1, 2, 103, 104], but there is no information on its pressure dependence. Considering pressure application purely as an effective carrier doping of the system then a similar competitive trend would be expected: in systems for which superconductivity is enhanced/supressed under high pressures, the CDW would be expected to be respectively supressed/enhanced. One should not however neglect the intrinsic pressure effect and the non-trivial pressure-induced structural distortion which could orient the effect into a different direction.

Aiming to shed more light in this unresolved issue and armed with the new Raman tool, we performed a high pressure Raman investigation on the low temperature lattice dynamics of *ortho*-II $YBa_2Cu_3O_{6.55}$. The choice of this member of the family with this particular doping level and oxygen superstructure was imposed by two requirements. Firstly, as already mentioned, chain oxygen atoms in oxygen deficient $YBa_2Cu_3O_{6+x}$ are known to reorder under high pressure application, resulting in oxygen superstructures different than the original ones. This undesired effect could be minimized either by performing the whole experiment at very low temperatures in order to reduce the oxygen diffusion or by working on highly ordered samples, ideally stoichiometric, with full Cu-O chains. The second requirement is appointed by the temperature and doping range over which the CDW state is observed by x-rays scattering: below ~200 K and for $0.09 \leq p \leq 0.13$, or equivalently $0.5 \leq x \leq 0.75$ [1]. It is therefore impossible to study the pressure effect on the CDW working entirely at very low temperatures or working at fully oxygenated $YBa_2Cu_3O_7$. The best candidate sample exhibiting high oxygen ordering and being close to the CDW instability is the highly ordered *ortho*-II $YBa_2Cu_3O_{6.55}$, in which empty and full Cu-O chains alternate along the *a*-axis with a ~100 Å correlation length.

4.2.2 Experimental Details

The Raman experiments were performed on the same high-quality detwinned $YBa_2Cu_3O_{6.55}$ single crystals which were also used for the ambient pressure measurements. The initial crystals had rectangular shapes with dimensions 3x3x1 mm^3, which are far too big for the sample size requirements of a DAC. Therefore the samples have been thinned down to ~40 μm using polishing papers of gradually reduced roughness and then cut into smaller pieces with typical surface dimensions 80x80 μm^2. The crystal orientation of the individual pieces was subsequently determined using the Raman selection rules.

For the room temperature Raman measurements under pressure a mixture of methanol-ethanol was used as pressure transmitting medium whereas for the Raman measurements at high pressure and low temperature conditions helium was employed as a pressure transmitting medium. It is worth to note that for the low temperature measurements the pressure was always increased at temperatures above the helium melting line and then the DAC was slowly cooled to low temperatures. This is because changing the pressure when the medium is in the liquid state reduces the shear stresses acting on the sample (this holds for helium for pressures up to ~12GPa when helium is in the liquid state at room temperature).

Information on the high pressure Raman scattering experiments presented here has been described in chapter 3. A technical comment regarding the polarized Raman measurements should be included. While for the ambient pressure measurements the desired incident and scattered light polarization can be easily selected though the appropriate rotation of the sample (inside or outside the cryostat), for the high pressure measurements the random orientation of the sample inside the DAC requires the rotation of the entire DAC . This is possible for the measurements at room temperature during which the DAC can be easily rotated under the microscope objective. The alternative solution is to rotate the incident light polarization and select the scattered light polarization through the use of optical polarizers and analyzers, although this leads a to substantial reduction of the measured signal. This method was used for the low temperature measurements for which the entire DAC could not be rotated due to the fixed vertical position of the helium bath cryostat. The above technical difficulties in combination with the slight polarization rotation induced upon light propagation through the diamonds, results in small polarization leaks in the polarized high pressure Raman spectra.

4.2.3 Room temperature measurements

Prior to the low temperature Raman measurements which are relevant for the study of the CDW state, room temperature measurements were performed under high pressure conditions in order to get a first impression on the effect of pressure on the system and to detect potential pressure-induced drastic changes, e.g. structural transitions. In Fig. 4.14 are plotted the room temperature Raman spectra of $YBa_2Cu_3O_{6.55}$ in the xx and yy scattering geometries at selected pressures upon pressure increase. All of the expected A_g symmetry

phonons of the *ortho*-I structure are clearly observed and labeled accordingly, whereas the weak superstructure related phonons of the *ortho*-II structure are hardly visible, with the exception of the mode assigned to Y vibrations along the *a*-axis. The sharp peaks which are present at low frequencies up to ~100 cm^{-1} are due to laser scattering from air in the optical path.

Until 10 GPa no remarkable changes are observed in the Raman spectra upon pressure increase, besides the expected hardening of the phonon frequencies and small changes in their relative intensities. Above 10 GPa though, the intensity of the defect broken chain Cu_{chain} mode, appearing at ambient conditions at ~230 cm^{-1}, is strongly enhanced upon pressure increase. At ambient conditions the defect mode is absent in the xx scattering geometry confirming the excellent detwinning quality of our sample (black spectrum, left panel in Fig. 4.14). Nevertheless, its enhanced intensity above 10 GPa in combination with the small polarization leak under high pressure results in the observation of the mode also in the xx geometry as a small feature much weaker in intensity compared to the yy geometry (indicated by the black arrow).

The large intensity increase of the Cu_{chain} mode could be connected with the occurrence of a pressure-induced structural distortion of the system, presumably related to the Cu-O

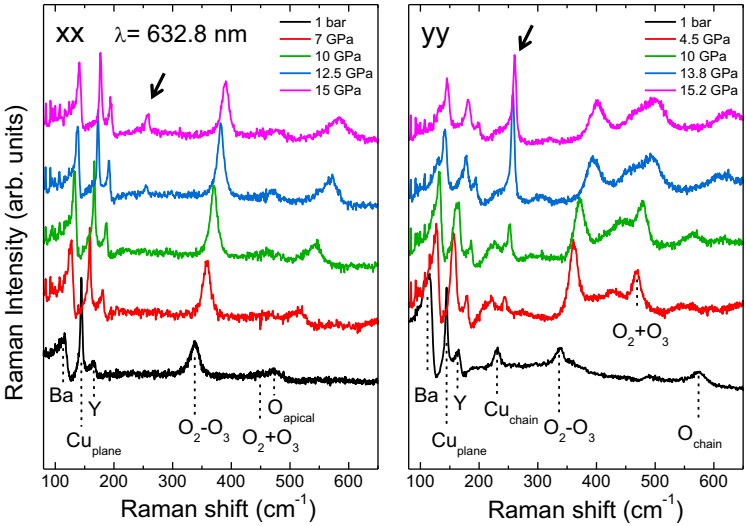

Figure 4.14: High pressure Raman spectra of detwinned $YBa_2Cu_3O_{6.55}$ in the xx (left) and yy (right) geometry taken with a He^+/Ne^+ laser line (λ=632.8 nm) at room temperature. The phonons are assigned according to the analysis presented in chapter 2. The black arrows indicate the broken chain Cu_{chain} mode. The spectra taken at different pressures have been vertically shifted.

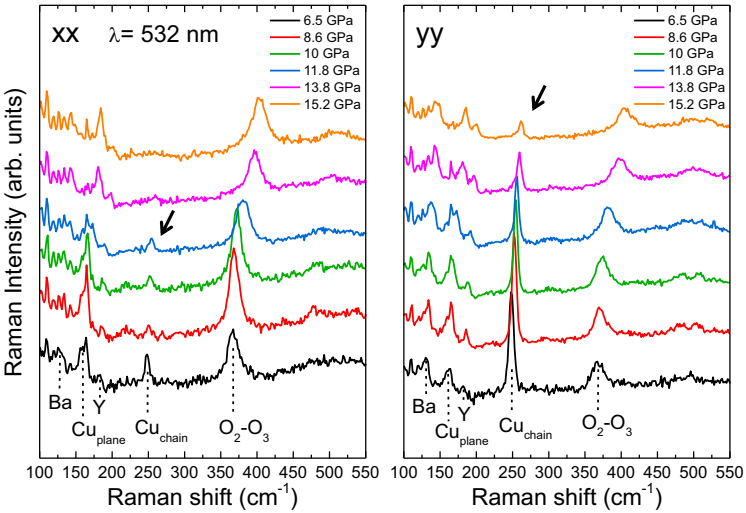

Figure 4.15: High pressure Raman spectra of detwinned $YBa_2Cu_3O_{6.55}$ in the xx (left) and yy (right) geometry taken with the λ=532 nm light of a Nd:YAG laser at room temperature. The phonons are assigned according to the analysis presented in chapter 2. The black arrows indicate the broken chain Cu_{chain} mode. The spectra taken at different pressures have been vertically shifted.

chains. A similar intensity increase for the same chain mode has also been observed in the high pressure Raman spectra of $YBa_2Cu_3O_{6.45}$ (not shown here). In order to further investigate the effect, we looked in the high pressure Raman spectra using a different laser light, namely the 532 nm light of a Nd:YAG laser. The recorded Raman spectra are plotted in Fig. 4.15 for the xx and yy scattering geometries. Again due to a small polarization leak, the defect chain mode is observed under pressure at both polarization geometries, albeit much weaker in the xx configuration. Comparing Fig. 4.14 to Fig. 4.15 it is clear that at low pressures the relative intensity of the Cu_{chain} defect mode is significantly higher using the green light instead of the red light. Interestingly, as pressure is further increased the relative intensity of the mode of interest continuously decreases up to the highest pressure (15.2 GPa), in contrast to the behavior observed with the red light.

The effect is illustrated in Fig. 4.16 where the pressure dependence of the normalized intensity ratio of the Cu_{chain} defect mode to the one of the buckling mode is plotted for the two different excitation energies. The strong dependence of the intensity evolution on the energy of the incident laser light strongly suggests that this is not a structural effect but rather an electronic effect related to the resonance conditions of the defect chain modes.

Strong resonance effects have been widely reported for the defect phonon modes [273, 275]. The resonance profile of the 230 cm^{-1} mode (taken from reference [275]) is plot-

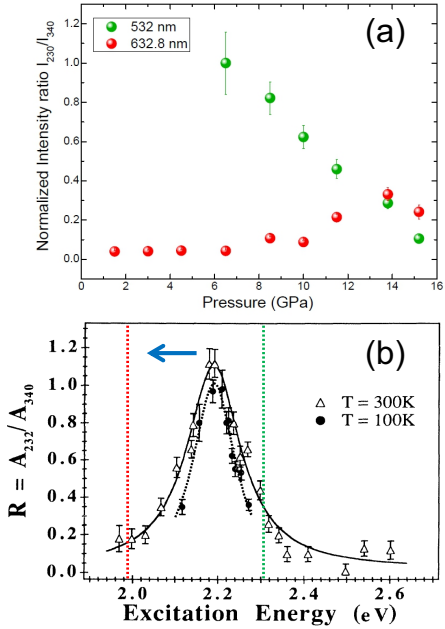

Figure 4.16: (a) Pressure dependence of the normalized intensity ratio of the Cu_{chain} defect mode and the buckling phonon mode using the red (632.8 nm) and the green (532 nm) laser lights. Each point is the ratio of the integrated area under the 232 cm^{-1} peak to that under the buckling phonon peak. (b) Resonance profile of the 230 cm^{-1} phonon at 300 and 100 K [275]. The green and red dashed lines mark the energies of the incident green and red laser lights respectively used in our measurements. The blue arrow indicates the pressure-induced shift of the resonance profile (see main text for details).

ted in the low panel of Fig. 4.16, according to which the intensity of the defect mode is maximized at ~2.2 eV, therefore when using the yellow laser light (568.2 nm). The resonance profile is quite sharp with a width of ~0.2 eV, inferring the existence of a narrow electronic band of a comparable width [273]. The polarization dependence, clearly mirrored in our ambient pressure data and also well reported in the literature, in combination with the dependence of the resonance on the doping level [273, 275, 336] imply that the involved electronic band is related to the Cu-O chains.

The vertical dashed red and green lines in Fig. 4.16 mark the energies of the used red and green laser lights respectively. The pronounced intensity changes upon pressure application in correlation with the strong resonance behavior are suggestive of a pressure-induced red-shift of the resonance profile, as indicated by the blue arrow. This would imply a corresponding shift of the involved electronic band towards lower energies as a result of the pressure-induced changes in the atomic parameters.

It is worth mentioning that all of the presented high pressure effects appear reversible upon pressure decrease. The downstroke measurements show that the Raman modes return to their original positions, the initial intensity of the chain defect mode is re-established and the original Raman spectrum is recovered upon pressure release.

4.2.4 Low temperature measurements

In Fig. 4.17 are plotted the low temperature xx Raman spectra of detwinned $YBa_2Cu_3O_{6.55}$ single crystals recorded at a constant pressure of 2 GPa with the 648 nm laser light. The vertical dashed lines mark the positions where the CDW-related features appear at ambient pressure conditions. According to the experimental data of Fig. 4.17, no CDW related features similar to the ones of the 1 bar data are observed upon cooling at 2 GPa. It is worth emphasizing that the crystals used for the high pressure experiments were the same as the ones used for the ambient pressure measurements for which the CDW related modes were clearly observed.

While the CDW-related modes are absent at 2 GPa, new features appear in the low temperature Raman spectra at ~189, 215, 413 and 652 cm^{-1}, as indicated by the red arrows in Fig. 4.17. Some of these new features (e.g. the one at 215 cm^{-1}) are present already at room temperature (with much lower intensity), rendering thus unlikely a possible connection with the charge ordering. While the features at 189 and 215 cm^{-1} are relatively sharp, the one at ~413 cm^{-1} and especially the one at ~652 cm^{-1} are particularly broad, suggesting that they do not originate from a one-phonon scattering mechanism.

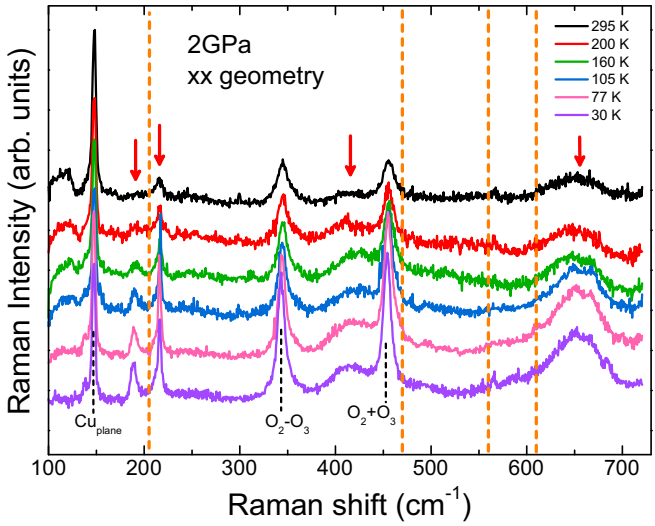

Figure 4.17: Low temperature Raman spectra of detwinned $YBa_2Cu_3O_{6.55}$ at 2 GPa in the xx scattering geometry taken with the red light of a Krypton laser (λ=648 nm). The phonons of the *ortho*-I structure are labeled according to the analysis of the previous chapter. The orange lines mark the positions of the CDW related modes at ambient conditions. The red arrows indicate new features growing at low temperatures. The spectra taken at different temperatures have been vertically shifted.

Whereas in the xx scattering geometry new modes are clearly not expected, even if a polarization leak is taken into account the origin of the new features still cannot be unambiguously determined. Concentrating on the two sharp features at 189 and 215 cm^{-1} and considering the known infrared and Raman active phonons, the mode at 189 cm^{-1} appears close in energy to the B_{1u} symmetry IR active phonon mode corresponding to Y/Cu2 vibrations along the *c*-axis, while the one at 215 cm^{-1} is close in energy to the B_{2g} symmetry vibrations of the apical oxygen O4, shown also in the zx Raman spectra of Fig. 4.6 [270, 337]. Despite the proximity in energy, both the B_{1u} and B_{2g} symmetry modes are by symmetry not expected in the polarization configuration of the shown measurements. Moreover, even if their presence is justified by a symmetry breaking or by a polarization leak, their intensity is expected to be much weaker than the *ortho*-I A_g symmetry modes, e.g the buckling mode, which is clearly not the case for the data of Fig. 4.17. The same holds also for a potential connection of the new features with modes originating from the formed oxygen superstructures of the Cu-O chains.

The origin of these features was further investigated by Raman measurements at higher pressures. The pressure dependence of the Raman spectra at 20 K is shown in Fig. 4.18. Both the known *ortho*-I phonon modes as well as the new features move towards higher

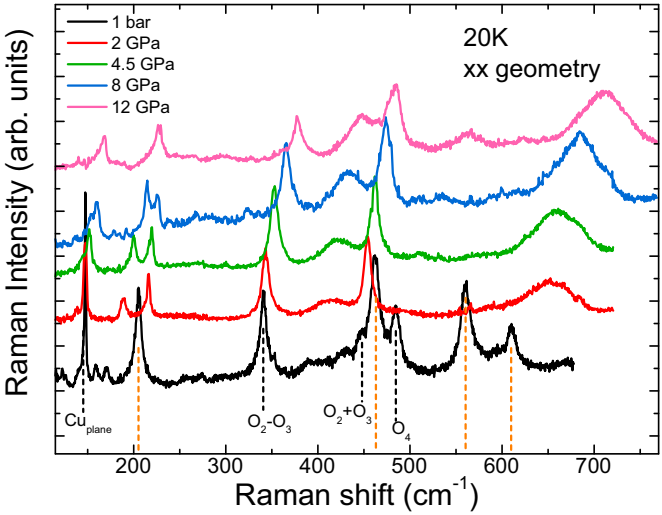

Figure 4.18: Pressure dependence of the Raman spectra of $YBa_2Cu_3O_{6.55}$ at 20K in the xx scattering geometry taken with the red light of a Krypton laser (λ=648 nm). The phonons of the *ortho*-I structure are labeled according to the analysis presented in chapter 2. The orange lines mark the positions of the CDW related modes at ambient conditions. The spectra taken at different pressures have been vertically shifted for clarity.

frequencies upon pressure increase. The new features are present up to the highest pressure measured here, 12 GPa, and moreover the intensity of the broad features at 413 and 652 cm^{-1} increases upon pressure increase. The pressure derivatives of their energies are different so that as pressure increases the 189 cm^{-1} mode approaches the one at 215 cm^{-1} and the two modes overlap at ~227 cm^{-1} at 12 GPa.

4.2.5 Discussion

The main conclusion arising from the presented results is that the CDW related features observed in the ambient pressure Raman data are not present under high pressure conditions. This holds already at the lowest pressure applied in our study (2 GPa) and remains so until the highest applied pressure (12 GPa).

The absence of the CDW modes in the high pressure spectra raises different scenarios regarding the pressure evolution of the CDW order. On one hand, our observations could be attributed to a pressure-induced suppression of the charge ordering, either due to the competition with superconductivity or due to drastic changes in the system, e.g. modulations of the oxygen sublattice. On the other hand, since we are probing the CDW indirectly through the Raman modes, it is possible that the CDW Raman modes are no longer observable under pressure even in the presence of the charge ordering, e.g. due to changes in the resonance conditions.

A pressure-induced suppression of the CDW appears compatible with an effective charge transfer as well as with what is expected from the competing phase scenario. As already mentioned, the numerous high pressure transport data reported in the literature exhibit pronounced discrepancies due to differences in the hydrostatic conditions and to collateral oxygen relaxation effects. Hence it is difficult to make a quantitative description of the pressure-induced charge transfer through the determination of the number of transferred holes per GPa. The situation gets further complicated in view of the doping dependence of the pressure effect, which needs to be taken into account to acquire an accurate value for the *ortho*-II sample measured here. Structural measurements on a $YBa_2Cu_3O_{6.6}$ sample with a T_c=60 K in combination with a valence band sum analysis indicate a charge transfer value of ~0.008 holes/GPa [144]. On the other hand, high pressure Hall coefficient measurements on fully oxygenated $YBa_2Cu_3O_7$ samples suggest that holes are transferred towards the CuO_2 planes at a typical rate of ~9%/GPa, therefore ~0.016 holes/GPa [141]. Taking into account these approximate values and assuming a simple charge transfer model, we then estimate that it is required to apply a pressure of ~2.2-3.5 GPa on the *ortho*-II sample in order to reach the doping level of the $YBa_2Cu_3O_{6.75}$ sample (the sample with the highest doping level for which the CDW peaks were observed). From this rough estimate, it is therefore not unlikely that already a pressure of 2 GPa is enough to effectively dope the sample beyond the doping regime of the CDW phase.

From a different perspective, in contrast to the reported magnetic field effect, pressure application on underdoped $YBa_2Cu_3O_{6+x}$ leads to the increase of the superconducting

transition temperature (see e.g. the susceptibility data under hydrostatic pressure without relaxation effects of reference [5]), enhancing superconductivity and thus suppressing the competing charge density wave. A similar pressure-induced suppression of the charge ordering has been reported for the case of the stripe-ordered $La_{1.875}Ba_{0.125}CuO_4$. In this case diffraction data have shown that upon pressure application the charge-stripe order is gradually suppressed and disappears above ~3.5 GPa while simultaneously T_c is slightly increased [3, 4]).

A different possible explanation for the absence of the CDW related features, which does not necessarily imply the suppression of the CDW, is associated with the observed resonance effects. Using different excitation energies our room temperature measurements have demonstrated that in the case of the defect Cu_{chain} mode pressure induces a gradual red shift of the resonance conditions. In addition to this, the ambient pressure data shown that also the CDW related modes exhibit a pronounced resonance with the 632.8 nm laser light, while they are hardly visible with different excitation energies (e.g the blue laser light). Therefore we can not neglect the possibility that the application of high pressure changes the resonance conditions of the CDW modes rendering them "hidden" for the used 648 nm laser light. Further high pressure Raman data with different excitation energies are needed to provide a definite answer.

A suppression of the CDW could also be the result of a structural change. X-ray measurements have revealed that the charge ordering occurs in the CuO_2 planes. A major pressure-induced distortion of the structure, including the CuO_2 planes appears unlikely since firstly it has not been reported in high pressure diffraction measurements and secondly it is not reflected in the Raman spectrum. Moreover, the pressure dependence of the known A_g phonons frequencies does not exhibit any anomalies which would point towards that direction. The most plausible pressure effect on the structure appears to be a reordering of the oxygen sublattice of the Cu-O chains in line with previous high pressure reports [5, 148, 152, 153]. Such a change would not alter directly the charge ordered CuO_2 planes but would significantly affect their doping level which is sensitively dependent on the Cu-O chains. One way to test a potential pressure-induced change in the oxygen order of the chains would be through the superstructure specific Raman active modes. Unfortunately, as already mentioned and showed in Fig. 4.1 these modes are significantly weaker compared to the other A_g symmetry modes of the *ortho*-I structure. Their low intensity in combination with the signal weakening through the DAC do not allow their observation.

Despite the highly ordered Cu-O chains of our *ortho*-II samples, the reordering possibility cannot be excluded in the presence of oxygen vacancies. The "clean" case of a stoichiometric underdoped cuprate of the same family, namely $YBa_2Cu_4O_8$ will be presented in chapter 5. Since the relaxation effects are specific to the "123" family due to the presence of the Cu-O chains, an alternative way to overcome the oxygen ordering problem would be to study an underdoped cuprate of another structural family without Cu-O chains, e.g. $Bi_2Sr_{2-x}La_xCuO_{6+\delta}$ or $HgBa_2CuO_{4+\delta}$.

Chapter 5

Raman study of $YBa_2Cu_4O_8$

5.1 Ambient Pressure Results

5.1.1 Introduction

Within the various members of the cuprate superconductors family, $YBa_2Cu_4O_8$ holds a special position: it is the only underdoped cuprate of stoichiometric composition. The double chain structure of the compound renders its oxygen content highly robust and enhances its chemical and structural stability, offering a uniquely defect-free system for the study of the underdoped part of the phase diagram.

$YBa_2Cu_4O_8$ has a doping level $p{\sim}0.14$ and is therefore positioned on the verge of the CDW regime of the phase diagram as directly measured by x-rays. X-ray scattering measurements in $YBa_2Cu_4O_8$ have not detected any signal related to charge ordering. Nevertheless, following what was found earlier for highly-ordered underdoped $YBa_2Cu_3O_{6.5}$ [88], quantum oscillation experiments have revealed the existence of small Fermi surface pockets on $YBa_2Cu_4O_8$ [89, 90, 338]. Underdoped $YBa_2Cu_4O_8$ and $YBa_2Cu_3O_{6.5}$ display comparable quantum oscillation frequencies, indicating that under high magnetic fields a similar Fermi surface reconstruction occurs at both compounds, which was suggested to involve a CDW order [85, 91]. The magnitude of the magnetic fields applied for the quantum oscillation experiments is very challenging for an x-ray scattering experiment, especially in view of the weak CDW signal, and no x-ray scattering measurements have been reported for $YBa_2Cu_4O_8$ under high magnetic fields.

The new Raman features seen in underdoped $YBa_2Cu_3O_{6+x}$ and related to the emergence of the CDW state offer a new tool to address this issue. We have used Raman spectroscopy to look for signatures of charge ordering in underdoped $YBa_2Cu_4O_8$ and to compare our results with those of the x-rays measurements. A straightforward reasoning behind this attempt derives from the fact that small but clear Raman signatures of the CDW have been observed in the low temperature spectra of $YBa_2Cu_3O_{6.45}$ before

the direct observation of CDW ordering by x-rays scattering measurements on the same compound [334, 335].

5.1.2 Experimental Details

For the Raman measurements we used high quality untwinned $YBa_2Cu_4O_8$ single crystals grown at ambient air pressure by a flux method described in references [339, 340]. The samples were individually detwinned under uniaxial pressure upon observation through a polarized microscope, as described in a previous chapter [131, 133]. Information on the low temperature Raman scattering experiments presented here has been given in chapter 3.

5.1.3 Low Temperature measurements

In Fig. 5.1 are plotted the low temperature Raman spectra of detwinned $YBa_2Cu_4O_8$ single crystals (T_c= 83 K) in the xx and yy scattering geometries at selected temperatures upon cooling. The recorded Raman spectra are of excellent quality despite the relatively weak Raman signal, and all of the expected A_g symmetry phonon modes are observed and labeled accordingly [281, 283]. Unlike the case of underdoped $YBa_2Cu_3O_{6+x}$ and in line

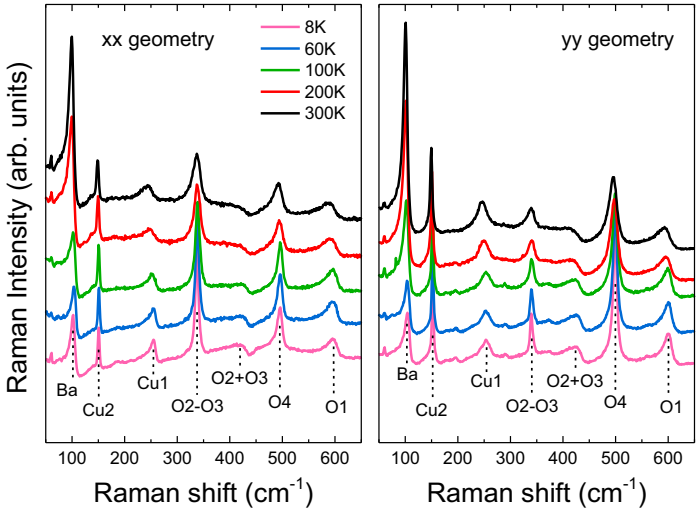

Figure 5.1: Raman spectra of detwinned $YBa_2Cu_4O_8$ single crystals recorded in the xx (left) and yy (right) scattering geometries with a He^+/Ne^+ laser line (λ=632.8 nm) at selected temperatures upon cooling. The observed Raman modes are labeled according to the group symmetry analysis [281].

with the results of x-rays data, no significant changes in the Raman spectra of $YBa_2Cu_4O_8$ are observed upon cooling: we do not observe the appearance of new Raman modes in any scattering geometry and throughout the whole studied temperature range.

Apart from the nonappearance of new Raman features, in our data we observe clear renormalizations of the phonons and the electronic background below the pseudogap and superconducting gap opening temperatures in agreement with previous reports. This is illustrated in the raw data and the fitting results of Fig. 5.2 for the cases of the Ba and O2-O3 phonon modes and will be discussed next.

5.1.4 Discussion

We start the discussion from the absence of CDW Raman features in the low temperature spectra of $YBa_2Cu_4O_8$. As already mentioned earlier, for $YBa_2Cu_4O_8$ unlike its close relative *ortho*-II, no charge ordering associated signal has been detected by x-rays scattering that could account for the results of the quantum oscillations experiments. Even though our Raman results retain this differentiation between the two compounds and support the x-ray scattering result, it should be underlined that a potential CDW state linked to the results of the quantum oscillation measurements would be realized under conditions similar to those of the measurements, therefore under magnetic fields of the range ~45-60 T. A recent neutron scattering study of the vortex lattice suggests that any magnetic field induced charge-density-wave order in $YBa_2Cu_4O_8$ could exist only for fields above 6 T [341]. Therefore the apparent discrepancy between the quantum oscillation and the x-rays data could solely imply that while a zero magnetic field CDW state is realized in $YBa_2Cu_3O_{6.55}$, high magnetic fields are required to induce charge ordering in $YBa_2Cu_4O_8$.

A possible reasoning behind this contrast could be related to the recently suggested formation of CDW nanodomains in underdoped cuprates. The spatially inhomogeneous CDW domain state has been proposed in analogy to the behavior of materials undergoing structural phase transitions in the fluctuation regime above the transition temperature (see reference [319] and references therein). In that case, an elastic peak appears at temperatures higher than the transition temperature and is understood as a defect-induced nucleation of finite-size domains of the low-temperature phase.

In underdoped cuprates, a detailed analysis of high-resolution inelastic x-rays scattering data suggests the existence of CDW domains with typical dimensions of ~1-10 nm (inferred from the momentum widths of the CDW peaks). Both local lattice distortions due to oxygen disorder in the Cu-O chains as well as extended defects such as dislocations may act as pinning centers for CDW nanodomains. Despite the fact that lattice defects are present in all superconducting cuprates, the mechanism of nanodomains formation is closely linked to the specific realization of lattice disorder in the different compounds. In this perspective, $YBa_2Cu_4O_8$ is much less favorable for nanodomain formation compared to underdoped $YBa_2Cu_3O_{6+x}$ compounds, since it is stoichiometric and thus much less susceptible to doping inhomogeneities and local distortions related to the Cu-O chains.

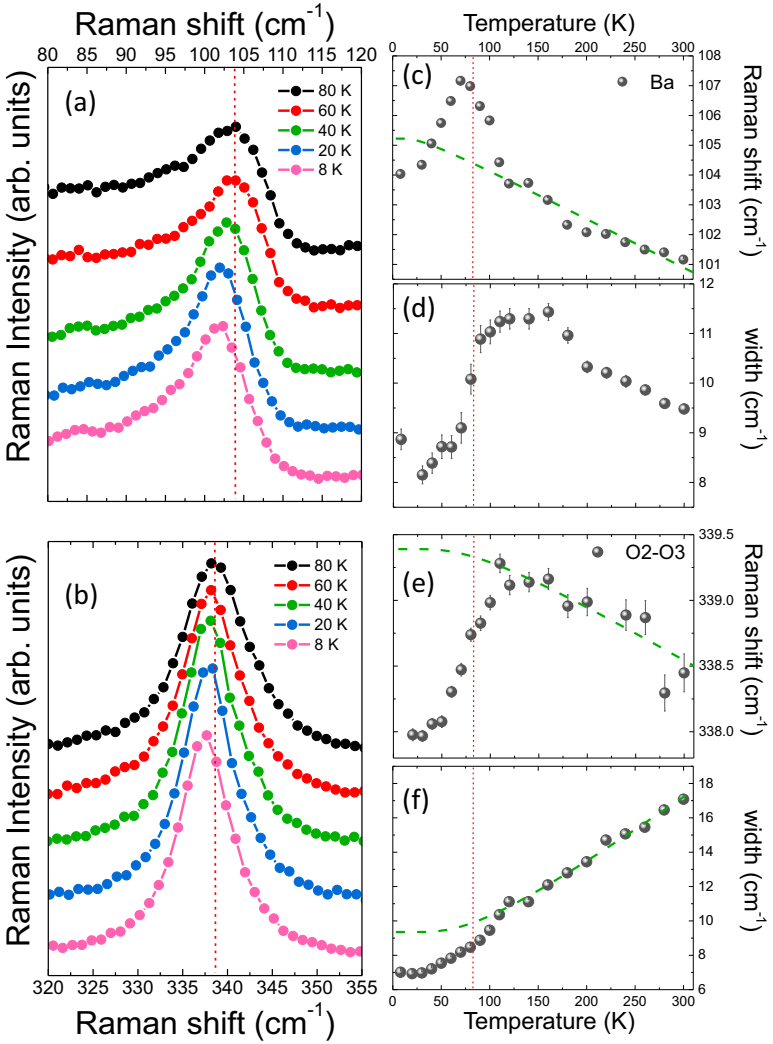

Figure 5.2: Raman spectra of $YBa_2Cu_4O_8$ in the frequency region of (a) the Ba phonon mode and (b) the O2-O3 buckling phonon mode, recorded in the xx geometry at selected temperatures upon cooling from room temperature. (c-f) Temperature dependence of the frequencies and linewidths of the A_g Ba and O2-O3 phonon modes. The vertical red line marks the superconducting transition temperature, whereas the dashed green lines are fits to an anharmonic decay of optical phonons model (see text for more details) [251].

From a different perspective, the well-established strong competition between CDW correlations and superconductivity should be taken into account. In the presence of superconducting long-range order, inhomogeneity and therefore formation of CDW nanodomains, is strongly suppressed and only under the presence of magnetic fields high enough to destabilize superconductivity have thermodynamic signatures of static CDW order been reported [342]. In a recent report, Achkar *et al.* suggest that the short range nature of the CDW order has an intrinsic origin related to the competition between CDW order and superconductivity rather than being a result of sample disorder [343]. Recent thermal conductivity measurements have determined the upper critical field to be H_{c2}=44±2 T for $YBa_2Cu_4O_8$ (at T=1.6 K) and H_{c2}=22±2 T for $YBa_2Cu_3O_{6+x}$ at $p\simeq$0.11 (*ortho*-II compound at T=1.6 K) [344]. Thus, considerably higher magnetic fields are required to be applied on $YBa_2Cu_4O_8$ in order to substantially weaken superconductivity, establishing a stronger competition between the robust superconducting state and any potential competitive state, like the CDW. Although the technical challenge is undoubtedly very high, a low temperature Raman study under high enough magnetic fields would offer further insights in this unclear picture.

Finally, it should be highlighted once again that the new CDW Raman modes seen in underdoped $YBa_2Cu_3O_{6+x}$ constitute a useful yet indirect way of studying the CDW state. The realization of a potential CDW state in underdoped $YBa_2Cu_4O_8$ would not necessarily occur at the same ordering wavevector as the one observed for $YBa_2Cu_3O_{6+x}$ and would therefore lead to a different folding of the otherwise very similar phonon dispersion curves [270, 345].

Before moving to the high pressure measurements, we address shortly the low temperature behavior of the Raman modes of $YBa_2Cu_4O_8$. Our Raman data indicate pronounced renormalizations of the phonon modes that are most strongly coupled to the electronic continuum, similar to the data and the analysis presented on the previous chapter for the case of $YBa_2Cu_3O_{6+x}$. This is clearly illustrated in Fig. 5.2 for two particular phonons, namely the A_g symmetry Ba and O2-O3 phonons: in both cases we observe a softening of the phonon frequencies in the superconducting state already discernable in the raw data and clearly illustrated in the fitting results.

Our ambient pressure Raman measurements are in excellent agreement with earlier studies [346, 347, 348, 349]. More specifically, below T_c the Ba phonon mode softens by ∼4 cm^{-1} while its width decreases in agreement with earlier reports [346, 347, 348]. Similar observations apply also for the case of the O2-O3 buckling phonon mode, for which a softening of ∼1 cm^{-1} is observed in the superconducting state, in combination with a narrowing of the phonon lineshape. Other modes exhibit similar renormalizations of smaller amplitude, in accordance with the results of the very early report of Heyen *et al* [346]. According to the superconductivity-induced phonon self-energy renormalizations described in references [255, 256] a phonon softening occurs if the superconducting gap is near or just above the phonon frequency, giving indications for the energy of the superconducting gap and taking into account the gap anisotropy. In addition, electronic

Raman scattering measurements have clearly identified the opening of an anisotropic gap in the electronic continuum [346, 349]. A small depletion of the low energy electronic continuum at low temperatures is already observable in our raw data plotted in Fig. 5.1.

A final remark is that according to the data of Fig. 5.2 the phonon renormalizations start at temperatures well above T_c: ~160 K for the Ba mode and ~125 K for the O2-O3 mode. This agrees well with previous phononic and electronic Raman scattering reports, according to which the interplay between electronic and vibrational degrees of freedom is affected in the normal state upon the opening of the pseudogap [348, 349, 350].

5.2 High Pressure Results

5.2.1 Introduction

The ambient pressure results presented in section 5.1 show that charge ordering related features are completely absent in the Raman data of $YBa_2Cu_4O_8$, in good agreement with earlier Raman studies as well as with what was suggested by x-ray scattering data. Taking into consideration the pressure-induced enhancement of superconductivity in the same compound, as will be analyzed in detail in the followings, the emergence of a CDW state under high pressure conditions appears improbable.

However, the high pressure behavior of $YBa_2Cu_4O_8$ has attracted a lot of attention and numerous high pressure studies have appeared in the literature. The main motiva-

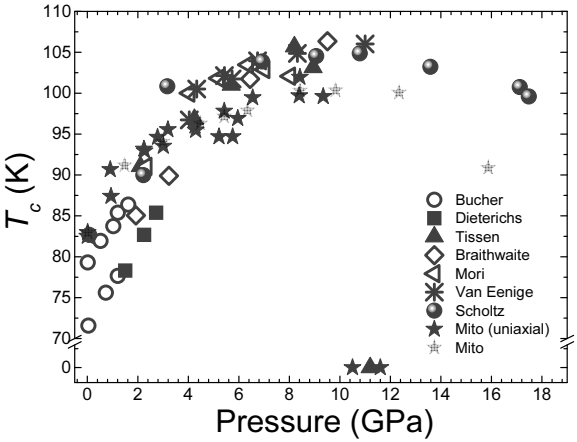

Figure 5.3: Pressure dependence of T_c in $YBa_2Cu_4O_8$. The data plotted here are taken from the high pressure resistivity and susceptibility measurements of references [7, 135, 351, 352, 353, 354, 355, 356, 357].

tion behind this scientific interest is the significant enhancement of the superconducting transition temperature under high pressure conditions. The pressure dependence of T_c has been studied by multiple groups using both resistivity and susceptibility measurements, the results of which are summarized in Fig. 5.3 [7]. Upon pressure application T_c rapidly increases with an initial pressure derivative of ~5 K/GPa (up to ~5 GPa), which is notably higher than the respective derivative for most underdoped $YBa_2Cu_3O_{6+x}$ samples for which $dT_c/dP \approx 2$ K/GPa [5]. A maximum value of $T_c \sim 105$ K is obtained at 10 GPa and a "plateau" is formed in the pressure dependence. At higher pressures, the situation is more controversial, and depending on the pressure conditions, T_c is reported either to decrease [355, 356, 357] or to disappear [353, 357]. It is worth to emphasize that all the pressure-induced chain oxygen reordering phenomena which were earlier discussed for the case of underdoped $YBa_2Cu_3O_{6+x}$ are no longer present in stoichiometric $YBa_2Cu_4O_8$, facilitating largely the interpretation of the high pressure data. Nevertheless, there is still a certain controversy in the literature, mostly on the behavior of T_c above 10 GPa, originating from the differences in the pressure conditions and the sample quality.

Interestingly, a recent x-ray diffraction (XRD) study performed at room temperature conditions revealed the occurrence of a first-order, pressure-induced, structural phase transition around ~10 GPa, presumably related with the pressure dependence of T_c [6]. The structures of the original (space group *Cmmm*) and new high pressure phase (space group *Imm*2) are plotted together in Fig. 5.4. According to the refinement of the XRD data, the double CuO_2 planes of the initial structure remain almost unaffected by the transition and solely slide with respect to each other along the *ab*-plane. On the other hand, the double Cu-O chains undergo a tilt and a major distortion, changing the coordina-

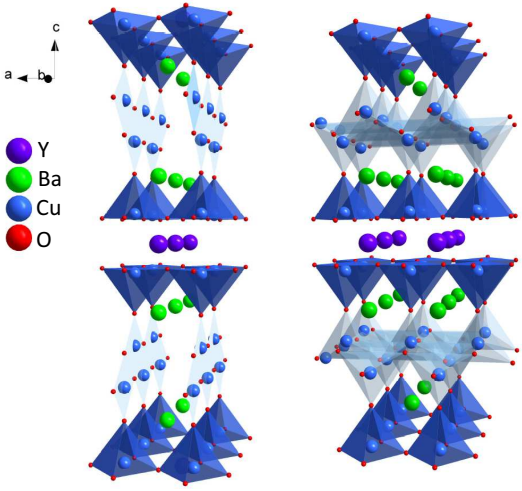

Figure 5.4: Crystal structure of $YBa_2Cu_4O_8$ in the original *Cmmm* phase (left) and high pressure *Imm*2 phase (right). The structures are plotted based on the diffraction data of reference [6].

tion and the oxidation state of the Cu1 atoms and affecting the charge distribution in the unit cell. Such a structural transition is expected to influence considerably the electronic properties of the system and the emergence of superconductivity.

It should be highlighted that in contrast to the original phase, the high pressure structure of $YBa_2Cu_4O_8$ is non-centrosymmetric. As shown in Fig. 5.3, according to some previous studies a T_c of ~100 K is observed above 10 GPa and thus in the high pressure non-centrosymmetric phase of the compound [355, 356, 357]. This is highly surprising given that there are only a limited number of non-centrosymmetric superconductors, all with rather modest T_c but highly unconventional properties, such as very large, non-Pauli limited, upper critical fields [358]. One should keep in mind though that unlike the XRD measurements of reference [6], the pressure conditions of the transport data were non-hydrostatic.

While there have been several high pressure studies of the structure and the transition temperature of $YBa_2Cu_4O_8$, the Raman studies are very few due to the weak phononic Raman signal at ambient conditions and to its additional decrease in the DAC [359, 360, 361, 362]. Moreover they are all limited to pressures smaller than 10 GPa. In order to address all of the above issues and aiming to investigate further the reported structural transition and the lattice dynamics of the compound under high pressure conditions we have performed a high pressure Raman study of $YBa_2Cu_4O_8$.

5.2.2 Experimental Details

The same high-quality detwinned $YBa_2Cu_4O_8$ single crystals which were used for the ambient pressure measurements were also used for the high pressure Raman experiment. For this purpose, crystals of the right dimensions (~80x80x30 μm^3) have been selected to fit the requirements of the DAC.

A mixture of methanol-ethanol 4:1 has been used as a pressure transmitting medium for the room temperature measurements, whereas condensed helium was used for the low temperature measurements in order to guarantee the best possible hydrostatic conditions. Pressure was always increased at room temperature to avoid residual stresses and the sample was afterwards cooled under constant pressure conditions. The expected drop of pressure occurred upon cooling and was compensated by external monitoring. The biggest pressure drop occurred during the solidification of helium, while no further pressure change took place upon cooling helium in the solid state. The temperature dependence of the Raman spectra reported here were recorded under constant pressure conditions within a pressure error of ±0.2 GPa.

The room temperature Raman measurements were performed under selected polarization conditions, whereas the low temperature measurements were unpolarized. The determination of the crystal orientation was performed using the Raman selection rules for the phonon spectrum.

5.2.3 Room Temperature measurements

In Fig. 5.5 are plotted the Raman spectra of $YBa_2Cu_4O_8$ at selected pressures upon pressure increase recorded at room temperature in the xx and yy scattering geometries. At low pressures all the expected A_g Raman active phonon modes are observed and their positions are in good agreement with previous high pressure studies [6].

As pressure increases all the modes exhibit the expected pressure-induced hardening of their frequencies, the pressure dependence of which is plotted in Fig. 5.6. In our data and within the applied pressure step (~1.5 GPa) we did not observe any pronounced deviation from linearity in the pressure dependence of the O2+O3 and Cu2 phonon modes frequencies and no splitting of the in-phase O2+O3 mode as a double peak, like those reported in previous Raman studies [359, 360, 361, 362, 363]. The pressure coefficients of the phonon frequencies up to 10 GPa are summarized and compared with the results of reference [362] in Table 5.1.

Above 10 GPa the Raman spectrum is drastically altered, evidencing the transition to the new structural phase (Fig. 5.5). In addition to the "descendants" of the O2-O3, O2+O3 and O4 phonon modes of the initial phase, several new phonon modes appear around 100,

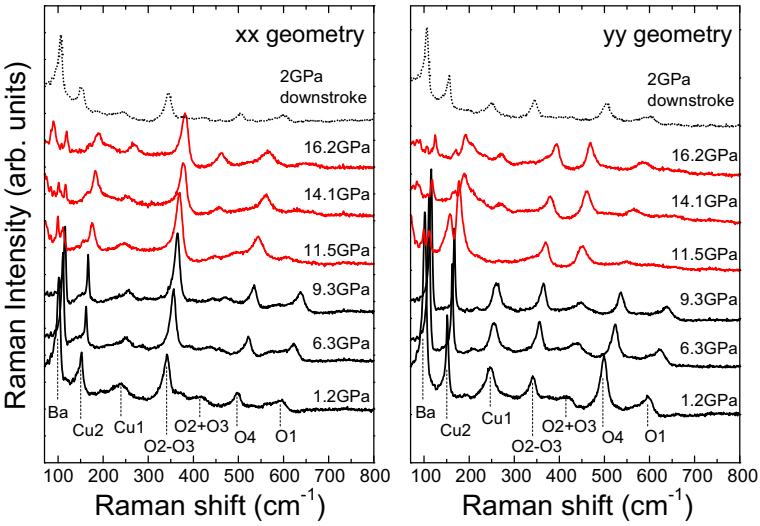

Figure 5.5: Room temperature Raman spectra of $YBa_2Cu_4O_8$ in the xx (left) and yy (right) scattering geometries, recorded with a He^+/Ne^+ laser line (λ=632.8 nm) at selected pressures upon pressure increase. The black spectra correspond to the *Cmmm* phase, whereas the red spectra to the high pressure *Imm*2 phase. The top dashed line spectra correspond to the downstroke measurements. The modes are assigned according to the group theory analysis [281].

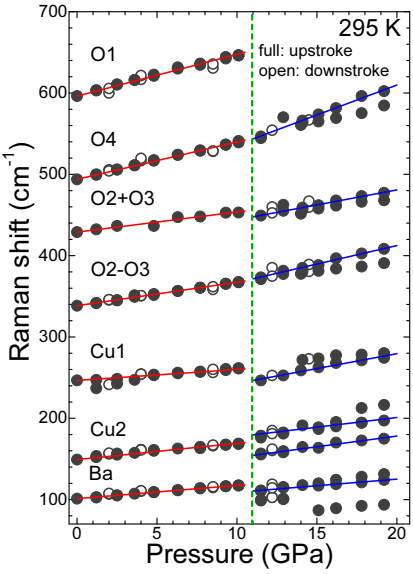

Figure 5.6: Frequencies of the Raman modes of $YBa_2Cu_4O_8$ as a function of pressure at room temperature. Solid and open circles correspond to data measured upon pressure increase and decrease, respectively (both xx and yy polarizations are included). The error bars in the figure are smaller than the data symbols. The red and blue lines represent linear fits to the data. The vertical dashed line marks the pressure where the structural transition occurs.

110, 155 and 175 cm^{-1} at high pressure. Qualitatively, this is not surprising given that the CuO_2 planes remain almost unaffected by the structural change and retain their initial topology. Contrary to this, the O1 and Cu1 chain-related modes are largely suppressed in the new phase, in accordance with the collapse of the double chains suggested by the XRD data. A more quantitative description of the new modes will be given in a following section (see 5.2.4). The overall Raman spectrum of the new phase is similar to the one reported at room temperature by Su *et al.* [6].

Our downstroke measurements indicate that the structural transition is reversible and that the original low pressure Raman spectrum is fully recovered upon pressure release, without any noticeable hysteresis effects (dotted black spectrum on Fig. 5.5). Moreover, the spectra quality of the downstroke measurements is comparable to that of the upstroke pressure measurements, indicating that the crystal is not damaged throughout the entire high pressure experiment.

Before moving to the low temperature results, it is worth underlining that our high pressure Raman studies in the $YBa_2Cu_3O_{6+x}$ family did not reveal any similar pressure-induced phase transition up to ~20 GPa. A previous high pressure transport study of nearly optimally doped $YBa_2Cu_3O_{6+x}$ showed a sudden disappearance of superconductivity above 25 GPa, an observation which could be related to the occurrence of a structural phase transition [364]. High pressure x-ray diffraction studies above 25 GPa are required to clarify this finding. Nevertheless, the structural transition is seen here at

Mode Assignment	ω (cm^{-1})	dω/dP (cm^{-1}) current data	dω/dP (cm^{-1}) ref. [362]
Ba	101.2	1.63	2
Cu2	149.2	2	2.4
Cu1	246.58	1.34	1.7
O2-O3	338.45	2.89	3.5
O2+O3	428.93	2.48	2.3
O4	493.82	4.61	5.0
O1	596.22	5.14	5.8

Table 5.1: Assignment, mode frequencies at ambient conditions and room temperature pressure coefficients of the Raman modes of $YBa_2Cu_4O_8$ in the original *Cmmm* phase. The pressure coefficients given in reference [362] are also included for comparison.

significantly lower pressures (10 GPa), an observation which is probably related to the special characteristics of the $YBa_2Cu_4O_8$ structure. The presence of the double Cu-O chains and the empty channel between them (Fig. 5.4) renders the structure more compressible with respect to the one of the $YBa_2Cu_3O_{6+x}$ compounds and more susceptible to a pressure-induced structural transition [6, 365, 366, 367].

5.2.4 Low Temperature measurements

While the previous XRD and Raman report on the structural transition was limited to room temperature measurements [6], we have performed a detailed high pressure Raman study at low temperature conditions where superconductivity appears. The main motivation behind this study was to examine the effect of pressure on the low temperature lattice dynamics of the initial and the new structural phase and most importantly the impact of the phase transition on the emergence of superconductivity. Raman scattering at combined low temperature and high pressure conditions is particularly suitable to address this issue for two reasons: on the one hand, as shown in section 5.1, at ambient pressure a clear renormalization of some of the Raman active phonons is seen across the superconducting transition and, on the other hand, the structural transition is clearly reflected in the high pressure Raman spectra of $YBa_2Cu_4O_8$ with the appearance of several new modes (see Fig. 5.5).

In addition, *ab initio* calculations of the electronic structure and the lattice dynamics have been performed by Dr. Alaska Subedi and will be presented in the present section in parallel to our results, offering a more comprehensive understanding of the experimental data.

Phonons: experiment and calculations

Fig. 5.7 shows the low temperature (15 K) Raman spectra of $YBa_2Cu_4O_8$ just before (10 GPa) and just after (11 GPa) the structural transition. At low temperatures the Raman modes are sharper and therefore more clearly distinguishable, allowing us to identify 10 modes in the Raman spectrum of the new phase (8 are seen a the room temperature spectra of 5.5, in which the double phonon modes at ~ 246.5 cm^{-1} and ~373.3 cm^{-1} appear as a single broad phonon). Based on group theory considerations, the symmetries and the number of the expected Raman active modes in the *Imm*2 phase are [368]:

$$\Gamma = 15A_1 + 7A_2 + 15B_1 + 8B_2 \tag{5.1}$$

According to the selection rules only modes of A_1 (for xx and yy polarizations) and A_2 (for xy polarization) symmetry are observable for incident and scattered light propagating along the *c*-axis. The spectra of Fig. 5.7 are recorded with the incident and scattered light in the *ab*-plane but without selecting any particular polarization, therefore both A_1 and A_2 symmetry modes are probed. However, comparing the spectrum of Fig. 5.7 to the ones of Fig. 5.5 which were recorded in the xx and yy geometries and therefore probing only A_1 symmetry modes, indicates that the 10 modes seen in Fig. 5.7 have the A_1 symmetry.

To gain more insights about the new modes, density functional theory (DFT) calculations were carried out within the local density approximation (LDA) with plane-wave

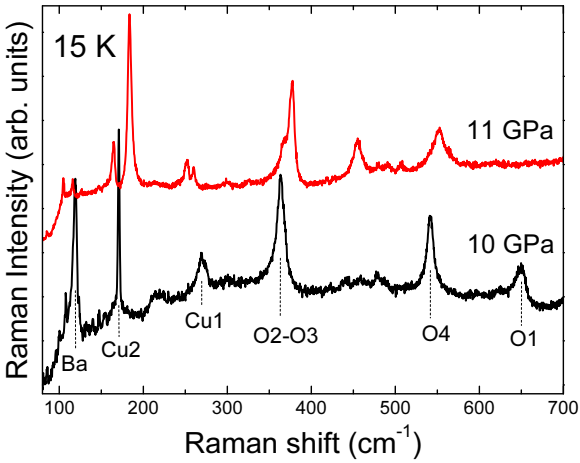

Figure 5.7: Unpolarized Raman spectra of $YBa_2Cu_4O_8$, recorded at 15 K with the λ=648 nm line of a Krypton laser. The black spectrum is taken at 10 GPa, therefore in the initial phase and the red spectrum at 11 GPa, therefore in the new structural phase.

Mode Assignment	ω (cm^{-1})	dω/dP (cm^{-1})
A_1 Ba, Cu1, O1 in-plane	99.5	-
A_1 Ba c-axis	115.9	1.6
A_1 Cu2, O1 c-axis	165.2	2.6
A_1 Y, Cu2, O2 c-axis	183.6	2.4
A_1 O1 c-axis	251.7	3.7
A_1 O4 in-plane	260.1	3.7
A_1 O2-O3 c-axis	366.4	4.5
A_1 O2, O3 in-plane	377.7	4.5
A_1 O2+O3 c-axis	453.3	3.7
A_1 O4 c-axis	551.8	7.4

Table 5.2: Assignment, experimental frequencies ω and pressure coefficients $\partial\omega/\partial P$ (both at 15 K) of the observed Raman active phonon modes in the *Imm*2 phase. The Raman frequencies are given at 11 GPa, while the pressure coefficients are derived from linear fits of the experimental data shown in Fig. 5.8.

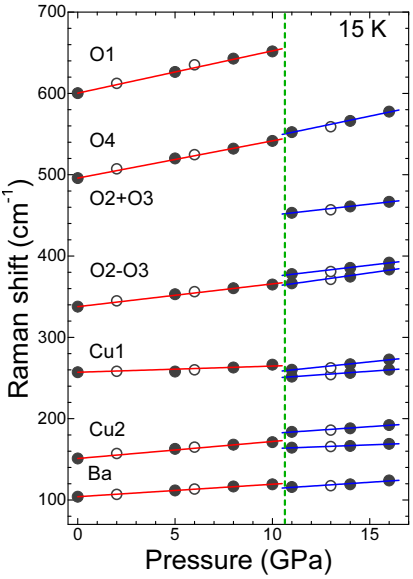

Figure 5.8: Frequencies of the Raman modes of $YBa_2Cu_4O_8$ as a function of pressure at 15 K. Solid and open circles correspond to data measured upon pressure increase and decrease. The error bars in the figure are smaller than the data symbols. The red and blue lines represent linear fits to the data. The vertical dashed line marks the pressure where the structural transition occurs.

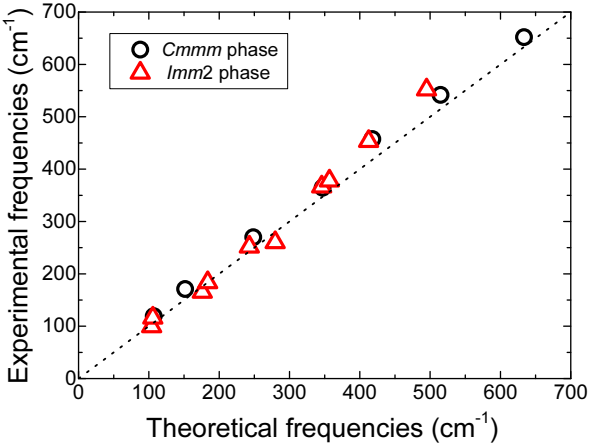

Figure 5.9: Comparison between the experimentally observed and calculated frequencies of the Raman modes in the two structural phases. The experimental frequencies are measured at 10 GPa and 15 K for the *Cmmm* phase and at 11 GPa and 15 K for the *Imm*2 phase, while the calculations were done using the experimental structural parameters of reference [6].

basis sets and projector augmented wave pseudopotentials [369, 370] as implemented in the VASP software package [371]. An energy cut-off of 950 eV was used for the basis set and an $8 \times 8 \times 8$ k-point grid was used for the Brillouin zone integration during the self-consistency. In the calculation of the equation of state, the internal coordinates were relaxed for each volume. The *ab initio* calculations reproduce very accurately the new crystal structure [6] as well as the transition pressure. The phonon frequencies and electron-phonon couplings were calculated using density functional perturbation theory [372] as implemented in the Quantum ESPRESSO package [373]. Ultrasoft pseudopotentials and cutoffs of 50 and 500 Ry were used for basis-set and charge-density expansions, respectively. An $8\times8\times8$ **k** point grid was used for Brillouin-zone integration during the self-consistency, while a denser $16\times16\times16$ grid was used for the double-delta integration in the calculation of electron-phonon couplings.

Table 5.2 presents the assignments of the observed A_1 symmetry phonons of the new phase, as derived from the lattice dynamics calculations. In the same table are also summarized the experimental phonon frequencies and their pressure coefficients (at 15 K and above 10 GPa). Fig. 5.8 shows the pressure dependence of the phonon frequencies at 15 K (including also the ones of the original phase below 10 GPa). The calculated phonon frequencies of both phases are in excellent agreement with the experimentally observed ones, as shown in Fig. 5.9. The calculations were done using the experimental lattice parameters at hydrostatic pressures of 10 (*Cmmm* phase with a volume of 188.32 $Å^3$) and

11 GPa (*Imm*2 phase with a volume of 177.10 Å^3), but with relaxed internal parameters.

(P,T) Phase diagram

As shown in Fig. 5.5, the first order structural phase transition seen in the room temperature x-ray data is clearly reflected in the Raman spectra, providing a useful tool to map in detail the (P,T) phase diagram and determine the transition line between the two phases. To this scope we performed temperature dependent Raman measurements at constant pressure values, with special emphasis in the critical pressure region close to ~10 GPa.

Fig. 5.10 shows Raman spectra recorded at selected temperatures while cooling the sample at constant pressures of 8, 10 and 11 GPa. At 8 GPa we observe no significant changes upon cooling down to 15 K, besides superconductivity-induced phonon renormalizations (the phonon anomalies under high pressure conditions will be discussed next). At 10 GPa while at room temperature the compound is in the new structural phase, the Raman spectrum of the initial $YBa_2Cu_4O_8$ structure is recovered upon cooling below 225 K. This behavior is also observed for other pressures close to the critical pressure of 10 GPa (not shown here). Upon pressure increase the transition temperature from the new to the initial phase gradually decreases and finally at 11 GPa the compound remains in the new structural phase from room temperature down to the lowest studied temperature (15 K). For pressures higher than 11 GPa the compound is in the new structural phase for

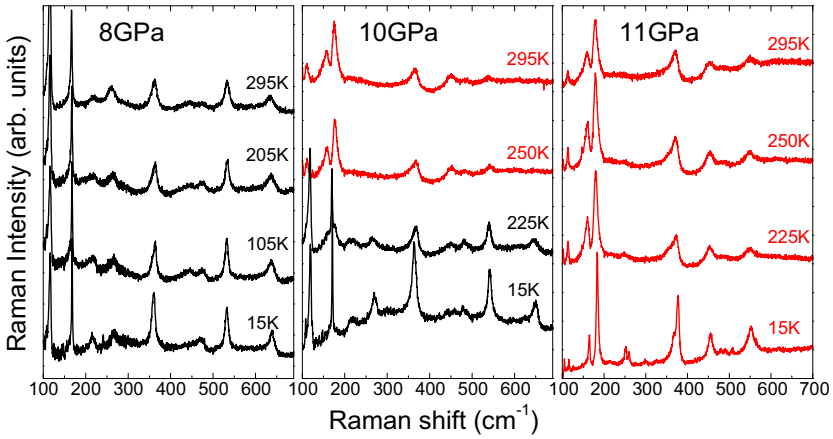

Figure 5.10: Raman spectra of $YBa_2Cu_4O_8$ recorded with a Krypton laser line (λ=648 nm) at selected temperatures upon cooling at constant pressures of 8, 10 and 11 GPa (upstroke measurements). With black are the Raman spectra of the initial phase and with red are those of the new phase.

the entire studied temperature range[i].

The (P,T) phase diagram of Fig. 5.11 shows the structural transition temperature derived from our low temperature Raman measurements, together with the earlier reported pressure dependence of T_c (see Fig. 5.3). As already deduced from the raw data of Fig. 5.10, the structural transition is not completely vertical in the (P,T) phase diagram, but exhibits a big pressure slope. It is important to emphasize though that the hydrostatic conditions of our high pressure Raman measurements differ substantially to those of the transport and susceptibility measurements [ii]. This is particularly important in the presence of the observed structural phase transition above 10 GPa, which under poor hydrostatic conditions like the ones of references [355] and [356] is not unlikely to be smeared out over a wide pressure range.

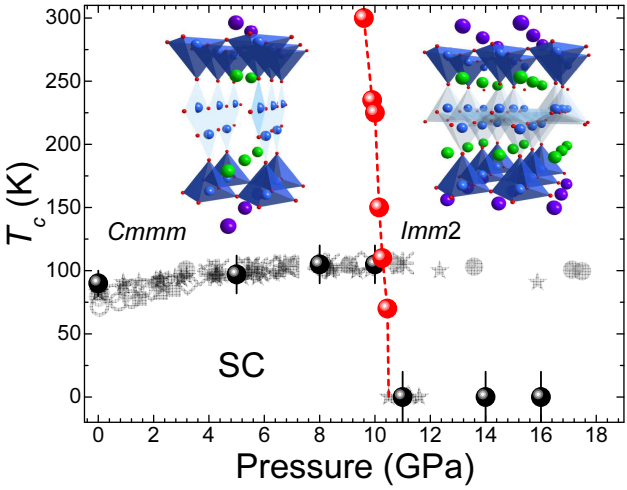

Figure 5.11: (P,T) phase diagram of $YBa_2Cu_4O_8$. The red (black) symbols show the structural (superconducting) transition temperature T_{str} (T_c) as derived from our Raman measurements and the grey symbols are the ones of Fig. 5.3. The illustrated structures of the two phases are based on the data of reference [6] (see also Fig. 5.4).

[i] Our high pressure Raman data indicate the occurrence of a potential second phase transition at ~16 GPa, as will be discussed later on.

[ii] Moreover, given that the samples used for our room temperature and low temperature measurements were always the same, the small differences in the pressure values where the structural transition is observed in our room temperature Raman data (~11.5 GPa and 10 GPa using methanol-ethanol 4:1 and condensed helium as pressure transmitting media respectively) could be attributed to the small differences in the hydrostatic conditions.

Phonon anomalies

We now turn to the effect of pressure on the lattice dynamics of the system and focus first on the low pressure structural phase of the compound up to 10 GPa. Fig. 5.12 shows Raman spectra in the frequency region of the B_{1g}-like buckling phonon mode recorded at ambient pressure, 5, 8 and 10 GPa in two different temperatures, the higher one just above the superconducting transition and the lower one in the lowest measured temperature in the superconducting state. According to the raw data, the superconductivity-induced phonon softening observed at ambient pressure (see Fig. 5.2) not only survives upon pressure application but moreover gets strongly enhanced from ~1 cm^{-1} at 1 bar to become as large as ~5 cm^{-1} at 10 GPa. This can be seen on Fig. 5.12-e, where the amplitude of the phonon softening is plotted as function of the reduced temperature T/T_c (defining T_c as the onset of the softening yields a good agreement with published transport data, as shown in Fig. 5.11-d with the black symbols). The pressure-enhanced softening is also accompanied by a small pressure-induced increase in the asymmetry of the O2-O3 phonon lineshape. All the of the observed pressure effects appear reversible, as was checked with detailed measurements upon pressure decrease (the downstroke measurements will be presented next).

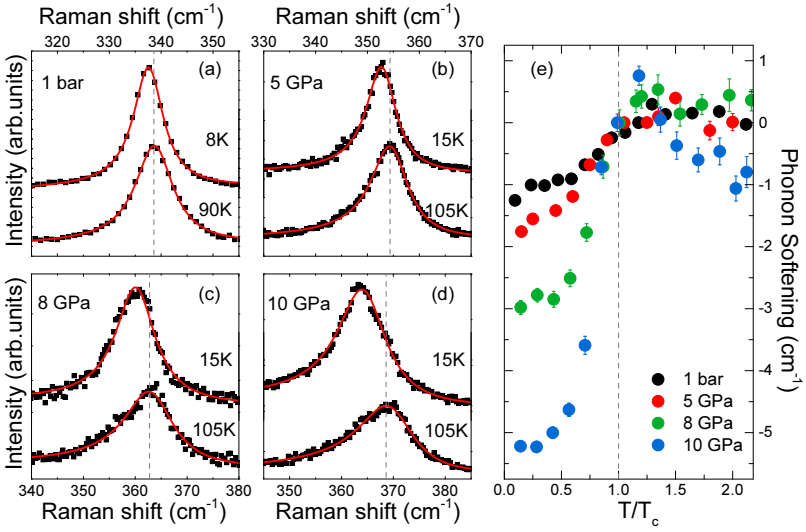

Figure 5.12: (a-d) Raman spectra of $YBa_2Cu_4O_8$ in the frequency region of the B_{1g}-like buckling phonon mode, recorded above and below the superconducting transition temperature at ambient pressure, 5, 8 and 10 GPa. (e) Softening of the buckling phonon mode in the superconducting state at ambient pressure, 5, 8 and 10 GPa.

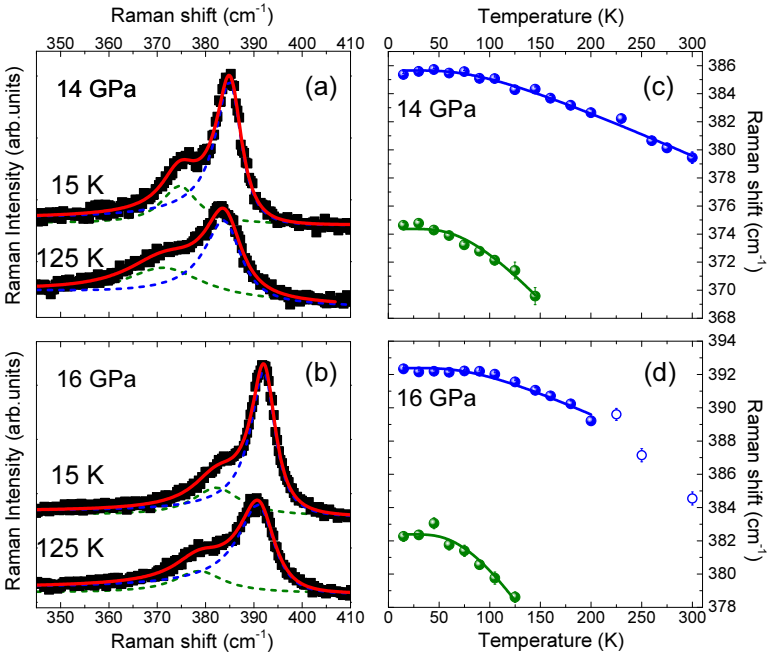

Figure 5.13: (a,b) Raman frequency region of the A_1 symmetry buckling phonon mode in the *Imm*2 phase at 125 and 15 K and (c, d) temperature dependence of the observed phonons at 14 and 16 GPa. The solid lines are fits based on the anaharmonic decay of optical phonons model [251].

Above 10 GPa, the behavior of the buckling phonon becomes very different. Fig. 5.13 presents Raman spectra at 14 and 16 GPa recorded at 125 K and 15 K in the frequency region where the "O(2)-O(3)" buckling mode (which in the new phase has the A1 symmetry) is seen in the *Imm*2 phase. In this spectral region whereas one broad asymmetric peak appears at room temperature (see Fig. 5.5 and reference [6]), two discrete phonon peaks are revealed around 370 cm^{-1} and 380 cm^{-1} at low temperatures. Based on our calculations, we assign the lower energy one to the buckling mode, and the higher energy one to in-plane vibrations of plane oxygen atoms (see also Table 5.2). The previously observed superconductivity-induced and pressure-enhanced softening of the buckling phonon mode up to 10 GPa is replaced in the new high pressure phase by a clear hardening of the two new modes upon cooling, in line with an anharmonic decay of optical phonons model. While this is clearly visible already in the raw data, it is better illustrated in the temperature dependence of the frequencies shown in Fig. 5.13 together with the the results of a fit to a symmetric anharmonic decay model [251]. No renor-

malization effects are observed in their positions and linewidths, at variance with the remarkable renormalization of the buckling phonon mode before the structural transition. As temperature increases, the low energy mode broadens significantly and its position above 150 K can not be accurately determined, therefore we include fittings of this mode only up to this temperature. Note that the two modes exhibit different slopes in their temperature dependence, neglecting any connection of the presence of the two peaks with non-hydrostatic pressure conditions.

In addition to the absence of renormalization effects in the two modes of Fig. 5.13, no anomalies have been observed for any of the phonon modes of the new structural phase, unlike the many reported for those of the *Cmmm* phase under ambient or high

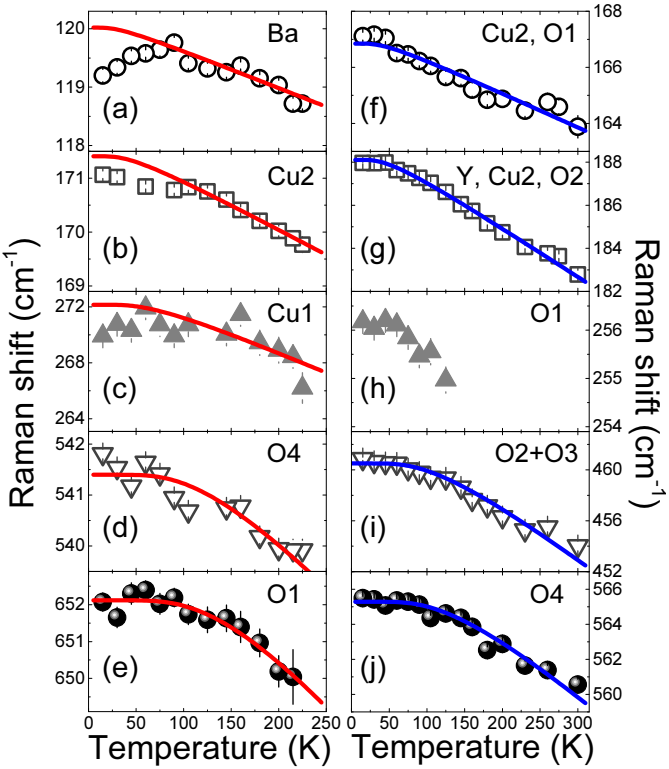

Figure 5.14: Temperature dependence of the frequencies of the strongest Raman active phonon modes at (a-e) 10 GPa (*Cmmm* phase) and (f-j) 14 GPa (*Imm*2 phase). The solid red and blue lines correspond to a fit based on a conventional phonon anharmonic decay model [251].

pressure conditions. Fig. 5.14 shows the temperature dependence of the frequencies of the strongest Raman phonons in the initial and high pressure phases (at 10 and 14 GPa respectively), excluding the buckling phonon and the respective A_1 symmetry modes shown in Fig. 5.12 and Fig. 5.13. A small softening of the A_{1g} Ba mode in the superconducting phase is observed at 10 GPa, following the reported softening at ambient pressure conditions [346]. However, given that the cut-off frequency of the razor edge filter used in our experimental setup is very close to the frequency of the Ba phonon, we can not exclude that the amplitude of the softening could be a bit larger than the observed one. The rest of the phonons follow the expected behavior of a symmetric anharmonic phonon decay, whereas none of the phonon modes of the new phase (including the *c*-axis polarized Ba mode) presents any anomaly in its temperature dependence.

Before moving to the results of the downstroke measurements, a last observation will be included. At 16 GPa and above 250 K the frequency of the ~380 cm^{-1} phonon mode exhibits a small drop and deviates from the anharmonic decay curve (open symbols in Fig. 5.13). Fig. 5.15 shows the Raman spectra of $YBa_2Cu_4O_8$ at 16 GPa, for temperatures above 200 K. Above 225 K we observe the subtle appearance of new features (e.g. the ones marked with the black arrow) as well as a sudden suppression of the relative intensities of the phonon modes at 150-200 cm^{-1}, which might be indications of an upcoming phase transition above 16 GPa. Upon cooling below 225 K the original Raman spectrum of the *Imm*2 phase is again recovered. This requires further investigation with

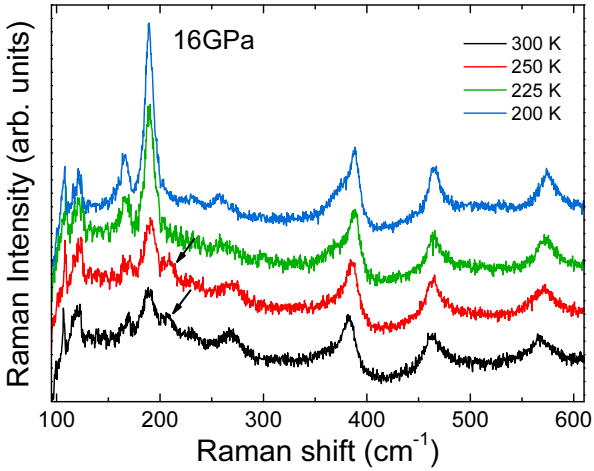

Figure 5.15: Raman spectra recorded at selected temperatures upon cooling the sample at a constant pressure of 16 GPa. The black arrows indicate the new features appearing at this pressure above 225 K (more information is given in the main text).

low temperature measurements at pressures higher than 16 GPa and will not be discussed further.

Downstroke pressure measurements

The high quality of our Raman data is maintained not only throughout the increase of external pressure, but also in our downstroke pressure measurements. This is depicted in the Raman spectra of Fig. 5.16 which were recorded at 2 GPa upon pressure decrease and are clearly of comparable quality to the upstroke ones of Fig. 5.10. Moreover, as shown in the inset of Fig. 5.16, the renormalization of the buckling phonon mode in the superconducting state is also recovered upon decreasing pressure and re-adopting the *Cmmm* phase. Note also that the amplitude of the softening is comparable to the one seen upon increasing pressure. Our downstroke measurements therefore illustrate not only the reversibility of the structural transition and the robustness of superconductivity in the original structure but also demonstrate the excellent condition of our single crystal throughout the whole experiment.

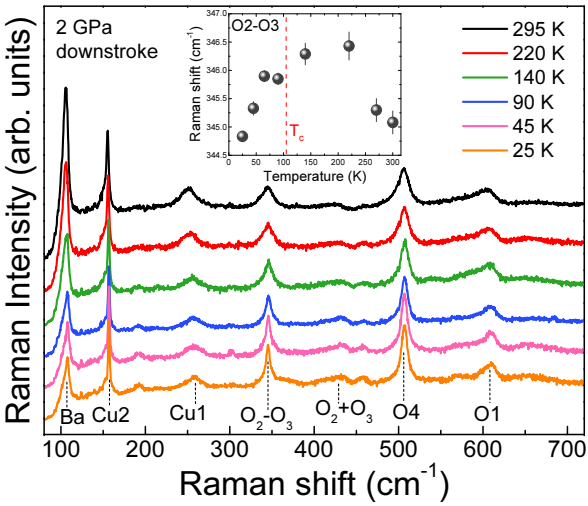

Figure 5.16: Raman spectra of $YBa_2Cu_4O_8$ recorded with a Krypton laser line (λ=648 nm) at selected temperatures upon cooling at 2 GPa upon pressure decrease. Inset: Temperature dependence of the O2-O3 phonon frequency at 2 GPa (downstroke). The vertical red line marks the T_c.

5.2.5 Discussion

As expected from our ambient pressure measurements and from the pressure evolution of T_c, our high pressure data do not reveal any charge ordering related Raman features. On the other hand, the well-known phonon modes of the original *Cmmm* crystal structure as well as the ones of the new *Imm*2 structure behave very interestingly under pressure.

Starting from the initial crystal structure, the evolution of the buckling phonon mode renormalization in $YBa_2Cu_4O_8$ under high pressure conditions is qualitatively reminiscent of the effect of hole doping in $YBa_2Cu_3O_{6+x}$ [328, 331, 374]. Altendorf *et al.* have investigated systematically the softening of this mode as a function of oxygen concentration in $YBa_2Cu_3O_{6+x}$ and have shown that the amplitude of the renormalization is strongly enhanced as doping is increased from the underdoped regime towards the optimal doping level. This is also shown in Fig. 4.10 for our Raman data in underdoped $YBa_2Cu_3O_{6+x}$. Moreover there seems to be a quantitative relation between the effect of doping and that of pressure: for optimally doped $YBa_2Cu_3O_{6.95}$, the observed softening is approximately 4-5 cm^{-1} [327, 328], which coincides with the softening we observe for $YBa_2Cu_4O_8$ at 10 GPa, where T_c also reaches its maximum value under pressure (see Fig. 5.17). This is an indirect manifestation of the role of external pressure as an alternative route to lead the system towards the conditions of optimal doping and maximum T_c. Interestingly, while further increase of the hole doping above x=6.95 in $YBa_2Cu_3O_{6+x}$ leads to the overdoped

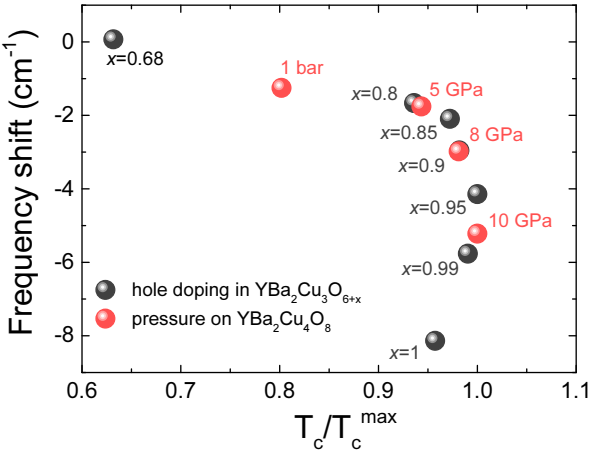

Figure 5.17: Softening of the O2-O3 phonon mode in the superconducting state as a function of hole doping in $YBa_2Cu_3O_{6+x}$ (black symbols) and as a function of hydrostatic pressure in $YBa_2Cu_4O_8$ (red symbols). The T_c scale is normalized with respect to its highest value under hole doping and under external pressure.

regime of the phase diagram and to the decrease of T_c, further pressure increase above 10 GPa on $YBa_2Cu_4O_8$ leads to the new structural phase.

As already discussed in the previous chapter, the superconductivity-induced frequency shift directly relates to the real part of the phonon self-energy by:

$$\frac{\Delta\omega}{\omega_0} = \frac{1}{N_F}\lambda_{ph} Re\Pi(\omega_0) \tag{5.2}$$

where N_F is the the electronic density of states at the Fermi level, λ_{ph} is the electron-phonon coupling constant and $Re\Pi(\omega_0)$ is the real part of the phonon self-energy. In the case of $YBa_2Cu_3O_{6+x}$ the doping-induced increase of the renormalization amplitude is essentially attributed to $Re\Pi(\omega_0)$, that is, in the case of a *d*-wave superconducting gap, maximized as the phonon frequency ω_0 matches the amplitude of the superconducting gap 2Δ.

The observed enhancement of the O2-O3 phonon renormalization in $YBa_2Cu_4O_8$, could also originate from a similar increase of $Re\Pi(\omega_0)$ under high pressure conditions. This could occur due to the pressure-induced hardening of the phonon frequency (as discussed in the data of reference [375] for similar observations in underdoped $YBa_2Cu_3O_{6+x}$ under pressure) combined with pressure-induced changes in the energy of the superconducting gap 2Δ (in line with a previous electronic Raman study on the same compound [376]). However, we can not rule out an additional contribution due to a pressure-induced increase of λ_{ph}, supported by the experimentally observed increase of the normal state phonon lineshape asymmetry with pressure (see Fig. 5.12). In all cases, these data demonstrate that $YBa_2Cu_4O_8$ in the *Cmmm* phase remains superconducting up to 10 GPa.

The pressure-induced enhancement of the renormalization amplitude in the original phase is followed by the complete suppression of all phonon renormalizations in the new structural phase. According to our previous discussion, this observation could either be related to a decrease of the λ_{ph} in the high pressure phase or to a drastic change in the underlying electronic continuum, such as the absence of superconductivity.

While the presence of considerable electron-phonon coupling is qualitatively manifested through the asymmetry of several phonon lineshapes in the new phase (see Fig. 5.10), in order to gain a more quantitative understanding we have calculated the electronic structure and the electron-phonon coupling constant for each zone center phonon in both phases [iii]. The calculated Fermi surface and band structure in the *Cmmm* phase is shown in Fig. 5.18-a,c and is in good agreement with previous reports [89, 377]. It consists of two hole like quasi-2D cylinders with mostly plane character centered around the Brillouin zone corner J=(π,π) and two 1D open sheets of mostly chain character running along the k_x direction.

In the *Imm*2 phase, the Fermi surface retains its major characteristics exhibiting again two closed sheets centered around (π,π) and a distorted open sheet running along the k_x direction (see Fig. 5.18-b,d). In this case though, the initial outer antibonding plane

[iii] The electronic structure calculations were also performed by Dr. Alaska Subedi.

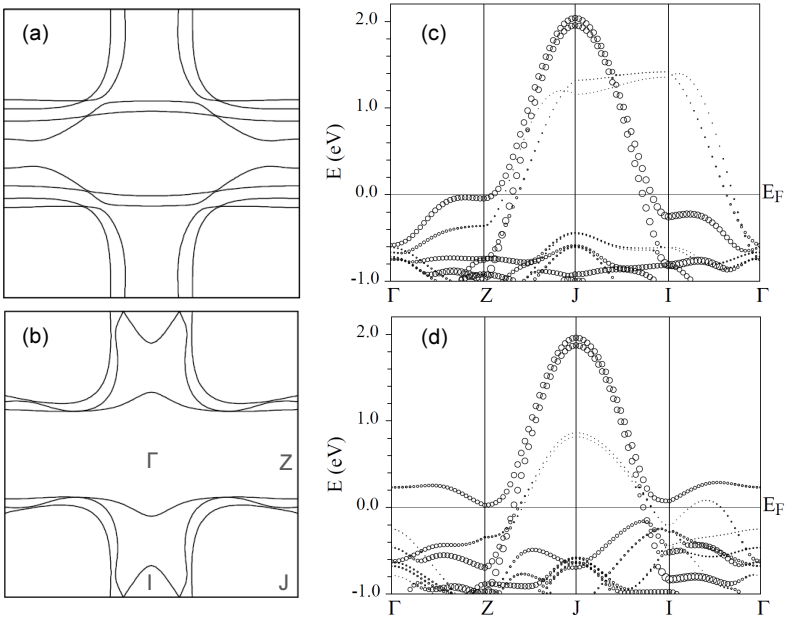

Figure 5.18: (a,b) Fermi surface of $YBa_2Cu_4O_8$ in the (a) original *Cmmm* and the (b) high pressure *Imm2* structural phase. The Fermi surface is viewed along the k_z direction. (c,d) Cu d-character band structure along selected symmetry directions in the basal plane in the (c) original and (d) new phase. The selected symmetry points of the band structure are shown in the Fermi surface of panel (b). The circle size reflects the band character, with the bigger size corresponding to Cu plane character and the smaller size corresponding to Cu chain character.

band is lifted and no longer crosses the Fermi level. The inner and outer sheets of the Fermi surface have now a chain character (due to the collapse of the double Cu-O chains structure, chain bands that were initially 1D become 2D in the new structure and disperse both along the k_x and the k_y directions), while the open sheet is formed by the bonding band of the CuO_2 planes.

The electron-phonon linewidth and coupling can be calculated using:

$$\gamma_{ph}^{\mathbf{q},\nu} = \frac{2\pi}{N_k} \sum_{\mathbf{k},n,m} |g^{\nu}_{\mathbf{k}n,\mathbf{k}+\mathbf{q}m}|^2 \delta(\epsilon_{\mathbf{k}n}) \delta(\epsilon_{\mathbf{k}+\mathbf{q}m}) \tag{5.3}$$

$$\lambda_{ph}^{\mathbf{q},\nu} = \frac{1}{2\pi N(F)} \frac{\gamma_{ph}}{\omega^2_{\mathbf{q}\nu}} \tag{5.4}$$

where N_k is the number of k points in the sum, $\epsilon_{\mathbf{k}n}$ is the electronic energy at wave vector $\mathbf{k}$ and band index n measured with respect to the Fermi level, $|g^{\nu,n,m}_{\mathbf{k},\mathbf{k}+\mathbf{q}}|^2$ is the matrix element for an electron in the state $|n\mathbf{k}\rangle$ scattering to $|m\mathbf{k}+\mathbf{q}\rangle$ through a phonon $\omega_{\mathbf{q}\nu}$ with wave vector $\mathbf{q}$ and branch index ν, and $N(F)$ is the electronic density of states at the Fermi level. The calculated electron-phonon coupling constants for all the phonon modes in the two phases are shown in Fig. 5.19.

According to the computational results of Fig. 5.19, in the new structural phase the electron-phonon coupling constant of the A_1 symmetry buckling mode is reduced by about ~35% compared to the value of the respective A_g symmetry mode of the *Cmmm* phase (which is the most strongly renormalized phonon mode across T_c). Therefore, this comparably smaller but finite value of λ_{ph} would clearly lead to a sizeable superconductivity-induced renormalization if, as suggested by transport data [355, 356, 357], T_c were only marginally affected across the structural phase transition. Note also that the temperature dependence of the Cu2-O1 (c-axis) and O1 (c-axis) phonon frequencies, which according to the calculations present the largest electron-phonon coupling constants (see Fig. 5.19), does not display any anomalies at low temperatures (see Fig. 5.14).

In view of the considerable values of the electron-phonon coupling constants, the suppression of all phonon renormalizations in our Raman data suggests that the high pressure structural phase of $YBa_2Cu_4O_8$ is non-superconducting, or that T_c is at least much lower than at low pressures. The substantial changes in the electronic structure of the new

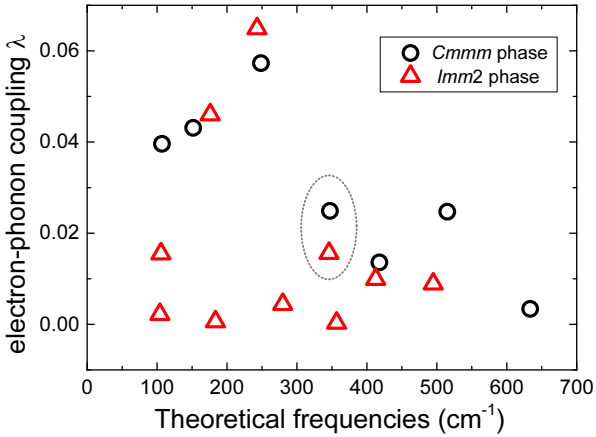

Figure 5.19: Calculated electron-phonon coupling constants λ for the observed phonon modes. The black circles correspond to the *Cmmm* phase, while the red triangles to the *Imm*2 phase. The grey circle marks the A_g and A_1 symmetry buckling phonon mode (in the *Cmmm* and *Imm*2 phase respectively).

phase compared to the one of the original structure (see Fig. 5.18) also provide a supportive ground for a potential disappearance of superconductivity. The lack of inversion symmetry in the high pressure crystal structure points as well towards the same direction.

It should be however noted that even though the overall high pressure structure is non-centrosymmetric, the structure of the CuO_2 planes remains locally unchanged and very similar to the one of the original structure. Moreover, based on our high pressure Raman data we can not completely rule out the possibility of a superconducting ground state at much lower temperatures, but we can estimate an upper limit of ~30 K in the new phase.

A non-superconducting high pressure phase is clearly not in line with a number of earlier high pressure resistivity and susceptibility studies, according to which above 10 GPa the sample not only remains superconducting but moreover has comparable T_c values to the ones before 10 GPa (see Fig. 5.3) [355, 356, 357]. However, under non-hydrostatic pressure conditions (such as the ones of the transport and susceptibility measurements), the crystal is not freely contracting but is forced to undergo selective shrinkage according to the applied uniaxial stresses. Under these conditions it is possible that the structural transition is smeared out in pressure or even that the structural details of the new crystal structure are different to the expected ones under hydrostatic conditions. It is worth mentioning that Tissen *et al.* have observed with high pressure magnetization measurements under quasi-hydrostatic conditions the disappearance of the superconducting transition above 10 GPa and have suggested its connection to a structural phase transition, not supported by earlier high pressure x-ray diffraction data [353, 365]. A very recent magnetization study by Mito *et al.* indicates that superconductivity disappears under a uniaxial in-plane or out-of-plane contraction of ~10 GPa while it survives at least up to 16 GPa under quasi-hydrostatic conditions [357]. Therefore, the broad disagreement between the results of various groups above 10 GPa, in combination with the extensively non-hydrostatic pressure conditions of all the relevant reported data pinpoint the need for new, reliable measurements of T_c using condensed helium as a pressure transmitting medium and high quality single crystals.

Chapter 6

SmFeAsO under Pressure

6.1 Introduction

The emergence of superconductivity in the "1111" family (either upon chemical doping or upon external pressure) is generally accompanied by the suppression of the magnetic and structural transitions of the parent compounds. Nevertheless, the details of the suppression, especially close to the emergence of superconductivity, differ among the various family members. This leads to a diversity in the experimentally determined phase diagrams (this is also partially related to sample quality issues) [177, 183]. The two main points of differentiation lie on how abruptly/gradually the magnetic transition is suppressed and on whether superconductivity coexists with magnetism or not. Moreover, the interplay between the magnetic and structural transitions, especially in the picture of an electronic nematic phase, still remains an open question [187].

In the case of the $SmFeAsO_xF_{1-x}$ system studied here, an additional complexity arises from a controversy concerning the evolution of the structural phase transition upon fluorine doping. While the structural transition was found early on to be gradually suppressed upon doping and to disappear for $x \leq 0.15$ [8], a more recent study has suggested the retention of the tetragonal-to-orthorhombic phase transition in the superconducting state even at optimal doping conditions [9]. It has been argued that this experimental disagreement derives from inhomogeneities in the doping level of the studied samples, related to the difficulties in determining accurately the fluorine and oxygen content in the superconducting members of the "1111" family [378]. In addition, the structural phase transition involves a very small orthorhombic distortion of the original tetragonal *a*- and *b*- axes, which results only in minor differences in the corresponding x-ray diffraction (XRD) patterns. However, the retention of the orthorhombic transition well into the superconducting regime has been subsequently reported also for other systems in relation to the symmetry breaking of the nematic phase [379].

For the purpose of the current thesis, we address this unresolved issue by applying external pressure on the parent SmFeAsO compound as an alternative tuning parameter to suppress the magnetic transition and induce superconductivity, avoiding the misleading complexity of chemical doping and the uncertainties concerning the doping level. For the study of the structural transition we performed x-ray diffraction measurements under combined high pressure and low temperature conditions, while we probe the magnetic transition indirectly through the SDW-induced renormalization of the Raman active phonon modes.

6.2 Experimental Details

For the XRD and Raman measurements we used high quality undoped SmFeAsO single crystals grown under high pressure conditions as described in references [380, 381]. The dimensions of the samples were ~60x60 μm^2 in the *ab*-plane and ~30 μm along the *c*-axis. Magnetization measurements using a superconducting quantum interference device (SQUID) indicate that the magnetic ordering takes place at T_N=140 K. Information on the XRD and Raman scattering experiments presented here was given in chapter 3. We used a Stuttgart-type diamond anvil cell for the high pressure Raman experiments and a membrane cell for the high pressure XRD experiments. A mixture of methanol-ethanol 4:1 and condense helium were used as pressure transmitting media for measurements at room and low temperatures respectively. The pressure was always increased at temperatures above the helium melting line (for measurements up to 10 GPa) and was kept constant upon cooling through external monitoring.

6.3 X-ray Diffraction Study

6.3.1 X-ray Diffraction Data

Undoped SmFeAsO crystallizes at room temperature in the *P4/nmm* tetragonal structure and at low temperatures (below the structural transition temperature T_{str}) in the orthorhombic *Cmma* structure. Fig. 6.1 shows the diffraction pattern of our SmFeAsO single crystal recorded at ambient pressure and temperature conditions. After the readout from the image plate detector the diffraction pattern was radially integrated using the FIT2D software [382], yielding the intensity vs 2θ diagram shown in Fig. 6.2-a (lower grey spectrum).

Fig. 6.2 shows also typical x-ray diffraction patterns of polycrystalline $SmFeAsO_{1-x}O_x$ samples in the tetragonal and orthorhombic phases (on black and red respectively), recorded both at 20 K but for different doping levels (taken from reference [8]). For the case of our single crystal, due to the preferred orientation of the studied sample inside the DAC we only observe a number of the total allowed reflections seen in the powder XRD spectrum. The observed Bragg reflections are very sharp (FWHM~0.04°), reassuring the excellent

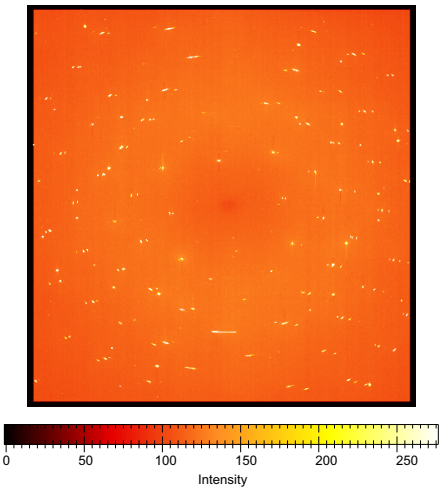

Figure 6.1: Two-dimensional diffraction pattern of a SmFeAsO single crystal recorded on an image plate detector under ambient conditions (λ=0.414894 Å). Angular integration of the diffraction pattern gives the intensity as a function of diffraction angle 2θ plotted in Fig. 6.2 (grey spectrum).

quality of our single crystal. Moreover, in addition to the reflections of the studied sample we also observe a number of Bragg reflections originating from the diamonds of the DAC, as the one marked with the asterisk in Fig. 6.2-a (the x-ray beam goes through a ~50 times longer path in the diamond than in the sample).

Close examination of the overall very similar diffraction patterns of the two phases shows that some of the initial Bragg reflections of the *P*4/*nmm* phase split into reflection doublets of the orthorhombic phase. An example is shown in Fig. 6.2-c which shows a zoom of the $(220)_T$ tetragonal reflection splitting into the orthorhombic $[(040)_O$-$(400)_O]$ doublet. In other cases the splitting is very small and can only be observed as a broadening of the initial Bragg reflection, as happens for the case of the $(212)_T$ tetragonal reflection splitting into the orthorhombic $[(132)_O$-$(312)_O]$ doublet (not shown here). The tetragonal reflections that do not split get transformed in the respective orthorhombic ones, as is shown in Fig. 6.2-b for the case of the $(200)_T/(220)_T$ tetragonal/orthorhombic reflection.

The splitting (or the broadening when the splitting can not be resolved) of the tetragonal reflections is therefore a direct signature of the transition to the orthorhombic phase and can be used as a probe of its pressure dependence. For this purpose we followed in detail the temperature dependence of the $(220)_T$ reflection and other reflections which split in the orthorhombic phase for various hydrostatic pressure values up to 85 kbars (due to time limitations imposed by the synchrotron x-ray beamtime). Fig. 6.3-a shows the 2θ region of the $(220)_T$ Bragg peak for selected temperatures upon cooling under a constant pressure of 45 kbars. As the temperature is lowered, the $(220)_T$ peak first begins to broaden and then clearly splits into two discrete peaks signaling the transition to the

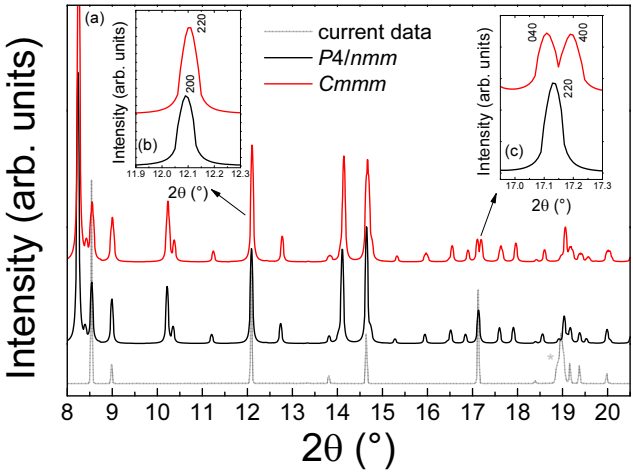

Figure 6.2: Synchrotron x-ray (λ=0.414894 Å) powder-diffraction spectra of $SmFeAsO_{1-x}O_x$ in the tetragonal *P*4/*nmm* (black spectrum) and orthorhombic *Cmma* (red spectrum) phases, taken from reference [8]. The grey spectrum is the XRD profile of our studied undoped SmFeAsO single crystal at ambient conditions. The grey asterisk marks the reflection arising from the diamonds of the DAC. The insets show selected zooms of the XRD profiles in the regions of the tetragonal $(200)_T$ and $(220)_T$ reflections.

low-temperature orthorhombic structure. Note that the amplitude of the splitting is small (~0.05°), rendering necessary for its study not only the use of a high brilliant synchrotron x-ray source but also working in the angular resolution limits of the detector (0.025° for the used MAR555 detector). Similar broadenings/splittings have also been observed for other Bragg reflections, e.g. the $(110)_T$ and $(212)_T$ peaks.

For comparison, Fig. 6.3 also shows the 2θ region of the $(200)_T$ Bragg peak under the same measuring conditions. According to crystallographic considerations and to the literature data shown in Fig. 6.2, the $(200)_T$ Bragg reflection does not split in the orthorhombic phase. In good agreement with what is expected, the raw data of Fig. 6.3-b display no evidence of broadening for the $(200)_T$ peak throughout the whole studied temperature/pressure range.

6.3.2 Discussion

A quantitative overview of the observed splitting is given in Fig. 6.4 which shows the temperature dependence of the width of the $(220)_T$ and $(200)_T$ reflections for all the measured pressure values. The width was obtained through a fit of the experimental data to a single symmetric Pearson peak lineshape. In contrast to the width of the $(200)_T$ peak which

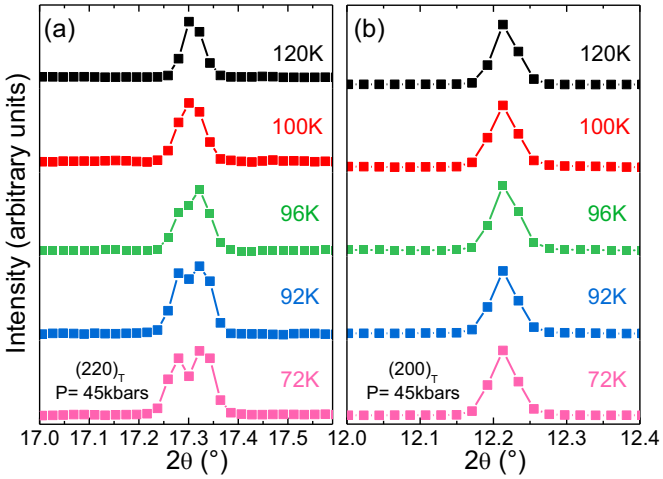

Figure 6.3: Single crystal synchrotron x-ray (λ=0.414894 Å) diffraction data of SmFeAsO in the 2θ region of the (a) $(220)_T$ and (b) $(200)_T$ tetragonal Bragg reflections measured at 45 kbars. The data collected at different temperatures are vertically shifted for clarity.

shows no observable change under all the different experimental conditions (Fig. 6.4-b), the $(220)_T$ reflection displays a clear broadening at low temperatures (Fig. 6.4-a). The broadening survives up to the highest pressure measured here (85 kbars) indicating the retention of the orthorhombic distortion up to this pressure.

In order to obtain the *a*- and *b*- axis lattice constants in the orthorhombic phase, one should apply the Bragg's law for the θ values of the $(040)_O$ and $(400)_O$ peaks. More specifically, in the orthorhombic system the d_{hkl} spacing of the crystallographic planes is related to the lattice parameters a, b and c through the relation:

$$d_{hkl} = \left[\frac{h^2}{a^2} + \frac{k^2}{b^2} + \frac{l^2}{c^2}\right]^{-\frac{1}{2}} \tag{6.1}$$

where *hkl* are the Miller indices of the lattice planes. Combining Eq. 6.1 with the Bragg's law, we obtain for the case of the $(040)_O$ and $(400)_O$ reflections:

$$\begin{aligned} a &= \frac{2\lambda}{\sin\theta_{(400)_O}} \\ b &= \frac{2\lambda}{\sin\theta_{(040)_O}} \end{aligned} \tag{6.2}$$

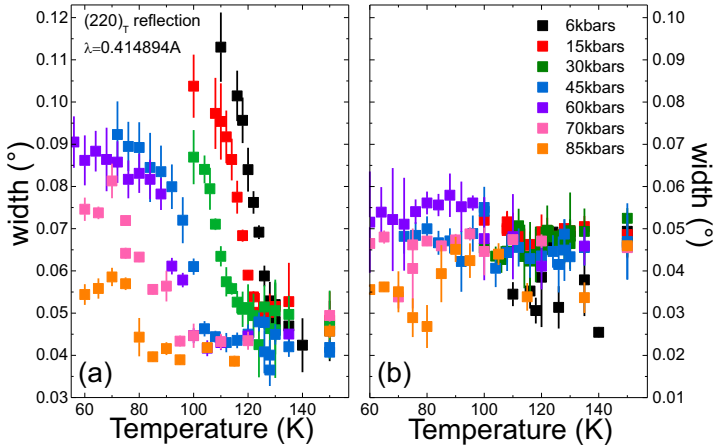

Figure 6.4: Temperature and pressure dependence of the width (FWHM) of the tetragonal (a) $(220)_T$ and (b) $(200)_T$ Bragg reflections. The widths are obtained through a fitting of the experimental data to a Pearson lineshape.

An example is given in Fig. 6.5 which shows the temperature evolution of the *a*- and *b*-axis lattice parameters at 6.5, 45, 60 and 70 kbars.

Therefore the 2θ splitting of the $(040)_O$ and $(400)_O$ Bragg peaks is indicative of the difference between the values of the *a*- and *b*- axis lattice constants, with the higher splitting corresponding to a more pronounced orthorhombic distortion. According to the data of Fig. 6.4 and Fig. 6.5, as pressure is increased the broadening of the initial $(220)_T$ peak, and thus the splitting of the $(040)_O$ and $(400)_O$ reflections, gradually decreases. This correlates to a related pressure-induced decrease of the structural orthorhombicity, in direct correspondence to the initially reported effect of chemical doping in $SmFeAsO_xF_{1-x}$ [8]. It should be mentioned that at 85 kbars the broadening is ~0.02° (comparable to the angular resolution of the detector) which in combination with the continuously decreasing tendency of the orthorhombic distortion suggests an upcoming complete suppression of the structural transition at slightly higher pressure values.

Regarding the onset temperature of the orthorhombic distortion, as pressure is increased the broadening of the $(220)_T$ peak and thus the structural transition temperature is shifted towards lower values, in line with previous high pressure structural reports on undoped members of the "122" family [232, 233, 234]. Fig. 6.6 shows the (P,T) phase diagram of parent SmFeAsO, in which the structural transition temperature is determined based on the onset of the $(220)_T$ reflection splitting of our XRD data.

The same figure includes the results of high pressure resistivity measurements on polycrystalline samples of undoped SmFeAsO and LaFeAsO from reference [383]. Ac-

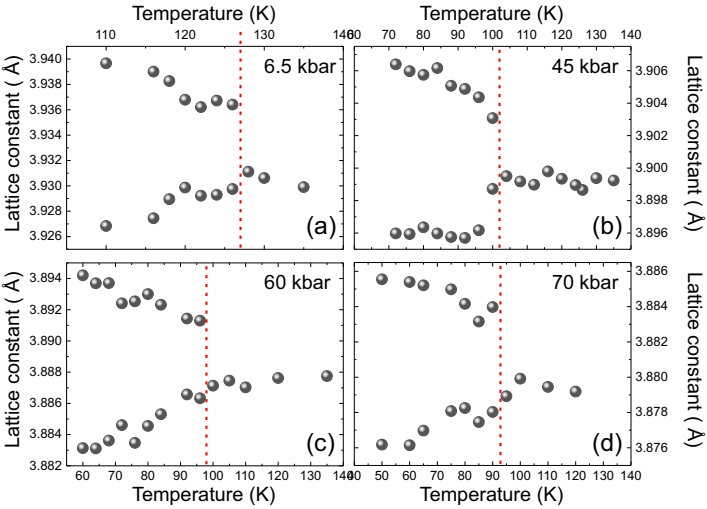

Figure 6.5: Temperature evolution of the *a*- and *b*- axis lattice parameters of SmFeAsO at 6.5, 45, 60 and 70 kbars. The vertical dashed lines mark the structural transition temperature at the respective pressures. The lattice constants are divided by $\sqrt{2}$ at temperatures below the tetragonal-to-orthorhombic transition.

cording to the transport data, pressure-induced superconductivity appears in undoped LaFeAsO at ~2 GPa and further pressure increase results in the usual dome-like shaped T_c dependence encountered in most Fe-based superconductors. Surprisingly, SmFeAsO does not exhibit the same trend: in this case superconductivity appears at ~9 GPa already at its maximum value (T_c=11 K), while further pressure increase leads to an immediate gradual decrease of T_c. This unexpected contrast in the behavior of these two very similar systems has been attributed to the very slow suppression of the magnetic transition in SmFeAsO (dT_N/dT=-6 K/GPa), whose retention hinders the emergence of superconductivity (the pressure dependence of the magnetic transition will be addressed again in the next section in view of our high pressure Raman results). However it should be taken into account that the resistivity data of reference [383] were obtained on polycrystalline samples and under high pressure conditions strongly deviating from hydrostaticity.

In view of these being currently the only reported results on the pressure dependence of T_c in the "1111" family, the two different T_c dependencies shown in Fig. 6.6 for SmFeAsO and LaFeAsO raise two different scenarios for the interplay between the various transitions. For the case of the SmFeAsO transport data, the phase diagram implies only a very small (if any) overlap between the orthorhombic and the superconducting phase (given the XRD indications for a complete suppression of the structural transition slightly

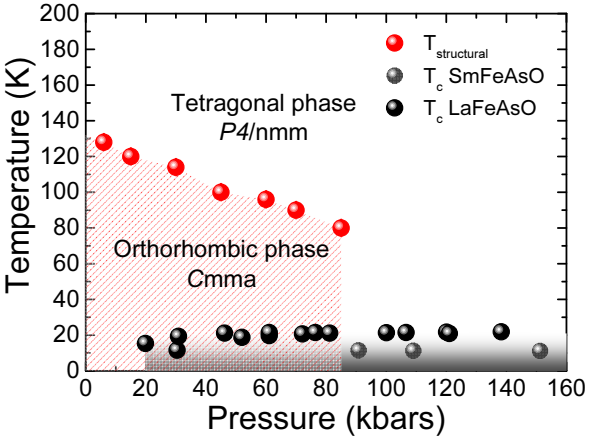

Figure 6.6: (P,T) phase diagram of SmFeAsO. The red symbols correspond to the structural transition temperature T_{str}, as determined form our high pressure XRD data, while the black and grey symbols show the pressure dependence of the superconducting transition temperature T_c for LaFeAsO and SmFeAsO respectively (taken from reference [383]).

above 8.5 GPa). This behavior is very similar to the originally suggested doping effect in the $SmFeAsO_xF_{1-x}$ system [8]. On the other hand, the transport data on LaFeAsO in combination with our structural results on SmFeAsO suggest that the orthorhombic distortion survives well into the superconducting phase, almost up to the pressure under which T_c is maximized, resembling strongly the latest reported retention of the structural transition in $SmFeAsO_xF_{1-x}$ [9]. Moreover, taking into consideration the bigger size of the La ions compared to the Sm ions, the structural transition in LaFeAsO is expected to be suppressed at even higher pressure values, with the orthorhombic distortion therefore expanding over an even wider part of the superconducting regime.

6.4 Raman Study

6.4.1 Structural transition: the E_g modes

Following the structural results of section 6.3, we begin our presentation of the phononic Raman data with the vibrational modes of E_g symmetry, which are sensitive to the occurrence of the orthorhombic distortion. According to the group symmetry analysis presented on an earlier chapter, the E_g modes correspond to atomic vibrations in the *ab*-plane and are in the tetragonal structure doubly degenerate for vibrations either along the *a*- or the *b*-axis direction. A lift of the degeneracy takes place upon the transition to the orthorhombic phase, in which the vibrations along the *a*- and *b*-axis are no longer

equivalent and the E_g modes split in the B_{2g} and B_{3g} modes.

The observation of the E_g symmetry modes is experimentally challenging for two reasons. On one hand, according to the selection rules, the E_g modes are observed for (incident or scattered) light polarization along the *c*-axis, therefore requiring Raman measurements on the *ac*- or *bc*-plane. This is particularly difficult since the grown "1111" samples are platelike, with ~30 μm dimensions along the *c*-axis (see schematic on Fig. 6.7). On the other hand, the Raman intensity of the E_g phonons is considerably lower compared to the already weak intensity of the rest Raman active A_{1g} and B_{1g} modes, thus demanding very long measuring times and fine polished sample surfaces.

The measured room temperature Raman spectrum of parent SmFeAsO in the $x'(zy')x'$ geometry is given in Fig. 6.7. The observed modes are labeled according to the atomic vibrations they involve, based on lattice dynamics calculations and assignments of earlier Raman studies [286, 287, 384]. Despite their very low intensity, all of the 4 E_g modes expected are clearly distinguishable in the room temperature spectrum. Note that in addition to the expected by the selection rules E_g modes, also modes of A_{1g} symmetry are observed, possibly due to a polarization leak or to a small misorientation of the sample.

Fig. 6.8 shows low temperature Raman spectra of SmFeAsO in the frequency region of the E_g modes corresponding to the vibrations of the Sm (~120 cm^{-1}) and O (~500 cm^{-1}) atoms (see insets). The raw Raman data clearly show that upon cooling through the structural transition temperature the E_g modes of the high temperature tetragonal phase split

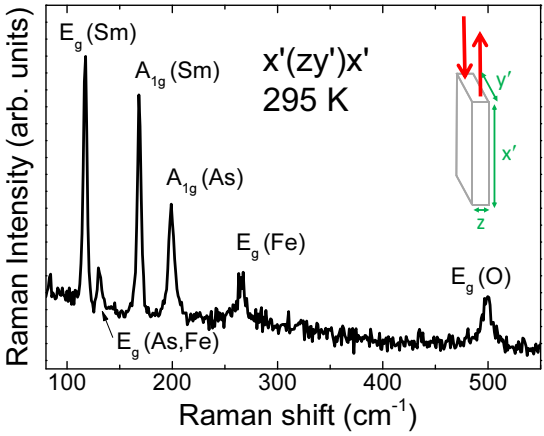

Figure 6.7: Room temperature Raman spectrum of SmFeAsO in the $x'(zy')x'$ configuration probing the E_g symmetry modes. The spectrum was recorded with a He^+/Ne^+ laser line (λ=632.8 nm). The observation of the strongest A_{1g}(Sm) and B_{1g}(Fe) modes is due to some polarization leak. The modes are labeled according to the analysis presented in chapter 2 [287]. The inset shows a schematic of the scattering geometry.

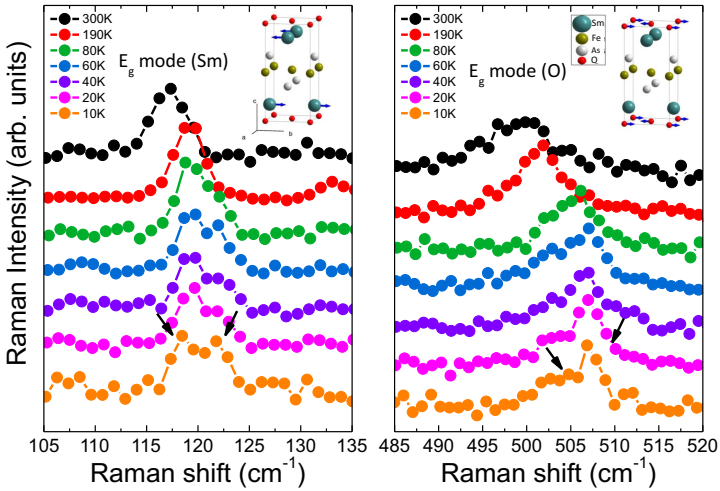

Figure 6.8: Low temperature Raman spectra of SmFeAsO measured in the $x'(zy')x'$ configuration. The frequency region of the E_g (Sm) and E_g (O) phonons are given on the left and on the right panel, respectively. The insets show the eigenvectors of the respective phonon modes. The spectra recorded at different temperatures are vertically shifted for clarity.

into the non-degenerate B_{2g} and B_{3g} modes of the low temperature orthorhombic phase. For the rest two E_g modes corresponding to vibrations of the As-Fe and Fe atoms and within our experimental spectral resolution (~2 cm^{-1}) we did not observe the expected splitting at low temperatures. Moreover, their very weak Raman signal does not allow for an accurate observation of a potential phonon broadening related to an unresolved splitting of the respective modes.

For a more quantitative insight on the splitting, Fig. 6.9 shows the temperature dependence of the E_g (Sm) and E_g (O) phonon frequencies. It is worth to comment that even though the weak signal does not allow for a definite determination of the splitting onset temperature, two distinct phonon peaks are clearly resolved only for temperatures lower than ~80-90 K, which is well below the XRD derived structural transition temperature (~130 K [8]). However, since the raw Raman data below 120 K indicate a broadening of the E_g (Sm) and E_g (O) phonons, this observation could be attributed to an unresolved smaller splitting for temperatures between 80-140 K.

Concerning the splitting amplitude, early on it was theoretically suggested that it would be too small to be resolved experimentally, due to the very small difference between the *a*- and *b*-axis lattice parameters [286]. Later on however, the splitting was clearly observed in the "122" family for both the doubly degenerate Raman active E_g modes and the infrared active E_u modes [385, 386, 387]. Moreover Raman measurements in

underdoped $Ba(Fe_{1-x}Co_x)_2As_2$ showed that the amplitude of the splitting is significantly larger than expected (around 7% of the mode energy) [385]. Based on this observation it was argued that the enhanced splitting may be linked to the presence of strong spin-phonon coupling rather than solely to the occurrence of the structural distortion. In the case of the SmFeAsO system studied here (see Fig. 6.8), the splitting is ~4 cm^{-1} for the E_g (Sm) mode (~2.8% of its energy) and ~3 cm^{-1} for the E_g (O) mode (~0.9% of its energy). Following a simple expression linking the phonon frequency ω to the nearest neighbor bond length l ($\omega^2 \sim 1/l^3$), as was done in references [289, 384, 385], and using the ambient pressure crystallographic data of reference [8], the orthorhombic distortion would lead to an E_g modes splitting of less than ~1 cm^{-1} and ~3 cm^{-1} for the E_g (Sm) and (O) modes respectively. Our experimentally determined splitting is therefore bigger compared to this rough purely crystallographic estimate, but still significantly smaller than what was found in the suggested spin-lattice interaction case of the "122" family. Raman measurements of the E_g modes in other members of the "1111" family are needed for further insights.

6.4.2 Magnetic transition: the A_{1g} and B_{1g} modes

We now move on to the *c*-axis polarized A_{1g} and B_{1g} symmetry modes. The temperature dependence of the Raman spectra in the $z(x'x')z$ and $z(x'y')z$ scattering configurations, probing the A_{1g} and B_{1g} modes respectively, is given in Fig. 6.10. All of the phonon modes expected by group theory considerations are observed, displaying symmetric lineshapes in the entire temperature range studied (down to 5 K). The modes are assigned based on lattice dynamics calculations and on earlier experimental Raman studies [287, 384]. The temperature dependence of the raw Raman data does not present any peculiarity, with all the phonons undergoing the qualitatively expected hardening and sharpening as the temperature is lowered. Unlike the E_g symmetry phonons, these modes are non-degenerate and they are not affected by the structural distortion.

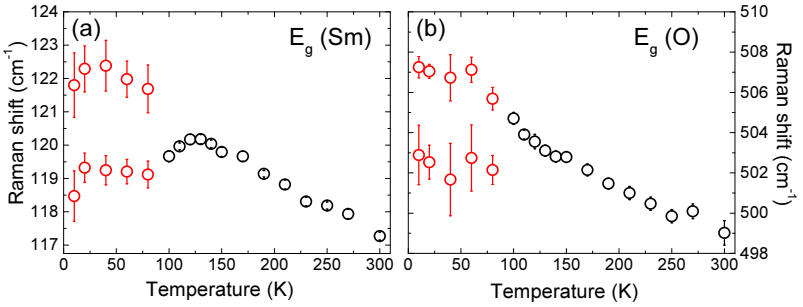

Figure 6.9: Temperature evolution of the (a) E_g Sm and (b) E_g O phonon frequencies.

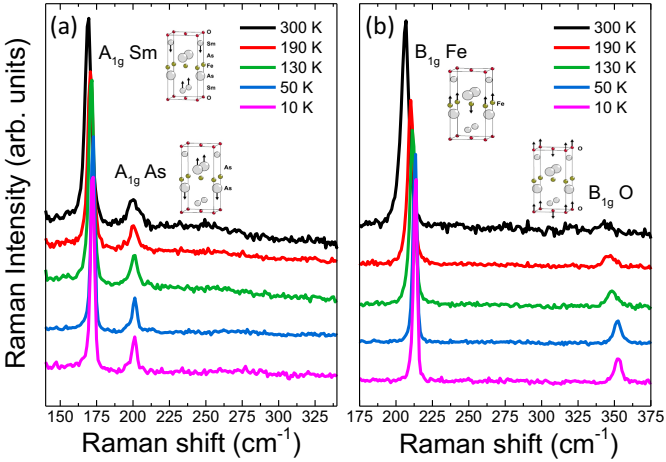

Figure 6.10: Temperature dependence of the Raman spectra of SmFeAsO in the (a) $z(x'x')z$ and (b) $z(x'y')z$ scattering configurations, probing the A_{1g} and B_{1g} modes respectively. The insets show the eigenvectors of the respective phonon modes. The spectra recorded at different temperatures were vertically shifted for clarity.

Fig. 6.11 shows the temperature dependence of the frequencies and linewidths of the A_{1g} Sm and B_{1g} Fe phonons. These are the two phonons exhibiting the highest intensity in the $z(x'x')z$ and $z(x'y')z$ geometries (see Fig. 6.10), for which the most reliable fitting results could be therefore acquired. The vertical dashed lines mark the magnetic transition temperature (T_N=140 K) as determined by magnetization measurements, while the red solid lines correspond to the fit of a conventional anharmonic phonon decay model based on phonon-phonon interactions [251]. Whereas the phonon frequencies follow reasonably well the expected anharmonic behavior, presenting only a small kink at T$\simeq T_N$, the phonon linewidths exhibit a pronounced deviation from the anharmonic decay curve at low temperatures (Fig. 6.11-b,d). More precisely, below T_N we observe a clear change in the temperature dependence of the linewidths of both phonon modes, presenting an enhanced continuous narrowing.

This linewidth behavior has not been reported until now in previous phononic Raman studies of the "1111" family [285, 387, 388, 389, 390], but it has been seen in many undoped and moderately doped members of the widely studied "122" family [10, 385, 391, 392]. In many of these cases, the linewidth anomaly is also accompanied by a simultaneous discontinuous jump of the phonon frequency, reaching in some compounds even $\sim$4 cm^{-1} [10, 391, 392]. The anomalies in the temperature dependence of the phonon frequencies have been attributed (at least partially) to the contraction of the lattice upon

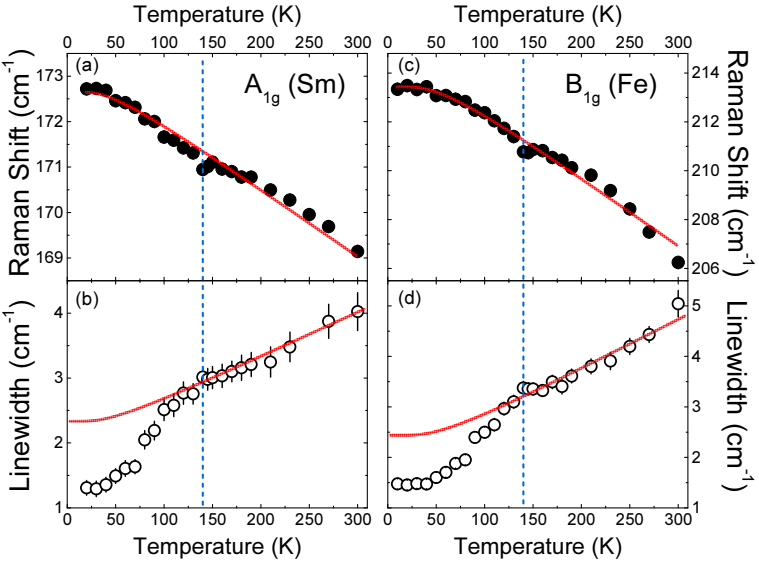

Figure 6.11: Temperature evolution of the frequencies and linewidths of the (a,b) A_{1g} Sm and (c,d) B_{1g} Fe phonon modes. The vertical dashed line marks the magnetic transition temperature, as determined from magnetization measurements. The red lines are fits of the temperature dependence using a conventional phonon anharmonic model [251].

the structural phase transition ($T_S \simeq T_N$ in the "122" family). This behavior is clearly not observed in the case of our SmFeAsO Raman data, which solely show a small frequency change at $\sim T_N$, without any discontinuity or major deviation from the fit based on the symmetric anharmonic decay model (see Fig. 6.10-a,c).

On the other hand, the observed linewidth deviation cannot be understood neither in view of the lattice modification, nor taking into account a phonon decay model based only on phonon-phonon interactions. As already suggested for the "122" family [10, 391, 392], the contribution of the electron-phonon interaction has to be taken into consideration: the opening of the SDW gap in the electronic continuum leads to a reduction of the electronic density of states at the Fermi level and to a decrease of the available phonon decay channels. As a result, the phonon lifetime increases and subsequently the inversely proportional phonon linewidth decreases, in line with our experimental observations.

The electron-phonon coupling induced linewidth anomalies of the A_{1g} Sm and B_{1g} Fe phonons is consistent with the results of *ab initio* density functional theory calculations according to which the strongest electron-phonon coupling is observed for the A_{1g} Sm, A_{1g} As and B_{1g} Fe zone center phonon modes [196]. For the sake of completeness, it

is worth to mention that a similar linewidth anomaly is also seen in our experimental data for the A_{1g} As phonon mode, although in this case the considerably lower Raman intensity results in bigger error bars and less reliable fitting results. On the other hand, the very low intensity of the B_{1g} (O) and E_g modes (~4 times lower than that of the A_{1g} and B_{1g} modes) does not allow for an accurate determination of their linewidth temperature dependence.

In conclusion, the low temperature phononic Raman data of the SmFeAsO compound provide a wealth of information concerning the observed magnetostructural transition. While the splitting of the E_g modes presented in the previous section constitutes a benchmark for the transition to the low temperature orthorhombic phase, the linewidth renormalization of the A_{1g} Sm and B_{1g} Fe phonons is an indirect criterium for the occurrence of the magnetic transition. The possibility of performing Raman measurements under extreme conditions, e.g. high pressure conditions, offers therefore a useful probe of the evolution of the magnetic and structural transitions through their fingerprints in the Raman spectra.

High Pressure Raman Study

In contrast to the numerous high pressure XRD and resistivity studies of iron pnictides, Raman scattering studies under high pressure conditions are very limited, not only in the moderately studied "1111" family but also in all Fe-based superconductors [393, 394]. This is mainly due to the difficulties encountered in collecting an inelastic scattering signal from these weak metallic Raman scatterers under the additional signal decrease imposed by the high pressure cell. This is especially limiting in the case of the E_g symmetry modes, whose very low intensity and scattering geometry requirements are prohibiting for Raman measurements through a diamond anvil cell. On the other hand, the relatively higher intensity of the A_{1g} and B_{1g} phonons allowed us to perform high pressure Raman measurements and to follow the observed SDW-related linewidth anomaly under high pressure conditions.

Starting from the room temperature conditions, Fig. 6.12-a shows our unpolarized Raman data at selected pressures upon pressure increase. The Raman spectra show qualitatively the expected behavior under pressure, with the smooth hardening of all the observed phonon modes. The originally low intensity of the B_{1g} O phonon is enhanced upon pressure increase, allowing us to follow accurately this phonon up to the highest pressure. The intensity increase could possibly originate from a pressure-induced resonance effect, although high pressure measurements with different incident energies are required to investigate this further. On the other hand, the intensity of the A_{1g} As phonon mode is very low in this random scattering geometry, so that the mode is only observed as a "shoulder" on the B_{1g} Fe phonon. We performed additional experimental runs which were more favorable for the observation of the A_{1g} As phonon and allowed us to determine its pressure coefficient.

The pressure dependence of the phonon frequencies of all 4 A_{1g} and B_{1g} phonons is

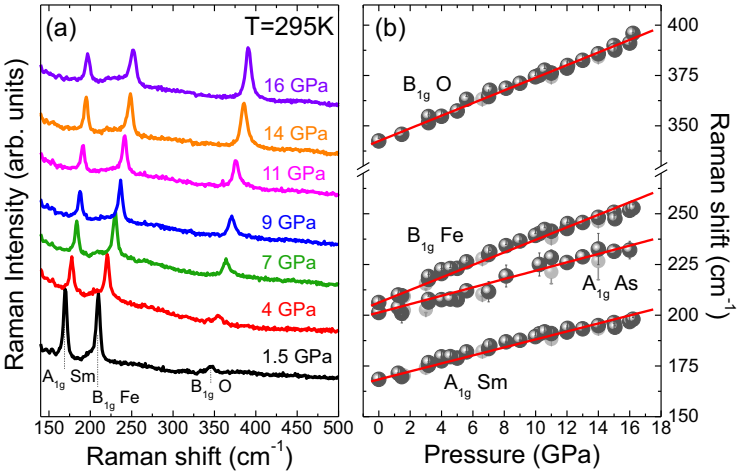

Figure 6.12: (a) Unpolarized room temperature Raman spectra of SmFeAsO, recorded with a He^+/Ne^+ laser line (λ=632.8 nm) at selected pressures upon pressure increase. The modes are assigned based on previous studies [384]. The random scattering geometry shown here is not favorable for the observation of the A_{1g} As mode (see main text). (b) Pressure dependence of the Raman frequencies at room temperature. Dark grey and light grey spheres correspond to data measured upon pressure increase and decrease respectively. The red lines result from a linear fit of the data.

Mode Assignment	ω **(cm^{-1})**	**dω/dP (cm^{-1}) current data**	**dω/dP (cm^{-1}) ref. [394]**
Sm (A_{1g})	168.4	1.97±0.04	1.44±0.04
As (A_{1g})	201.4	2.06±0.06	1.85±0.09
Fe (B_{1g})	206.2	3.09±0.05	1.7±0.2
O (B_{1g})	342.5	3.14±0.03	-

Table 6.1: Assignment, mode frequencies at ambient conditions and room temperature pressure coefficients of the Raman modes of parent SmFeAsO. The pressure coefficients given in reference [394] are also included for comparison.

shown in Fig. 6.12-b, whereas the pressure coefficients are summarized and compared with the results of reference [394] in Table 6.1. There exists a certain deviation of our experimentally determined coefficients from the ones of reference [394] potentially aris-

ing from the different pressure ranges studied: the one of reference [394] is limited up to 6 GPa, whereas ours is up to ~18 GPa. We can therefore not exclude the possibility of having a small contribution from the solidification of the pressure transmitting medium (methanol-ethanol 4:1 in this case). We do not observe any signatures of a structural phase transition up to ~18 GPa or any considerable deviation from linearity in the pressure dependence of the phonon frequencies, in line with our high pressure structural data up to 8.5 GPa. A pressure-induced transition towards the often-observed collapsed tetragonal structure at higher pressure values (above 8.5 GPa) would lead to a sudden decrease of the *c*-axis lattice parameter. This would presumably affect strongly the *c*-axis polarized phonon modes, which is clearly not supported by our experimental results. Finally, our downstroke measurements are in very good agreement with the upstroke measurements and the original Raman spectrum of SmFeAsO is recovered upon pressure release.

We now move on to the most interesting low temperatures regime where the magnetic ordering takes place. In addition to the ambient pressure data, we performed low temperature scans at constant hydrostatic (helium) pressures of 3.8, 6 and 8 GPa aiming to follow the pressure evolution of the linewidth renormalization. To our knowledge, these are the first combined high pressure and low temperature Raman data on Fe-based superconductors. Despite the very low Raman signal and its additional attenuation through both the diamond anvil cell and the cryostat window, using samples with well polished surfaces and long measuring times we managed to get Raman spectra of very high quality, comparable to those obtained at ambient pressure conditions (see Fig. 6.10). The Raman spectra we collected upon cooling at a constant pressure of 6 GPa are given for selected temperatures in Fig. 6.13. We obtained spectra of comparably high quality also for the rest of the studied pressures. All of the observed phonon modes remain symmetric in the entire temperature and pressure range studied here (up to 8 GPa and down to 20 K). In agreement with what is expected from a phonon decay process and with the ambient pressure results, the phonon modes sharpen significantly at low temperatures.

The vertical position of the high pressure cryostat in combination with the random orientation of the sample in the high pressure cell did not allow us to select a specific polarization direction of the incident and scattered light on the *ab*-plane, therefore the high pressure spectra shown on Fig. 6.13 are unpolarized. In our scattering geometry we observe all the 4 modes expected, with the A_{1g} Sm phonon exhibiting the highest Raman scattering intensity. Therefore this is the phonon mode for which the most reliable fittings could be acquired and the one we will be focusing on for the following discussion.

The temperature dependence of the frequencies and linewidths of the A_{1g} Sm phonon are given in Fig. 6.14. Starting from the phonon frequencies, Fig. 6.14-a shows the relative frequency shift of the Sm phonon with respect its room temperature value at every respective pressure. The absolute room temperature frequencies under helium pressure are shown in the inset and are in very good agreement with our room temperature measurements under a methanol-ethanol pressure transmitting medium. The phonon frequency hardens upon cooling, in line with the expected behavior from an anharmonic

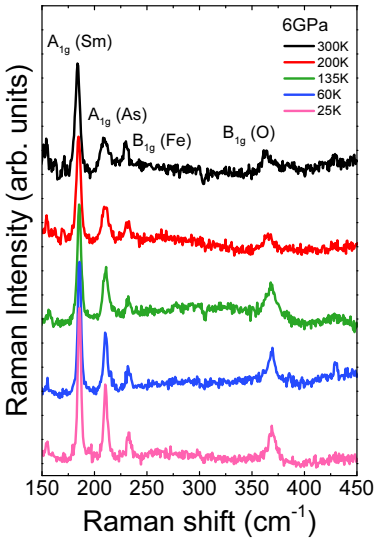

Figure 6.13: Low temperature unpolarized Raman spectra of SmFeAsO recorded upon cooling at a constant pressure of 6 GPa. The modes are assigned based on previous studies [384]. The spectra recorded at different temperatures are vertically shifted for clarity.

decay model and with the ambient pressure data. Nevertheless, as pressure increases the amplitude of the low temperature phonon hardening gradually decreases from ~3.5 cm^{-1} at 1 bar to ~1.5 cm^{-1} at 8 GPa. This could potentially be attributed to a reduced compressibility, as the structure becomes more stiff upon pressure increase.

The temperature dependence of the Sm phonon linewidth is shown in Fig. 6.14-(b-e) for 1 bar, 3.5 GPa, 6 GPa and 8 GPa, together with the results of a data fit based on an anharmonic decay model (solid lines). The SDW-induced renormalization of the phonon linewidth seen at ambient pressure, is also clearly observed under a pressure of 3.8 and 6 GPa. Even though determining the renormalization onset temperature from the Raman data has a limited accuracy, the deviation of the experimental data from the anharmonic decay fit shows a tendency of moving towards lower temperatures as pressure is increased (this is better seen for the 6 GPa data, in which the deviation starts below 90 K). What is clear though from Fig. 6.14-(b-e) is that upon pressure increase the amplitude of the renormalization gradually decreases from ~1 cm^{-1} at 1 bar to ~0.3 cm^{-1} at 6 GPa (note that the error bars are smaller than the data symbols). This results in the complete disappearance of the linewidth renormalization (within our experimental accuracy) under a pressure of 8 GPa. The 8 GPa data follow the expected anharmonic decay without any significant deviation down to the lowest temperature measured (20 K).

It is worth to highlight that at room temperature the linewidth of the Sm phonon remains practically unchanged with pressure (~4 cm^{-1}, see Fig. 6.14-(b-e)). This observation neglects any possible connection of the low temperature linewidth increase at 3.8,

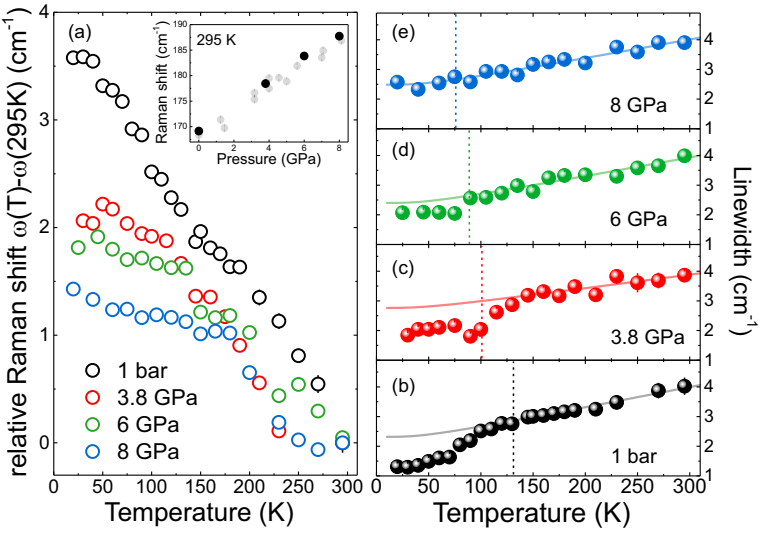

Figure 6.14: (a) Relative frequency shift of the A_{1g} Sm phonon with respect to the room temperature frequency at 1 bar, 3.5 GPa, 6 GPa and 8 GPa. The inset shows the room temperature pressure dependence of the phonon frequency measured under helium (black data) and under methanol-ethanol 4:1 (grey data- see also Fig. 6.11). (b-e) Temperature dependence of the linewidth of the A_{1g} Sm phonon at 1 bar, 3.5 GPa, 6 GPa and 8 GPa. The solid lines are a fit of the experimental data based on an anharmonic phonon decay model [251], whereas the vertical dashed lines mark the structural transition temperatures as determined from our high pressure XRD data. The error bars are smaller than the symbol size.

6 and 8 GPa to the presence of pressure-induced disorder. The later would induce a decrease of the phonon lifetime (i.e. an increase of the phonon linewidth) not only at low temperatures as observed here, but throughout the whole studied temperature range leading to an overall phonon broadening.

6.4.3 Discussion

Given that the linewidth renormalization of the A_{1g} (Sm) phonon mode is tightly connected to the opening of the SDW gap in the electronic continuum, its pressure evolution is indicative of the impact of high pressure on the magnetic transition. Therefore the gradual decrease of the renormalization amplitude and its complete disappearance at 8 GPa suggest the gradual pressure-induced closing of the SDW gap and the suppression of the magnetic transition. This comes in good agreement with the generally observed behavior of the magnetic transition through resistivity and susceptibility measurements

under high pressure conditions, both in the "122" [395, 396, 397] and in the "1111" [11] families. Furthermore, the previously reported abrupt disappearance of the magnetic transition [395, 396, 397], is also in line with our high pressure Raman data which indicate a renormalization onset temperature of ~90 K at 6 GPa and its complete disappearance at 8 GPa. A direct correlation between the amplitude of the phonon renormalization and the size of SDW gap is nevertheless still lacking. Systematic doping dependent measurements of the SDW gap (e.g. by ARPES or optical conductivity) and Raman measurements of the phonon renormalization would offer a more computable understanding.

In Fig. 6.14-(b-e) the vertical dashed lines mark the temperature of the structural phase transition at the various pressures as determined from our high pressure XRD results. In agreement with previous reports, our Raman data show that upon pressure increase the magnetic transition follows the structural transition towards lower temperatures. Interestingly though, the orthorhombic distortion survives up to (at least) 85 kbars, while no SDW-ordering related phonon renormalization is observed above 6 GPa. Therefore, our data (within out sensitivity limits) indicate a pressure-induced decoupling of the structural and magnetic transitions with the structural transition surviving over a wider pressure range.

A pressure-induced decoupling of the initially simultaneous structural and magnetic transitions was recently reported for the $BaFe_2As_2$ compound through synchrotron Mössbauer spectroscopy and XRD measurements [398]. In this case though, it was found that the magnetic ordering precedes the structural transition at high pressures and survives over a wider pressure range. These observations have been attributed to spin fluctuations in the electronic nematic phase before the establishment of the long-range magnetic order. With our Raman measurements on the other hand, we are probing the magnetic transition only indirectly through the electron-phonon coupling induced renormalization of the phonon modes. This renormalization however requires the presence of a well defined SDW gap, limiting therefore our sensitivity to the presence of spin fluctuations.

Finally, regarding the (P,T) phase diagram of Fig. 6.5, our Raman data suggest that the magnetic transition temperature in SmFeAsO decreases at a rate of $dT_N/dT \simeq$ -8.3 K/GPa and that the magnetic ordering disappears completely before 8 GPa. This result on one hand contrasts the previous value of -6 K/GPa obtained by non-hydrostatic transport measurements [383] and on the other hand suggests that the magnetic transition in SmFeAsO is completely suppressed well before the emergence of superconductivity under pressure (above 9 GPa). This behavior is clearly distinct from all the doping dependent phase diagrams suggested for the $SmFeAsO_{1-x}F_x$ system [8, 9, 399]. Given the reported extreme sensitivity of the iron pnictides on the exact pressure conditions [219], transport or magnetization measurements on single crystalline samples under hydrostatic helium conditions are required in order to unify the results of different experimental methods and to determine accurately the correlation between the suppression of the structural and magnetic transitions and the emergence of superconductivity.

Summary

The current thesis studies experimentally the effect of high external pressure on high-T_c superconductors. The structure and lattice dynamics of several members of the high-T_c cuprate and Fe-based superconductors families were investigated by means of Raman spectroscopy and x-ray diffraction under well-controlled, hydrostatic high pressure and low temperature conditions.

In the complex phase diagrams of these systems, the interplay between the various competing ground states is delicately tuned by external parameters, such as chemical doping or high pressure application. Experiments under high pressure conditions constitute an ideally "clean" tool for their study, avoiding the complexity often introduced by chemical substitutions, while parallel measurements on chemically doped samples allow for a direct comparison of the effect of external pressure and the effect of doping on the phase transitions of these systems.

The lattice dynamics of the high-T_c superconductor $YBa_2Cu_3O_{6+x}$ have been investigated systematically by Raman spectroscopy as a function of doping (x = 0.95, 0.75, 0.60, 0.55, and 0.45) and external pressure. Under ambient pressure conditions, in addition to the Raman modes expected from group theory, we observe new Raman active phonons upon cooling the underdoped samples, at temperatures well above the superconducting transition temperature. No such new phonons are observed in the Raman spectra of the optimally doped samples. The new phonons are resonant with the red incident laser light (1.96 eV) and have the A_g symmetry according to the Raman selection rules. The doping dependence and the onset temperatures of the new Raman features suggest that they are associated with the incommensurate charge density wave (CDW) state recently discovered in underdoped cuprates using synchrotron x-ray scattering techniques [1, 2]. In the CDW state, the backfolding of the original $YBa_2Cu_3O_{6+x}$ phonon dispersion in the new Brillouin zone would generate new optical modes at the Γ point and render them observable in the Raman spectra.

Under high pressure conditions and within the studied pressure range (from 2 to 12 GPa), our Raman measurements on highly ordered underdoped $YBa_2Cu_3O_{6.55}$ samples do not show any of the new Raman phonons seen at ambient pressure. Within the framework of the CDW state, this could be related to a pressure-induced suppression of the

charge ordering, as expected from a competing phase scenario and in correspondence with earlier observations in the stripe ordered $La_{1.875}Ba_{0.125}CuO_4$ [3, 4] or to pressure-induced oxygen relaxation effects in the oxygen deficient Cu-O chains, as suggested in earlier high pressure magnetization measurements [5]. Moreover, in our high pressure data we observe a pronounced pressure-induced red-shift of the resonance conditions for the chain-defect-induced Raman modes. A similar pressure-induced shift of the resonance conditions for the new modes would also explain their absence at high pressures.

High pressure and low temperature Raman measurements have been performed on the underdoped superconductor $YBa_2Cu_4O_8$, which thanks to the stoichiometric composition is free of all the complexities introduced by oxygen deficiencies and the relevant pressure-induced relaxation effects. A clear renormalization of some of the Raman phonons is seen below T_c as a result of the changes in the phonon self-energy upon the opening of the superconducting gap, with the most prominent one being that of the B_{1g}-like buckling phonon mode. The amplitude of this renormalization strongly increases with pressure, resembling the effect of hole doping in $YBa_2Cu_3O_{6+x}$, where the phonon renormalization is weak in the underdoped regime and becomes larger (with amplitude comparable to the one of $YBa_2Cu_4O_8$ at 10 GPa) at optimal doping. At ~10 GPa, the system undergoes a reversible pressure-induced structural phase transition to a non-centrosymmmetric structure, in which the CuO_2 planes remain almost unaffected whereas the double Cu-O chains collapse (space group *Imm*2) [6]. The structural transition is clearly reflected in the high pressure Raman data through the appearance of several new modes, allowing us to map in detail the (P,T) phase diagram and determine the transition line between the two phases. In the new phase, the renormalization of the buckling mode is completely suppressed, while no anomalies are observed in any of the other Raman active phonons. According to *ab initio* calculations which reproduce very accurately the new structural phase and the experimentally determined phonon frequencies, the coupling of the buckling mode to the electronic system is not significantly affected by the structural phase transition. The absence of phonon renormalizations in the presence of sizable electron-phonon coupling, indicate that, in contrast to earlier transport studies [7], $YBa_2Cu_4O_8$ is not superconducting anymore under hydrostatic pressures higher than 10 GPa.

Finally we proceeded with the investigation of the high pressure structural and vibrational properties of SmFeAsO, a member of the "1111" family (space group *P*4/*nmm*) of the Fe-based superconductors, in which superconductivity is commonly induced either by substituting F/H for O or by applying high pressures on the parent magnetic compound. The magnetic transition of the undoped compound is accompanied with a tetragonal-to-orthorhombic structural distortion, both of which are commonly suppressed upon the emergence of superconductivity. In the $SmFeAsO_xF_{1-x}$ system while the magnetic transition is totally suppressed already at low doping levels, structural studies have reported either the gradual suppression of the orthorhombic distortion [8] or its retention over a wide regime of the superconducting phase [9]. We addressed this controversy using high pressure as an alternative tuning parameter to suppress the magneto-structural transition

and induce superconductivity in the parent compound. Our high pressure, low temperature x-ray diffraction measurements on single crystals of SmFeAsO have revealed that the tetragonal-to-orthorhombic transition survives with the application of high pressures up to 85 kbars, whereas as pressure increases the structural transition temperature is suppressed towards lower values and the orthorhombicity decreases. The structural transition is also reflected in our low temperature Raman spectra through the splitting of the doubly degenerate E_g symmetry phonon modes of SmFeAsO. In addition, our Raman data reveal a linewidth renormalization of the *c*-axis polarized A_{1g} and B_{1g} Raman phonons through the magnetic transition, similar to the one previously observed in the "122" family and attributed to the opening of the spin density wave gap [10]. The renormalization is gradually suppressed under high pressure, in line with an earlier high pressure magnetization study which reported the pressure-induced decrease of the magnetic transition temperature [11]. The linewidth anomaly disappears at 8 GPa suggesting the complete suppression of the magnetic transition at this pressure.

Finally, a concluding comment concerns the significance of high pressure studies for high-T_c superconductors. The contributions of high pressure experiments in the field are multiple, such as creating new superconductors, achieving record values of T_c, providing experimental information needed for a better understanding of the responsible mechanism and testing the existing theoretical models. However, as has been strongly highlighted at several points in this thesis, having a good control of the exact conditions of the applied pressure is of pivotal importance in order to reach a detailed quantitative understanding. For this purpose, all the high pressure results of the current thesis were obtained under well controlled hydrostatic conditions and using elaborate experimental equipment, reassuring the high quality of the acquired data. Comparing or unifying high pressure data, especially on anisotropic systems and on strongly correlated electron systems with delicately tunable competing interactions, is only reasonable when those are obtained under similar conditions of hydrostaticity or uniaxiality.

Acknowledgements

Upon completion of this thesis I would like to express my gratitude to a number of people who offered me precious professional and personal support during my doctoral studies.

I would like to thank Professor Bernhard Keimer for giving me the valuable chance to be a member of his group, carry out my PhD thesis on such a uniquely scientifically exciting and inspiring environment and for his continuous support and advice.

I am very grateful to Dr. Mathieu Le Tacon for his day-by-day supervision, for the many things I learned from his vast knowledge and way of working and for his pleasant company, patience and care over the last years.

I thank deeply Professor Karl Syassen for his guidance on the high pressure studies, for transferring me his valuable knowledge and expertise and for his kind interest on my doctoral studies.

I am thankful to Professor Martin Dressel and Professor Hans Peter Büchler for kindly accepting to read and review my thesis and to be members of my PhD committee.

I thank the patient secretaries of the department, Sonja Balkema and Claudia Hagemann, and the coordinator of the International Max Planck Research School for Condensed Matter Science, Dr. Hans-Georg Libuda for their frequent help.

It has been a great pleasure working with the former and current members of our department: Alireza Akbari, Eva Benckiser, Santi Blanco-Canosa, Martin Bluschke, Alexander Boris, Jiri Chaloupka, Alex Charnukha, Christopher Dietl, Nadir Driza, Alex Frano, Gerd Friemel, Giorgi Ghambashidze, Hlynur Gretarsson, Daniel Haug, Matthias Hepting, George Jackeli, Anil Jain, Giniyat Khalliulin, B.J. Kim, Timo Larkin, Yuan Li, Toshi Loew, Yi Lu, Yulia Matiks, Matteo Minola, Jitae Park, Darren Peets, Juan Porras, Daniel Pröpper, Martin Rahlenbeck, Nakheon Sung, Youngje Um, Friederike Wrobel, Meng Wu, Peter Yordanov, Ioannis Zegkinoglou. Thank you all for your scientific collaboration and pleasant company.

Many special thanks to the technicians of the Max Planck Institute who have not only helped me massively during my experiments, but have also taught me a lot from their many skills and rich experience: Benjamin Bruha, Werner Dietrich, Uwe Engelhardt, Manfred Ohl, Armin Schulz, Michael Schulz, Heiko Uhlig.

I am deeply thankful to my dearest friends and family members whose thoughts, ad-

vices, love and frequent calls and visits filled me with courage, inspiration and energy to overcome the difficulties I found on my way over the last 4 years: Agapi, Chrysanthi, Chrisa and Giwrgos, Christina, Maria-Olga, Revekka, Tarsi, giagia, Mary, Sandro, Sofi and Alexandros and baby, Giannis and Olga, Tasia, Kostas, Panagiwtis and Elisa, Olga and Anastasia, Dimitris, Giannis, Ilias, Chiara, Elisa, Giwrgos, Ioanna, Zoi. Everything would be much more difficult without my shiny, happy people.

Very special thanks to my Thanos for his love and patience in everything big and everything small, and for the true blessing of his daily presence.

Last but definitely not least, no words would ever be enough to express my everlasting gratitude to my dear parents, Giwrgos and Miranda and my sister Lena for their continuous love, motivation, never-ending support and trust from the first day until the last day of my thesis.

Bibliography

[1] Ghiringhelli, G. *et al.* Long-Range Incommensurate Charge Fluctuations in (Y,Nd)$Ba_2Cu_3O_{6+x}$. *Science* **337**, 821–825 (2012). 9, 35, 36, 37, 123, 124, 179

[2] Chang, J. *et al.* Direct observation of competition between superconductivity and charge density wave order in $YBa_2Cu_3O_{6.67}$. *Nature Physics* **8**, 871–876 (2012). 9, 35, 36, 37, 124, 179

[3] Hücker, M. *et al.* Spontaneous symmetry breaking by charge stripes in the high pressure phase of superconducting $La_{1.875}Ba_{0.125}CuO_4$. *Phys. Rev. Lett.* **104**, 057004 (2010). 10, 132, 180

[4] Fabbris, G., Hücker, M., Gu, G. D., Tranquada, J. M. & Haskel, D. Local structure, stripe pinning, and superconductivity in $La_{1.875}Ba_{0.125}CuO_4$ at high pressure. *Phys. Rev. B* **88**, 060507 (2013). 10, 132, 180

[5] Sadewasser, S., Schilling, J., Paulikas, A. & Veal, B. Pressure dependence of T_c to 17 GPa with and without relaxation effects in superconducting $YBa_2Cu_3O_x$. *Phys. Rev. B* **61**, 741–749 (2000). 10, 44, 45, 132, 139, 180

[6] Su, F. H. *et al.* Structural phase transition in $YBa_2Cu_4O_8$ under pressure. In *Joint 21st AIRAPT and 45th EHPRG Int. Conf. on High Pressure Science and Technology, Catania* (2007). 10, 139, 140, 141, 142, 143, 146, 148, 150, 180

[7] Chen, X. J., Lin, H. Q. & Gong, C. D. Pressure dependence of T_c in Y-Ba-Cu-O superconductors. *Phys. Rev. Lett* **85**, 2180–2183 (2000). 10, 138, 139, 180

[8] Margadonna, S. *et al.* Crystal structure and phase transitions across the metal-superconductor boundary in the $SmFeAsO_{1-x}F_x$ (x= 0, 0.20) family. *Phys. Rev. B* **79**, 014503 (2009). 11, 159, 160, 162, 164, 166, 168, 169, 177, 180

[9] Martinelli, A. *et al.* Retention of the tetragonal to orthorhombic structural transition in F-substituted SmFeAsO: A new phase diagram for $SmFeAs(O_{1-x}F_x)$. *Phys. Rev. Let.* **106**, 227001 (2011). 11, 159, 166, 177, 180

[10] Rahlenbeck, M. *et al.* Phonon anomalies in pure and underdoped $R_{1-x}K_xFe_2As_2$ (R=Ba, Sr) investigated by Raman light scattering. *Phys. Rev. B* **80**, 064509 (2009). 11, 170, 171, 181

[11] Lorenz, B. *et al.* Effect of pressure on the superconducting and spin-density-wave states of $SmFeAsO_{1-x}F_x$. *Phys. Rev. B* **78**, 012505 (2008). 11, 59, 177, 181

[12] Kamerlingh Onnes, H. *Commun. Phys. Lab.Univ. Leiden* 120b,122b,124c (1991). 13

[13] Meissner, W. & Ochsenfeld, R. Ein neuer Effekt bei Eintritt der Supraleitfähigkeit. *Die Naturwissenschaften* **21**, 787 (1933). 13

[14] London, F. & London, H. The Electromagnetic Equations of the Supraconductor. *Proceedings of the Royal Society of London* **149**, 71 (1935). 13

[15] Ginzburg, V. & Landau, L. On the theory of superconductivity. *Zh. Eksp. Teor. Fiz.* **20**, 1064 (1950). 13

[16] Bardeen, J., Cooper, L. & Schrieffer, J. Theory of superconductivity. *Phys. Rev.* **108**, 1175 (1957). 13

[17] Maxwell, E. Isotope Effect in the Superconductivity of Mercury. *Phys. Rev.* **78**, 477 (1950). 13

[18] Reynolds, C. A., Serin, B., Wright, W. H. & Nesbitt, L. B. Superconductivity of Isotopes of Mercury. *Phys. Rev.* **78**, 487 (1950). 13

[19] Steglich, F. *et al.* Superconductivity in the Presence of Strong Pauli Paramagnetism: $CeCu_2Si_2$. *Phys. Rev. Lett.* **43**, 1892 (1979). 13

[20] Bednorz, J. & Müller, K. Possible high T_c superconductivity in the Ba-La-Cu-O system. *Zeitschrift für Physik B Condensed Matter* **64**, 189 (1986). 13

[21] Kamihara, Y. *et al.* Iron-based layered superconductor: LaOFeP. *Journal of the American Chemical Society* **128**, 10012 (2006). 14, 47

[22] Schilling, J. *Handbook of High-Temperature Superconductivity Theory and Experiment*, chap. High-Pressure Effects (Springer , New York, 2007). 15, 43

[23] Plakida, N. *High Temperature Cuprate Superconductors*. Springer series in Solid State Sciences (Springer, 2010). 17, 20, 26, 28

[24] Gao, L. *et al.* Superconductivity up to 164 K in $HgBa_2Ca_{m-1}Cu_mO_{2m+2+\delta}$ (m=1, 2 and 3) under quasihydrostatic pressures. *Phys. Rev. B* **50**, 4260 (1994). 17, 43

[25] Chu, C. W. *et al.* Superconductivity above 150 K in $HgBa_2Ca_2Cu_3O_{8+\delta}$ at high pressures. *Nature* **365**, 323 (1993). 17, 43

[26] Barišić, N. *et al.* Universal sheet resistance and revised phase diagram of the cuprate high-temperature superconductors. *Proceedings of the National Academy of Sciences* **110**, 12235 (2013). 17, 18

[27] Ott, H. *Superconductivity Volume 2: Novel Superconductors*, chap. High-T_c superconductivity (Springer, 2008). 17

[28] Radaelli, P. *Neutron Scattering in Layered Copper-Oxide Superconductors*, chap. Structural anomalies, oxygen ordering and superconductivity in $YBa_2Cu_3O_{6+x}$ (Kluwer Academic Publishers, 1998). 17

[29] Mourachkine, A. *High-Temperature superconductivity in Cuprates: The Nonlinear Mechanism and Tunneling Measurements* (Kluwer Academic Publishers, 2002). 17, 26, 30, 31

[30] Schilling, A., Cantoni, M., Guo, J. D. & Ott, H. R. Superconductivity above 130 K in the Hg-Ba-Ca-Cu-O system. *Nature* **363**, 56 (1993). 17

[31] Hussey, N. E. *Handbook of High-Temperature Superconductivity Theory and Experiment*, chap. Normal State Transport Properties (Springer , New York, 2007). 18, 30

[32] Armitage, N. P., Fournier, P. & Greene, R. L. Progress and perspectives on electron-doped cuprates. *Rev. Mod. Phys.* **82**, 2421 (2010). 18

[33] Presland, M., Tallon, J., Buckley, R., Liu, R. & Flower, N. General trends in oxygen stoichiometry effects on T_c in Bi and Tl superconductors. *Physica C* **176**, 95 (1991). 19

[34] Liang, R., Bonn, D. A. & Hardy, W. N. Evaluation of CuO_2 plane hole doping in $YBa_2Cu_3O_{6+x}$ single crystals. *Phys. Rev. B* **73**, 180505 (2006). 19, 41, 42, 108

[35] Damascelli, A., Hussain, Z. & Shen, Z. Angle-resolved photoemission studies of the cuprate superconductors. *Rev. Mod. Phys.* **75**, 473 (2003). 20, 23, 28, 31

[36] Pickett, W. E. Electronic structure of the high-temperature oxide superconductors. *Rev. Mod. Phys.* **61**, 433 (1989). 20, 21

[37] Hubbard, J. Electron correlations in narrow energy bands. *Proceedings of the Royal Society of London* **276**, 238 (1963). 21

[38] Emery, V. J. Theory of high-T_c superconductivity in oxides. *Phys. Rev. Lett.* **58**, 2794 (1987). 23

[39] Zhang, F. C. & Rice, T. M. Effective hamiltonian for the superconducting Cu oxides. *Phys. Rev. B* **37**, 3759–3761 (1988). 24

[40] Taillefer, L. Scattering and Pairing in Cuprate Superconductors. In *Annual Reviews of Condensed Matter Physics, Vol.1*, vol. 1, 51–70 (2010). 24, 30

[41] Regnault, L., Bourges, P. & Burlet, P. *Neutron scattering in layered copper oxide superconductors*, chap. Phase Diagrams and spin correlations in (Kluwer Academic Publishers, 1998). 25

[42] Tranquada, J. *Handbook of High-Temperature Superconductivity Theory and Experiment*, chap. Neutron Scattering Studies of Antiferromagnetic Correlations in Cuprates (Springer , New York, 2007). 25, 29

[43] Jurgens, M. *et al.* Magnetic phase diagram of $YBa_2Cu_3O_{6+x}$. *Physica B* **156-157**, 846 – 850 (1989). 25, 26

[44] Tranquada, J., Shirane, G., Keimer, B., Shamoto, S. & Sato, M. Neutron scattering study of magnetic excitations in $YBa_2Cu_3O_{6+x}$. *Phys. Rev. B* **40**, 4503–4516 (1989). 25

[45] Shamoto, S., Sato, M., Tranquada, J. M., Sternlieb, B. J. & Shirane, G. Neutron-scattering study of antiferromagnetism in $YBa_2Cu_3O_{6.15}$. *Phys. Rev. B* **48**, 13817–13825 (1993). 25

[46] Casalta, H. *et al.* Absence of a second antiferromagnetic transition in pure $YBa_2Cu_3O_{6+x}$. *Phys. Rev. B* **50**, 9688–9691 (1994). 25

[47] Haug, D. *et al.* Neutron scattering study of the magnetic phase diagram of underdoped $YBa_2Cu_3O_{6+x}$. *New Journal of Physics* **12**, 105006 (2010). 26, 35, 123

[48] Julien, M.-H. Magnetic order and superconductivity in $La_2Sr_xCuO_4$: a review. *Physica B* **329-333**, 693–696 (2003). 26

[49] Norman, M. & Pepin, C. The electronic nature of high temperature cuprate superconductors. *Reports on Progress in Physics* **66**, 1547–1610 (2003). 26, 32

[50] Leggett, A. What DO we know about high T_c? *Nature Physics* **2**, 134–136 (2006). 26

[51] Bonn, D. & Hardy, W. *Handbook of High-Temperature Superconductivity Theory and Experiment*, chap. Microwave Electrodynamics of High Temperature Superconductors (Springer , New York, 2007). 26

[52] Kleiner, R. & Müller, P. Intrinsic Josephson effects in high-T_c superconductors. *Phys. Rev. B* **49**, 1327–1341 (1994). 26

[53] Tsuei, C. C. & Kirtley, J. R. Pairing symmetry in cuprate superconductors. *Rev. Mod. Phys.* **72**, 969–1016 (2000). 27, 28, 56

[54] Gough, C. *et al.* Flux quantization in a high-T_c superconductor. *Nature* **326**, 855 (1987). 27

[55] Wollman, D. A., Van Harlingen, D. J., Lee, W. C., Ginsberg, D. M. & Leggett, A. J. Experimental determination of the superconducting pairing state in YBCO from the phase coherence of YBCO-Pb dc SQUIDs. *Phys. Rev. Lett.* **71**, 2134–2137 (1993). 28

[56] Ding, H. *et al.* Angle-resolved photoemission spectroscopy study of the superconducting gap anisotropy in $BiSr_2CaCu_2O_{8+x}$. *Phys. Rev. B* **54**, 9678–9681 (1996). 28

[57] Kirtley, J. *et al.* Angle-resolved phase-sensitive determination of the in-plane gap symmetry in $YBa_2Cu_3O_{7-\delta}$. *Nature Physics* **2**, 190–194 (2006). 29

[58] Scalapino, D. J. A common thread: The pairing interaction for unconventional superconductors. *Rev. Mod. Phys.* **84**, 1383–1417 (2012). 29

[59] Scalapino, D. The case for $d_{x^2-y^2}$ pairing in the cuprate superconductors. *Physics Reports* **250**, 329–365 (1995). 29

[60] Dahm, T. *et al.* Strength of the spin-fluctuation-mediated pairing interaction in a high-temperature superconductor. *Nature Physics* **5**, 217–221 (2009). 29

[61] Le Tacon, M. *et al.* Intense paramagnon excitations in a large family of high-temperature superconductors. *Nature Physics* **7**, 725–730 (2011). 29

[62] Mackenzie, A. P., Julian, S. R., Sinclair, D. C. & Lin, C. T. Normal-state magnetotransport in superconducting $Tl_2Ba_2CuO_{6+\delta}$ to millikelvin temperatures. *Phys. Rev. B* **53**, 5848–5855 (1996). 29, 30

[63] Ando, Y., Komiya, S., Segawa, K., Ono, S. & Kurita, Y. Electronic Phase Diagram of High-T_c Cuprate Superconductors from a Mapping of the In-Plane Resistivity Curvature. *Phys. Rev. Lett.* **93**, 267001 (2004). 29, 30

[64] Hussey, N. E. Phenomenology of the normal state in-plane transport properties of high-T_c cuprates. *Journal of Physics: Condensed Matter* **20**, 123201 (2008). 30

[65] Norman, M., Pines, D. & Kallin, C. The pseudogap: friend or foe of high T_c? *Adnances in Physics* **54**, 715–733 (2005). 30, 31, 33

[66] Valla, T. *et al.* Evidence for quantum critical behavior in the optimally doped cuprate $Bi_2Sr_2CaCu_2O_{8+\delta}$. *Science* **285**, 2110–2113 (1999). 30

[67] Nakamae, S. *et al.* Electronic ground state of heavily overdoped nonsuperconducting $La_{2-x}Sr_xCuO_4$. *Phys. Rev. B* **68**, 100502 (2003). 30

[68] Proust, C., Boaknin, E., Hill, R. W., Taillefer, L. & Mackenzie, A. P. Heat Transport in a Strongly Overdoped Cuprate: Fermi Liquid and a Pure *d*-Wave BCS Superconductor. *Phys. Rev. Lett.* **89**, 147003 (2002). 30

[69] Timusk, T. & Statt, B. The pseudogap in high-temperature superconductors: an experimental survey. *Reports on Progress in Physics* **62**, 61 (1999). 30, 31

[70] Ishida, K. *et al.* Pseudogap behavior in single-crystal $Bi_2Sr_2CaCu_3O_{8+\delta}$ probed by Cu NMR. *Phys. Rev. B* **58**, 5960–5963 (1998). 31

[71] Warren, W. W. *et al.* Cu spin dynamics and superconducting precursor effects in planes above T_c in $YBa_2Cu_3O_{6.7}$. *Phys. Rev. Lett.* **62**, 1193–1196 (1989). 31

[72] Alloul, H., Ohno, T. & Mendels, P. ^{89}Y NMR Evidence for a Fermi-Liquid Behavior in $YBa_2Cu_3O_{6+x}$. *Phys. Rev. Lett.* **63**, 1700–1703 (1989). 31

[73] Tallon, J. & Loram, J. The doping dependence of T^* - what is the real high-T_c phase diagram? *Physica C* **349**, 53–68 (2001). 31

[74] Bucher, B., Steiner, P., Karpinski, J., Kaldis, E. & Wachter, P. Influence of the spin gap on the normal state transport in $YBa_2Cu_4O_8$. *Phys. Rev. Lett.* **70**, 2012–2015 (1993). 31

[75] Basov, D. N. & Timusk, T. Electrodynamics of high-T_c superconductors. *Rev. Mod. Phys.* **77**, 721–779 (2005). 31

[76] Huefner, S., Hossain, M. A., Damascelli, A. & Sawatzky, G. A. Two gaps make a high-temperature superconductor? *Reports on Progress in Physics* **71**, 062501 (2008). 32

[77] Rullier-Albenque, F., Alloul, H., Colson, D. & Forget, A. High field determination of superconducting fluctuations in high-T_c cuprates. ArXiv:1311.5205v1. 32

[78] Emery, V. J. & Kivelson, S. A. Importance of phase fluctuations in superconductors with small superfluid density. *Nature* **374**, 434 (1995). 32

[79] Anderson, P. W. The Resonating Valence Bond State in La_2CuO_4 and superconductivity. *Science* **235**, 1196–1198 (1987). 32

[80] Kivelson, S. A. *et al.* How to detect fluctuating stripes in the high-temperature superconductors. *Rev. Mod. Phys.* **75**, 1201–1241 (2003). 33

[81] Varma, C. M. Theory of the pseudogap state of the cuprates. *Phys. Rev. B* **73**, 155113 (2006). 33

[82] Daou, R. *et al.* Broken rotational symmetry in the pseudogap phase of a high-T_c superconductor. *Nature* **463**, 519 (2010). 33

[83] Xia, J. *et al.* Polar Kerr-effect measurements of the high-temperature $YBa_2Cu_3O_{6+x}$ superconductor: Evidence for broken symmetry near the pseudogap temperature. *Phys. Rev. Lett.* **100**, 127002 (2008). 33

[84] Shekhter, A. *et al.* Bounding the pseudogap with a line of phase transitions in $YBa_2Cu_3O_{6+\delta}$. *Nature* **498**, 75 (2013). 33, 123

[85] Vignolle, B., Vignolles, D., Julien, M.-H. & Proust, C. From quantum oscillations to charge order in high-T_c copper oxides in high magnetic fields. *Comptes Rendus Physique* **14**, 39–52 (2013). 34, 133

[86] Taillefer, L. Fermi surface reconstruction in high-T_c superconductors. *Journal of Physics: Condensed Matter* **21**, 164212 (2009). 34

[87] Vignolle, B. *et al.* Quantum oscillations in an overdoped high-T_c superconductor. *Nature* **455**, 952–955 (2008). 34

[88] Doiron-Leyraud, N. *et al.* Quantum oscillations and the Fermi surface in an underdoped high-T_c superconductor. *Nature* **447**, 565–568 (2007). 34, 133

[89] Bangura, A. F. *et al.* Small fermi surface pockets in underdoped high temperature superconductors: Observation of Shubnikov-de Haas oscillations in $YBa_2Cu_4O_8$. *Phys. Rev. Lett.* **100**, 047004 (2008). 34, 133, 155

[90] Yelland, E. A. *et al.* Quantum oscillations in the underdoped cuprate $YBa_2Cu_4O_8$. *Phys. Rev. Lett.* **100**, 047003 (2008). 34, 133

[91] Sebastian, S. E., Harrison, N. & Lonzarich, G. G. Towards resolution of the Fermi surface in underdoped high-T_c superconductors. *Reports on Progress in Physics* **75**, 102501 (2012). 34, 133

[92] Barišić, N. *et al.* Universal quantum oscillations in the underdoped cuprate superconductors. *Nature Physics* **9**, 761 (2013). 34

[93] Wu, T. *et al.* Magnetic-field-induced charge-stripe order in the high-temperature superconductor $YBa_2Cu_3O_y$. *Nature* **477**, 191–194 (2011). 35

[94] Wu, T. *et al.* Emergence of charge order from the vortex state of a high-temperature superconductor. *Nature Communications* **4**, 2113 (2013). 35

[95] Tranquada, J. M., Sternlieb, B. J., Axe, J. D., Nakamura, Y. & Uchida, S. Evidence for stripe correlations of spins and holes in copper oxide superconductors. *Nature* **375**, 561 (1995). 35

[96] Ichikawa, N. *et al.* Local magnetic order vs superconductivity in a layered cuprate. *Phys. Rev. Lett.* **85**, 1738–1741 (2000). 35

[97] Fujita, M., Goka, H., Yamada, K., Tranquada, J. M. & Regnault, L. P. Stripe order, depinning, and fluctuations in $La_{1.875}$ $Ba_{0.125}Cu_3O_4$ and $La_{1.875}$ $Ba_{0.125}$ $Sr_{0.050}Cu_3O_4$. *Phys. Rev. B* **70**, 104517 (2004). 35

[98] da Silva Neto, E. H. *et al.* Ubiquitous interplay between charge ordering and high-temperature superconductivity in cuprates. *Science* **343**, 393–396 (2014). 35

[99] Comin, R. *et al.* Charge order driven by Fermi-Arc instability in $Bi_2Sr_{2-x}La_xCuO_{6+\delta}$. *Science* **343**, 390–392 (2014). 35, 36, 37

[100] Fong, H. F. *et al.* Spin susceptibility in underdoped $YBa_2Cu_3O_{6+x}$. *Phys. Rev. B* **61**, 14773–14786 (2000). 35

[101] Dai, P., Mook, H. A., Hunt, R. D. & Doğan, F. Evolution of the resonance and incommensurate spin fluctuations in superconducting $YBa_2Cu_3O_{6+x}$. *Phys. Rev. B* **63**, 054525 (2001). 35

[102] Achkar, A. J. *et al.* Distinct Charge Orders in the Planes and Chains of *Ortho*-III-Ordered $YBa_2Cu_3O_{6+\delta}$ Superconductors Identified by Resonant Elastic X-ray Scattering. *Phys. Rev. Lett.* **109**, 167001 (2012). 35, 123

[103] Blackburn, E. *et al.* X-Ray Diffraction Observations of a Charge-Density-Wave Order in Superconducting *Ortho*-II $YBa_2Cu_3O_{6.54}$ Single Crystals in Zero Magnetic Field. *Phys. Rev. Lett.* **110**, 137004 (2013). 35, 124

[104] Blanco-Canosa, S. *et al.* Momentum-Dependent Charge Correlations in $YBa_2Cu_3O_{6+\delta}$ Superconductors Probed by Resonant X-Ray Scattering: Evidence for Three Competing Phases. *Phys. Rev. Lett.* **110**, 187001 (2013). 35, 36, 123, 124

[105] Cava, R. *et al.* Structural anomalies, oxygen ordering and superconductivity in oxygen deficient $Ba_2YCu_3O_x$. *Physica C* **165**, 419–433 (1990). 38

[106] Jorgensen, J. D. *et al.* Oxygen ordering and the orthorhombic-to-tetragonal phase transition in $YBa_2Cu_3O_{7-x}$. *Phys. Rev. B* **36**, 3608–3616 (1987). 37, 86

[107] Jorgensen, J. *et al.* Structural Properties of oxygen deficient $YBa_2Cu_3O_{7-\delta}$. *Phys. Rev. B* **41**, 1863–1877 (1990). 37, 39, 41

[108] Andersen, N., Lebech, B. & Poulsen, H. The structural phase diagram and oxygen equilibrium partial pressure of $YBa_2Cu_3O_{6+x}$ studied by neutron powder diffraction and gas volumetry. *Physica C* **172**, 31 – 42 (1990). 37

[109] Andersen, N. *et al.* Superstructure formation and the structural phase diagram of $YBa_2Cu_3O_{6+x}$. *Physica C* **317-318**, 259–269 (1999). 37, 38, 39, 82

[110] Zimmermann, M. V. *et al.* Oxygen-ordering superstructures in underdoped $YBa_2Cu_3O_{6+x}$ studied by hard x-ray diffraction. *Phys. Rev. B* **68**, 104515 (2003). 38, 39, 82

[111] Zeiske, T., Sonntag, R., Hohlwein, D., Andersen, N. & Wolf, T. Local oxygen ordering in superconducting $YBa_2Cu_3O_{6.4}$ observed by neutron diffraction. *Nature* **353**, 542 (1991). 38

[112] Fleming, R. M. *et al.* X-ray-scattering study of finite-range order in $Ba_2YCu_3O_{6.7}$. *Phys. Rev. B* **37**, 7920–7923 (1988). 38

[113] Strempfer, J. *et al.* Oxygen superstructures throughout the phase diagram of $(Y,Ca)Ba_2Cu_3O_{6+x}$. *Phys. Rev. Lett.* **93**, 157007 (2004). 38, 39

[114] Alario-Franco, M., Chaillout, C., Capponi, J., Chenavas, J. & Marezio, M. A family of non-stoichiometric phases based on $Ba_2YCu_3O_{7-\delta}$. *Physica C* **156**, 455–460 (1988). 38

[115] Beyers, R. *et al.* Oxygen ordering, phase separation and the 60-K and 90-K plateaus in $YBa_2Cu_3O_x$. *Nature* **340**, 619–621 (1989). 38

[116] Reyes-Gasga, J. *et al.* 3-d oxygen vacancy ordered superstructures in $YBa_2Cu_3O_{7-\delta}$ prepared by the constant stoichiometry cooling method. *Solid State Communications* **71**, 269–273 (1989). 38

[117] Islam, Z. *et al.* Four-unit-cell superstructure in the optimally doped $YBa_2Cu_3O_{6.92}$ superconductor. *Phys. Rev. Lett.* **93**, 157008 (2004). 39

[118] Liang, R., Bonn, D. & Hardy, W. N. Preparation and x-ray characterization of highly ordered *ortho*-II phase $YBa_2Cu_3O_{6.50}$ single crystals. *Physica C* **336**, 57 – 62 (2000). 39

[119] Schwer, H., Kaldis, E., Karpinski, J. & Rossel, C. Effect of structural changes on the transition temperatures in $Y_2Ba_4Cu_7O_{14+x}$ single crystals. *Physica C* **211**, 165 – 178 (1993). 40

[120] Karpinski, J., Kaldis, E., Jilek, E., Rusiecki, S. & Bucher, B. Bulk synthesis of the 81-K superconductor $YBa_2Cu_4O_8$ at high oxygen-pressure. *Nature* **336**, 660–662 (1988). 40, 84

[121] Zandbergen, H. W., Gronsky, R., Wang, K. & Thomas, G. Structure of $(CuO)_2$ double layers in superconducting $YBa_2Cu_3O_7$. *Nature* **331**, 596–599 (1988). 40

[122] Cava, R. J. *et al.* Synthesis of bulk superconducting $YBa_2Cu_4O_8$ at one atmosphere oxygen pressure. *Nature* **338**, 328–330 (1989). 40

[123] Marsh, P. *et al.* Crystal-structure of the 80-K superconductor $YBa_2Cu_4O_8$. *Nature* **334**, 141–143 (1988). 40, 84

[124] Fischer, P., Karpinski, J., Kaldis, E., Jilek, E. & Rusiecki, S. High pressure preparation and neutron-diffraction study of the high T_c superconductor $YBa_2Cu_4O_{8+-x}$. *Solid State Communications* **69**, 531–533 (1989). 40

[125] Zaanen, J., Paxton, A. T., Jepsen, O. & Andersen, O. K. Chain-fragment doping and the phase diagram of $YBa_2Cu_3O_{7-x}$. *Phys. Rev. Lett.* **60**, 2685–2688 (1988). 41

[126] Zenner, T. *et al.* Electronic transport and specific heat of Ca-doped $YBa_2Cu_3O_x$-single crystals. *Journal of Low Temperature Physics* **105**, 909–914 (1996). 41

[127] Bernhard, C. & Tallon, J. L. Thermoelectric power of $Y_{1-x}Ca_xBa_2Cu_3O_{7-\delta}$: Contributions from CuO_2 planes and CuO chains. *Phys. Rev. B* **54**, 10201–10209 (1996). 41

[128] Jorgensen, J. D. *et al.* Structural and superconducting properties of orthorhombic and tetragonal $YBa_2Cu_3O_{7-x}$: The effect of oxygen stoichiometry and ordering on superconductivity. *Phys. Rev. B* **36**, 5731–5734 (1987). 41

[129] LaGraff, J. R. & Payne, D. A. Chemical diffusion of oxygen in single-crystal and polycrystalline $YBa_2Cu_3O_{6+x}$ determined by electrical-resistance measurements. *Phys. Rev. B* **47**, 3380–3390 (1993). 41

[130] Dechamps, M., Favrot-Colson, D. & Rosova, A. *Diffusionless Phase Transitions in Oxides and some Reconstructive and Martensitic Phase Transitions, vol.101-102 of Key Enginnering Materials*, chap. Twins and domain structure of YBaCuO (Trans Tech Publications, 1995). 42

[131] Voronkova, V. & Wolf, T. Thermomechanical detwinning of $YBa_2Cu_3O_{7-x}$ single crystals under reduced oxygen partial pressure. *Physica C* **218**, 175–180 (1993). 42, 108, 134

[132] Vlasko-Vlasov, V., Indenbom, M. & Ossipyan, Y. Polarization-optical study of $YBa_2Cu_3O_{7-x}$ single crystals. *Physica C* **153-155**, 1677–1678 (1988). 42

[133] Lin, C. & Kulakov, A. In situ observation of ferroelastic detwinning of YBCO single crystals by high temperature optical microscopy. *Physica C* **408-410**, 27–29 (2004). 42, 43, 108, 134

[134] Schilling, J. & Klotz, S. *Physical properties of high temperature superconductors Vol. III*, chap. The influence of High Pressure on the Superconducting and Normal Properties of High Temperature Superconductors (World Scientific, Singapore, 1992). 43, 44

[135] Takahashi, H. & Môri, N. *Studies of high temperature superconductors, vol.16*, chap. Recent Progress in High Pressure Investigation for high-T_c Superconductor (Nova Sci. Publ., New York, 1997). 43, 138

[136] Griessen, R. Pressure dependence of high-T_c superconductors. *Phys. Rev. B* **36**, 5284–5290 (1987). 43

[137] Monteverde, M. *et al.* High-pressure effects in fluorinated $HgBa_2Ca_2Cu_3O_{8+\delta}$. *EPL (Europhysics Letters)* **72**, 458 (2005). 43

[138] Hardy, F. *et al.* Enhancement of the Critical Temperature of $HgBa_2CuO_{4+\delta}$ by Applying Uniaxial and Hydrostatic Pressure: Implications for a Universal Trend in Cuprate Superconductors. *Phys. Rev. Lett.* **105**, 167002 (2010). 44

[139] Milic, M. M. Study on the Pressure Effect in $YBa_2Cu_3O_x$ as a Function Oxygen Content x. *Journal of Low Temperature Physics* **170**, 152–159 (2013). 44

[140] Neumeier, J. J. & Zimmermann, H. A. Pressure dependence of the superconducting transition temperature of as a function of carrier concentration: A test for a simple charge-transfer model. *Phys. Rev. B* **47**, 8385–8388 (1993). 44

[141] Murayama, C. *et al.* Correlation between the pressure-induced changes in the Hall-coefficient and T_c in superconducting cuprates. *Physica C* **183**, 277–285 (1991). 44, 131

[142] Huang, T., Itoh, M., Yu, J., Inaguma, Y. & Nakamura, T. Appearance of a maximum in the superconducting transition temperature of a $Bi_{2.2}Sr_{1.8}CaCu_2O_{8+y}$ single crystal under pressure. *Phys. Rev. B* **48**, 7712–7715 (1993). 44

[143] Parker, I. D. & Friend, R. H. The pressure dependence of the transport properties of $YBa_2Cu_3O_{7-\delta}$. *Journal of Physics C: Solid State Physics* **21**, 345 (1988). 44

[144] Jorgensen, J. *et al.* Pressure-induced charge transfer and dT_c/dP in $YBa_2Cu_3O_{7-x}$. *Physica C* **171**, 93–102 (1990). 44, 131

[145] Gupta, R. P. & Gupta, M. Relationship between pressure-induced charge transfer and the superconducting transition temperature in superconductors. *Phys. Rev. B* **51**, 11760–11766 (1995). 44

[146] Almasan, C. C. *et al.* Pressure dependence of T_c and Charge Transfer in $YBa_2Cu_3O_x$ ($6.35 \leq x \leq 7$) single crystals. *Phys. Rev. Lett.* **69**, 680–683 (1992). 44

[147] Cao, Y. *et al.* High-temperature superconducting $YSr_2Cu_3O_{7.5}$ under pressure. *Phys. Rev. B* **58**, 11201–11203 (1998). 44

[148] Fietz, W. *et al.* Giant pressure effect in oxygen deficient $YBa_2Cu_3O_x$. *Physica C* **270**, 258–266 (1996). 44, 45, 132

[149] Sieburger, R., Müller, P. & Schilling, J. Pressure dependence of the superconducting transition temperature in $Bi_2Sr_2CaCu_2O_{8+y}$ as a function of oxygen content. *Physica C* **181**, 335–339 (1991). 44, 45

[150] Wijngaarden, R. J., Jover, D. T. & Griessen, R. Intrinsic and carrier density effects on the pressure dependence of T_c of high-temperature superconductors. *Physica B* **265**, 128–135 (1999). 44

[151] Marsiglio, F. & Hirsch, J. E. Hole superconductivity and the high-T_c oxides. *Phys. Rev. B* **41**, 6435–6456 (1990). 44

[152] Sadewasser, S. *et al.* Pressure-dependent oxygen ordering in strongly underdoped $YBa_2Cu_3O_{7-y}$. *Phys. Rev. B* **56**, 14168–14175 (1997). 45, 132

[153] Sadewasser, S. *et al.* Relaxation effects in the transition temperature of superconducting $HgBa_2CuO_{4+\delta}$. *Phys. Rev. B* **60**, 9827–9835 (1999). 45, 132

[154] Veal, B. W. *et al.* Observation of temperature-dependent site disorder in $YBa_2Cu_3O_{7-x}$ below 150 °C. *Phys. Rev. B* **42**, 6305–6316 (1990). 45

[155] Kamihara, Y., Watanabe, T., Hirano, M. & Hosono, H. Iron-based layered superconductor $LaO_{1-x}F_xFeAs$ (x= 0.05-0.12) with T_c = 26 K. *Journal of the American Chemical Society* **130**, 3296 (2008). 47, 58

[156] Ishida, K., Nakai, Y. & Hosono, H. To what extent iron-pnictide new superconductors have been clarified: A progress report. *Journal of the Physical Society of Japan* **78**, 062001 (2009). 47

[157] Basov, D. N. & Chubukov, A. V. Manifesto for a higher T_c . *Nature* **7**, 272–276 (2011). 48

[158] Mizuguchi, Y. *et al.* Anion height dependence of T_c for the Fe-based superconductor. *Superconductor Science and Technology* **23**, 054013 (2010). 49

[159] Lee, C. *et al.* Relationship between crystal structure and superconductivity in iron-based superconductors. *Solid State Communications* **152**, 644 – 648 (2012). 49

[160] Johnston, D. The puzzle of high temperature superconductivity in layered iron pnictides and chalcogenides. *Advances in Physics* **59**, 803–1061 (2010). 49, 53

[161] Lee, C.-H. *et al.* Effect of structural parameters on superconductivity in fluorine-free LnFeAsO$_{1-y}$ (Ln = La, Nd). *Journal of the Physical Society of Japan* **77**, 083704 (2008). 49

[162] Horigane, K., Hiraka, H. & Ohoyama, K. Relationship between Structure and Superconductivity in FeSe$_{1-x}$Te$_x$. *Journal of the Physical Society of Japan* **78**, 074718 (2009). 49

[163] Kimber, S. *et al.* Similarities between structural distortions under pressure and chemical doping in superconducting BaFe$_2$As$_2$. *Nature Materials* **8**, 471–475 (2009). 49

[164] Garbarino, G. *et al.* Direct observation of the influence of the As-Fe-As angle on the T_c of superconducting SmFeAsO. *Phys. Rev. B* **84**, 024510 (2011). 49

[165] Garbarino, G. *et al.* Direct observation of the influence of the FeAs$_4$ tetrahedron on superconductivity and antiferromagnetic correlations in Sr$_2$VO$_3$FeAs. *EPL* **96**, 57002 (2011). 49

[166] Singh, D. & Du, M.-H. Density functional study of LaFeAsO$_{1-x}$F$_x$: A low carrier density superconductor near itinerant magnetism. *Phys. Rev. Lett.* **100**, 237003 (2008). 50

[167] Lu, D. *et al.* Electronic structure of the iron-based superconductor LaOFeP. *Nature* **455**, 81–84 (2008). 51

[168] Carrington, A. Quantum oscillation studies of the fermi surface of iron-pnictide superconductors. *Reports on Progress in Physics* **74**, 124507 (2011). 51

[169] Izyumov, Y. & Kurmaev, E. *High-T_c Superconductors Based on FeAs Compounds* (Springer Series in Materials Science, 2010). 51

[170] Mazin, I., Singh, D., Johannes, M. & Du, M. Unconventional superconductivity with a sign reversal in the order parameter of LaFeAsO$_{1-x}$F$_x$. *Phys. Rev. Lett.* **101**, 057003 (2008). 52, 56

[171] Mazin, I. & Schmalian, J. Pairing symmetry and pairing state in ferropnictides: Theoretical overview. *Physica C* **469**, 614–627 (2009). 52

[172] Paglione, G. R., J. High-temperature superconductivity in iron-based materials. *Nature Physics* **6**, 645–658 (2010). 52, 56, 60

[173] Liu, C. *et al.* Evidence for a Lifshitz transition in electron-doped iron arsenic superconductors at the onset of superconductivity. *Nature Physics* **6**, 419–423 (2010). 52

[174] Shimojima, T. *et al.* Pseudogap formation above the superconducting dome in iron pnictides. *Phys. Rev. B* **89**, 045101 (2014). 52

[175] Sun, L. *et al.* Re-emerging superconductivity at 48 kelvin in iron chalcogenides. *Nature* **483**, 67–69 (2012). 52

[176] Iimura, S. *et al.* Two-dome structure in electron-doped iron arsenide superconductors. *Nature Communications* **3**, 943 (2012). 52, 59

[177] Lumsden, M. D. & Christianson, A. D. Magnetism in Fe-based superconductors. *Journal of Physics: Condensed Matter* **22**, 203203 (2010). 53, 58, 159

[178] Dai, P., Hu, J. & Dagotto, E. Magnetism and its microscopic origin in iron-based high-temperature superconductors. *Nature Physics* **8**, 709–718 (2012). 53

[179] Tranquada, J. M., Xu, G. & Zaliznyak, I. A. Superconductivity, antiferromagnetism, and neutron scattering. *Journal of Magnetism and Magnetic Materials* **350**, 148 – 160 (2014). 53

[180] Subedi, A., Zhang, L., Singh, D. J. & Du, M. H. Density functional study of FeS, FeSe, and FeTe: Electronic structure, magnetism, phonons, and superconductivity. *Phys. Rev. B* **78**, 134514 (2008). 54

[181] Gretarsson, H. *et al.* Revealing the dual nature of magnetism in iron pnictides and iron chalcogenides using x-ray emission spectroscopy. *Phys. Rev. B* **84**, 100509 (2011). 54

[182] Ferber, J., Jeschke, H. O. & Valentí, R. Fermi Surface Topology of LaFePO and LiFeP. *Phys. Rev. Lett.* **109**, 236403 (2012). 54

[183] Stewart, G. R. Superconductivity in iron compounds. *Rev. Mod. Phys.* **83**, 1589–1652 (2011). 54, 159

[184] Park, J. T. *et al.* Electronic Phase Separation in the Slightly Underdoped Iron Pnictide Superconductor $Ba_{1-x}K_xFe_2As_2$. *Phys. Rev. Lett.* **102**, 117006 (2009). 54

[185] Cai, P. *et al.* Visualizing the microscopic coexistence of spin density wave and superconductivity in underdoped $NaFe_{1-x}Co_xAs$. *Nature Communications* **4**, 1596 (2013). 54

[186] Yi, M. *et al.* Dynamic competition between spin-density wave order and superconductivity in underdoped $Ba_{1-x}K_xFe_2As_2$. *Nature Communications* **5** (2014). 54

[187] Fernandes, R. M., Chubukov, A. V. & Schmalian, J. What drives nematic order in iron-based superconductors? *Nature Physics* **10**, 97–104 (2014). 54, 55, 159

[188] Davis, J. C. & Hirschfeld, P. J. Iron-based superconductors: Enigmatic nematic. *Nature Physics* **10**, 184–185 (2014). 54

[189] Chu, J.-H. *et al.* In-plane resistivity anisotropy in an underdoped iron arsenide superconductor. *Science* **329**, 824 (2010). 55

[190] Nandi, S. *et al.* Anomalous Suppression of the Orthorhombic Lattice Distortion in Superconducting $Ba(Fe_{1-x}Co_x)_2As_2$ Single Crystals. *Phys. Rev. Lett.* **104**, 057006 (2010). 55

[191] Fradkin, E., Kivelson, S. A., Lawler, M. J., Eisenstein, J. P. & Mackenzie, A. P. Nematic fermi fluids in condensed matter physics. *Annual Review of Condensed Matter Physics* **1**, 153–178 (2010). 55

[192] Hirschfeld, P. J. Gap symmetry and structure of Fe-based superconductors. *Reports on progress in physics* **74**, 124508 (2011). 56

[193] Chubukov, A. Pairing Mechanism in Fe-Based Superconductors. *Annual Review of Condensed Matter Physics* **3**, 57–92 (2012). 56, 57

[194] Song, C.-L. & Hoffman, J. E. Pairing insights in iron-based superconductors from scanning tunneling microscopy. *Current Opinion in Solid State and Materials Science* **17**, 39 – 48 (2013). 56

[195] Xianhui, C., Pengcheng, D., Donglai, F., Tao, X. & Fu-Chun, Z. Iron based high transition temperature superconductors. Arxiv1403.2612v1. 56

[196] Boeri, L., Dolgov, O. & Golubov, A. Is $LaFeAsO_{1-x}F_x$ an electron-phonon superconductor? *Phys. Rev. Lett.* **101**, 026403 (2008). 56, 87, 171

[197] Grafe, H.-J. *et al.* ^{75}As NMR Studies of Superconducting $LaFeAsO_{0.9}F_{0.1}$. *Phys. Rev. Lett.* **101**, 047003 (2008). 56

[198] Ding, H. *et al.* Observation of Fermi-surface-dependent nodeless superconducting gaps in $Ba_{0.6}K_{0.4}Fe_2As_2$. *Europhysics Letters* **83**, 47001 (2008). 56

[199] Evtushinsky, D. *et al.* Momentum-resolved superconducting gap in the bulk of $Ba_{1-x}K_xFe_2As_2$ from combined ARPES and μSR measurements. *New Journal of Physics* **11**, 055069 (2009). 56

[200] Inosov, D. *et al.* Normal-state spin dynamics and temperature-dependent spin-resonance energy in optimally doped $BaFe_{1.85}Co_{0.15}As_2$. *Nature Physics* **6**, 178–181 (2010). 56, 57

[201] Boeri, L., Calandra, M., Mazin, I. I., Dolgov, O. V. & Mauri, F. Effects of magnetism and doping on the electron-phonon coupling in $BaFe_2As_2$. *Phys. Rev. B* **82**, 020506 (2010). 56

[202] Kuroki, K. *et al.* Unconventional Pairing Originating from the Disconnected Fermi Surfaces of Superconducting $LaFeAsO_{1-x}F_x$. *Phys. Rev. Lett.* **101**, 087004 (2008). 56

[203] Moriya, T. & Ueda, K. Antiferromagnetic spin fluctuation and superconductivity. *Reports on Progress in Physics* **66**, 1299 (2003). 56

[204] Park, J. *et al.* Magnetic resonant mode in the low-energy spin-excitation spectrum of superconducting $Rb_2Fe_4Se_5$ single crystals. *Phys. Rev. Lett.* **107**, 177005 (2011). 56

[205] Hanaguri, T., Niitaka, S., Kuroki, K. & Takagi, H. Unconventional *s*-Wave Superconductivity in Fe(Se,Te). *Science* **328**, 474–476 (2010). 56

[206] Kontani, H. & Onari, S. Orbital-fluctuation-mediated superconductivity in iron pnictides: Analysis of the five-orbital hubbard-holstein model. *Phys. Rev. Lett.* **104**, 157001 (2010). 57

[207] Onari, S., Kontani, H. & Sato, M. Structure of neutron-scattering peaks in both s_{++}-wave and $s_{\pm}$-wave states of an iron pnictide superconductor. *Phys. Rev. B* **81**, 060504 (2010). 57

[208] Nandi, S. *et al.* Strong coupling of Sm and Fe magnetism in SmFeAsO as revealed by magnetic x-ray scattering. *Phys. Rev. B* **84**, 054419 (2011). 58

[209] Ren, Z.-A. *et al.* Superconductivity at 55 K in iron-based F-doped layered quaternary compound $SmO_{1-x}F_xFeAs$. *Chinese Physics Letters* **25**, 2215–2216 (2008). 57

[210] Ueda, S., Takeda, S., Takano, S., Yamamoto, A. & Naito, M. High-T_c and high-J_c SmFeAs(O,F) films on fluoride substrates grown by molecular beam epitaxy. *Applied Physics Letters* **99**, 232505 (2011). 57

[211] Kawaguchi, T. *et al.* Epitaxial Growth of NdFeAsO Thin Films by Molecular Beam Epitaxy. *Applied Physics Express* **2**, 093002 (2009). 57

[212] Takeda, S., Ueda, S., Takano, S., Yamamoto, S. & Naito, M. Growth of superconducting SmFeAs(O,F) epitaxial films by F diffusion. *Superconductor Science and Technology* **25**, 035007 (2012). 57

[213] Hanna, T. *et al.* Hydrogen in layered iron arsenides: Indirect electron doping to induce superconductivity. *Phys. Rev. B* **84**, 024521 (2011). 59

[214] Hosono, H. & Matsuishi, S. Superconductivity induced by hydrogen anion substitution in 1111-type iron arsenides. *Current Opinion in Solid State and Materials Science* **17**, 49–58 (2013). 59

[215] Kito, H., Eisaki, H. & Iyo, A. Superconductivity at 54 K in F-Free $NdFeAsO_{1-y}$. *Journal of the Physical Society of Japan* **77**, 063707 (2008). 59

[216] Wen, H.-H., Mu, G., Fang, L., Yang, H. & Zhu, X. Superconductivity at 25 K in hole-doped $(La_{1-x}Sr_x)OFeAs$. *Europhysics Letters* **82**, 17009 (2008). 59

[217] Wang, C. *et al.* Effects of cobalt doping and phase diagrams of $LFe_{1-x}Co_xAsO$ (L=La and Sm). *Phys. Rev. B* **79**, 054521 (2009). 59

[218] Chu, L. B., C.W. High pressure studies on Fe-pnictide superconductors. *Physica C* **469**, 385 (2009). 59

[219] Sefat, A. Pressure effects on two superconducting iron-based families. *Reports on progress in physics* **74**, 12 (2011). 59, 177

[220] Schilling, J., Hillier, N. & Foroozani, N. What have we learned from high-pressure experiments on Cu-oxide and Fe-based superconductors? *Journal of Physics: Conference Series* **449**, 012021 (2013). 59, 60

[221] Okada, H. *et al.* Superconductivity under high pressure in LaFeAsO. *Journal of the Physical Society of Japan* **77**, 113712 (2008). 60

[222] Alireza, P. *et al.* Superconductivity up to 29 K in $SrFe_2As_2$ and $BaFe_2As_2$ at high pressures. *Journal of Physics Condensed Matter* **21**, 012208 (2009). 60

[223] Duncan, W. J. *et al.* High pressure study of $BaFe_2As_2$- the role of hydrostaticity and uniaxial stress. *Journal of Physics: Condensed Matter* **22**, 052201 (2010). 60

[224] Hillier, N. J. *et al.* Intrinsic dependence of T_c on hydrostatic (He-gas) pressure for superconducting LaFePO, PrFePO, and NdFePO single crystals. *Phys. Rev. B* **86**, 214517 (2012). 60

[225] Bi, W. *et al.* Anomalous He-gas high-pressure studies on superconducting $LaO_{1-x}F_xFeAs$. *New Journal of Physics* **12**, 023005 (2010). 60

[226] Uhoya, W. *et al.* Phase transition and superconductivity of $SrFe_2As_2$ under high pressure. *Journal of Physics: Condensed Matter* **23**, 122201 (2011). 61

[227] Uhoya, W. *et al.* Collapsed tetragonal phase and superconductivity of $BaFe_2As_2$ under high pressure. *Phys. Rev. B* **82**, 144118 (2010). 61

[228] Mittal, R. *et al.* Ambient- and low-temperature synchrotron x-ray diffraction study of $BaFe_2As_2$ and $CaFe_2As_2$ at high pressures up to 56 GPa. *Phys. Rev. B* **83**, 054503 (2011). 61

[229] Uhoya, W. *et al.* Anomalous compressibility effects and superconductivity of $EuFe_2As_2$ under high pressures. *Journal of Physics Condensed Matter* **22**, 292202 (2010). 61

[230] Zhao, J. *et al.* Structure stability and compressibility of iron-based superconductor $Nd(O_{0.88}F_{0.12})FeAs$ under high pressure. *Journal of the American Chemical Society* **130**, 13828 (2008). 61

[231] Kumar, R. S. *et al.* Pressure induced structural transition and enhancement of superconductivity in Co doped CeFeAsO. *Applied Physics Letters* **98**, 012511 (2011). 61

[232] Goldman, A. I. *et al.* Lattice collapse and quenching of magnetism in $CaFe_2As_2$ under pressure: A single-crystal neutron and x-ray diffraction investigation. *Phys. Rev. B* **79**, 024513 (2009). 61, 164

[233] Yu, W. *et al.* Absence of superconductivity in single-phase $CaFe_2As_2$ under hydrostatic pressure. *Phys. Rev. B* **79**, 020511 (2009). 61, 164

[234] Kreyssig, A. *et al.* Pressure-induced volume-collapsed tetragonal phase of $CaFe_2As_2$ as seen via neutron scattering. *Phys. Rev. B* **78**, 184517 (2008). 61, 164

[235] Bishop, M. *et al.* Formation of collapsed tetragonal phase in $EuCo_2As_2$ under high pressure. *Journal of Physics Condensed Matter* **22**, 425701 (2010). 61

[236] Devereaux, T. P. & Hackl, R. Inelastic light scattering from correlated electrons. *Rev. Mod. Phys.* **79**, 175–233 (2007). 64

[237] Cardona, M. *Light Scattering in Solids II* (Springer, 1981). 64, 70

[238] Strohm, T. *Electronic Raman scattering in high-temperature superconductors*. Ph.D. thesis, Universität Stuttgart (1999). 64

[239] Cardona, M. *Raman Scattering in Materials Science* (Springer, 2000). 64, 77, 85, 86

[240] N. Ashcroft, N. D. M. *Solid State Physics* (Brooks/Cole, 1975). 65

[241] Pines, D. *Elementary Excitations in Solids : Lectures on Phonons, Electrons, and Plasmons* (Westview Press, 1999). 65, 68

[242] Long, D. *The Raman Effect: A Unified Treatment of the Theory of Raman Scattering by Molecules* (Wiley and Sons Ltd, 2002). 67

[243] Wallis R.F., B. M. *Many-Body Aspects of Solid State Spectroscopy* (North Holland Physics Publishing, 1986). 68, 70, 71

[244] Taylor, P. & Heinonen, O. *A Quantum Approach to Condensed Matter Physics* (Cambridge University Press, 2002). 68

[245] Yu, P. & Cardona, M. *Fundamentals of Semiconductors* (Springer, 2005). 70

[246] Klein, M. *Light Scattering in Solids IV*, chap. Electronic Raman Scattering (Springer, 1984). 71

[247] Cowley, R. A. Anharmonic crystals. *Reports on Progress in Physics* **31**, 123 (1968). 71, 72

[248] Mahan, G. *Many Particle Physics* (third edition, Kluwer Academic/Plenum Publishers, 2000). 71

[249] Menéndez, J. & Cardona, M. Temperature dependence of the first-order raman scattering by phonons in Si, Ge, and α-Sn: Anharmonic effects. *Phys. Rev. B* **29**, 2051–2059 (1984). 72

[250] Lucazeau, G. Effect of pressure and temperature on raman spectra of solids: anharmonicity. *Journal of Raman Spectroscopy* **34**, 478–496 (2003). 73, 75, 76

[251] Klemens, P. G. Anharmonic decay of optical phonons. *Phys. Rev.* **148**, 845–848 (1966). 73, 136, 150, 151, 170, 171, 176

[252] Fano, U. Effects of configuration interaction on intensities and phase shifts. *Phys. Rev.* **124**, 1866–1878 (1961). 74

[253] Thomsen, C. & Cardona, M. *Physical propertiesof high temperature superconductors I* (World Scientific, Singapore, 1992, 1988). 74, 77

[254] Hadjiev, V. G. *et al.* Strong superconductivity-induced phonon self-energy effects in $HgBa_2Ca_3Cu_4O_{10+\delta}$. *Phys. Rev. B* **58**, 1043–1050 (1998). 74

[255] Zeyher, R. & Zwicknagl, G. Superconductivity-induced phonon self-energy effects in high-T_c superconductors. *Zeitschrift für Physik B Condensed Matter* **78**, 175–190 (1990). 74, 118, 137

[256] Nicol, E., Jiang, C. & Carbotte, J. Effect of *d*-wave energy-gap symmetry on Raman shifts. *Phys. Rev. B* **47**, 8131–8139 (1993). 74, 118, 137

[257] Weinstein, B. & Zallen, R. *Light Scattering in Solids IV*, chap. Pressure-Raman effects in Covalent and Molecular Solids (Springer, 1984). 75, 76

[258] Goncharov, A. Raman spectroscopy at high pressures. *International Journal of Spectroscopy* **2012**, 617528 (2012). 75

[259] Special Issue: "Raman Spectroscopy under Extreme Conditions". *Journal of Raman Spectroscopy* **34**, 475–637 (2003). 75

[260] Goncharov, A. & Struzhkin, V. Raman spectroscopy of metals, high-temperature superconductors and related materials under high pressure. *Journal of Raman Spectroscopy* **34**, 532–548 (2003). 75

[261] Debernardi, A., Ulrich, C., Syassen, K. & Cardona, M. Raman linewidths of optical phonons in *3C-SiC* under pressure: First-principles calculations and experimental results. *Phys. Rev. B* **59**, 6774–6783 (1999). 76

[262] Merlin, R., Pinczuk, A. & Weber, W. *Raman Scattering in Materials Science*, chap. Overview of phonon Raman Scattering in Solids (Springer, 2000). 77

[263] Rousseau, D., Bauman, R. & Porto, S. Normal mode determination in crystals. *Journal of Raman Spectroscopy* **10**, 253–290 (1981). 77

[264] Cardona, M. Raman scattering in high T_c superconductors: phonons, electrons, and electron-phonon interaction. *Physica C* **317-318**, 30 – 54 (1999). 77, 109

[265] Stavola, M. *et al.* Cu-O vibrations of $Ba_2YCu_3O_x$. *Phys. Rev. B* **36**, 850–853 (1987). 79

[266] Liu, R. *et al.* Frequencies, eigenvectors, and single-crystal selection rules of k=0 phonons in $YBa_2Cu_3O_{7-\delta}$: Theory and experiment. *Phys. Rev. B* **37**, 7971–7974 (1988). 79, 80

[267] Humlíček, J. *et al.* Lattice vibrations of $Y_{1-y}Pr_xBa_2Cu_3O_7$: theory and experiment. *Physica C* **206**, 345 (1993). 79, 80, 81

[268] McCarty, K. F., Liu, J. Z., Shelton, R. N. & Radousky, H. B. Raman-active phonons of a twin-free $YBa_2Cu_3O_7$ crystal: A complete polarization analysis. *Phys. Rev. B* **41**, 8792–8797 (1990). 79, 109, 113

[269] Ambrosch-Draxl, C. *et al.* Raman scattering in $YBa_2Cu_3O_7$: A comprehensive theoretical study in comparison with experiments. *Phys. Rev. B* **65**, 064501 (2002). 79, 81

[270] Bohnen, K., Heid, R. & Krauss, M. Phonon dispersion and electron-phonon interaction for $YBa_2Cu_3O_7$ from first-principles calculations. *Europhys. Lett.* **64**, 104–110 (2003). 79, 81, 121, 122, 130, 137

[271] Bakr, M. *Electronic and Phononic Raman Scattering in Twin-Free $YBa_2Cu_3O_{6+x}$*. Ph.D. thesis, Universität Stuttgart (2010). 81, 82, 109

[272] Bahrs, S. *et al.* Raman spectroscopy with UV excitation on untwinned single crystals of $YBa_2Cu_3O_{7-\delta}$. *Phys. Stat. Solidi (b)* **241**, 63–66 (2004). 81

[273] Panfilov, A. G., Limonov, M. F., Rykov, A. I., Tajima, S. & Yamanaka, A. Superconductivity-induced effect on "Raman-forbidden" modes in underdoped $YBa_2Cu_3O_{7-x}$ single crystals. *Phys. Rev. B* **57**, 5634–5637 (1998). 81, 112, 114, 115, 127, 128

[274] Thomsen, C., Cardona, M., Gegenheimer, B., Liu, R. & Simon, A. Untwinned single crystals of $YBa_2Cu_3O_{7-\delta}$: An optical investigation of the a-b anisotropy. *Phys. Rev. B* **37**, 9860–9863 (1988). 81

[275] Wake, D. R., Slakey, F., Klein, M. V., Rice, J. P. & Ginsberg, D. M. Optically induced metastability in untwinned single-domain $YBa_2Cu_3O_7$. *Phys. Rev. Lett.* **67**, 3728–3731 (1991). 81, 112, 115, 127, 128

[276] Iliev, M., Thomsen, C., Hadjiev, V. & Cardona, M. Resonant Raman scattering of oxygen-deficient $YBa_2Cu_3O_{7-\delta}$: Evidence for the coexistence of *ortho*-I, *ortho*-II, and tetragonal microstructures. *Phys. Rev. B* **47**, 12341–12344 (1993). 82

[277] Misochko, O., Tajima, S., Miyamoto, S. & Koshizuka, N. Raman study of *ortho*-II phase of the $YBa_2Cu_3O_7$ single crystal: Role of local oxygen ordering in the doping. *Solid State Communications* **92**, 877 – 882 (1994). 82, 111

[278] Iliev, M. *et al.* Raman study of twin-free *ortho*-II $YBa_2Cu_3O_{6.5}$ single crystals. *Phys. Rev. B* **77**, 174302 (2008). 83, 111, 113, 115

[279] Blumberg, G. E. *et al.* Raman-scattering spectra of $YBa_2Cu_3O_{6.5}$ superconductor with ordered oxygen vacancies. *JETP Lett.* **49**, 439 (1989). 82

[280] Iliev, M. N., Hadjiev, V. G. & Ivanov, V. G. Raman spectroscopy of local structure and reordering processes in $YBa_2Cu_3O_{7-\delta}$-type compounds. *Journ. of Raman Spect.* **27**, 333–342 (1996). 83, 109, 111

[281] Heyen, E. T. *et al.* Optical phonons in $YBa_2Cu_4O_8$ and $Y_2Ba_4Cu_7O_{15-\delta}$. *Phys. Rev. B* **41**, 11058–11067 (1990). 85, 86, 134, 141

[282] Trajnerowicz, A. *et al.* Isotope effect on the optical phonons of $YBa_2Cu_4O_8$ studied by far-infrared ellipsometry and Raman scattering. *Phys. Rev. B* **74**, 104513 (2006). 85, 86

[283] Krantz, M., Rosen, H., Macfarlane, R., Asmar, N. & Morris, D. Raman spectra and normal mode assignments of superconducting $YBa_2Cu_4O_8$ single crystals. *Physica C* **162-164**, 1089 – 1090 (1989). 86, 134

[284] Bordet, P. *et al.* Single crystal study of the 80K superconductor $YBa_2Cu_4O_8$. *Physica C* **162-164**, 524 – 525 (1989). 86

[285] Zhang, L. *et al.* Spin-dependent electron-phonon interaction in smfeaso by low-temperature raman spectroscopy. *Journal of the American Chemical Society* **132**, 15223 (2010). 87, 170

[286] Yildirim, T. Origin of the 150-K anomaly in LaFeAsO: Competing antiferromagnetic interactions, frustration, and a structural phase transition. *Phys. Rev. Lett.* **101**, 057010 (2008). 87, 167, 168

[287] Zhao, S. *et al.* Raman spectra in iron-based quaternary $CeO_{1-x}F_xFeAs$ and $LaO_{1-x}F_xFeAs$. *Superconductor Science and Technology* **22**, 015017 (2009). 87, 89, 167, 169

[288] Marini, C. *et al.* The optical phonon spectrum of SmFeAsO. *Europhys. Lett.* **84**, 67013 (2008). 87

[289] Litvinchuk, A. *et al.* Raman-scattering study of $K_xSr_{1-x}Fe_2As_2$ (x=0.0,0.4). *Phys. Rev. B* **78**, 06050 (2008). 87, 169

[290] Wertheim, G. K., Butler, M. A., West, K. W. & Buchanan, D. N. E. Determination of the Gaussian and Lorentzian content of experimental line shapes. *Review of Scientific Instruments* **45**, 1369 (1974). 89

[291] Jayaraman, A. Diamond anvil cell and high-pressure physical investigations. *Rev. Mod. Phys.* **55**, 65 (1983). 93

[292] Eremets, M. I. *High Pressure Experimental Methods* (Oxford Science Publications, 1996). 93, 100

[293] Lawson, A. W. & Tang, T. Y. A diamond bomb for obtaining powder pictures at high pressures. *Rev. Sci. Instrum.* **21**, 815 (1950). 93

[294] Jamieson, J. C., Lawson, A. W. & Nachtrieb, N. D. New device for obtaining x-ray diffraction patterns from substances exposed to high pressure. *Rev. Sci. Instrum.* **30**, 1016 (1959). 94

[295] Weir, C. E., Lippincott, E. R., van Valkenburg, A. & Bunting, E. N. *J. Res. Natl. Bur. Stand., Sect. A* **63**, 55 (1959). 94

[296] Valkenburg, A. V. *Proceedings of Conference Internationale Sur-les-Hautes Pressions* (LeCreusot, Saone-et-Loire, France, 1965). 94

[297] Forman, R. A., Piermarini, G. J., Barnett, J. D. & Block, S. Pressure measurement made by the utilization of the ruby sharp-line luminescence. *Science* **176**, 284 (1972). 94, 97

[298] Piermarini, G. J., Block, S. & Barnett, J. D. Hydrostatic limits in liquids and solids to 100 kbar. *J. Appl. Phys.* **44**, 5377 (1973). 94, 100

[299] Papadopoulos, A. & Anastassakis, E. Optical Properties of Diamond. *Phys. Rev. B* **43**, 5090–5097 (1991). 94

[300] Phillip, H. & Taft, E. Optical Properties od Diamond in Vacuum Ultraviolet. *Phys. Rev.* **127**, 159–161 (1962). 94

[301] Kaiser, W. & Bond, W. Nitrogen, a major impurity in common type-I diamond. *Physical Review* **115**, 857–863 (1959). 94

[302] Huber, G., Syassen, K. & Holzapfel, W. B. Pressure dependence of 4f levels in europium pentaphosphate up to 400 kbar. *Phys. Rev. B* **15**, 5123 (1977). 95

[303] Letoullec, R., Pinceaux, J. P. & Loubeyre, P. The membrane diamond anvil cell: A new device for generating continuous pressure and temperature variations. *High Pressure Research* **1**, 77–90 (1988). 96

[304] Syassen, K. Ruby under pressure. *High Pres. Res.* **28**, 75 (2008). 96

[305] Sugano, S. & Tanabe, Y. Absorption spectra of Cr^{3+} in Al_2O_3, part a. theoretical studies of the absorption bands and lines. *J. Phys. Soc. Jpn.* **13**, 880 (1958). 97

[306] Sugano, S., Tanabe, Y. & Kimura, H. *Multiplets of transition metal ions in crystals* (Academic Press, New York, 1970). 97

[307] Finger, L. W. & Hazen, R. M. Crystal structure and comparison of ruby to 46 kbar. *J. Appl. Phys.* **49**, 5823 (1978). 97

[308] Piermarini, G. J., Block, S., Barnett, J. D. & Forman, R. A. Calibration of the pressure dependence of the R1 Ruby Fluorescence line to 195 kbar. *J. Appl. Phys.* **46**, 2774 (1975). 97

[309] Mao, H. K., Xu, J. & Bell, P. Calibration of the Ruby Pressure Gauge to 800 kbar Under Quasi-Hydrostatic Conditions. *J. Geophys. Res.* **91**, 4673 (1986). 98

[310] Ulrich, C. *Untersuchungen elektronisch und gitterdynamischer Eigenschaften von Halbleitern unter hohem Druck*. Ph.D. thesis, Stuttgart (1997). 98, 99

[311] McCumber, D. E. & Sturge, M. D. Linewidth and temperature shift of the R lines in ruby. *J. Appl. Phys.* **34**, 1682 (1963). 98

[312] Wunder, S. L. & Schoen, P. E. Pressure measurement at high temperatures in the diamond anvil cell. *J. Appl. Phys.* **52**, 3772 (1981). 99

[313] Klotz, S., Chervin, J.-C., Munsch, P. & Le Marchand, G. Hydrostatic limits of 11 pressure transmitting media. *Journal of Physics D-Applied Physics* **42**, 075413 (2009). 100

[314] I. Fujishiro, S. B., G. J. Piermarini & Munro, R. G. *Proc. 8th AIRAPT Conf., Uppsala, (Arkitektkopia, Uppsala, 1982), vol.II* 608 (1981). 100

[315] Loubeyre, P. *et al.* Equation of state and phase diagram of solid ^{4}He from single-crystal x-ray diffraction over a large P-T domain. *Phys. Rev. Lett.* **71**, 2272 (1993). 100

[316] Mao, H. K. *et al.* High pressure phase diagram and equation of state of solid helium from single crystal x-ray diffraction up to 23.3 GPa. *Phys. Rev. Let.* **60**, 2649 (1988). 100

[317] Dewaele, A. & Loubeyre, P. Pressurizing conditions in helium-pressure-transmitting medium. *High Pressure Research* **27**, 419–429 (2007). 100

[318] Monceau, P. Electronic crystals: an experimental overview. *Advances in Physics* **61**, 325–581 (2012). 107

[319] Le Tacon, M. *et al.* Inelastic X-ray scattering in $YBa_2Cu_3O_{6.6}$ reveals giant phonon anomalies and elastic central peak due to charge-density-wave formation. *Nature Physics* **10**, 52–58 (2014). 107, 122, 135

[320] Blackburn, E. *et al.* Inelastic x-ray study of phonon broadening and charge-density wave formation in *Ortho*-II-ordered $YBa_2Cu_3O_{6.54}$. *Phys. Rev. B* **88**, 054506 (2013). 107, 122

[321] Tassini, L. *et al.* Dynamical Properties of Charged Stripes in $La_{2-x}Sr_xCuO_x$. *Phys. Rev. Lett.* **95**, 117002 (2005). 107

[322] Caprara, S., Di Castro, C., Grilli, M. & Suppa, D. Charge-Fluctuation Contribution to the Raman Response in Superconducting Cuprates. *Phys. Rev. Lett.* **95**, 117004 (2005). 107

[323] Sugai, S., Takayanagi, Y. & Hayamizu, N. Phason and Amplitudon in the Charge-Density-Wave Phase of One-Dimensional Charge Stripes in $La_{2-x}Sr_xCuO_x$. *Phys. Rev. Lett.* **96**, 137003 (2006). 107

[324] Lin, C., Liang, B. & Chen, H. Top-seeded solution growth of Ca-doped YBCO single crystals. *J. of Cryst. Growth* **237-239**, 778–782 (2002). 108

[325] Thomsen, C. *et al.* Systematic Raman and infrared studies of the superconductor $YBa_2Cu_3O_{7-x}$ as a function of oxygen concentration (0≤x≤1). *Solid State Communications* **65**, 55 – 58 (1988). 109

[326] Macfarlane, R. M., Rosen, H. J., Engler, E. M., Jacowitz, R. D. & Lee, V. Y. Raman study of the effect of oxygen stoichiometry on the phonon spectrum of the high-T_c superconductor $YBa_2Cu_3O_x$. *Phys. Rev. B* **38**, 284–289 (1988). 109

[327] Bakr, M. *et al.* Electronic and phononic Raman scattering in detwinned $YBa_2Cu_3O_{6.95}$ and $Y_{0.85}Ca_{0.15}Ba_2Cu_3O_{6.95}$: *s*-wave admixture to the $d_{x^2-y^2}$-wave order parameter. *Phys. Rev. B* **80**, 064505 (2009). 109, 118, 119, 154

[328] Altendorf, E., Chen, X. K., Irwin, J., Liang, R. & Hardy, W. Temperature Dependences of the 340 cm^{-1}, 440 cm^{-1} and 500 cm^{-1} Raman modes of $YBa_2Cu_3O_y$ for 6.7≤y≤7.0. *Phys. Rev. B* **47**, 8140–8150 (1993). 109, 118, 154

[329] Burns, G., Dacol, F., Feild, C. & Holtzberg, F. Oxygen mobility in $YBa_2Cu_3O_{7-\delta}$: A Raman study. *Solid State Communications* **75**, 893 – 896 (1990). 113

[330] Heyen, E. T. *et al.* Resonant Raman scattering in $YBa_2Cu_3O_7$: Band theory and experiment. *Phys. Rev. Lett.* **65**, 3048–3051 (1990). 114, 115

[331] Friedl, B., Thomsen, C. & Cardona, M. Determination of the superconducting gap in $RBa_2Cu_3O_{7-\delta}$. *Phys. Rev. Lett.* **65**, 915–918 (1990). 118, 154

[332] Sugai, S. Lattice Vibrations in the Charge-Density-Wave States of Layered Transition Metal Dichalcogenides. *Physica Status Solidi (b)* **129**, 13–39 (1985). 121

[333] Bakr, M. *et al.* Lattice dynamical signature of charge density wave formation in underdoped $YBa_2Cu_3O_{6+x}$. *Phys. Rev. B* **88**, 214517 (2013). 123

[334] Blanco-Canosa, S. *et al.* Resonant X-ray Scattering Study of Charge Density Wave Correlations in $YBa_2Cu_3O_{6+x}$. ArXiv:1406.1595. 123, 134

[335] Hücker, M. *et al.* Competing charge, spin, and superconducting orders in underdoped $YBa_2Cu_3O_y$. Arxiv:1405.7001. 123, 134

[336] Panfilov, A. G., Rykov, A. I., Tajima, S. & Yamanaka, A. Photoinduced oxygen reordering in $YBa_2Cu_3O_{7-x}$ single crystals. *Phys. Rev. B* **58**, 12459–12466 (1998). 128

[337] Bernhard, C. *et al.* In-plane polarized collective modes in detwinned $YBa_2Cu_3O_{6.95}$ observed by spectral ellipsometry. *Solid State Communications* **121**, 93 – 97 (2002). 130

[338] LeBoeuf, D. *et al.* Electron pockets in the Fermi surface of hole-doped high-T_c superconductors. *Nature* **450**, 533–536 (2007). 133

[339] Song, Y., Peng, J., Wang, X., Sun, G. & Lin, C. Ambient-condition growth of superconducting $YBa_2Cu_4O_8$ single crystals using KOH flux. *Journal of Crystal Growth* **300**, 263 – 266 (2007). 134

[340] Sun, G. L., Song, Y. T. & Lin, C. T. Investigation of $YBa_2Cu_4O_8$ single crystal growth by KOH flux. *Superconductor Science and Technology* **21**, 125001 (2008). 134

[341] White, J. S. *et al.* Magnetic field dependence of the basal-plane superconducting anisotropy in $YBa_2Cu_4O_8$ from small-angle neutron scattering measurements of the vortex lattice. *Phys. Rev. B* **89**, 024501 (2014). 135

[342] LeBoeuf, D. *et al.* Thermodynamic phase diagram of static charge order in underdoped $YBa_2Cu_3O_y$. *Nature Physics* **9**, 79–83 (2013). 137

[343] Achkar, A. J. *et al.* Impact of quenched oxygen disorder on charge density wave order in $YBa_2Cu_3O_{6+x}$. ArXiv:1312.6630v1. 137

[344] Grissonnanche, G. *et al.* Direct measurement of the upper critical field in cuprate superconductors. *Nature Communications* **5**, 3280 (2014). 137

[345] Yim, K., Oitmaa, J. & Elcombe, M. Lattice dynamics of $YBa_2Cu_4O_8$. *Solid State Communications* **77**, 385 – 388 (1991). 137

[346] Heyen, E. T., Cardona, M., Karpinski, J., Kaldis, E. & Rusiecki, S. Two superconducting gaps and electron-phonon coupling in $YBa_2Cu_4O_8$. *Phys. Rev. B* **43**, 12958–12975 (1991). 137, 138, 152

[347] Käll, M., Litvinchuk, A., Berastegui, P., Johansson, L. & Börjesson, L. Temperature Dependence of Phonon Raman Scattering in $Y_2Ba_4Cu_7O_{15-\delta}$. *Physica C* **225**, 317–324 (1994). 137

[348] Bäckström, J. *et al.* Raman scattering in $YBa_2Cu_4O_8$ and $PrBa_2Cu_4O_8$: Indications of pseudogap effects in nonsuperconducting $PrBa_2Cu_4O_8$. *Phys. Rev. B* **61**, 7049–7054 (2000). 137, 138

[349] Quilty, J. W., Tajima, S., Adachi, S. & Yamanaka, A. Evidence of the pseudogap and superconducting gap in the *ab*-plane electronic raman continuum of $YBa_2Cu_4O_8$. *Phys. Rev. B* **65**, 094513 (2002). 137, 138

[350] Litvinchuk, A., Thomsen, C. & Cardona, M. Phonon anomalies above T_c in $YBa_2Cu_4O_8$ and $YBa_2Cu_3O_{7-\delta}$ superconductors: An effect of coupling to spin excitations. *Solid State Communications* **83**, 343–347 (1992). 138

[351] Bucher, B., Karpinksi, J., Kaldis, E. & Wachter, P. Strong Pressure Dependence of T_c of the new 80-K phase $YBa_2Cu_4O_{8+x}$. *Physica C* **157**, 478–482 (1989). 138

[352] Diederichs, J. *et al.* Critical Currents in Tl-2122 and Y-124 Sinters under High Hydrostatic Pressure. *Supercond. Sci. and Technol.* **4**, 97–99 (1991). 138

[353] Tissen, V., Nefedova, M., Emel'chenko, G., Bukhtiyaro, P. & Saifullin, N. Disappearance of superconductivity in $YBa_2Cu_4O_8$ at a pressure of about 11 GPa. *Superconductivity: Physics, Chemistry, Technology* **4**, 586–588 (1991). 138, 139, 158

[354] Braithwaite, D. *et al.* The superconducting properties of $YBa_2Cu_4O_8$ single crystals under hydrostatic pressure (up to 9.5 GPa). *Physica C* **178**, 75 – 80 (1991). 138

[355] Van Eenige, E. *et al.* Superconductivity at 108 K in $YBa_2Cu_4O_8$ at pressures up to 12 GPa. *Physica C* **168**, 482–488 (1990). 138, 139, 140, 148, 157, 158

[356] Scholtz, J., Van Eenige, E., Wijngaarden, R. & Griessen, R. Pressure dependence of T_c and H_{c2} of $YBa_2Cu_4O_8$. *Phys. Rev. B* **45**, 3077–3092 (1992). 138, 139, 140, 148, 157, 158

[357] Mito, M. *et al.* Effective Disappearance of the Meissner Signal in the Cuprate Superconductor $YBa_2Cu_4O_8$ under Uniaxial Strain. *Journal of the Physical Society of Japan* **83**, 023705 (2014). 138, 139, 140, 157, 158

[358] Bauer, E. & Sigrist, M. (eds.) *Non-centrosymmetric Superconductors: Introduction and Overview* (Springer Heidelberg, 2011). 140

[359] Watanabe, N., Kosuge, M., Koshizuka, N., Adachi, S. & Yamauchi, H. Phonon Raman scattering of polycrystalline $YBa_2Cu_4O_8$ under hydrostatic pressure. *Phys. Rev. B* **49**, 9226–9229 (1994). 140, 141

[360] Kakihana, M. *et al.* Anomalous behaviour of the 147 cm^{-1} Cu(2) raman mode in $YBa_2Cu_4O_8$ under high pressure. signature of change in the electronic state of the CuO_2 plane. *Physica C* **230**, 199 – 206 (1994). 140, 141

[361] Osada, M., Kakihana, M., Käll, M. & Börjesson, L. Pressure-induced effects in high-T_c superconductors: Raman scattering as a probe of charge-lattice dynamics under high pressure. *Physica C* **357-360**, 142–145 (2001). 140, 141

[362] Lampakis, D., Palles, D., Liarokapis, E., Kazakov, S. & Karpinski, J. Hydrostatic-pressure-induced phase separation in the $YBa_2Cu_4O_8$ superconductor. *Phys.Rev. B* **72**, 014539 (2005). 140, 141, 143

[363] Boley, M. S., Chandrasekhar, M., Chandrasekhar, H., Wu, Y. & Boolchand, P. Hydrostatic-pressure Studies of the Raman-active Phonon Modes In the Bulk High-temperature Superconductor $YBa_2Cu_4O_8$. *AIP Conf. Proc.* **309**, 681 (1994). 141

[364] Muramatsu, T., Pham, D. & Chu, C. W. A possible pressure-induced superconducting-semiconducting transition in nearly optimally doped single crystalline $YBa_2Cu_3O_{7-\delta}$. *Applied Physics Letters* **99**, 052508 (2011). 142

[365] Ludwig, H. A. *et al.* X-ray investigations of $Y_1Ba_2Cu_4O_8$ under high pressure. *Physica C* **167**, 335–338 (1990). 143, 158

[366] Nelmes, R., Loveday, J., Kaldis, E. & Karpinski, J. The crystal structure of $YBa_2Cu_4O_8$ as a function of pressure up to 5GPa. *Physica C* **172**, 311 – 324 (1990). 143

[367] Yamada, Y. *et al.* Structural changes of superconducting $YBa_2Cu_4O_8$ under high pressure. *Physica C* **173**, 185–194 (1991). 143

[368] Kroumova, E. *et al.* Bilbao Crystallographic Server : Useful Databases and Tools for Phase-Transition Studies. *Phase Transitions* **76**, 155–170 (2003). 144

[369] Blöchl, P. E. Projector augmented-wave method. *Phys. Rev. B* **50**, 17953–17979 (1994). 146

[370] Kresse, G. & Joubert, D. From ultrasoft pseudopotentials to the projector augmented-wave method. *Phys. Rev. B* **59**, 1758–1775 (1999). 146

[371] Kresse, G. & Furthmüller, J. Efficient iterative schemes for *ab initio* total-energy calculations using a plane-wave basis set. *Phys. Rev. B* **54**, 11169–11186 (1996). 146

[372] Baroni, S., de Gironcoli, S., Dal Corso, A. & Giannozzi, P. Phonons and related crystal properties from density-functional perturbation theory. *Rev. Mod. Phys.* **73**, 515 (2001). 146

[373] Giannozzi, P. *et al.* QUANTUM ESPRESSO: a modular and open-source software project for quantum simulations of materials. *J. Phys.: Condens. Matter* **21**, 395502 (2009). 146

[374] Limonov, M. F., Tajima, S. & Yamanaka, A. Phononic and electronic raman spectroscopy of the pseudogap state in underdoped $YBa_2Cu_3O_{7-x}$. *Phys. Rev. B* **62**, 11859–11863 (2000). 154

[375] Goncharov, A., Struzhkin, V. & Syassen, K. Superconductivity-induced phonon self-energy effects and electronic Raman scattering in $YBa_2Cu_3O_{7-x}$ single crystals under pressure. *AIP Conference Proceedings* **309**, 707 (1994). 155

[376] Zhou, T., Syassen, K., Cardona, M., Karpinski, J. & Kaldis, E. Electronic Raman scattering in $YBa_2Cu_4O_8$ at high pressure. *Solid State Communications* **99**, 669–673 (1996). 155

[377] Yu, J., Park, K. T. & Freeman, A. Electronic structure and properties of $YBa_2Cu_4O_8$. *Physica C* **172**, 467–476 (1991). 155

[378] Rotundu, C. Comment on "Retention of the tetragonal to orthorhombic structural transition in F-substituted SmFeAsO: A new phase diagram for $SmFeAs(O_{1-x}F_x)$)". *Phys. Rev. Let.* **110**, 209701 (2013). 159

[379] Kasahara, S. *et al.* Electronic nematicity above the structural and superconducting transition in $BaFe_2$ $(As_{1-x}P_x)_2$. *Nature* **486**, 382 (2012). 159

[380] Zhigadlo, N. *et al.* Single crystals of superconducting $SmFeAsO_{1-x}F_y$ grown at high pressure. *Journal of Physics Condensed Matter* **20**, 342202 (2008). 160

[381] Karpinski, J. *et al.* Single crystals of $LnFeAsO_{1-x}F_x$ (Ln = La, Pr, Nd, Sm, Gd) and $Ba_{1-x}Rb_xFe_2As_2$: Growth, structure and superconducting properties. *Physica C* **469**, 370 (2009). 160

[382] Hammersley, A., Svensson, S., Hanfland, M., Fitch, A. & Hausermann, D. Two-dimensional detector software: From real detector to idealised image or two-theta scan. *High Pressure Research* **14**, 235 (1996). 160

[383] Takahashi, H. *et al.* High-pressure studies on superconductivity in $LaFeAsO_{1-x}F_x$ and $SmFeAsO_{1-x}F_x$. *Journal of Superconductivity and Novel Magnetism* **22**, 595 (2009). 164, 165, 166, 177

[384] Hadjiev, V., Iliev, M., Sasmal, K., Sun, Y.-Y. & Chu, C. Raman spectroscopy of RFeAsO (R =Sm, La). *Phys. Rev. B* **77**, 220505 (2008). 167, 169, 173, 175

[385] Chauvière, L. *et al.* Doping dependence of the lattice dynamics in $Ba(Fe_{1-x}Co_x)_2As_2$ studied by Raman spectroscopy. *Phys. Rev. B* **80**, 094504 (2009). 168, 169, 170

[386] Schafgans, A. A. *et al.* Phonon splitting and anomalous enhancement of infrared-active modes in $BaFe_2As_2$. *Phys. Rev. B* **84**, 052501 (2011). 168

[387] Zhang, A. & Zhang, Q. Raman scattering in iron-based superconductors. *Modern Physics Letters B* **26**, 12300207 (2012). 168, 170

[388] Gallais, Y. *et al.* Temperature dependence and resonance effects in Raman scattering of phonons in $NdFeAsO_xF_{1-x}$ single crystals. *Phys. Rev. B* **78**, 132509 (2008). 170

[389] Granath, M., Bielecki, J., Holmlund, J. & Börjesson, L. Anharmonic softening of Raman active phonons in iron-pnictides: Estimating the Fe isotope effect due to anharmonic expansion. *Phys. Rev. B* **79**, 235103 (2009). 170

[390] Zhang, L. *et al.* Doping and temperature dependence of Raman scattering from $NdFeAsO_{1-x}F_x$ (x=0-0.2) superconductor. *Phys. Rev. B* **79**, 052507 (2009). 170

[391] Choi, K.-Y. *et al.* Lattice and electronic anomalies of $CaFe_2As_2$ studied by Raman spectroscopy. *Phys. Rev. B* **78**, 212503 (2008). 170, 171

[392] Choi, K.-Y. *et al.* Self-energy effects and electron-phonon coupling in Fe-As superconductors. *Journal of Physics Condensed Matter* **22**, 115802 (2010). 170, 171

[393] Siranidi, E. *et al.* Micro-Raman and infrared study of $NdFeAsO_{0.85}$. *Journal of Alloys and Compounds* **487**, 430–433 (2009). 172

[394] Liarokapis, E., Calamiotou, M., Zhigadlo, N., Katrych, S. & Karpinski, J. Nonlinear lattice response of Sm oxypnictides to hydrostatic pressure. *Journal of Physics and Chemistry of Solids* **74**, 1465 (2013). 172, 173, 174

[395] Colombier, E., Bud'Ko, S., Ni, N. & Canfield, P. Complete pressure-dependent phase diagrams for $SrFe_2As_2$ and $BaFe_2As_2$. *Phys. Rev. B* **79**, 224518 (2009). 177

[396] Fukazawa, H. *et al.* Suppression of magnetic order by pressure in $BaFe_2As_2$. *Journal of the Physical Society of Japan* **77**, 105004 (2008). 177

[397] Matsubayashi, K. *et al.* Intrinsic properties of AFe_2As_2 (A = Ba, Sr) Single Crystal under highly hydrostatic pressure conditions. *Journal of the Physical Society of Japan* **78**, 073706 (2009). 177

[398] Wu, J. J. *et al.* Pressure-decoupled magnetic and structural transitions of the parent compound of iron-based 122 superconductors $BaFe_2As_2$. *Proceedings of the National Academy of Sciences* **110**, 17263 (2013). 177

[399] Liu, R. *et al.* Anomalous transport properties and phase diagram of the FeAs-based $SmFeAsO_{1-x}F_x$ superconductors. *Phys. Rev. Lett* **101**, 087001 (2008). 177